Seismology of magnetic massive stars

Bram Buysschaert

THÈSE DE DOCTORAT

de l'Université de recherche Paris Sciences et Lettres
PSL Research University

Préparée dans le cadre d'une cotutelle entre l'observatoire de Paris et le KU Leuven

Asteroseismology of magnetic massive stars

Ecole doctorale n°127

Astronomie et Astrophysique d'Île-de-France

Spécialité Astrophysique

COMPOSITION DU JURY :

Mme. CHARBONNEL Corinne
Université de Geneve, Rapportrice

M. CHARPINET Stéphane
IRAP, Rapporteur

Mme. NEINER Coralie
LESIA, Directrice de thèse

Mme. AERTS Conny
KU Leuven, Directrice de thèse

M. HEYDARI-MALAYERI Mohammad
LERMA, Président du jury

M. VAN DOORSSELAERE Tom
KU Leuven, Membre du jury

Soutenue par
Bram BUYSSCHAERT
le 26 avril 2018

Dirigée par **Coralie NEINER**
et **Conny AERTS**

l'Observatoire de Paris

PSL RESEARCH UNIVERSITY PARIS

Acknowledgements

It has been a long and winding road to reach this point in my career that stretched over four continents, past three telescopes, and over various mountains. Many people have accompanied and guided me along this journey, who ensured that this journey was truly memorable and a great success. I want to explicitly thank these people.

First and foremost, I want to thank my thesis supervisors Dr. Coralie Neiner and Prof. Conny Aerts, without whom this journey would never have taken place. You have continued to push me forward, both as a researcher and as a person, and have allowed this journey to pass along all these (scientifically) interesting places. Coralie, thank you for always making time to answer my questions, how trivial they might have been or at what time of the day they were asked, and providing an apt remark whenever I wanted more observations. (I know now that I indeed do not need more data.) Conny, thank you for your patience and honing my scientific instincts. You were always ready to help and provided the means and guidance to finish this thesis on time. I aspire to one day be as efficient as you. Péter, thank you for guiding me at the start of my thesis, teaching me everything you know about observing and data massaging.

To the members of my jury, thank you for providing me with constructive comments and suggestions to improve this manuscript.

To the various teams supporting the BRITE, CoRoT and K2 missions, the TBL, ESO and CFHT staff, the MESA and GYRE developers, thank you for enabling me to conduct my research to the fullest.

To those that supported me whenever a bug was plaguing my code, my star was doing something I was not expecting it do, when I was fed up writing, or when I was ready to give up. Thank you for bullying me to continue my journey and to not give up. (You know who you are.) (Yes, I do still owe you all a beer.)

To the amazing colleagues at the *Instituut voor Sterrenkunde* and the

Observatoire de Paris, thank you for creating a nice atmosphere at work and being great friends. You have defined much of the adventure along this journey. I hope we will continue to meet up for activities and drinks. (But, without the tequila!)

Konstanze, Timothy, Aurore, Victor, Dominic, Enya and Joey, thank you for having the impromptu brainstorm sessions in the office, potential nerf-wars and coping with all my loud music I was listening to during a caffeine-induced scripting spree.

To the BRITE karaoke team, thank you for creating many memorable moments at the conferences scattered along my journey. I will fondly remember these for years to come. To the New Zealand team, thank you for making that trip across that beautiful country.

Aan iedereen van Dorst en Annaporna, bedankt om me zo veel te komen bezoeken tijdens mijn verblijf in Paris en om de nodige afleiding te bezorgen.

Aan Maarten, Mattias, Marijke en Stein, bedankt voor jullie steun en de afleiding met klimmen en board-game namiddagen.

Coorteux, merci pour tous! Vous m'avez fait vivre Paris au maximum et tout ça sous le prétexte de faire l'escalade. Mon séjour à Paris n'aurait pas été le même sans vous! Vous me manquez profondément!

To all the passionate scientists I have spoken with or have worked with, thank you.

To all those other people I have met during my journey, thank you for making it together.

Een speciaal woord van dank gaat uit naar mijn vader en Isabelle. Bedankt voor alle kansen die jullie mij hebben gegeven en jullie onflaatbare steun en enthousiasme om dit mogelijk te maken. Bedankt aan mijn broer en zussen voor alle steun!

Friday April 13, 2018

Bram

Abstract

About ten percent of stars with spectral type O, B or A have a detectable stable strong large-scale magnetic field at their surface, which most often resembles a magnetic dipole. These large-scale magnetic fields extend into the radiative layers of the OBA stars. Theory and simulations predict that they alter the internal structure and physical properties of these stars. In particular, it is expected that these large-scale magnetic fields enforce uniform rotation in the radiative layers and may suppress convective core overshooting. This has consequences for the evolution of these magnetic hot stars and it has implications for galactic evolution. Therefore, we observed and investigated the internal structure of magnetic hot stars. To do so, asteroseismology is the best method as the oscillation properties are directly related to the internal physical conditions. Various types of stellar oscillations are known and they are classified based on their dominant restoring force. Of these, gravity modes are governed by the buoyancy force and have their strongest probing power in the near core region, which is the domain of our interest.

Our first objective was to identify pulsating magnetic hot stars and characterize their magnetic and seismic properties. We constructed a sample of magnetic candidate stars, by following indirect observational diagnostics for the presence of a large-scale magnetic field, to confirm with ground-based high-resolution optical spectropolarimetry taken with ESPaDOnS, Narval or HARPSpol. For two known magnetic stars, HD43317 and o Lup, we characterized the geometry and strength of the field in detail by analysing spectropolarimetric time series.

For each star in our sample, we obtained high-cadence high-precision space-based photometry from BRITE, CoRoT, or K2 to study (periodic) variability. Only HD43317 revealed tens of stellar pulsations mode frequencies that pointed towards gravity modes. For this star, many of the pulsation mode frequencies were lower or similar to the rotation frequency. Only a few other stars studied showed a few pulsation mode frequencies, unsuitable for seismic modelling.

We investigated the B3.5V star HD43317 in detail to determine the internal structure of a magnetic hot star. We did this by forward seismic modelling, where observed stellar pulsation mode frequencies in the CoRoT data covering ∼150d were fit to those of gravito-intertial modes computed with the pulsation code GYRE, coupled to MESA stellar structure models. We identified the pulsation mode frequencies as overlapping (l, m) = (1,-1) and (2,-1) mode series. The small convective core overshooting region derived from the seismic modelling was in line with the theoretical predictions. Yet, some of the parameters for the best fitted models were also compatible with literature values for non-magnetic pulsators within the derived uncertainties. We conclude that the CoRoT time series of ∼150d is too short to lead to stringent constraints and tests of the stellar interior to discriminate between magnetic and non-magnetic pulsating hot stars.

From our detailed modelling efforts of the best studied pulsating magnetic hot star HD43317, we were unable to observationally corroborate the theoretical predictions of an altered internal structure for magnetic hot stars. Simplifications and approximations were made during the forward seismic modelling due to the limited frequency resolution of the CoRoT data in terms of its time base. Further efforts to include magnetism in the pulsation codes, or magnetism, rotation, and angular momentum transport in the evolutionary models, are worthwhile to test whether magnetic signatures are present in the numerous (non-magnetic) gravito-inertial pulsators recently found in the nominal Kepler database (which has a ten times better frequency resolution compared to CoRoT).

Beknopte samenvatting

Naar schatting hebben 10 % van de sterren met spectraaltype O, B of A een meetbaar, sterk en stabiel grootschalig magneetveld aan hun oppervlak. In vele gevallen is het magnetisch veld te benaderen als een dipoolveld dat zich tot diep in de radiatieve lagen van de OBA sterren uitstrekt. Theoretische modellen en numerieke simulaties voorspellen dat dit magnetisch veld de interne sterstructuur en de interne fysische eigenschappen beïnvloedt. In het bijzonder zouden deze grootschalige magneetvelden uniforme rotatie afdwingen in de radiatieve lagen van de ster, alsook convectieve kernoverschrijding onderdrukken. Dit heeft impact op de verdere sterevolutie en bijgevolg ook voor de evolutie van de sterrenstelsels doordat deze zware sterren veel van de zware elementen in het heelal produceren. In dit werk trachten we meer observationeel inzicht te verwerven in de interne structuur van deze magnetische hete sterren. Hiertoe maken we gebruik van asteroseismologie, oftewel de studie van stertrillingen, die hiervoor de beste techniek is omdat de eigenschappen van de stertrillingen direct gerelateerd zijn aan de interne fysische omstandigheden. Er zijn verschillende soorten stertrillingen gekend en deze worden opgedeeld volgens hun dominante herstelkracht. Een type die voor deze studie van groot belang is zijn de graviteitsgolven, die bepaald worden door de stuwkracht van Archimedes, omdat deze trillingen het meest geschikt zijn om de omgeving rond de sterkern te bestuderen. Dit is de omgeving die we observationeel willen toetsen.

Het eerste doel van de thesis was om nieuwe magnetische pulserende hete sterren te identificeren en hun magnetische en seismische eigenschappen te beschrijven. Een selectie van zestien kandidaat magnetische hete sterren werd samengesteld op basis van hun indirecte kentekenen van het magneetveld. We bevestigden de aanwezigheid van een sterk magneetveld voor twaalf sterren met hoge-resolutie optische spectropolarimetrie genomen met het ESPaDOnS instrument. De vier andere sterren toonden enkel indirecte aanwijzingen van een zwak magneetveld door waargenomen chemische eigenaardigheden. Voor twee gekende magnetische hete sterren, namelijk HD 43317 en *o* Lup, hebben we

de sterkte, orientatie en geometrie van het magneetveld gekarakteriseerd. Dit gebeurde met spectropolarimetrische metingen over verscheidene rotatiefases met de ESPaDOnS, Narval en HARPSpol instrumenten. Daarnaast hebben we voor alle vermelde sterren een precieze fotometrische tijdreeks van minstens 60 d verkregen uit waarnemingen van de BRITE, K2 of CoRoT ruimtetelescopen. Deze studie liet ons toe om de (periodieke) variabiliteit van deze sterren te bestuderen. Slechts van enkele van de onderzochte magnetische sterren kon, na het in rekening brengen van de rotatieperiode, aangetoond worden dat de coherente periodieke variatie deels het gevolg was van stertrillingen. De sterren HD 158596, HD 177765 en *o* Lup vertoonden één of enkele stertrillingen, terwijl HD 43317 tientallen onafhankelijke frequenties vertoonden die graviteitsgolven suggereerden. Veel van de geobserveerde trillingen hebben een frequentie die kleiner of gelijkaardig is aan de rotatie frequentie, bijgevolg zal in deze gevallen de Coriolis kracht ook optreden als de herstelkracht van de stertrillingen.

In een vervolgstudie hebben we ons toegespitst op de ster HD 43317 om observationeel de interne structuur van deze magnetische hete ster te bepalen. We deden dit volgens de voorwaartse seismische modelleringsmethode. Hierbij werden de geobserveerde stertrillingfrequenties van de $\sim$150 d CoRoT data getoetst aan model frequenties van graviteitsgolven die berekend werden met de pulsatiecode GYRE voor MESA sterstructuurmodellen. Op deze manier werden de geobserveerde frequenties als overlappende series van $(\ell, m) = (1, -1)$ en $(2, -1)$ modi beschreven. De kleine hoeveelheid convectieve kernoverschrijding van het optimale MESA model was consistent met de theoretische voorspellingen. De betrouwbaarheidsintervallen op bepaalde fysische grootheden waren echter ook ruim en consistent met literatuurwaarden voor niet-magnetische pulserende hete sterren. Dit is het gevolg van een ontaarding tussen de verschillende sterstructuurmodellen door gelijke waarden voor de asymptotische periodespatiëring. Uit deze studie kon besloten worden dat de $\sim$150 d data ontoereikend zijn om de interne structuur van magnetische hete sterren op een eenduidige manier te bepalen, en bijgevolg om hun interne structuur van niet-magnetische hete sterren te kunnen onderscheiden.

Op basis van de gebruikte modellen en observaties kon de theoretisch voorspelde gewijzigde kernstructuur in de pulserende magnetische hete ster HD43317 niet bevestigd worden. Verscheidene aannames en vereenvoudigingen waren nodig tijdens het modelleren van de CoRoT data omwille van de beperkte frequentieresolutie. Verdere inspanningen om magnetisme in pulsatiecodes toe te voegen, alsook magnetisme en rotatie in sterevolutiecodes, zijn noodzakelijk indien men verder wil onderzoeken of magnetisme een mogelijke rol speelt voor de vele (niet-magnetische) hete sterren met graviteitsgolven gedetecteerd in de *Kepler* data (met een tien keer langere tijdsbasis dan CoRoT).

Résumé

Environ 10% des étoiles de type spectral O, B ou A ont un champ magnétique fort, détectable, stable et à grande échelle à leur surface, qui ressemble le plus souvent à un dipôle. Des modèles théoriques et des simulations numériques prédisent ces champs magnétiques vus en surface pénètrent aussi dans les zones radiatives et influencent la structure interne. Les modèles prédisent que ces champs magnétiques imposent une rotation uniforme dans les zones radiatives et peuvent supprimer la pénétration convective autour du cœur. Cela a des conséquences sur l'évolution de ces étoiles chaudes magnétiques. Pour ce faire, l'astérosismologie est la meilleure méthode car les paramètres des pulsations stellaires sont directement liés aux conditions physiques internes. Plusieurs types de pulsations stellaires sont connus et classés en fonction de leur force de rappel. Parmi eux, les plus à même de sonder les régions proches du cœur des étoiles, sur lequel se concentre notre intérêt dans cette thèse sont les modes de gravité, qui sont gouvernés par la force d'Archimède.

Notre premier objectif était d'identifier des étoiles chaudes, pulsantes et magnétiques et de caractériser leurs propriétés magnétiques et sismiques. Des étoiles ont été sélectionnées grâce à des diagnostics observationnels indirects de la présence d'un champ magnétique qou nous confirmons grâce à de la spectropolarimétrie optique à haute résolution obtenue avec ESPaDOnS, Narval et ESPaDOnS. Pour deux étoiles magnétiques connues, HD43317 et o Lup, nous avons caractérisé la géométrie et l'intensité du champ magnétique aves des séries temporelles spectropolarimétriques. Pour toutes les étoiles de notre échantillon, nous avons également obtenu des séries temporelles photométriques très précises grâce aux télescopes spatiaux BRITE, CoRoT ou K2 pour étudier leur variabilité (périodique) cohérente. Seulement HD43317 a révélé des dizaines de fréquences de pulsations stellaires, pointant plutôt vers des modes de gravité.

Nous nous sommes ensuite concentrés sur HD43317 dans pour déterminer observationellement la structure interne de cette étoile magnétique chaude. Nous avons fait usage de modélisation sismique: les fréquences des modes de

pulsations observées dans les données CoRoT, couvrant 150j, ont été ajustées à celles des modes gravito-inertiels calculés avec le code de pulsations GYRE couplé aux modèles MESA. Nous avons pu associer les fréquences des modes de pulsations à des séries de modes (l,m) = (1,1) et (2,1) se chevauchant. La petite zone de pénétration convective dans la zone radiative telle que déduite du modèle MESA optimal s'avère cohérente avec les prédictions théoriques. Néanmoins, les intervalles de confiance sur certains paramètres physiques issus des modèles sont très larges et compatibles avec les valeurs de la littérature pour des étoiles chaudes et pulsantes mais non-magnétiques. Nous en concluons que la série temporelle de 150j de données CoRoT est trop courte pour déterminer d'une manière non-équivoque la structure interne des étoiles magnétiques chaudes, et par conséquent pour distinguer leur structure interne de celle des étoiles chaudes non-magnétiques.

Malgré nos efforts de modélisation détaillée de la meilleure étoile chaude pulsantemagnétique HD43317, nous n'avons pas pu corroborer observationnellement les prédictions théoriques d'une structure interne altérée pour les étoiles chaudes magnétiques. Des simplifications et des approximations ont dû être faites au cours de la modélisation sismique en raison de la résolution en fréquence limitée des données CoRoT. D'autres efforts pour inclure le magnétisme dans les codes de pulsations ou le magnétisme, la rotation et le transfert du moment cinétique dans les modèles d'évolution stellaire seront nécessaires afin de déterminer si les signatures magnétiques sont présentes pour les nombreux pulsateurs gravito-inertiels récemment découverts dans la base de données de Kepler.

"*All life is an experiment. The more experiments you make the better.*"

Ralph Waldo Emerson

Contents

Part I

Introduction and outline

Chapter 1

Scientific framework: intermediate-mass and massive stars

1.1 Stellar structure and evolution

The structure and evolution of stars depends on their physical properties. Below we describe the structure and evolution of intermediate-mass and massive stars studied in this thesis.

1.1.1 Stellar structure

Stars are often described as large spheres of hot gas in equilibrium. While this description is very simplistic, it contains two assumptions still used in rigorous attempts to describe and model stars (excellent monographs are for example given by Maeder 2009 and Kippenhahn et al. 2012), namely that a star is a perfect sphere and that the net force on a macroscopic mass element is zero. The first assumption permits spherical symmetry to be used, and the latter is called hydrostatic equilibrium. If the effects of rotation and magnetism are ignored, these assumptions lead to the following set of differential equations, to

be fulfilled by the physical quantities that govern the stellar structure:

$$\frac{\partial P(m,t)}{\partial m} = -\frac{Gm}{4\pi r(m,t)^4} - \frac{1}{4\pi r(m,t)^2}\frac{\partial^2 r(m,t)}{\partial t^2}\,, \tag{1.1}$$

$$\frac{\partial r(m,t)}{\partial m} = \frac{1}{4\pi r(m,t)^2 \rho(m,t)}\,, \tag{1.2}$$

$$\frac{\partial L(m,t)}{\partial m} = \epsilon_n(m,t) - \epsilon_\nu(m,t) + \epsilon_{\rm grav}(m,t)\,, \tag{1.3}$$

$$\frac{\partial T(m,t)}{\partial m} = -\frac{GmT(m,t)}{4\pi r(m,t)^4 P(m,t)}\nabla(m,t)\,, \tag{1.4}$$

$$\frac{\partial X_i(m,t)}{\partial m} = \frac{m_i}{\rho(m)}\left[\sum_j r_{ji}(m) - \sum_k r_{ik}(m)\right] \text{ and } i = 1, ..., I\,. \tag{1.5}$$

These equations follow from the basic laws of physics. The unknowns represent the pressure $p(m)$, radius $r(m)$, density $\rho(m)$, luminosity $L(m)$, temperature $T(m)$, and mass fraction X_i of ions of type i inside the star as a function of the independent mass coordinate m, where m=0 at the center of the star and m=$M_\star$ at the surface of the star at a given time t. The quantities $\epsilon_n(m)$, $\epsilon_{\rm grav}(m)$, and $\epsilon_\nu(m)$ indicate the energy generated by nuclear fusion reactions, by gravitational contraction, and lost by emitted neutrinos, respectively. The temperature gradient $\nabla(m)$ is defined as $\frac{{\rm d}\ln T(m)}{{\rm d}\ln P(m)}$.

Ignoring the second term on the right-hand side of Eq. (1.1) leads to the physical form of the hydrostatic equilibrium assumption, stating that the pressure force exerted on a mass element at m is exactly counterbalanced by the gravity acting upon it (where G is the gravitational constant). If hydrostatic equilibrium is not fulfilled, the gas will undergo an accelerated motion.

The second equation (i.e., Eq. (1.2)) is called the mass continuity equation and describes the distribution of the mass inside the star, whereas Eq. (1.3) represents the conservation of energy.

Equation (1.4) indicates the energy transport happening inside the star under the condition of hydrostatic equilibrium. In case all energy is transported by radiation only (and conduction), $\nabla(m)$ can be expressed as

$$\nabla(m) = \nabla_{\rm rad}(m) = \frac{3}{16\pi acG}\frac{\kappa(m)L(m)P(m)}{mT(m)^4}\,, \tag{1.6}$$

where c is the speed of light, a the radiation density constant, and $\kappa(m)$ the Rossland mean opacity. The other distinct case is when part of the energy is

transported by means of convection, where macroscopic mass elements with a higher temperature compared to their environment travel inside the star (governed by buoyancy) to dissipate their energy elsewhere. Besides energy transport, this process also drastically increases the chemical mixing. The most widely used description of convection is the mixing length theory (see e.g., Böhm-Vitense 1958; Henyey et al. 1965; Cox & Giuli 1968, for a detailed description) that simplifies these highly chaotic convective motions to a one dimensional description applicable under the assumption of spherical symmetry. The energy transported by the macroscopic mass elements is expressed as a function of their free mean path, which is actually described as $\alpha_{\rm mlt} H_{\rm p}$. Here $\alpha_{\rm mlt}$ is the unit-less mixing length parameter and $H_{\rm p}$ the local pressure scale height defined as

$$H_{\rm p}(m) \equiv -\frac{{\rm d}r(m)}{{\rm d}\ln P(m)} = -P(m)\frac{{\rm d}r(m)}{{\rm d}P(m)}\,. \tag{1.7}$$

Larger values for $\alpha_{\rm mlt}$ indicate a more efficient energy transport by convection. The mixing length $\alpha_{\rm mlt}$ is a free parameter or is calibrated from observations[1], with typical values ranging from 1.0 to 2.0 when the borders of observed instability strips of intermediate-mass stars are considered (e.g., Dupret et al. 2005, see Sect. 1.3). Two different criteria have been developed to test whether convection occurs in a certain layer inside the star. The first is called the Schwarzschild criterion and states that convection occurs if

$$\nabla_{\rm ad}(m) \equiv \left(\frac{{\rm d}\ln T(m)}{{\rm d}\ln P(m)}\right)_{\rm S} < \nabla_{\rm rad}(m)\,, \tag{1.8}$$

with $\nabla_{\rm ad}(m)$ the adiabatic temperature gradient for the macroscopic mass element m. When a chemical gradient is accounted for, one can use the Ledoux criterion for convection

$$\nabla_{\rm ad}(m) + \frac{\phi(m)}{\delta(m)}\nabla_{\mu}(m) < \nabla_{\rm rad}(m)\,, \tag{1.9}$$

with

$$\phi(m) \equiv \left(\frac{\partial\ln\rho(m)}{\partial\ln\mu(m)}\right)_{P,T};\ \delta(m) \equiv -\left(\frac{\partial\ln\rho(m)}{\partial\ln T(m)}\right)_{P,\mu};\ \nabla_{\mu}(m) \equiv \left(\frac{{\rm d}\ln\mu(m)}{{\rm d}\ln P(m)}\right) \tag{1.10}$$

defined for the environment around the unstable mass elements. From the Ledoux criterion, it follows that the chemical gradient $\nabla_{\mu}(m)$ has a stabilising effect against convection. Regions in the star that are unstable against convection

[1] A famous calibration comes from the Sun, where model computations were compared to helioseismic observations, leading to $\alpha^{\odot}_{\rm mlt}$=1.99 (e.g., Christensen-Dalsgaard et al. 1996; Christensen-Dalsgaard 2002)

according to the Schwarzschild criterion but not the Ledoux criterion are called semi-convective.

Since travelling mass elements have a non-zero inertia, they can pass the exact stability boundaries defined by the two criteria. Such regions are defined as convective overshooting regions and are much smaller than the convective layers themselves. They extend over a distance $\alpha_{\rm ov} H_{\rm p}$, where $\alpha_{\rm ov} < \alpha_{\rm mlt}$ is an unknown free parameter.

The last set of equations (i.e., Eq. (1.5)) represents the nuclear reaction network inside the star for an ion i with mass m_i. The reaction rate $r_{ji}(m)$ indicates the number of reactions per unit mass (and unit time) that generated ion i, while $r_{ik}(m)$ gives the loss of ion i to k by various chemical reactions. In the equations for the nuclear reaction network (i.e., Eq. (1.5)), mixing processes are ignored. They are usually described by a separate set of equations not listed here (see e.g., Chapter 8 of Kippenhahn et al. 2012).

To be able to solve Eqs. (1.1) – (1.5), an equation of state (EOS) is needed to relate various physical properties to each other. The most commonly used EOS is the ideal gas law with the addition of radiation pressure (see Eq. (1.11)), which characterizes pressure $P(m)$ as a function of density $\rho(m)$, temperature $T(m)$, and chemical composition $X_i(m)$ The chemical composition is expressed as the mean molecular weight $\bar{\mu}(m)$, leading to

$$P(m) = \frac{\mathcal{R}}{\bar{\mu}(m)} \rho(m) T(m) + \frac{a}{3} T(m)^4 \,, \tag{1.11}$$

where $\mathcal{R}$ is the universal gas constant. From the assumed EOS, quantities such as $\kappa(m)$ or $\epsilon_n(m)$ can be further derived. More complicated EOS are also used, where additional physical interactions are accounted for. Such EOS are numerically solved and provided in tabulated versions, to solve the stellar structure equations. Widely used descriptions come from the Opacity Project (OP, Badnell et al. 2005) or OPAL (Rogers & Iglesias 1992; Iglesias & Rogers 1993, 1996). Finally, appropriate boundary conditions (at the stellar center and surface) and initial conditions have to be imposed to retrieve meaningful solutions to the stellar structure equations.

The stellar structure equations are also inherently time dependent. Yet, the time scales governing the temporal changes are not the same for all equations. Equations (1.1) – (1.4) vary on a dynamical time scale, following readjustments to the hydrostatic equilibrium, while Eq. (1.5) changes on the much longer nuclear time scale. As such, the stellar structure equations are very often solved for a given time t, representing a stellar model, while the stellar evolution is represented by computing stellar models at hydrostatic equilibrium at carefully crafted discrete time steps.

The above description of stellar structure becomes more complicated when effects of rotation or magnetism are included, breaking the spherical symmetry assumption. More rigorous two-dimensional (or even three-dimensional) descriptions are then needed, coming at a much higher computational cost. It is currently not feasible to compute stellar evolution models in 2D or 3D and this will not change in the foreseeable future.

1.1.2 Stellar evolution

A good understanding of the global effects of stellar evolution has been established by using stellar models computed with the above mentioned equations for stellar structure and comparing them to various observational diagnostics of many stars. Here, we summarize this for intermediate-mass stars ($2 \lesssim M_\star \lesssim 8\,\mathrm{M}_\odot$) and massive stars ($M_\star \gtrsim 8\,\mathrm{M}_\odot$), ignoring the possible effects of rotation, magnetism, and binarity. We refer again to Kippenhahn et al. (2012) for a more rigorous and mathematical description of the various stellar evolutionary phases. The evolution of stars with different birth masses throughout the Hertzprung-Russell diagram are indicated in the top panel of Fig. 1.1. The changes in stellar structure for a $5.8\,\mathrm{M}_\odot$ is given by a Kippenhahn diagram in the bottom panel of Fig. 1.1.

Stars form when a dense molecular cloud with sufficient mass becomes unstable due to a perturbation, often a shock generated close by or the passage of a density fluctuation in spiral arms. When this cloud becomes unstable, it collapses under its own gravity. This contraction phase initially happens isothermally, creating regions of enhanced density, causing the molecular cloud to fragment into many parts of various mass. The newly formed fragments continue to contract onto their central core and they become optically thick so only a limited amount of radiation can escape, heating up the matter in response. This temperature increase results in a pressure increase that will eventually counterbalance and stop the gravitational contraction, creating a proto-star in hydrostatic equilibrium. Moreover, the increasing temperature causes the molecular hydrogen to dissociate, opening the pathway to future nuclear burning once the central temperature is sufficiently high. Meanwhile, the pre-main-sequence (pre-MS) star continues to accrete gaseous matter from its close vicinity, while part of the more distant and cooler material will remain and may eventually form a planetary system. Once stable core hydrogen burning has been established due to the increasing central temperature and operates in full equilibrium, the star is said to have arrived at the zero-age main-sequence (ZAMS). Core hydrogen burning of intermediate-mass and massive stars happens in a fully convective core and predominantly by the CNO cycle, with only minor contributions from the proton-proton chains.

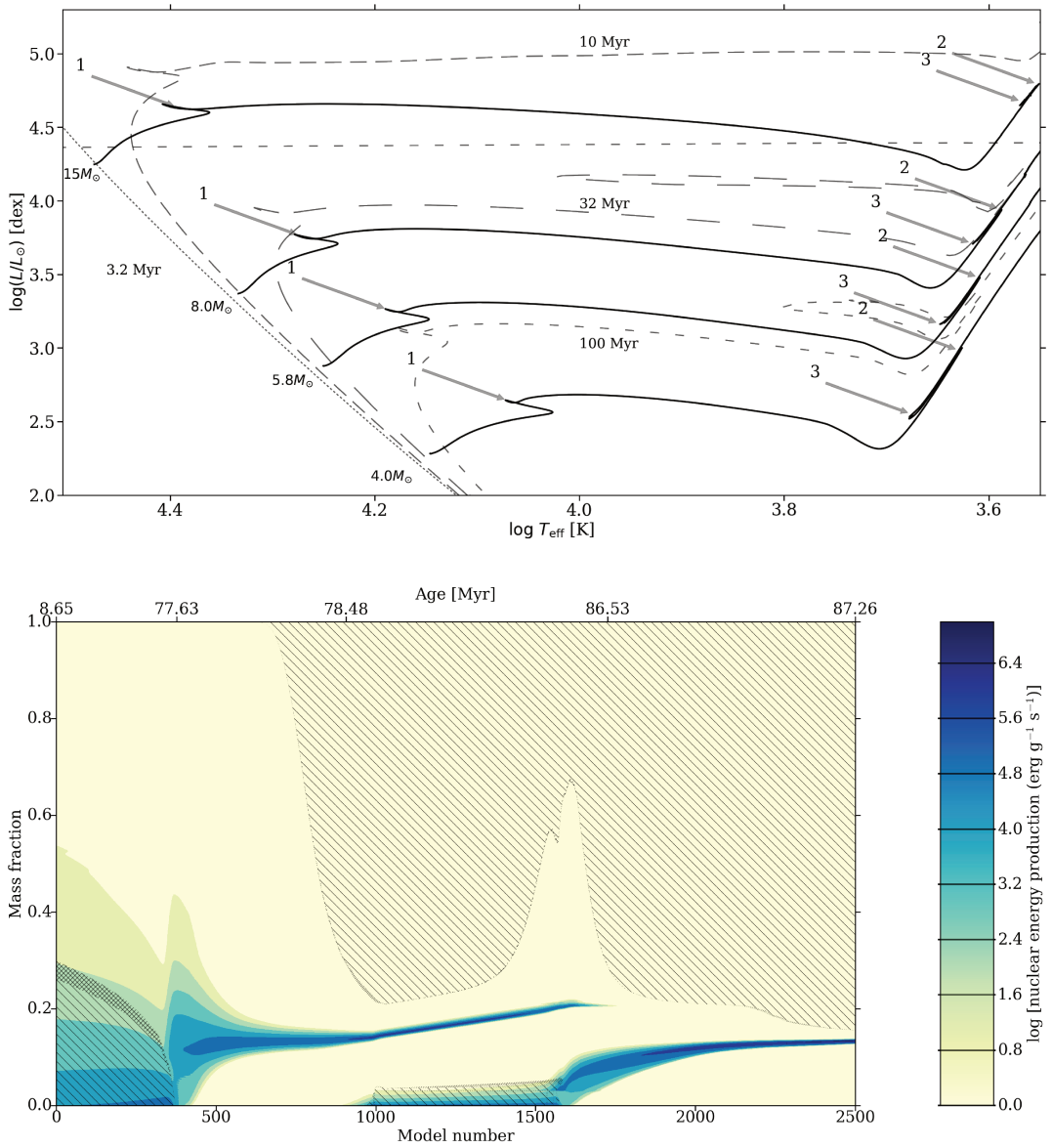

Figure 1.1: *Top*: Hertzsprung–Russell diagram with four evolutionary tracks indicated by the solid black lines (for an initial mass of 15.0, 8.0, 5.8 and 4.0 $M_\odot$) computed with MESA (v8118). Arrows respectively indicate the TAMS (1), the on-set of helium helium-burning (2), and the end of helium core-burning (3). Publicly available MIST isochrones are indicated for three different ages (grey dashed lines, computed with MESA v7503 and retrieved from Choi et al. 2016). *Bottom*: Kippenhahn diagram showing the change in internal structure due to the stellar evolution for the 5.8 $M_\odot$ evolutionary model depicted in the Hertzsprung-Russel diagram as a function of stellar model (i.e., stellar age) and mass fraction. The colour scale represents the nuclear energy production and the hatched areas indicate convective mixing is happening. Fully convective regions are marked by single hatching ('\\') and convective overshooting by the double hatching.

All stars spend the vast majority of their respective lifetimes on the main-sequence (MS), steadily burning hydrogen into helium in their core. The stars discussed later in this work are all thought to reside on the MS (except ζ Ori Aa; see Chapter 5). The more massive a star is, the faster it passes through this evolution as the nuclear burning happens much faster due to the increased dependence on the central temperature. Once the hydrogen runs out in the convective core, hydrogen core burning stops, and the star has arrived at the terminal-age main-sequence (TAMS; marked by the arrows with a '1' in the top panel of Fig. 1.1). The lack of nuclear burning leads to insufficient pressure to keep on balancing gravity. In response, the formed helium core contracts, increasing the central temperature, and the outer layers expand, decreasing the temperature in these layers. As the central temperature increases, the temperature just above the contracting helium core also increases, which ignites hydrogen burning in a concentric shell around the helium core once a necessary temperature has been achieved there. (The star ζ Ori Aa is likely in this fast evolutionary stage.) The star enters the red giant stage with a denser contracting helium core, a hydrogen burning shell, and an extended convective envelope. This convective envelope undergoes efficient chemical mixing, which can bring the results of the CNO burning to the stellar surface, depending on the birth mass (i.e., the first dredge-up).

The temperature in the contracting helium core continues to rise and eventually leads to core helium burning (marked by the arrows with a '2' in the top panel of Fig. 1.1), converting ^{4}He into ^{12}C by means of the 3α reaction. Once all helium in the core has been exhausted (marked by the arrows with a '3' in the top panel of Fig. 1.1), the red giant evolutionary stage comes to an end. At this point, a strong bifurcation happens according to the stellar mass $M_\star$ for the remainder of the stellar evolution. We first discuss the evolution for the intermediate-mass stars and then the massive stars.

The produced CO core of the intermediate-mass stars contracts, but reaches such a high density that the electrons can no longer reside in their shells, since the ions are too closely packed together. Instead, the electrons float in between the ions. The matter is said to be electron degenerate and a very different EOS is governing such matter. During the contraction of the CO core, hydrogen shell burning has continued and also helium shell burning starts. This is the asymptotic giant branch (AGB) stage. The convective envelope continues to expand and alters the surface chemical distribution during the second dredge-up. Stars in the AGB stage also undergo strong mass loss from their weakly bound envelope by means of a dust-driven stellar wind (see e.g., Lamers & Cassinelli 1999, for a thorough description of stellar winds). Because of different dependencies on the local conditions for the hydrogen and helium burning, a cyclic phenomenon occurs in the AGB stage. The hydrogen shell burning

produces additional helium in the inter-shell region. The helium shell continues to contract, and thus heat up. This increased temperature violently restarts the stalled helium shell burning due to the partial electron degeneracy. The layers above absorb the produced energy and expand outwards, which might possibly stall the hydrogen shell burning. The violent helium burning also creates a local convection layer that transports energy to the hydrogen rich layers, restarting the hydrogen shell burning. The helium shell burning creates a heavier CO core and expands, which causes the local temperature to decrease. At that point in time, hydrogen shell burning is again the only nuclear energy source and a new cycle starts. These cycles are called thermal pulses. They are also responsible for the production of many heavy chemical elements through the s-process (where slow neutron capture occurs). These heavy elements are then partly transported to the stellar surface during the third dredge-up. The thermal pulses also increase the mass loss of the hydrogen rich envelope. When the envelope is almost completely expelled, hydrogen shell burning stops and the mass loss as well. The degenerate CO core becomes visible and is called a white dwarf. No more nuclear reactions occur nor gravitational contraction, so the white dwarf gradually cools down on a very long time scale.

The contraction phase of the CO core after helium burning has ceased does not lead to a degenerate core for the massive stars (born with $M_\star \gtrsim 8\,\mathrm{M}_\odot$). Instead, it will continue to contract until the conditions are sufficient to start carbon core burning, mainly producing neon. Meanwhile, helium shell burning and hydrogen shell burning have started and continued, respectively. Once the carbon in the core has been exhausted, a new contraction phase follows, which will result in the onset of neon burning, mainly generating oxygen, as well as carbon shell burning, helium shell burning, and hydrogen shell burning. These fast evolutionary stages continue with oxygen core burning, producing silicon, and silicon core burning, generating iron and nickel, underneath consecutive layers of nuclear shell burning. Once an iron core has been formed, nuclear fusion in the core implies a loss of energy and does no longer provide a counterbalance for gravity: the core collapses and the weakly bound envelope is violently expelled outwards in a supernova explosion. During the supernova, photo-dissociation changes most of the iron and nickel into protons, electrons, and neutrons, and these neutrons are rapidly captured to produce neutron-rich heavy chemical elements in the expelled envelope through the r-process. In the end, only a neutron star (or a black hole) remain, with expanding material around it.

The intermediate-mass and massive stars return much of their initial mass back to their surroundings, which may eventually lead to the birth of new stars. Moreover, the expelled matter has a different chemical composition than the initial matter due to the many nuclear reactions. Thus, they continue to chemically enrich their host galaxy and the Universe as a whole.

1.1.3 MESA

Various tools have been developed to compute stellar structure models, using the stellar structure equations (Eqs. (1.1) – (1.5)), and to progress these throughout the star's evolution. One such tool is the STAR module of the Modules for Experiments in Stellar Astrophysics (MESA; Paxton et al. 2011, 2013, 2015) code, which is an open-source[2] one-dimensional stellar evolution code. It builds upon many additional modules that deal with various aspects of the theoretical models, such as the EOS, nuclear reaction networks, chemical composition, micro-physics, or macro-physics. The EOS and corresponding opacities or nuclear networks are provided in tabulated formats and can be selected by the user, while the micro-physics and macro-physics can be controlled by INLISTS of relevant parameters and settings. This makes MESA highly customizable and adaptable to a wide variety of study cases.

MESA works according to the Henyey principle (Henyey et al. 1959), where the star is sub-divided in a finite number of grid cells for which the local conditions are evaluated and computed from the surface inwards to the center by utilizing a Newton-Raphson solver. Relevant physical quantities are either defined at the cell boundaries (e.g., m, $r(m)$, $L(m)$) or as mean values over the complete cell (e.g., $T(m)$, $\rho(m)$, $X_i(m)$). We briefly summarize the four-step working principle of MESA. First, at a given time step, the code tests if it has to re-mesh the star differently compared to the previous time step, to accurately evaluate major structural changes compared to the previous step. Physical quantities are interpolated for newly created cells, if needed. At the beginning of the second step, mass lost by winds or mass gained by accretion is accounted for. Chemical abundances are adjusted following the mixing properties of the previous time step[3]. Next, convective diffusion parameters are calculated where cells were determined to be unstable against convection following the specified criterion. Finally, the Newton-Raphson solver computes the new stellar structure model using a trial solution from the previous time step. If the solver fails, MESA returns to the stellar model of the previous time step and decreases the adopted time step to repeat the process until the solver finds a stable solution. During this third step, the time step to the next evolutionary model is computed following user-defined criteria and the absolute and relative changes of many physical quantities over all cells. The fourth and final step creates output files, if needed.

We have used MESA (v8118) to compute stellar structure models of HD 43317 (see Chapter 7) to deduce its global and internal properties. This was done by creating a grid of non-rotating and non-magnetic models for discrete values for

[2] `http://mesa.sourceforge.net`

[3] All chemical mixing is defined as elemental diffusion in MESA.

the stellar mass $M_\star$, the parameter for exponential convective overshooting $f_{\rm ov}$, and the central hydrogen content X_c. We refer to Chapter 7 for further explicit details.

1.2 Magnetism in hot stars

Magnetic fields are detected in many different types of stars, covering much of the full mass range and all evolutionary stages. We overview the different types of known and anticipated magnetic fields for intermediate-mass and massive stars during the MS stage in Sect. 1.2.1 and how these interact with different regions inside and around the star, as well as with various astrophysical properties in Sect. 1.2.2. Section 1.2.3 provides more information on how magnetic fields are detected and observationally investigated as we have done in this thesis.

1.2.1 Types of magnetic fields

Large-scale magnetic fields

Magnetic fields are detected at the stellar surface of about 10 % of the intermediate-mass and massive stars, following recent dedicated observing campaigns such as MiMeS (Wade et al. 2016), the BOB campaign (Morel et al. 2015), and the BRITE spectropolarimetric survey (Neiner et al. 2016). The detected fields have simple geometries, often a magnetic dipole, and strengths ranging from a few 100 G up to several 10 000 G. They are typically represented by the oblique rotator model (e.g., Stibbs 1950, and depicted in Fig. 1.2), which describes the geometry as a dipolar magnetic field inclined to the rotation axis. This model is able to explain the variability of various diagnostics. The angle between the rotation symmetry axis and the magnetic symmetry axis is named the obliquity angle β. Because the detected large-scale magnetic fields seem to be stable over time spans of decades and because their properties do not correlate with any stellar properties, these large-scale magnetic fields must have been generated during early evolutionary stages. Two different scenarios have been proposed.

One scenario, called the binary merger hypothesis, interprets the detected magnetic fields as the result of a binary merger process of two proto-stars. During the merging, strong shears in the radiative layer create a dynamo magnetic field which freezes into the newly formed star (e.g., Bonnell et al. 1998; Bonnell & Bate 2002; Ferrario et al. 2009; Schneider et al. 2016). The hypothesis was mainly proposed to explain the lack of magnetic intermediate-mass and

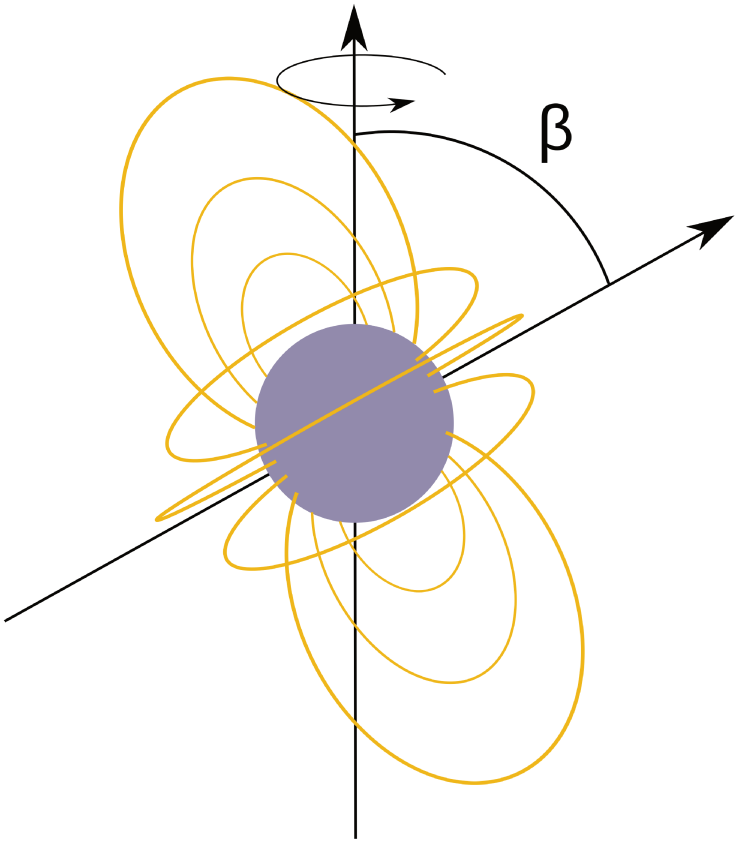

Figure 1.2: Schematic of the oblique rotator model, where the symmetry axis of the magnetic dipole is inclined to the rotation symmetry axis. This angle is referred as the obliquity angle β. Image created and provided by D. Bollen.

massive MS stars in close binary systems (Carrier et al. 2002; Alecian et al. 2015). However, meanwhile two magnetic B-type stars have been detected in the close binary system ϵ Lup (Shultz et al. 2015b) and the merger hypothesis cannot explain this system's properties properly. Moreover, magnetic fields are not found with a higher occurrence in known merger products, such as blue stragglers (Jason Grunhut, private communication). Therefore, the fossil field hypothesis (e.g., Mestel 1999; Neiner et al. 2015) seems to be more promising. This scenario explains how a seed field, a remnant magnetic field of the molecular cloud during star formation, has frozen in and has stabilized into the radiative layers of the stars. This seed magnetic field might have been further enhanced by a dynamo process during the fully convective evolutionary stage of the proto-stars. This has recently been observed by studying the spectroscopic and magnetic detection status of a large sample of intermediate-mass T Tauri stars (IMTTS; Villebrun et al. 2016). A magnetic field was detected for all the younger, fully convective IMTTSs. Yet only $\sim$10 % of the investigated older pre-MS stars hosted a magnetic field, in agreement with the results for

their corresponding main-sequence stars. The relaxation process, thought to be dominated by the magnetic helicity, would then explain why only a fraction of these stars keep their large-scale magnetic field (e.g., Duez & Mathis 2010).

Using semi-analytical descriptions (e.g., Markey & Tayler 1973; Duez et al. 2010; Duez & Mathis 2010) and numerical simulations (e.g., Braithwaite & Spruit 2004; Braithwaite & Nordlund 2006; Braithwaite 2007, 2008; Featherstone et al. 2009) the relaxation and stability of large-scale magnetic fields were investigated. These studies demonstrated that both a poloidal and toroidal component are needed to sustain the magnetic field in a stable configuration (as demonstrated earlier by e.g., Markey & Tayler 1973) and that they are deeply embedded in the complete radiative layer. This configuration appears as a magnetic dipole at the stellar surface, as is observed for the OBA stars. Moreover, Braithwaite (2008) illustrated that the magnetic energy increases compared to its value at the surface when going deeper into the radiative layer, suggesting that the large-scale magnetic field is several orders of magnitude stronger in the near-core region in the star compared to the surface. We make use of this result in Chapters 6 and 7.

Convective core dynamo

The electrically conducting matter in the convective core of intermediate-mass and massive stars is anticipated to generate a stable dynamo field (e.g., Moss 1989; Charbonneau & MacGregor 2001; Brun et al. 2005), through the combined effects of turbulent motion due to convection and stellar rotation. Numerical magnetohydrodynamical (MHD) simulations suggest that the generated fields can be locally, inside the convective core, as strong as a MG (e.g., Augustson et al. 2016). Moreover, they would influence the dynamics by suppressing much of the differential rotation inside the core (e.g., Brun 2005) and would cause a redistribution of angular momentum. It is considered unlikely that the magnetic dynamo field would produce an observable signature at the stellar surface, since the magnetic diffusion time scale for the magnetic flux from the core to the stellar surface is much longer than the lifetime of these stars (e.g., Moss 1989). Yet, this diffusion timescale can be greatly reduced through fast rotation-induced meridional circulation (e.g, MacGregor & Cassinelli 2003). In addition, if core dynamo fields would cause the observed surface magnetic fields, the measured longitudinal field strength should depend on the stellar rotation rate. This, however, is not observed. The topology of these diffused magnetic fields would be much more complex than the simple magnetic dipole fields detected. Finally, this hypothesis would also have issues to explain the $\sim$10% incident rate of detected magnetic fields in OBA-type stars, that would then be higher for faster rotators.

Small-scale magnetic fields

Main-sequence stars with an O, B, or A spectral type have a thin sub-surface convective layer, which becomes more substantial and closer to the stellar surface for increasing stellar mass. Dynamo fields can be produced in these sub-surface convective layers (Cantiello & Braithwaite 2011) that should diffuse to the stellar surface on reasonable time scales (of the order of a few years). However, such magnetic fields would result in small-scale magnetic fields with typical strengths below $\sim$50 G that would lead to complex Zeeman signatures in circular polarization observations (see Sect. 1.2.3 for details on how these fields are observed), while these are not observed with ultra-sensitive spectropolarimetric observations achieving a sub-Gauss precision (e.g., Wade et al. 2014; Neiner et al. 2014).

1.2.2 Implications of a large-scale magnetic field

It is now well established that the magnetic fields of intermediate-mass and massive stars are large-scale magnetic fields of a fossil origin. The detected large-scale magnetic fields lead to differences in and around the star compared to similar non-magnetic stars. Here, we overview some of these observational effects as well as theoretical predictions.

At the stellar surface

The chemical abundance distribution at the stellar surface (for simplicity assumed to be the photosphere) depends on the initial chemical composition, but also reflects the undergone stellar evolution since processes like dredge-ups (see Sect. 1.1.2) bring newly formed chemical elements to the surface. It was already noted with the first magnetic detections that magnetic A-type stars have peculiar surface abundance distributions (e.g., Babcock 1949; Babcock & Burd 1952). Moreover, Stibbs (1950) suggested that these stars may have surface abundance anomalies that lead to periodic spectroscopic and photometric variability coherent with the rotation period. Such stars are now classified as chemically peculiar A stars (denoted as Ap stars or CP-2 stars), and have corresponding hotter magnetic and chemically peculiar stars denoted as Bp stars (see for example, Sargent 1964).

Michaud (1970) suggested that the (internal component of the) large-scale magnetic field acts upon the competition between gravitational settling and radiative levitation. As a result, the effects of diffusion are clearer than for non-magnetic stars, due to the magnetic field itself and the slower rotation

rate, leading to an altered overall chemical abundance distribution at the stellar surface, especially for certain heavy elements (e.g., Si, Cr, Eu). In addition, the efficiency of diffusion will also be much higher for regions with magnetic field lines parallel to the gravitational field (Michaud 1970). Together with the inhibition of thermal convection in the ionization layers of helium and / or hydrogen (Chandrasekhar 1961), these processes explain the observed surface abundance inhomogeneities of chemical elements such as Fe, Si or He. Computations and simulations have been able to demonstrate this (e.g., Vauclair et al. 1979; Alecian & Vauclair 1981), but obtaining improvements remains an active research domain (e.g., Alecian 2015; Alecian & Stift 2017; Kochukhov & Ryabchikova 2018). This is especially important for the application of inversion methods that lead to tomographic images of certain surface element distributions (in combination with the detailed inversion of the large-scale magnetic field; see e.g., Kochukhov et al. 2014, 2015, 2017; Kochukhov & Wade 2016). These tomographic images indeed demonstrate the non-uniform surface abundance distribution and illustrate that the large-scale magnetic field has non-negligible toroidal components and weak higher-order (poloidal and toroidal) terms when combining the linear and circular polarization signature (e.g., Oksala et al. 2018).

In the circumstellar environment

Early B-type stars and O-type stars experience strong mass-loss during the MS stage by a radiatively-driven wind (described by e.g., Castor et al. 1975). It was quickly realized that this mass loss would not be happening uniformly in case the star hosts a large-scale magnetic field. The oblique rotator model suggested that, instead, the mass loss happens in narrow cones above the magnetic poles (e.g., Shore 1987; Shore & Brown 1990). In addition, the matter escaping through the magnetic poles is forced to follow the magnetic field lines around the star. As a consequence, particles coming from both hemispheres collide at the magnetic equator, forming a magnetosphere. Matter can either remain supported by the centrifugal force and form a so-called centrifugal magnetosphere or it can fall back onto the star from a density enhanced region which is constantly renewed and is named a dynamical magnetosphere. The difference between both scenarios is described by the magnetic confinement parameter that depends on the strength and orientation of the magnetic field, the mass-loss properties, and the rotation rate (e.g., ud-Doula & Owocki 2002; Townsend & Owocki 2005; Petit et al. 2013). The coupling between the wind and the large-scale magnetic field also leads to an amplified angular momentum loss rate (e.g., Schatzman 1962) and is referred to as magnetic braking.

Magnetospheres can lead to strong and bright (compared to similar non-magnetic

stars) X-ray emission due to shocks between the wind particles (e.g., Oskinova et al. 2011; Nazé et al. 2014) or a rotationally modulated Hα emission line profile (e.g., Oksala et al. 2015b). The variability in the Hα line is expected to be stable over a long time scale, since the large-scale magnetic field is stable over such a time scale and the mass loss is happening quasi-continuously during the main-sequence stage of these stars. As such, they are different from prominences seen for cooler M-type stars (e.g., Leitzinger et al. 2016), which are a transient phenomenon that dissipate after a few stellar rotation cycles.

Inside the stellar interior

Perhaps the most important consequence of the detected large-scale magnetic field is that it alters the stellar structure of the intermediate-mass and massive stars. This is caused by the competition between the Lorentz force and the pressure force and gravity.

Non-magnetic stars undergo moderate amounts of chemical mixing inside their radiative layers due to various processes leading to internal motions (both turbulent and structured). The presence of a stable large-scale magnetic field (in the radiative layer) limits or inhibits this chemical mixing. An axisymmetric magnetic field with respect to the rotation symmetry axis enforces a uniform rotation rate along the magnetic field lines (i.e., Ferraro's isorotation law, Ferraro 1937). Since these field lines extent throughout the complete star, from the near-core region to the surface, the radiative layer rotates (quasi) uniformly (e.g., Ferraro 1937; Moss 1992; Spruit 1999; Mathis & Zahn 2005; Zahn 2011). This leads to a critical strength for the magnetic field in the radiative layer to enforce uniform rotation (Spruit 1999; Mathis & Zahn 2005; Zahn 2011, see also Sect. 6.6.3). Moreover, the field operates on the chemical mixing processes in the radiative layer. The effects of a non-axisymmetric magnetic field remains an active field of study (requiring detailed numerical simulations), as both the poloidal and toroidal components of the magnetic field needs to be considered (see also Sec. 1.2.1). This uniform rotation (and the magnetic field itself) also causes a smaller penetration depth for convective structures with inertia compared to similar non-magnetic stars (e.g., Press 1981; Browning et al. 2004). This should be observable as a smaller convective core overshooting value (with one known example, namely V2052 Oph (Neiner et al. 2012a; Handler et al. 2012; Briquet et al. 2012).

As indicated earlier, the large-scale magnetic field can suppress thermal convection. This explains the abundance inhomogeneities observed at the stellar surface of magnetic early-type stars.

Finally, the magnetic field in the radiative layer can lead to various MHD instabilities (e.g., Spruit 1999, 2002) producing chemical mixing. Whether such instabilities influence the stability of the (internal) magnetic field remains an active debate (see e.g., Zahn et al. 2007; Zahn 2011).

Demonstrating that the large-scale magnetic field indeed changes the internal physical properties was the main goal of the work presented in this PhD thesis.

1.2.3 Observationally investigating magnetic fields

In this section, we provide some additional information on the most commonly adopted observational technique to detect the presence and investigate the properties of a magnetic field at the stellar surface. This is ground-based high-resolution and high-signal-to-noise optical spectropolarimetry that studies the polarization signature caused by the Zeeman effect in absorption lines.

Polarization of light

Polarization describes the geometrical orientation of a transverse wave, as various directions compared to the propagation direction are possible. For electromagnetic radiation, the convention is that polarization refers to the description of the electric field component (and not the magnetic field component). In case the light travels along the $\hat{z}$ direction of an orthogonal coordinate system, the variation of the electric field component can be written as

$$\vec{E}(z,t) = (A_x e^{i(kz-\omega t+\phi_x)}\hat{x}, A_y e^{i(kz-\omega t+\phi_y)}\hat{y}, 0)\,, \tag{1.12}$$

with A_i and ϕ_i the amplitude and phase along direction $\hat{\imath}$, ω the angular frequency of the radiation and k the wave number. The relation between A_i and ϕ_i describes the polarization, which is most often randomly oriented. Two special cases, however, occur: i) linear polarization when $\phi_x{=}\phi_y + n\pi$ (with n an integer) and ii) circular polarization when $A_x{=}A_y$ and $\phi_x{=}\phi_y \pm \pi/2$. The direction of the linear polarization is determined by the amplitudes A_i, while circular polarization is said to be left-handed ($0{<}\Delta\phi{<}\pi$) or right-handed ($\pi{<}\Delta\phi{<}2\pi$).

The variations of the electric field can be represented in a coherency matrix $\vec{\Phi}{=}\langle\vec{E}\vec{E}^{\dagger}\rangle$, written as

$$\vec{\Phi} = \begin{bmatrix} A_x^2 & A_x A_y e^{i(\phi_x-\phi_y)} \\ A_x A_y e^{-i(\phi_x-\phi_y)} & A_y^2 \end{bmatrix}. \tag{1.13}$$

Using the coherency matrix, the polarization of light can be described with the Stokes parameters

$$\vec{S} \equiv \begin{bmatrix} I \\ Q \\ U \\ V \end{bmatrix} = \begin{bmatrix} \Phi_{xx} + \Phi_{yy} \\ \Phi_{xx} - \Phi_{yy} \\ \Phi_{xy} + \Phi_{yx} \\ \Phi_{xy} - \Phi_{yx} \end{bmatrix} = \begin{bmatrix} A_x^2 + A_y^2 \\ A_x^2 - A_y^2 \\ A_x A_y \cos(\Delta\phi) \\ A_x A_y \sin(\Delta\phi) \end{bmatrix} , \tag{1.14}$$

with Stokes I the total intensity of the light from the star, Stokes Q and U the linear polarization of the light (where Stokes U and Q describe the linearly polarized light in two directions $\pi/4$ apart), and Stokes V the net right-handed circular polarization. We remark that the completely polarized light has $I^2 = I_c^2 \equiv Q^2+U^2+V^2$, while partly polarized light satisfies $I^2 > I_c^2 \equiv Q^2+U^2+V^2$.

Zeeman effect

Atomic energy levels are split into $2|\vec{J}| + 1$ equally spaced sub-levels in the presence of a non-zero static magnetic field, where the total angular momentum $\vec{J} = \vec{L} + \vec{S}$, with $\vec{L}$ the orbital angular momentum and $\vec{S}$ the spin angular momentum. This is called the Zeeman effect and is depicted in the top panel of Fig.1.3. In case a static electric field splits the atomic energy levels, it is named the Stark effect. When already polarized light is influenced by scattering effects, it is referred to as the Hanle effect. The energy difference between the sub-levels depends on the Landé factor g, which is related to the energy level of the given ion, and the strength of the magnetic field $\vec{B}$. It is usually assumed that the magnetic field is sufficiently weak that second-order terms in the expansion of the magnetic Hamiltonian ($H_B = \mu_0(\vec{L}+2\vec{s})\cdot\vec{B}$ with μ_0 referred to as the Bohr magneton) can be ignored. This is referred to as the weak-field hypothesis and is valid for the large-scale magnetic fields discussed here during the MS stage of intermediate-mass and massive stars. Following the transition rules between energy levels (i.e., $|\Delta m|\leq 1$), this leads to a wavelength difference between the split components of the absorption (or emission) line given as

$$\Delta\lambda_B = 4.6686 \cdot 10^{-10} \lambda_0^2 |\vec{B}| \Delta m \Delta g \,, \tag{1.15}$$

where $\Delta\lambda_B$ is given in mÅ, the wavelength of the unperturbed line λ_0 in Å, and the (static) magnetic field $\vec{B}$ in Gauss. Besides causing a wavelength difference, the Zeeman effect also influences the polarization of the absorbed (emitted) radiation. It does this differently for the possible transitions and is schematically given in the bottom panel of Fig.1.3.

Transitions with $\Delta m = -1$ and $\Delta m = +1$ are called the σ_r and σ_b components, respectively, and r(ed) and b(lue) denote the wavelength shift compared to

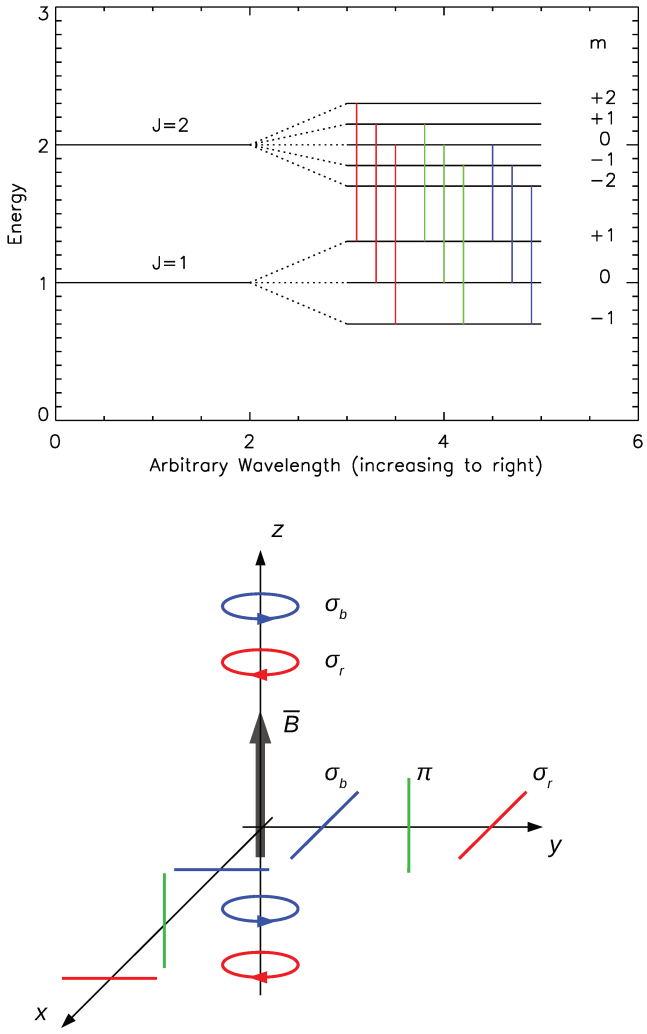

Figure 1.3: *Top*: Diagram showing the allowed transitions for $^3P_2$ - $^5P_1$. The transitions in case of the Zeeman effect are shown in increasing wavelength. Green lines are π components (Δm=0). Blue (red) lines correspond to σ_b (σ_r) transitions with $\Delta m = +1$ ($\Delta m = -1$). *Bottom*: Schematics of the corresponding polarization of the transitions, where the dominant observed polarization depends on the viewing angle. Top image created and provided by M. E. Oksala.

λ_0. An Δm=0 transition is named a π component and does not have a wavelength shift. For most viewing angles compared to the magnetic field $\vec{B}$ the σ components lead to net circular polarization of the radiation, while the π component has a net linear polarization.

Spectropolarimetry

Because the wavelength difference caused by a typical magnetic field through the Zeeman effect is small compared to other actors on the absorption lines (e.g., various types of line broadening, binarity, stellar pulsations, ...), one typically measures the net polarization created by the Zeeman effect rather than the wavelength difference to investigate the magnetic field using a spectropolarimeter. Such an instrument consists of a polarimeter and a spectrograph. Modern spectropolarimeters, such as ESPaDOnS (Donati et al. 2006), Narval (Aurière 2003), and HARPSpol (Piskunov et al. 2011), use a high-resolution spectrograph with a resolving power of at least 65 000. The polarizer consists of a retarder, which permits to select a given polarization state of the light, and a Wollaston prism that separates the light into two orthogonal components. Both orthogonal components are sent simultaneously through the spectrograph to get the corresponding measurement. In ESPaDOnS and Narval, the retarder consists of three achromatic wave plates (two half-wave plates and one quarter-wave plate). These wave plates are made out of birefringent material, whose refractive index depends on the polarization of the light, to select a polarization state in combination with the respective angles in between the wave plates. To measure the circular polarization (Stokes V) and intensity (Stokes I), four consecutive sub-exposures are taken with different and specific rotator angles between the wave plates that permit to reconstruct the Stokes V and I vectors. Different angles are required to recover Stokes Q and U. The measured orthogonal components are destructively co-added to create a diagnostic null profile N for an observation, that should be constant and zero. Strong deviations from zero indicate possible systematics in the instrument, variations in the conditions of observing during the measurement sequence, or stellar variability during the spectropolarimetric sequence.

Line averaging techniques

While the collected spectropolarimetric sequences already have a typical signal-to-noise ratio (S/N) of a few hundred, the Zeeman signature of a large-scale magnetic field in a given spectroscopic line can be quite weak (see left panel of Fig. 1.4 for the magnetic Ap star HD 107000). Instead of using a large amount of observing time to register the Zeeman signature in an individual spectral line, the complete wavelength information is used by averaging relevant spectroscopic information into one profile. Several line averaging techniques exist, such as Least-Squares Deconvolution (LDS, Donati et al. 1997; Kochukhov et al. 2010) or Single Value Decomposition (SVD, Carroll et al. 2012). Both mentioned techniques rely on a mathematical framework to rescale the absorption lines in

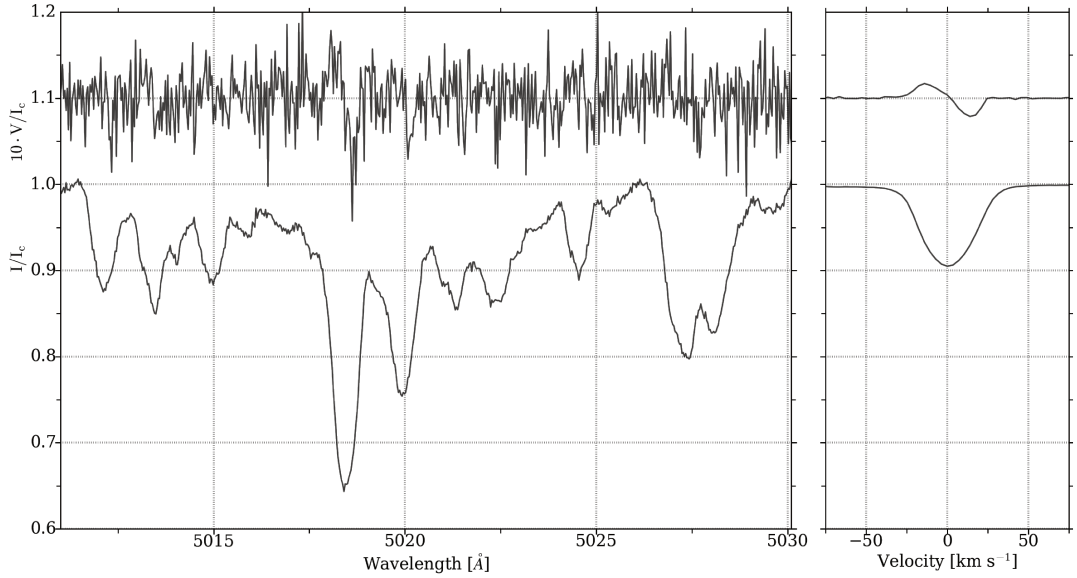

Figure 1.4: *Left*: Part of the wavelength domain for the spectropolarimetric sequence of the magnetic Ap star HD 107000. Stokes V observations are offset and multiplied by a factor ten for increased visibility. *Right*: LSD Stokes profiles V and I computed for all considered lines of the same spectropolarimetric sequence, drastically increasing the S/N.

intensity and polarization, together with their relevant atomic data to represent almost the complete spectrum as one profile. Line masks containing the necessary information, such as rest wavelength and Landé factor, are matched to the observations of a given star to determine the weights for the considered metal lines. Hydrogen lines and blends of metal lines with hydrogen lines, telluric features or known diffuse interstellar bands are removed from the adjusted line mask since these spectroscopic lines have a different or distorted shape compared to the isolated metal lines. By averaging the different metal lines, the S/N is increased with the number of included spectral lines, ranging from typically a factor 3 for massive stars to 30 for intermediate-mass stars (with an example shown in the right panel of Fig. 1.4 for the magnetic Ap star HD 107000). We refer to the provided references above for the explicit mathematical details of the LSD and SVD techniques. Only the LSD technique, however, was used in the work presented here.

Inferring the magnetic field from the measured polarization

To determine whether a Zeeman signature is present in the (LSD) Stokes V profile, the False Alarm Probability of a signal (FAP; Donati et al. 1992, 1997)

is calculated inside the (mean) absorption line. Definitive detections (DDs) show a clear signature and correspond to FAP$<10^{-3}$ %, while non-detections (NDs) have a FAP$>10^{-1}$ %. Marginal detections (MDs) fall in between these two categories and have $10^{-3}<$FAP$<10^{-1}$ %. A star is only said to be magnetic if an observation with a DD is obtained.

The net circular polarization also permits a measurement of the longitudinal magnetic field B_l (i.e., the magnetic field along the line of sight). Rees & Semel (1979) measured this as

$$B_l = -2.14 \cdot 10^{11} \frac{\int vV(v)\mathrm{d}v}{\lambda g c \int [1 - I(v)]\,\mathrm{d}v}\,, \tag{1.16}$$

where the longitudinal magnetic field B_l is given in Gauss. The (LSD) Stokes V and I profiles are given by $V(v)$ and $I(v)$, respectively, while g is the Landé factor of a given absorption line and λ is its rest wavelength in nm. When one works with LSD profiles, g and λ are the weighted mean values from all included absorption lines. The speed of light c and velocity v are given in $\mathrm{km\,s^{-1}}$. The integration takes place over the full width of the absorption line (or LSD Stokes I profile), and thus also over the full Zeeman signature.

Because the large-scale magnetic field is stable over a long time scale and often has a dominant dipolar geometry, the measured longitudinal magnetic field varies as a sine function with respect to the rotation period. Higher-order sine terms are needed to describe the periodic variability of B_l if the large-scale magnetic field has a more complex geometry. In case the inclination angle i has been independently measured, one can obtain the obliquity angle β (assuming a pure magnetic dipole) through the simple relation derived by Shore (1987):

$$\frac{B_{l,\mathrm{min}}}{B_{l,\mathrm{max}}} = \frac{\cos(i-\beta)}{\cos(i+\beta)}\,. \tag{1.17}$$

Here, $B_{l,\mathrm{min}}$ and $B_{l,\mathrm{max}}$ are deduced from the sine-fit model. Furthermore, the strength of the dipolar magnetic field can be measured by using the analytical equation given by Schwarzschild (1950):

$$B_{\mathrm{dip}} = \frac{4}{\cos(\beta-i)} \frac{15-5u}{15+u} B_{l,\mathrm{max}}\,, \tag{1.18}$$

where u is the limb-darkening coefficient computed for stellar parameters of the star (see e.g., Claret 2000, for tabulated values). Without the determined values for i and β and/or without a complete description of B_l over the rotation period, one defines the lower limit on the polar strength of the dipolar magnetic field as 3.0 to 3.5 times the maximal measured B_l value, which results from taking a mean factor on Eq. (1.18) (e.g., Preston 1967).

1.3 Asteroseismology

Asteroseismology allows to study the internal stellar structure properties by analysing and modelling stellar pulsation modes. It remains the best method in modern astronomy to observationally probe the stellar interior. While all observed stellar light is produced in the outer stellar layers, the pulsations travel through the star, causing the observed light to periodically change according to the physical conditions experienced by the pulsation mode. As such, the mode frequencies are dictated by the physical properties of the stellar interior.

In the current modern space-era, high-precision photometric instruments are sent out in space to collect unparalleled observations, pushing the understanding of both the stellar interior and the stellar pulsations forward at a fast rate. We discuss some of these and modern ground-based observations in more detail in Sect. 1.3.4. First, we provide a short overview of the theory governing stellar pulsations (Sects. 1.3.1 and 1.3.2) and then discuss the properties of various types of pulsating intermediate-mass and massive stars (Sect. 1.3.3). Section 1.3.5 discusses the relevance of internal gravity waves (IGWs). The working principle of the pulsation code GYRE is briefly mentioned in Sect. 1.3.6.

1.3.1 Stellar pulsations

The stellar structure equations discussed in Sect. 1.1.1 represent a star in hydrostatic equilibrium. However, a star may be pulsating around its equilibrium state because of various perturbations. Stellar pulsations are thus computed from a perturbative analysis of the stellar structure equations adopting a linear approximation for the displacement from spherical symmetry. We refer to Unno et al. (1989) and Chapter 3 of Aerts et al. (2010, and references therein) for a detailed and rigorous overview on the theory summarized in this section. By applying a linear perturbation to Eqs. (1.1) – (1.5) for a non-rotating, non-magnetic, spherically symmetric star, one can describe the displacement $\vec{\xi}$ of a local mass element due to one pulsation mode as

$$\xi_{n,r}(r,\theta,\phi,t) = a_n(r)\, Y_\ell^m(\theta,\phi)\, e^{-2\pi i f_n t}\,, \tag{1.19}$$

$$\xi_{n,\theta}(r,\theta,\phi,t) = b_n(r)\, \frac{\partial Y_\ell^m(\theta,\phi)}{\partial\theta}\, e^{-2\pi i f_n t}\,, \tag{1.20}$$

$$\xi_{n,\phi}(r,\theta,\phi,t) = \frac{b_n(r)}{\sin(\theta)}\, \frac{\partial Y_\ell^m(\theta,\phi)}{\partial\phi}\, e^{-2\pi i f_n t}\,. \tag{1.21}$$

Here, f_n is the cyclic frequency of the stellar pulsation mode described by the quantum numbers n, ℓ and m, and its displacement $\vec{\xi}$ is expressed in spherical

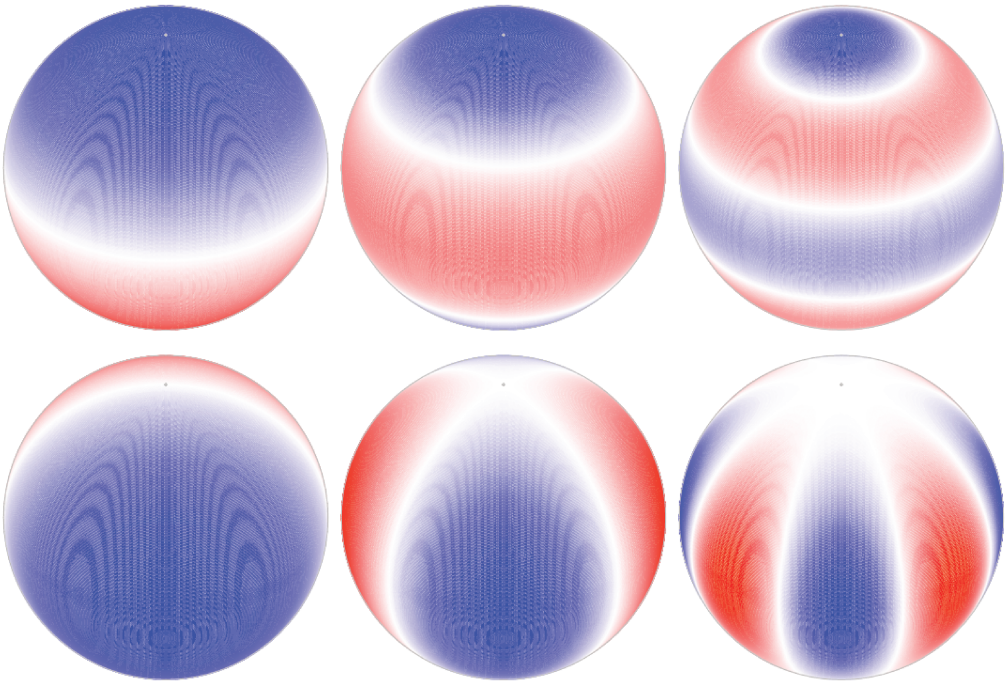

Figure 1.5: Snapshot of the radial component of various modes as seen by an observer under an inclination angle of 55°. The white bands represent the positions of the surface nodes; red (blue) represent sections of the star that are moving in (out) at any given time, then vice versa. *Top row*: zonal modes (i.e., $m = 0$) with, from left to right, $\ell = 1, 2, 4$. *Bottom row*: modes with (ℓ, m)=$(1, 1), (2, 2), (4, 4)$. Images created and provided by C. Aerts.

coordinates. The amplitudes of the radial and the horizontal displacement components are given by $a_n(r)$ and $b_n(r)$, respectively. The quantity $Y_\ell^m(\theta, \phi)$ is the spherical harmonic function given by

$$Y_\ell^m(\theta, \phi) = (-1)^m \sqrt{\frac{2\ell + 1}{4\pi} \frac{(\ell - m)!}{(l + m)!}} P_\ell^m(\cos(\theta)) e^{im\phi} \,, \tag{1.22}$$

with P_ℓ^m a Legendre polynomial function. Among the three quantum numbers (n, ℓ, m), the radial order n gives the number of nodal points of $\vec{\xi}$ along the radial direction, the spherical degree ℓ the number of surface nodal lines, and the azimuthal order m the number of surface nodal lines through the symmetry axis of the pulsation. Modes with ℓ=0 are called radial modes and with ℓ=1 or ℓ=2 dipole and quadrupole modes, respectively. Some examples of the radial component of $\vec{\xi}$ for various modes are shown in Fig. 1.5.

In the absence of rotation and magnetism, one of two restoring forces can act dominantly upon the stellar pulsation mode. Modes for which the pressure force

is the dominant restoring force are classified as pressure modes (p modes). They are predominantly sensitive to the outer radiative layers for intermediate-mass and massive stars. The other restoring force is buoyancy and when this one is dominant the modes are named gravity modes (g modes). These are particularly interesting for intermediate-mass and massive stars, since they mostly probe the near-convective-core region. Gravity modes cannot be radial modes and they can only propagate through radiative layers, as the buoyancy controls convection. Asymptotic theory (e.g., Tassoul 1980) states that high-order p modes with the same ℓ and consecutive n have a constant frequency spacing, while consecutive low-degree high-order g modes for a given l have a constant period spacing. For the stars considered later in this work, the typical amplitudes of p modes are higher than those of typical g modes and they also have higher pulsation mode frequencies. The dominant displacement for low-order p modes is along the radial direction, while for high-order g modes, it is in the transverse (i.e., the horizontal) direction[4].

While the previous equations provide an apt description for the stellar structure and stellar pulsations, most stars are observed to be rotating and they can even host a strong magnetic field, violating parts of the made assumptions. We describe how these affect the stellar pulsation modes.

The main effect of a uniform rotation rate $f_{\rm rot}$ is that we observe the pulsation modes from the inertial reference frame instead of the co-rotating reference frame in which the pulsation modes are generated. This so-called rotational splitting was first described by Ledoux (1951) following a first-order perturbation of Eqs. (1.1) – (1.5), while accounting for a uniform rotation rate and assuming the pulsation symmetry axis to coincide with the rotation symmetry axis, leading to

$$f_{n,\ell,m} = f_{n,\ell} + m\,(1 - C_{n,\ell})\,f_{\rm rot}\,. \tag{1.23}$$

Here, $f_{n,\ell,m}$ is the pulsation mode frequency with radial order n, spherical degree ℓ, and azimuthal order m in an inertial frame, resulting from the corresponding pulsation mode frequency $f_{n,\ell}$ in the co-rotating frame. The result in Eq. (1.23) indicates that the degeneracy with respect to the azimuthal order m is lifted when rotation occurs. The term $mf_{\rm rot}$ represents the change in pulsation mode frequency by changing the reference frame from a co-rotating one to an inertial one and the Ledoux constant $C_{n,\ell}$ (where $0 \leq C_{n,\ell} \leq 1$) represents the influence of the Coriolis force (under the first-order perturbative approach). The values for the Ledoux constant depend heavily on the mode degree and radial order, as well as on the stellar interior properties. Overall, rotation pushes pulsation mode frequencies with $m > 0$ ($m < 0$) to higher (lower) frequency values. Under a first-order perturbative approach, rotation does not affect the zonal modes

[4]This also explains why gravity modes cannot be radial modes.

($m = 0$). This is no longer the case under more elaborate second-order or third-order perturbative approaches (e.g., Dziembowski & Goode 1992; Soufi et al. 1998, where the centrifugal force is also partly accounted for). These more complex treatments are more suitable to describe the pulsations mode frequencies for stars above half their critical rate. For high-order g modes, as discussed later in this work, the so-called traditional approximation (see e.g., Eckart 1960; Townsend 2003) is often used to describe the effects of rotation on the pulsation modes. It assumes spherical symmetry and that the tangential component of the rotation vector can be ignored, which is applicable for the regions of strongest probing power of these modes just outside the convective core. When the Coriolis force provides a significant contribution to the restoring force in combination with buoyancy, the modes are classified as gravito-inertial modes.

Unlike the effects of rotation, the consequences of including a magnetic field on the pulsation modes and their frequencies are not well described for the general case and all types of pulsation modes. The effects of the internal magnetic field have to be simultaneously accounted for with the effects of rotation and they rely heavily on the assumed topology of the internal magnetic field. Therefore, no generic expression has been derived for all types of pulsation modes, since pressure and gravity modes probe different layers of sometimes structurally different stars that may have different internal magnetic fields. Overall, the presence of a strong magnetic field deforms the eigenfunctions of the pulsations (i.e., Eqs. (1.19) – (1.21)) such that spherical harmonics of different ℓ and m values get coupled and frequency shifts of the pulsation mode frequency occur. The magnetic frequency shift is anticipated to be smaller than that caused by uniform rotation for typically encountered fields, but may dominate over the effects of rotation for strong fields above several kiloGauss. These frequency changes are partly caused by a different alignment between the magnetic symmetry axis and the rotation symmetry axis. Most theoretical work describes the effect by a purely poloidal magnetic field on pressure modes to investigate the magneto-acoustic pulsation modes detected in rapidly oscillating (magnetic) Ap stars (e.g., Biront et al. 1982; Dziembowski & Goode 1985; Shibahashi & Takata 1993; Takata & Shibahashi 1995; Dziembowski & Goode 1996; Bigot et al. 2000), while some investigate the effect by a purely toroidal field on p modes (e.g., Gough & Taylor 1984; Gough & Thompson 1990). Goode & Thompson (1992) described the effect of a large-scale magnetic field on solar-like p modes. Only a few first-order descriptions are available for gravity modes in a magnetic star (e.g., Hasan et al. 2005), again assuming a purely poloidal magnetic field. So far, this has not led to concrete applications, since the effects caused by the Coriolis force are larger than those due to the Lorentz force. We provide such an application in Chapter 7. Mathis & de Brye (2011) accounted for the simultaneous effects of the Coriolis and the Lorentz forces in

a non-perturbative approach. Such a formalism should be used when the effects of the Coriolis force becomes comparable to those of the Lorentz force.

1.3.2 Excitation mechanisms of stellar pulsations

Pulsation modes are inherently damped since the perturbations are small and the stars try to return to their equilibrium state. Thus, they must almost constantly receive energy by some mechanism to be observable at the stellar surface. These are the excitation mechanisms, which can be subdivided into two main classes of self-excitation[5], namely the heat-driven mechanisms and stochastic excitation by convective motion.

Heat-driven mechanisms transfer thermal energy into kinetic energy through compression, by acting upon the opacity of certain chemical elements in their respective partial ionization layer. Inside these layers, part of the energy gained by compression is used for the further ionization of the element, resulting in less available energy for a temperature increase compared to the surrounding non-ionized layers. Consequently, this lower temperature along with a similar density leads to an increased opacity κ in the partial ionization zone through Kramers' law

$$\kappa \sim \rho T^{-7/2} \,, \tag{1.24}$$

trapping the radiation effectively. This results in a (radiation) pressure increase, causing the compressed layer to expand again but beyond its nominal reaction to the compression if the layer would not be partially ionized. Part of the ionized material recombines during the expansion, which donates energy to the layer that leads to a locally higher temperature and, thus, a lower local opacity. Hence, photons move more easily through the layer again, which compresses in response due to the lack of energy, and the cycle is repeated. The density in the partial ionization zone has to be just right, since a too high density will immediately damp the pulsations and a too low density will be unable to support any perturbations. This κ-mechanism is known to generate low-order modes in intermediate-mass and massive stars, as well as high-order g modes in massive stars, aside from being active in many other stars not treated in this thesis.

The stochastic and turbulent motions inside a convective layer can also drive stellar pulsation through resonance effects. Such stochastic pulsations have been studied in great detail for stars with significant (sub-)surface convective layers (e.g., Chaplin & Miglio 2013; Hekker & Christensen-Dalsgaard 2017, for recent reviews), but were also predicted to occur for massive stars (Samadi

[5]Tidal effects in close (and eccentric) binary systems may also excite stellar pulsations, which is not considered as self-excitation.

et al. 2010). They were subsequently detected for a rapidly rotating Be star (Neiner et al. 2012b). Further studies indicate that the Coriolis force plays a fundamental role in both the excitation mechanism and the restoring force of such stochastic gravito-inertial modes (e.g., Mathis et al. 2014).

1.3.3 Pulsating hot core-hydrogen burning stars

Different types of pulsation modes are excited by various mechanism throughout the Hertzsprung–Russell diagram (as schematically represented in Fig. 1.6). The corresponding dominant classes of pulsating stars have mostly historically been proposed from observational evidence, while refinements have occurred from theoretical results or additional (high-precision) observations. Below, we discuss the relevant classes of intermediate-mass and massive pulsators on the MS, and refer to Sect. 5.1 for an overview of periodically variable supergiants (PVSGs). A more extensive overview on the properties of these and all other classes of pulsator types is given in Chapter 2 of Aerts et al. (2010).

β Cep stars

The most massive pulsators during the MS stage are called β Cep pulsators, named after one of their prototypical stars. These pulsators have spectral types O9 – B2, roughly corresponding to stars with birth masses of $8\,M_\odot$ – $18\,M_\odot$. They all show one (e.g., ξ^1 CMa; Saesen et al. 2006) to about a dozen (e.g., β Cen; Pigulski et al. 2016) radial or non-radial p modes with pulsation periods of a few hours. Dziembowski & Pamiatnykh (1993) explained these modes to be driven by the κ-mechanism acting on a partial ionization layer of iron-like elements. Some β Cep stars also reveal detectable (low- and high-order) g modes with periods of the order of a few days, e.g., the B2 stars ν Eri (Handler et al. 2004), 12 Lac (Handler et al. 2006), and γ Peg (Handler et al. 2009). An extensive overview on the properties of β Cep pulsators from ground-based observations is given in Stankov & Handler (2005). Overall, pulsations are quite commonly detected for these massive stars. The majority of detailed studies were performed with long-term ground-based observations instead of modern space-based photometry, mainly because such stars were not present in the Field-of-View of the nominal *Kepler* mission, and only very few were observed with CoRoT.

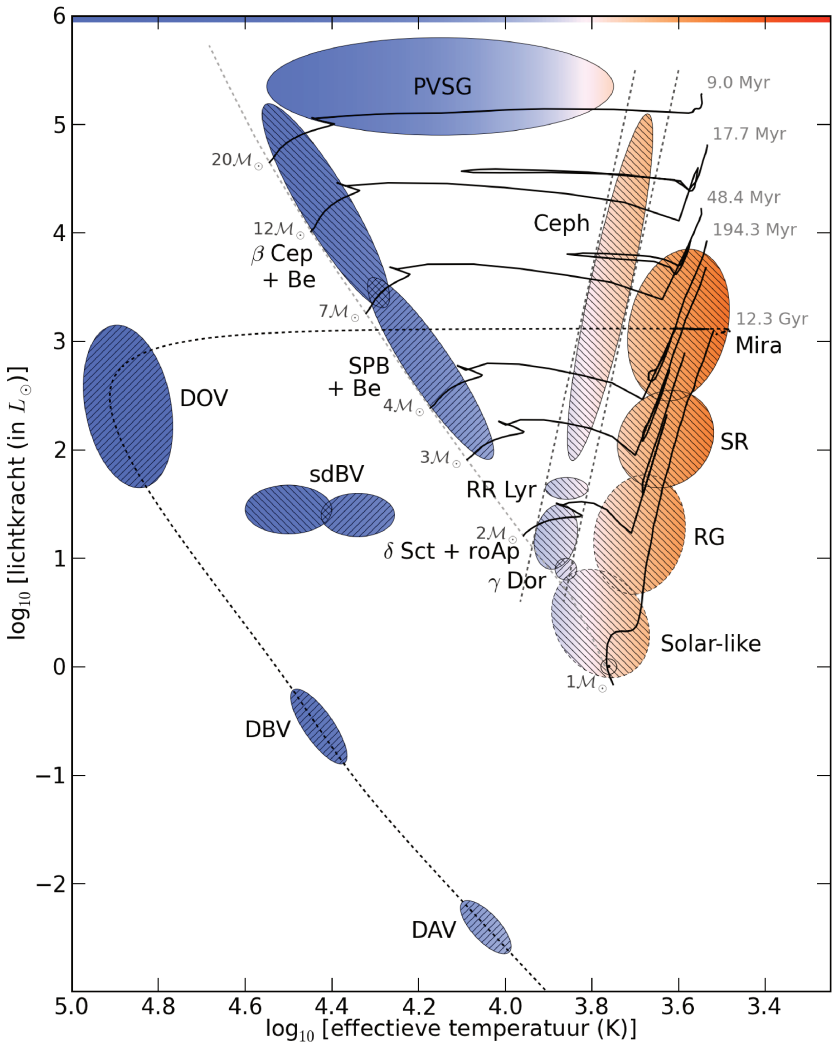

Figure 1.6: Hertzsprung–Russell diagram indicating theoretical instability regions of various pulsator classes, where the colour-scale indicates the $T_{\rm eff}$ and the hatching represents the dominant restoring force. Gravity modes are given as '///' and pressure modes as '\\\'. Pulsations are excited through an opacity mechanism for most classes, except the solar-like pulsators, the γ Dor stars, the pulsating red-giants (RGs) and the variable DA white dwarfs (DAVs) where a convective region is responsible for the dominant driving mechanism. Classes like the semi-regular (SR) and Mira variables, PVSGs and Be stars could have pulsations driven by both mechanisms, see also Fig. 1 of Jeffery & Saio (2016). Image created and provided by P. I. Pápics.

SPB stars

Slowly Pulsating B (SPB) stars were originally described by Waelkens (1991). They are a group of B2 – B9 stars (i.e., with mass range $3-8\,{\rm M}_\odot$) that host

pulsation modes with periods of the order of a few days. The high-order g modes are also excited by the κ-mechanism acting on a partial ionization layer of iron-like elements (e.g., Dziembowski et al. 1993; Gautschy & Saio 1993). While only a few independent high-amplitude pulsation mode frequencies were detected from ground-based observations (e.g., De Cat & Aerts 2002), high-precision space-photometry has shown that some SPB stars can show very rich frequency spectra (e.g., Pápics et al. 2012, 2014, 2015, 2017). These have been understood as sectoral dipole modes (ℓ=|m|=1) in extensive period spacing patterns. Such patterns were utilized to perform successful detailed modelling of their internal structure to constrain the amount of convective core overshooting (e.g., Moravveji et al. 2015, 2016). Seismic modelling of rotationally split dipole modes using high-quality space-photometry suggests that these B-type stars have a (quasi-)rigidly rotating radiative envelope (Aerts et al. 2017b). These results show the strength of these high-order g modes, as they are dominantly sensitive to the near-core region. Again, high-amplitude SPB pulsations are quite commonly detected for MS B-type stars, yet extensive period spacing series have only been obtained for a few stars from CoRoT or *Kepler* photometry.

Classical Be stars

Classical Be stars are non-supergiant rapidly-rotating early-type stars (with a spectral type O8 – B9), which have shown at least once an emission feature in one of their Balmer lines (see e.g., Rivinius et al. 2003, for an overview on Be stars). These emission lines are related to a circumstellar equatorial disk that is produced sporadic ejections of matter from the star. The origin of these ejections seems to be related to the rapid rotation and the presence of stellar pulsations (e.g., Rivinius et al. 1998, 2003; Neiner et al. 2013; Baade et al. 2016). Some Be stars host high-order g modes with periods of the order of several days, that are strongly influenced by the Coriolis force, while others host low-order p modes. These pulsation modes are expected to be driven by stochastic excitation (e.g., Neiner et al. 2012c) or by the κ-mechanism acting upon iron-like elements (e.g., Townsend 2005). The detected pulsation modes have been observed to change during the Be star's mass-loss event (Huat et al. 2009), confirming the causation between stellar pulsations and outburst events.

roAp stars

Pulsation modes have been detected in rare cases for magnetic and chemically peculiar Ap stars (i.e., $1.8 - 2.8\,M_\odot$). First described by Kurtz (1982), these rapidly oscillating Ap (roAp) stars host high-order pressure modes with periods of a few minutes. Mainly dipolar modes occur, heavily affected by the (dipolar)

large-scale magnetic field. Furthermore, the pulsation symmetry axis seems to be coinciding with the magnetic symmetry axis instead of the usual rotation symmetry axis (e.g., Kurtz 1982, 1990; Kurtz & Martinez 2000). The κ-mechanism acting upon the partial ionization zone of H II has been proposed as the excitation mechanism for the detected pulsations (e.g, Cunha 2002). However, the proposed mechanism is unable to explain all detected pulsation modes (e.g, Cunha et al. 2013). Because the pulsation periods are so short, most space-based photometry is of limited use due to the long integration times. Hence, high-cadence ground-based photometry has remained the main observing method (e.g., Kurtz et al. 2005), with the exception of the studies by Holdsworth et al. (2014), Smalley et al. (2015), and Holdsworth et al. (2016).

δ Sct stars

The class of δ Sct pulsators covers spectral types A2 – F2. These can still have fossil large-scale magnetic fields, but are not necessarily intermediate-mass stars according to our definition (i.e., stars above $2\,M_\odot$ while these stars correspond to $1.5 - 2.5\,M_\odot$). δ Sct pulsations are radial and non-radial low-order p modes driven through the κ-mechanism acting upon the partial ionization layer of He II (Breger 2000). This pulsation class contains stars with only one or a few high-amplitude modes as well as stars with rich frequency spectra.

1.3.4 Observational diagnostics of stellar pulsations

Stellar pulsations are detected and studied by investigating coherent periodic variability in photometric and spectroscopic time series (we refer to Chapter 4 of Aerts et al. 2010, for an extensive overview on used observing strategies and methods). Three quantities determine the quality of a given time series. First, the precision of the data, as overall better data is able to detect smaller variations. Next, the total time span of the time series dictates how accurately a given pulsation mode frequency can be retrieved. Finally, a high duty cycle within the total duration of the time series will lead to less aliasing structure and lower noise levels in the corresponding frequency spectra.

Photometry collected from dedicated space-missions improves on all three diagnostics compared to single-site ground-based observations. The quality of space-photometry often permits to reach a μmag precision compared to mmag levels for ground-based data. A noise level of $1\,\mu$mag was reached with the Convection Rotation and planetary Transits (CoRoT) space telescope for a V=5 mag star in the frequency domain of 1 – 10 mHz (see Fig. 28 of Auvergne et al. 2009), but the noise behaves in a non-Gaussian manner and is frequency

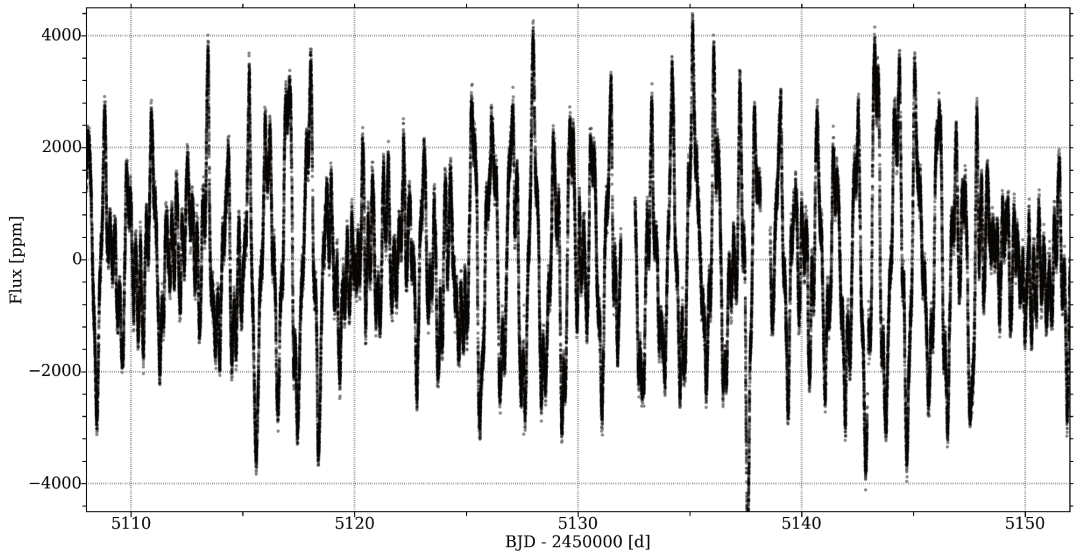

Figure 1.7: Part of the CoRoT light curve of HD 43317 indicating clear photometric variability that is dominated by beating effects between the large-amplitude frequencies.

dependent (as reported by Degroote et al. 2009b). Typically, a noise level of 10 – 20 μmag is obtained for a V=12 mag star with a four year light curve from the nominal *Kepler* mission (Gilliland et al. 2011). With a dedicated reduction, a noise level of about 1 μmag is obtainable for many stars. Howell et al. (2014) reports a noise level of 80 μmag for stars observed with the K2 mission. This can greatly be reduced through custom reduction tools (see e.g., Aigrain et al. 2015) to reach noise levels similar to the nominal *Kepler* mission. The BRIght Target Explorer-Constellation (BRITE) space photometry has a noise level of at least 700 μmag (see e.g., Ramiaramanantsoa et al. 2018 and Chapters 4 and 5). These dedicated missions result in light curves spanning from a few weeks up to several years with a duty cycle of more than 90 %, which is not feasible from ground-based single-site monitoring nor from multi-site campaigns. Noteworthy photometry space-missions used for asteroseismology are the Microvariability and Oscillations of STars satellite (MOST, Walker et al. 2003), the CoRoT telescope (Baglin et al. 2006), the *Kepler* mission (Koch et al. 2010; Borucki et al. 2010), the subsequent K2 mission (Howell et al. 2014) using the *Kepler* telescope, and the BRITE Constellation of nano-satellites (Weiss et al. 2014). A part of the CoRoT lightcurve of HD 43317 is shown in Fig. 1.7 as an example of high-duty photometric time series. However, (simultaneous) ground-based photometry is still used because it permits dedicated observing strategies, for example, to obtain simultaneous multi-colour photometry to estimate the mode geometry of a given pulsation mode frequency (e.g., Handler et al. 2017) or to monitor short-period variability (for example, for roAp stars).

The frequency analysis for pulsating intermediate-mass and massive stars is performed according to the iterative prewhitening method (e.g., Degroote et al. 2009a). Significant frequencies are accounted for by iteratively fitting a periodic model to the time series, removing it, and repeating the method on the created residuals.

Time series of high-resolution ground-based optical spectroscopy are also used to study the pulsation modes, since the shape of the periodic line profile variations (LPVs) of a given absorption line depends heavily on the mode geometry. The analysis is then done by investigating the moments of the absorption line (this is the moment method, see e.g., Aerts 1992, 1996; Briquet & Aerts 2003), in particular the equivalent width or radial velocity variations, or by using the pixel-by-pixel method (e.g., Gies & Kullavanijaya 1988; Telting & Schrijvers 1997; Zima 2006), which analyses the periodic variations in amplitude and phase per wavelength bin (i.e., pixel) throughout a carefully selected absorption line.

1.3.5 Internal Gravity Waves

Besides pulsation modes, most stars are expected to harbour internal gravity waves (IGWs). Such waves travel through the stably stratified radiative layers of a star and their (main) restoring force is gravity (similarly to the standing gravity modes). For rapidly rotating stars, the Coriolis force acts as an additional restoring force (e.g., Pantillon et al. 2007; Mathis et al. 2014), similarly to the gravito-inertial modes mentioned in Sect. 1.3.2. These IGWs are driven by the stochastic motions at the intersection of a convective layer with a radiative region (e.g., Goldreich & Kumar 1990; Montalbán & Schatzman 2000; Pantillon et al. 2007; Samadi et al. 2010; Rogers & MacGregor 2011; Shiode et al. 2013; Lecoanet & Quataert 2013). The location of convective regions inside a star depends on its birthmass and its evolutionary stage, indicating that the physical impacts of these IGWs also depend on these parameters. Stars discussed in this work are core-hydrogen burning stars with a fully convective core and a radiative envelope.

It was noted that these IGWs efficiently and quickly redistribute angular momentum inside a star (e.g., Press 1981; Kumar & Quataert 1997; Talon & Charbonnel 2003, 2004, 2005; Charbonnel & Talon 2005; Pantillon et al. 2007; Talon & Charbonnel 2008; Rogers et al. 2013). As such, these IGWs lead to (quasi-) uniformly rotating radiative layers by transporting angular momentum outwards whenever the IGWs dissipate. Rogers (2015) found it to depend whether predominantly prograde or retrograde waves dissipate at the surface to speed up or slow down the radiative layer of the star, respectively. Increasing observational evidence for (quasi-) uniformly rotating stars emerges

through asteroseismology of non-magnetic intermediate-mass MS stars (Aerts et al. 2017b), suggesting that IGWs, indeed, cause an efficient redistribution of angular momentum. However, this angular momentum transport happens in a non-diffusive manner (Rogers & McElwaine 2017), such that stellar evolution codes often do not account for this effect as it requires a complex and rigorous treatment (it was however included in the Geneva code and used by e.g., Charbonnel & Talon 2005; Talon & Charbonnel 2005). This may change in the foreseeable future when new descriptions coming from detailed (M)HD simulations become available.

Rogers & MacGregor (2010, 2011) studied how the IGWs interact with the magnetic fields in the radiative interior for a solar-like stellar model. The energy dissipation was affected, but the authors could not make any definitive conclusions regarding the angular momentum transport inside a magnetic layer. Recently, Lecoanet et al. (2017) demonstrated that a magnetic field interacts with the low-order IGWs and converts them into high-order IGWs or travelling Alfvén waves. Both waves are easily damped, causing the magnetic field to suppress IGWs.

IGWs also lead to additional chemical mixing throughout the radiative layer (Press 1981) and could explain the observed surface abundances of Lithium in low-mass MS stars with a convective envelope (e.g., Talon & Charbonnel 2003, 2004, 2005; Charbonnel & Talon 2005). Rogers & McElwaine (2017) demonstrated that the chemical mixing induced by IGWs can be treated as a diffusive process and provided a parametrization based on the wave amplitude spectrum of their simulations to be included in stellar evolutionary codes. This has recently been implemented in the MESA code and its effects on gravity modes was evaluated by Pedersen et al. (2018).

Aerts & Rogers (2015) showed that the velocity spectra for the IGWs from a simulation by Rogers et al. (2013) matched remarkably well with the frequency spectra of three observed O-stars by CoRoT (Blomme et al. 2011). Subsequent detections of IGW signatures have continued to follow for blue supergiants from *Kepler* photometry (Aerts et al. 2017a), spectroscopic time series (Simón-Díaz et al. 2017) and K2 photometry combined with a spectroscopic time series (Aerts et al. 2018). All these stars are subject to large macroturbulent spectral line broadening, such that this phenomenon can be explained as tangential velocity broadening caused by IGWs.

1.3.6 GYRE

GYRE is an open-source pulsation code to compute theoretical pulsation mode eigenmodes and frequencies for a given mode geometry and a given stellar

structure model (Townsend & Teitler 2013). It comes readily available with the stellar structure and evolution code MESA and couples easily with its structure models, but it can also be used with structure models computed by different codes or even with polytropic models.

GYRE solves the pulsation equations according to a multiple shooting method, which is a numerical technique to solve boundary value problems. This is done by subdividing the possible solution space into sub-intervals and solving the pulsation equation in these sub-intervals, assuming continuity conditions. This method has a high numerical stability to solve the set of homogeneous linear differential equations. The pulsation code can compute the pulsation mode frequencies in both the adiabatic and non-adiabatic approximation. Different treatments for uniform rotation are included, such as first-order pertubation and the traditional approximation (Townsend 2003). The effect of an internal magnetic field is not included in GYRE.

We have used the adiabatic module of GYRE (v4.1) together with MESA (v8118) to compute high-order g modes, while accounting for the measured uniform rotation rate using the traditional approximation, to perform detailed forward seismic modelling of HD 43317 (for which part of the light curve is given in Fig. 1.7) in Chapter 7.

1.4 Scientific goals and outline of the thesis

We had set out two goals for this thesis that are strongly related and were inspired by the work performed on the hot magnetic pulsator V2052 Oph (Neiner et al. 2012a; Handler et al. 2012; Briquet et al. 2012). The first goal was to observe known or candidate magnetic hot stars to search for stellar pulsations using modern space-based photometry. Additional ground-based high-resolution and high-S/N spectropolarimetry was collected to aid the magnetometric analysis of the possibly pulsating magnetic intermediate-mass and massive stars. By combining these observational techniques, we expected to create a small sample of magnetic hot stars that exhibit g modes and which we could use to perform detailed seismic modelling. The second and main goal of the thesis was to determine whether the presence of a large-scale magnetic field alters the internal stellar structure. We have divided the main matter of the thesis into two parts, following the work performed to achieve the two defined goals.

Part II discusses the observational study with modern space-based photometry to detect stellar pulsations in magnetic stars. Chapter 2 demonstrates that K2 photometry could be used to study the periodic variability of O-type stars, a class not treated by the nominal *Kepler* mission. While this research did not directly

lead to pulsating magnetic stars, as we could not hunt for magnetic fields due to the faint nature of these O-type pulsators, it did demonstrate the possibilities of the K2 mission in its commissioning run (Campaign 0). Subsequently, we collected K2 photometry of 16 candidate magnetic stars (indicated by their peculiar chemical distribution) and used this to investigate their photometric variability in Chapter 3. In addition, ground-based spectropolarimetry was collected to confirm the presence of the expected large-scale magnetic field. Next, we characterized the geometry of the large-scale magnetic field of the known magnetic star *o* Lup (Alecian et al. 2011) and used BRITE photometry to analyse its periodic variability (Chapter 4). Finally, we utilized BRITE photometry in trying to detect stellar pulsations for the only known magnetic O-type supergiant ζ Ori Aa (Blazère et al. 2015) in Chapter 5.

Because none of our observations and their analyses yielded any new suitable magnetic g mode pulsators with a sufficient number of detected pulsation mode frequencies, we continued the research with asteroseismology of the only known such star, namely HD 43317 (Pápics et al. 2012; Briquet et al. 2013) in Part III. A new time series of spectropolarimetry was combined with archival data to characterize the large-scale magnetic field at the surface of HD 43317 in detail (Chapter 6). In Chapter 7, we continued the analysis by investigating the CoRoT light curve to deduce a conservative list of candidate pulsation mode frequencies. The latter were used to perform detailed seismic modelling of HD 43117. This led to the first seismic probing of the stellar structure of a massive magnetic g-mode pulsator.

Finally, we end this manuscript with conclusions and future outlook in Part IV.

Part II

Searching for suitable magnetic pulsating hot stars

Chapter 2

Investigating the photometric variability of O-type stars with K2

This chapter was originally published as

Kepler's first view of O-star variability: K2 data of five O stars in Campaign 0 as a proof-of-concept for O-star asteroseismology

B. Buysschaert, C. Aerts, S. Bloemen, J. Debosscher, C. Neiner, M. Briquet, J. Vos, P. I. Pápics, R. Manick, V. S. Schmid, H. Van Winckel, and A. Tkachenko

Monthly Notices of the Royal Astonomical Society, 2015, 453, 89 (12 pages)

Original abstract:

We present high-precision photometric light curves of five O-type stars observed with the refurbished *Kepler* satellite during its Campaign 0. For one of the stars, we also assembled high-resolution ground-based spectroscopy with the Hermes spectrograph attached to the 1.2-m Mercator telescope. The stars EPIC 202060097 (O9.5V) and EPIC 202060098 (O7V) exhibit monoperiodic variability due to rotational modulation with an amplitude of 5.6 mmag and 9.3 mmag and a rotation period of 2.63 d and 5.03 d, respectively. EPIC 202060091 (O9V) and EPIC 202060093 (O9V:pe) reveal variability at

low frequency but the cause is unclear. EPIC 202060092 (O9V:p) is discovered to be a spectroscopic binary with at least one multi-periodic β Cep-type pulsator whose detected mode frequencies occur in the range $0.11 - 6.99\,\mathrm{d}^{-1}$ and have amplitudes between 0.8 and 2.0 mmag. Its pulsation spectrum is shown to be fully compatible with the ones predicted by core-hydrogen burning O-star models. Despite the short duration of some 33 d and the limited data quality with a precision near 100 μmag of these first K2 data, the diversity of possible causes for O-star variability already revealed from campaigns of similar duration by the MOST and CoRoT satellites is confirmed with *Kepler*. We provide an overview of O-star space photometry and give arguments why future K2 monitoring during Campaigns 11 and 13 at short cadence, accompanied by time-resolved high-precision high-resolution spectroscopy opens up the possibility of in-depth O-star seismology.

2.1 Introduction

From the point of view of chemical evolution of our Milky Way, supernova progenitors, i.e., stars with masses above $\sim 8\,\mathrm{M}_\odot$ having an extended convective core and a radiative envelope at birth, are the objects that matter (Maeder 2009). Despite their large importance for massive star evolution theory, O-type stars have hardly been monitored in high-cadence uninterrupted space photometry. If available, such monitoring was so far restricted to mmag precision obtained by the WIRE, MOST (Walker et al. 2003), and Coriolis (SMEI instrument, Jackson et al. 2004) satellites, while CoRoT (Baglin et al. 2006) observed six O stars during 34 d leading to a level of brightness variations with $\sim 100\,\mu$mag in precision. Except for the SMEI light curves, which are seven to eight months long, all of the available time series have a duration of the order of a month only.

Unfortunately, O stars were absent in the nominal *Kepler* Field-of-View (FoV), aside from the recently studied O9.5Iab star HD 188209, whose scattered light was collected and investigated (Aerts et al. 2017a). Hence we do not have long-term μmag-level precision photometry of O stars at hand, preventing detailed asteroseismic calibrations of massive star models as it was achieved for the less massive B stars (e.g., Aerts 2015, for a summary). Similarly to the O stars, B stars have an extensive convective core but they do not exhibit a strong radiation-driven wind. Two of the B stars that were seismically modelled based upon period spacings of their high-order dipole g-mode pulsations are ultra-slow rotators ($v \sin i < 10\,\mathrm{km\,s}^{-1}$, Degroote et al. 2012; Moravveji et al.

2015), while the third B star is a moderate rotator ($v \sin i = 62 \pm 5\,\mathrm{km\,s^{-1}}$, Moravveji et al. 2016). Their modelling required the inclusion of extra diffusive mixing, in addition to core overshooting, to bring the theoretical models in agreement with the μmag-precision seismic data of duration five months (for the B3V star HD 50230, Degroote et al. 2012) and four years (for the B8V stars KIC 10526294, Moravveji et al. 2015 and KIC 7760680, Moravveji et al. 2016). It would be highly beneficial to perform similar seismic inference studies for O-type stars, whose theoretical models are the most uncertain of all the mass ranges, while they are mainly responsible for the global chemical enrichment of the Milky Way.

Two rapidly rotating O stars were monitored by the MOST satellite. It concerns ξ Per (O7IIInf) with $v \sin i \simeq 200\,\mathrm{km\,s^{-1}}$ revealing variability due to rotational modulation with a period of 4.18 d, in the absence of pulsations (Ramiaramanantsoa et al. 2014) and ζ Oph (O9.5Vnn, $v \sin i \simeq 400\,\mathrm{km\,s^{-1}}$) whose WIRE, MOST, and SMEI photometry led to the detection of multi-periodic variability due to pulsations with frequencies in the range $1 - 10\,\mathrm{d^{-1}}$ and amplitudes up to $\simeq 10$ mmag. These modes turn out to be variable on a time scale of some 100 d (Howarth et al. 2014). The rapid rotator ζ Pup was monitored by SMEI during several long-term runs, but these data revealed only two dominant frequencies. Howarth & Stevens (2014) attributed this variability to non-adiabatic g modes, yet recent work with additional BRITE photometry indicates the variability is caused by rotational modulation due to evolving bright surface inhomogeneities (Ramiaramanantsoa et al. 2018). The variability derived from the space photometry for ξ Per and ζ Oph is in line with assessments from their high-precision time-resolved line-profile variability. It is also in agreement with high-precision time-resolved spectroscopy of the rapidly rotating O9Vp star HD 93521, whose multi-periodicity has a yet unclear origin (e.g., Fullerton et al. 1996; Rauw et al. 2008, $v \sin i \simeq 400\,\mathrm{km\,s^{-1}}$). Seismic modelling of rapidly rotating O stars was not achieved so far.

One of the CoRoT short runs (SRa02) was devoted to the monitoring of six O-type stars during 34 d with the asteroseismology CCD of the mission, having a cadence of 32 s (Auvergne et al. 2009). Among these six stars were two binaries. Plaskett's star (HD 47129) is a high-mass interacting binary (O7.5I+O6II) with a magnetic secondary (Grunhut et al. 2013). Its CoRoT light curve revealed hints of g-mode pulsations with frequencies near $\sim 0.8\,\mathrm{d^{-1}}$ and harmonics, as well as modulation with multiples of the orbital period of 14.39625 d (Linder et al. 2008) — see Mahy et al. (2011) for a discussion. A seismic interpretation was not possible for this complex system. The eccentric ($e = 0.59 \pm 0.02$) long-orbit ($P_{\mathrm{orbit}} = 829 \pm 4\,\mathrm{d}$) binary HD 46149 revealed a primary with stochastic pressure-mode pulsations with frequencies in the range 3.0 to $7.2\,\mathrm{d^{-1}}$. These correspond to a regular frequency pattern of separation $0.48\,\mathrm{d^{-1}}$. Unfortunately,

these p modes did not lead to an unambiguous interpretation in terms of seismic models (Degroote et al. 2010b). Further, the "red noise" power excess found by Blomme et al. (2011) in the CoRoT amplitude spectra of the three moderately rotating O stars HD 46150 (O5.5f, $v \sin i \simeq 100\,\mathrm{km\,s^{-1}}$), HD 46223 (O5f, $v \sin i \simeq 100\,\mathrm{km\,s^{-1}}$), and HD 46966 (O8.5V, $v \sin i \simeq 50\,\mathrm{km\,s^{-1}}$) were interpreted in terms of convectively-driven Internal Gravity Waves (IGWs, Aerts & Rogers 2015, see also Sect. 1.3.5).

Note added at time of PhD print: Recently, the O9.5Iab star HD 188209 was also interpreted to host IGWs thanks to ∼4 years of scattered light with the *Kepler* mission (Aerts et al. 2017a). The binary systems δ Ori and ι Ori exhibit periodic variability that has been interpreted as tidally induced pulsations. The variability of δ Ori was detected in both the ∼22 d MOST light curve and in the high-resolution spectroscopic multi-site campaign as deviations from the variability caused by the binary system (Pablo et al. 2015). For ι Ori, a clear heartbeat signature was observed in the two-colour BRITE light curves as well as up to seven frequencies that are explained as tidally induced pulsations (Pablo et al. 2017). Johnston et al. (2017) studied a part of the K2 light curve of the eclipsing binary system HD 165246 that was collected during Campaign 9. Besides variability caused by the binary system itself, evidence of heat-driven pulsations was detected. It remains to be seen if these come from the O8V component or the B7V component.

The only seismic inference was achieved for the O9V star HD 46202, which revealed β Cep-type pressure-mode pulsations with frequencies in the range from 0.5 to $4.9\,\mathrm{d^{-1}}$ (Briquet et al. 2011). Seismic modelling of this star led to a mass $M = 24.1 \pm 0.8\,\mathrm{M_\odot}$, an age of 4.3 ± 0.5 Myr, and a core overshooting parameter of 0.10 ± 0.05 expressed in units of the local pressure scale height H_p and using a step-function formulation.

To remedy the lack of seismic calibration of massive star models, we defined a K2 (Howell et al. 2014) observing programme of O-type stars with the aim to monitor a sample of such objects at μmag precision during 3-month runs. The present work reports on the first results of this programme and offers a proof-of-concept of K2's capabilities for future O-star asteroseismology.

We first discuss the collected K2 photometry in Sect. 2.2 and how the detrending for known instrumental effects was accounted for. Section 2.3 expands upon the frequency analysis of the K2 photometry, and EPIC 202060092 is analysed in further detail in Sect. 2.4. Finally, we summarize the current state of affairs for high-precision photometry of O-type stars in Sect. 2.5.

Table 2.1: The five O stars observed in Campaign 0 of K2, with some information from the online SIMBAD database and the EPIC catalogue. The dominant frequency in the K2 data is listed, along with its amplitude.

EPIC ID	Other ID	RA (J2000)	DEC (J2000)	V (mag)	SpT	Frequency (d^{-1})	Amplitude (ppt)
202060091	HD 44597	06 23 28.538	+20 23 31.63	9.05	O9V	—	—
202060092	HD 256035	06 22 58.243	+22 51 46.15	9.21	O9V:p	3.4248	1.827
202060093	HD 255055	06 19 41.647	+23 17 20.22	9.40	O9V:p(e)	—	—
202060097	Cl* NGC 2175 H 98	06 08 31.999	+20 39 24.01	13.7	O9.5V	0.3801	5.209
202060098	2MASS J06245986+2649194	06 24 59.870	+26 49 19.42	15.11	O7V	0.1988	8.594

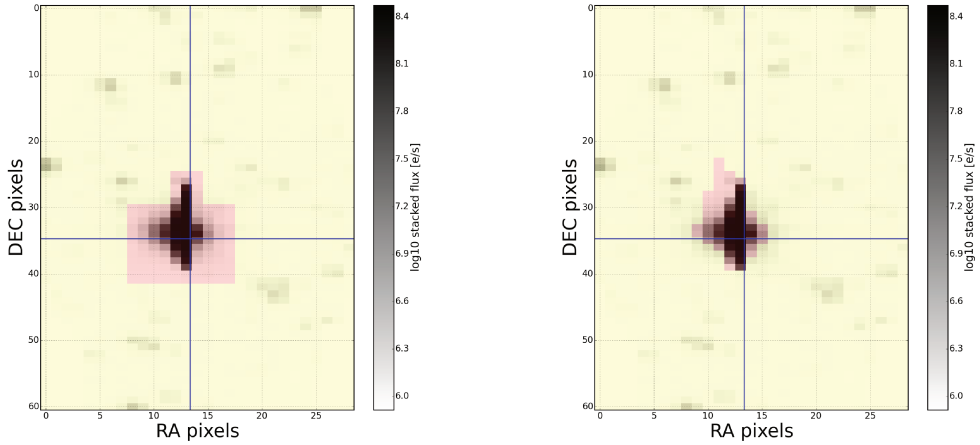

Figure 2.1: Our adopted aperture (left) versus the one used by the automatic analysis of Vanderburg (right) for the light curve extraction of EPIC 202060091 as indicated in pink. The position of the star is indicated by the blue cross.

2.2 Extraction of the Light Curves

We proposed the five O-type stars listed in Table 2.1 for photometric monitoring with K2 in Campaign 0. We developed a photometric reduction method that accounts for the spacecraft (re)pointing and the non-uniform pixel response of the K2 CCDs, starting from the pixel frames in the Mikulski Archive for Space Telescopes (MAST archive; release of 7 Nov. 2014). The time series of Campaign 0 contain two large gaps related to safety events of the spacecraft. We only used data after the largest safety event, i.e., after the *Kepler* Barycentric Julian Day 1939.1, providing us with photometric measurements covering 33.038 d. These data have a frequency resolution corresponding to the Rayleigh frequency limit of $\delta f_{\rm ray} = 1/33.038\,{\rm d} = 0.0302\,{\rm d}^{-1}$ (0.35μHz), which represents an upper limit for the frequency uncertainty of any periodic signal in the data (Aerts et al. 2010, Chapter 5). Further, we ignored all measurements taken during a thruster firing or a repointing event of the spacecraft.

With the aim to exclude as much as possible instrumental effects in the light curves, we first defined an optimal constant aperture mask customized to each of the five targets from visual inspection, such that blending with nearby targets is avoided as much as possible. We show these aperture masks in the left panels of Fig. 2.1 to 2.5. The counts for each pixel in these apertures were summed up to provide the time series of the raw photometric measurements. To account for the varying background during the measurements, we used iterative sigma

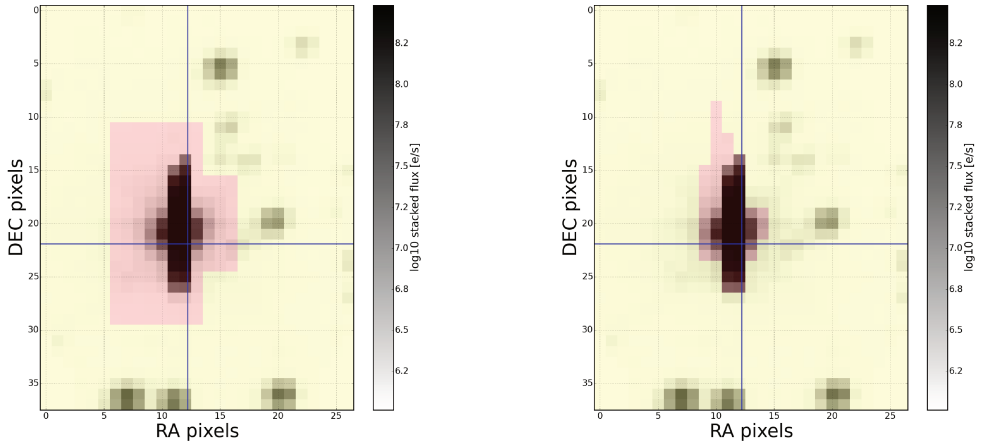

Figure 2.2: Same as Fig. 2.1, but for EPIC 202060092.

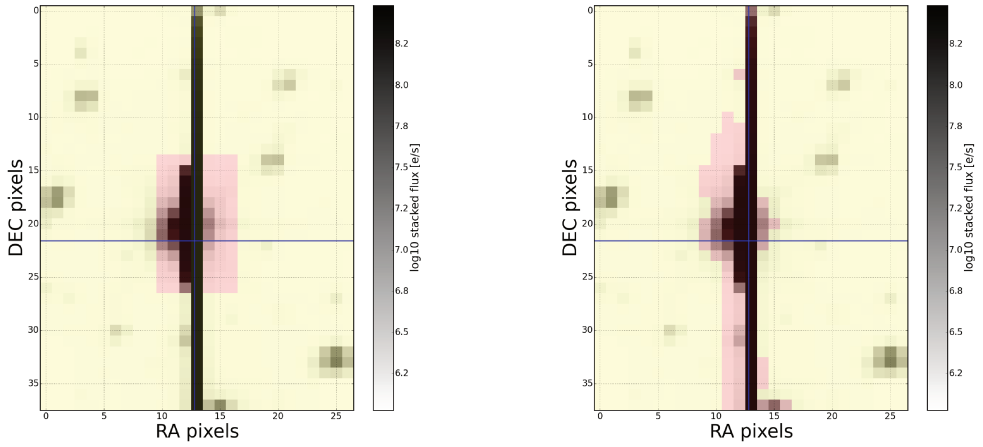

Figure 2.3: Same as Fig. 2.1, but for EPIC 202060093. For this target, the aperture mask on the left excluded the central saturated column to produce the photometry shown as black circles in the top panel of Fig. 2.6, while this column was used to produce the Vanderburg version of the light curve shown as grey crosses in the top panel of Fig. 2.6.

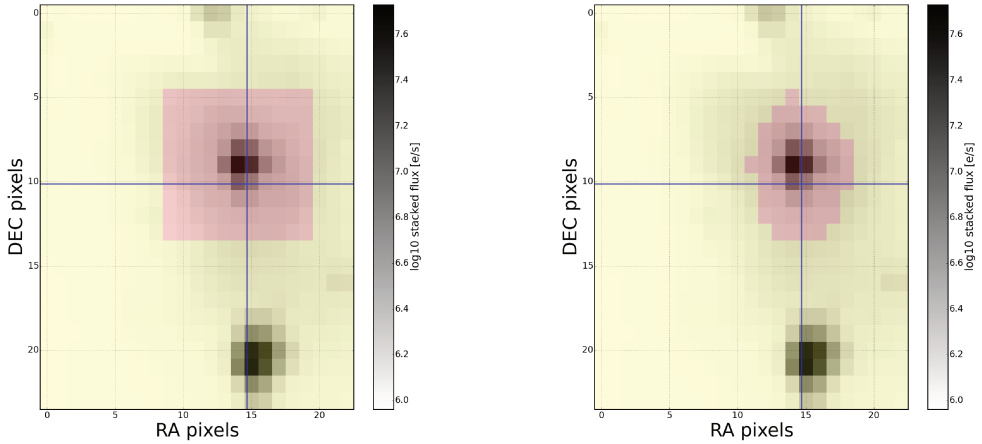

Figure 2.4: Same as Fig. 2.1, but for EPIC 202060097.

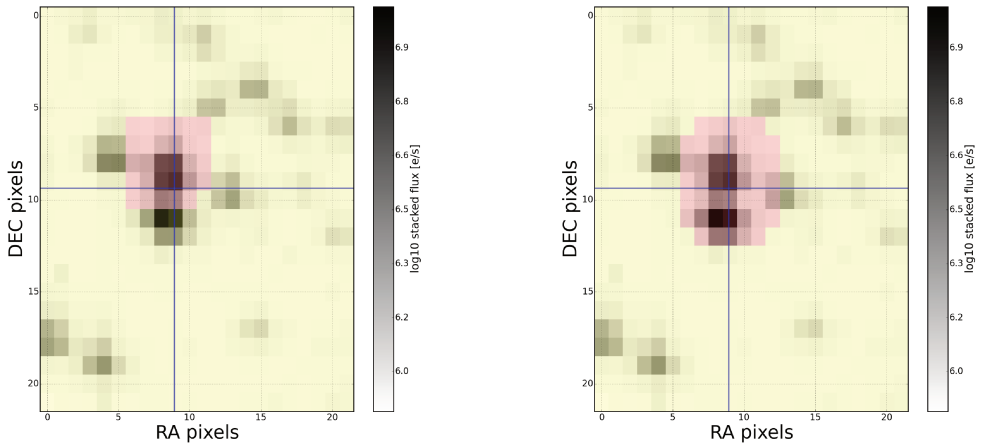

Figure 2.5: Same as Fig. 2.1, but for EPIC 202060098.

clipping. All pixels of the frame at a given time step were deselected when their signal was larger than 1.2 times the median signal of the frame. This procedure was iterated until we obtained a stable median for that time step and no further de-selection was needed. The achieved median was then taken to be the background signal in a given pixel in the frame. We subtracted this background level from the raw light curve, accounting for the considered number of pixels in the aperture mask.

Outliers were identified and removed by self-flat-fielding through spline fitting, along with further detrending of the photometry by third-order polynomial fitting, in an iterative scheme. In each step, the photometry was divided by the polynomial fit, which allowed us to work with relative brightness units instead of electrons per second. Five iteration steps turned out to be sufficient.

This raw light curve was then used as a starting point to account for the instrumental effects caused by K2's attitude control system, which involves a roll manoeuvre every six hours. Due to that, we had to redetermine the position of the star on the CCD and connect it to the instrumental brightness variations that occurred at that position. In order to derive an appropriate relation for the correction factor versus star position, we determined the position of the star on the CCD by fitting a 2D Gaussian function to the photometry, representing the point-spread-function. Following the principal component analysis defined by Vanderburg & Johnson (2014), we rotated the two-dimensional CCD position according to its largest eigenvalue and fitted a fifth-order polynomial, allowing us to define an arc length connected with the instrumental brightness for each time step. We then assumed that all the power in the Fourier transform of the time series of the measured brightness centred at $4.08\,\mathrm{d}^{-1}$ and its higher harmonics at 8.16, 12.24, 16.32, and $20.40\,\mathrm{d}^{-1}$ had instrumental origin. A bandpass filter in the Fourier domain was constructed using the bands $j \times 4.08\,\mathrm{d}^{-1} \pm 5\,f_{\mathrm{res}}$, with f_{res} the Rayleigh limit and $j = 1, \ldots, 5$. All the power in these bands was assumed to be due to instrumental effects, while all power outside these bands was considered as stellar signal. The inverse Fourier transform then allowed to connect the instrumental brightness variations to the position of the star on the CCD. This method worked well for four of the five stars, with EPIC 202060093 suffering from a too small on-board sub-raster and saturation of many pixels leading to leakage outside of the frame. The light curves are shown with black circles in the upper panel of Fig. 2.6. These flux variations are expressed in parts-per-thousand (ppt).[1]

In order to compare our reduction scheme for the individual stars and its effectiveness, we also used the reduced light curves as made available by

[1] The conversion factor between brightness variations expressed in mmag and flux variations expressed in ppt amounts to $2.5 \log_{10} e = 1.0857$.

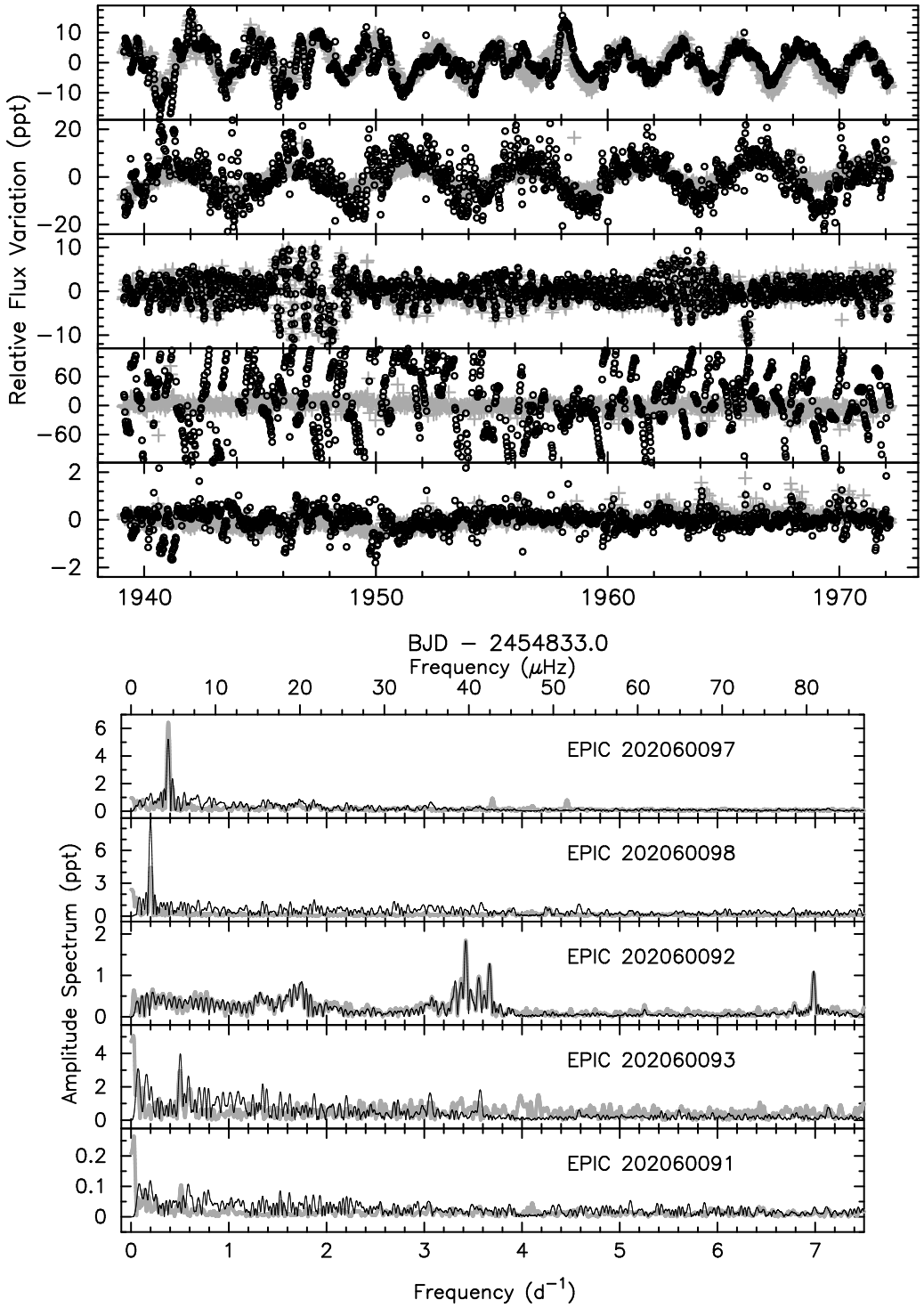

Figure 2.6: K2 light curves (top) and their amplitude spectra (bottom) of the five monitored O stars. The black circles and thin black lines are derived from our reduction of the raw pixel data, while the grey crosses and thick grey lines are the Vanderburg (2014) light curves.

Vanderburg (2014, release date of 10 April 2015[2]). This is an automated reduction based on their self-flat-fielding approach combined with high-pass filtering, designed from the viewpoint of optimal exoplanet hunting, as previously developed by Vanderburg & Johnson (2014) to which we refer for details. While our aperture determination and noise treatment was done manually and tuned to each star individually and locally, Vanderburg (2014) used a semi-automated mask determination and made use of the instrumental effects of thousands of stars. Our method is tuned to get the optimal signal, while their method is focused on reducing the global noise as much as possible. The aperture used by Vanderburg are shown in the right panels of Figs 2.1 to 2.5.

Despite the quite different masking, the two independent reduction methods give consistent results in terms of frequency spectrum, the major difference occurring in the lowest frequency regime of the Fourier transform. This is similar to the difference already encountered for light curves of the nominal *Kepler* mission when reduced globally from the viewpoint of optimal planet hunting versus individually and tuned towards optimal asteroseismic applications. For the latter, it is typically advantageous to consider more pixels than done in the standard exoplanet pipeline, because the aim is to gather as much signal as possible for a whole range of frequencies, given the multi-periodic character of the variability. For exoplanet hunting, however, one aims to find singly periodic low-amplitude signal and therefore avoids too noisy pixels. Masking for asteroseismology as we have done here avoids complicated detrending and filters out long-term instrumental frequencies more easily, as illustrated and discussed in Tkachenko et al. (2013), but is not optimal in terms of global noise properties.

A comparison between the light curves resulting from the two independent reduction methods for the five O stars considered here is given in Fig. 2.6. In general, the agreement is good, except for EPIC 202060098 and EPIC 202060093. For the former star, the dominant frequency is fully consistent but its amplitude differs in value, due to the different shape and position of the chosen aperture masks in the two methods. With our apertures, we have avoided the nearby target (see Fig. 2.5) contributing to the overall light curve. This explains the higher amplitude compared to the "Vanderburg" light curve, while the latter leads to less power at low frequencies (cf. bottom panel of Fig. 2.6). For EPIC 202060093, both light curves suffer from the saturation and leakage across the CCD, but again the frequency amplitude is higher when derived from our light curve. In the rest of the paper, we used our reduced light curves to derive the frequencies and amplitudes of the five target stars, after having verified that all the listed frequencies are consistently recovered from those two versions.

[2] `https://www.cfa.harvard.edu/~avanderb/`

Table 2.2: The frequencies and amplitudes of EPIC 202060092 determined from Fourier analysis followed by non-linear least-squares fitting. The computation of the errors is explained in the text. The S/N was computed as the amplitude divided by the noise level of the residual light curve averaged over $0 - 10\,\mathrm{d}^{-1}$.

ID	Frequency (d^{-1})	Amplitude (ppt)	S/N	Remark
f_1	3.4243 ± 0.0054	1.827 ± 0.079	16.9	
f_2	3.6663 ± 0.0066	1.352 ± 0.084	12.5	
f_3	6.9853 ± 0.0088	1.091 ± 0.104	10.1	
f_4	3.3173 ± 0.0113	0.938 ± 0.103	8.7	
f_5	3.5583 ± 0.0089	0.998 ± 0.105	9.2	
f_6	1.7453 ± 0.0092	0.941 ± 0.083	8.7	$f_3/4$
f_7	1.6693 ± 0.0085	0.953 ± 0.106	8.8	$f_4/2$
f_8	1.7193 ± 0.0091	0.784 ± 0.106	7.3	$f_1/2$
f_9	3.4863 ± 0.0113	0.646 ± 0.096	6.0	$f_3/2$
f_{10}	0.2223 ± 0.0113	0.705 ± 0.100	6.5	$2f_{12}$
f_{11}	0.3313 ± 0.0125	0.585 ± 0.104	5.4	$3f_{12}$
f_{12}	0.1123 ± 0.0129	0.566 ± 0.074	5.2	$f_1 - f_4 = f_2 - f_5$
f_{13}	1.3223 ± 0.0134	0.535 ± 0.095	5.0	

2.3 Frequency Analysis of K2 data

We computed the Lomb-Scargle periodograms (Lomb 1976; Scargle 1982) of the two versions of the light curves. These are shown in the lower panel of Fig. 2.6. The thin black lines are for our reduced light curves while the thick grey lines are for the Vanderburg (2014) light curves.

For the stars EPIC 202060097 and 202060098, we find one isolated significant frequency corresponding to a period of 2.631 d and 5.030 d, respectively (Table 2.1). We interpret their variability as due to rotational modulation.

The cause of the variability of EPIC 202060091 and 202060093 is less clear. Despite the limitations of the aperture mask for EPIC 202060093 (see Fig. 2.3), its frequency spectrum is similar to the one of EPIC 202060091, but there is a factor more than ten difference in the level of variability. None of these two stars shows clear periodic variability with isolated frequencies. Nevertheless, they display several low-frequency peaks that stand out of the noise level without being formally significant. This is somewhat similar to the frequency spectra of three O stars observed with the CoRoT satellite, revealing red noise power excess at low frequency that was recently interpreted in terms of convectively driven internal gravity waves (Aerts & Rogers 2015). However, we currently consider this interpretation as speculative.

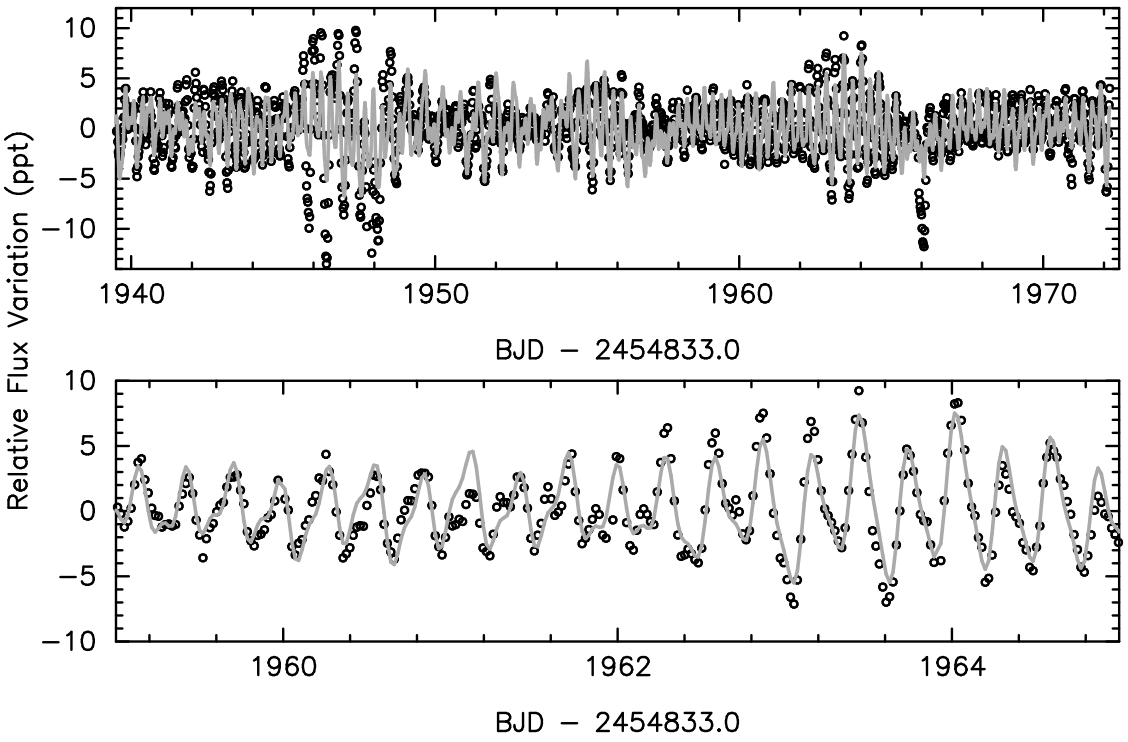

Figure 2.7: Fit (grey line) to the K2 light curve of EPIC 202060092 (black circles repeated from the central panel of the top panel of Fig. 2.6) based on the 13 frequencies listed in Table 2.2.

EPIC 202060092 turns out to be a multi-periodic pulsator compatible with heat-driven pulsation modes, similar to HD 46202 (Briquet et al. 2011). We performed iterative prewhitening and found 13 significant frequencies when we adopted the conservative criterion of considering a frequency to be significant when its amplitude reaches above five times the noise level in the residual light curve averaged over the frequency range $0 - 10\,\mathrm{d}^{-1}$. The frequencies and amplitudes along with their errors are listed in Table 2.2 while the fit to the light curve based on those 13 frequencies is shown in Fig. 2.7. For the computation of the frequency and amplitude errors, we took into account that the formal errors resulting from a non-linear least squares fit are only in agreement with those obtained in the Fourier domain in the case of uncorrelated data with white noise and with sufficiently high frequency resolution (e.g., Aerts et al. 2010, Chapter 5). Here, we encounter two complications: the data have only a short time base of some 33 d, leading to a limited resolving power of $1.5/33.038\,\mathrm{d} = 0.04541\,\mathrm{d}^{-1}$ (Loumos & Deeming 1978). Further, as is usually the case for highly sampled space photometry, the data may be correlated. This requires incorporation of a correction factor in the error estimates of the frequencies

and their amplitudes (Schwarzenberg-Czerny 2003). Following Degroote et al. (2009a), we computed this correction factor to be 2.51 and obtained the error estimates listed in Table 2.2. The fit shown in Fig. 2.7 is generally good, but not perfect. This is due to there being additional frequencies whose amplitudes are between 3 and 5 times the noise level. Due to the limited frequency resolution, we are unable to pinpoint their value with respect to the frequencies already listed in Table 2.2 and this explains why a level of unresolved beating still occurs in some parts of the light curve (bottom panel of Fig. 2.7).

2.4 Follow-up study of EPIC 202060092

The nature of the frequencies f_6 to f_{13} listed in Table 2.2 is unclear. Given the limited frequency resolution, they could either be identified as sub-multiples or combinations based on f_1 to f_5, or be due to independent g modes occurring in the densely-packed g-mode frequency regime, or both. The interpretation of all the detected frequencies in terms of identification of their degree ℓ, radial order n, and azimuthal order m requires additional observational information, such as the rotational frequency of the star. We also note that the light curve of EPIC 202060092 shows a marked dip near day 1966 and remarkable beating from days 1946 to 1948 and to a lesser extent also from days 1963 to 1965 (Fig. 2.7, where the listed and shown dates are with respect to *Kepler* Barycentric Julian Data, indicated here as BJD 2454833.0). With the aim to test if the dips could be connected with binarity and to derive the projected rotation velocity of the pulsator, we gathered spectroscopic measurements.

2.4.1 EPIC 202060092 is a spectroscopic binary

The 1.2-m Mercator telescope is dedicated to the long-term monitoring of variable stars, including heat-driven pulsators (e.g., De Cat et al. 2007; Cuypers et al. 2009) and evolved low-mass stars (e.g., van Winckel et al. 2009). A large fraction of the telescope time in the recent years has been used for the spectroscopic monitoring of bright *Kepler* targets (e.g., Lehmann et al. 2011; Tkachenko et al. 2012; Beck et al. 2014; Niemczura et al. 2015; Van Reeth et al. 2015). In view of its photometric behaviour and of recent theoretical predictions that more than 70% of all O-type stars occur in binaries (Sana et al. 2012), we added EPIC 202060092 to the observing programme for measurements with the HERMES spectrograph (Raskin et al. 2011).

A total of 22 high-resolution (HRF mode, resolution of 85 000) optical spectra were taken so far, with integration times between 600 s and 1800 s between

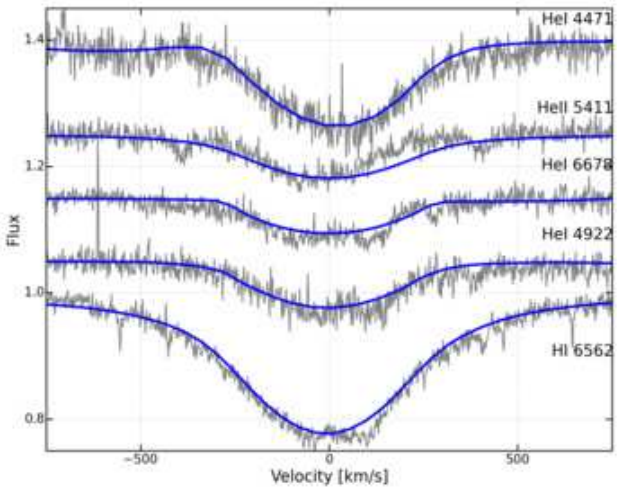

Figure 2.8: Selected H and He lines in the highest S/N HERMES spectrum of EPIC 202060092. The blue line is the prediction for a NLTE atmosphere model with parameters listed in the text.

November 2014 and March 2015. The S/N per exposure ranged from 30 to 60. The raw exposures were treated with the HERMES pipeline, including cosmic-hit removal, merging of orders, and barycentric correction. Subsequently, all spectra were rectified following the method outlined in Pápics et al. (2013).

Comparison with rotationally broadened synthetic spectra derived from plane-parallel NLTE O-star atmosphere models (Lanz & Hubeny 2003, OSTAR2002 grid) led to the estimates $T_{\rm eff} \simeq 35\,000\,{\rm K}$, $\log g \simeq 4.5\,{\rm dex}$, and $v \sin i \simeq 270\,{\rm km\,s^{-1}}$ for solar metallicity and a fixed micro-turbulent velocity of $10\,{\rm km\,s^{-1}}$. The agreement between the theoretical line spectrum and the measured profiles for the highest S/N spectrum is illustrated in Fig. 2.8 for a few selected lines. Despite the modest S/N, it can be seen that structure occurs in some of the observed He lines. This may be connected to the pulsations but higher S/N is needed to firmly establish this.

Given the scarcity of spectral lines due to the large broadening and limited S/N, we estimated the radial velocity values from fits to the detected H and He lines. The outcome is very similar for the Hα, Hβ, Hγ, and Hϵ lines, so we averaged their radial velocity estimates and computed the standard deviation as a proxy for the errors. We detect radial velocity variations with a peak-to-peak value around $30\,{\rm km\,s^{-1}}$. Given the low amplitude of the photometric variations (cf. Table 2.2) we do not assign these radial-velocity variations to pulsations, but rather interpret them in terms of binarity. Globally, the velocities from the

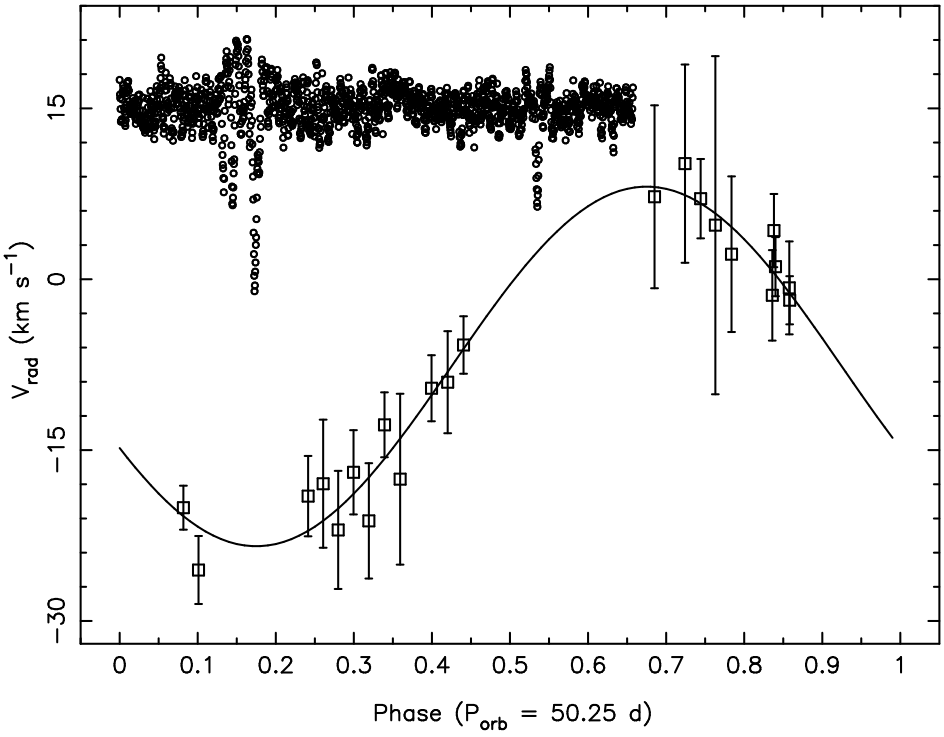

Figure 2.9: Phased radial velocity measurements of EPIC 202060092 deduced from its Balmer lines. The residual K2 light curve after prewhitening the fit in Fig. 2.2 is indicated in the top part in ppt according to the same phase and shifted up with value 15 for visibility reasons. Follow-up spectroscopic observations have been taken at the time of the PhD print to constrain the binary parameters in more detail during an upcoming study.

Balmer lines are consistent with those based on the dominant He lines, such as He I 4922Å, He I 5875Å, He I 6678Å, He II 4541Å, and He II 5411Å, but for some of those we encounter too large uncertainties to achieve conclusive values, as already illustrated by Fig. 2.8. This might point towards a contribution of more than one star to some of these lines, but this needs further study from new spectra with higher S/N.

Our spectroscopy does not allow to deduce a high-precision orbital solution. Nevertheless, we clearly establish spectroscopic binarity and find a rough preliminary period estimate of $P_{\rm orb} \sim 50\,{\rm d}$ from the Balmer lines. These data were folded with the most likely period in Fig. 2.9, where we also show the phased residual K2 light curve after prewhitening the 13 frequencies listed in Table 2.2 (i.e., the black circles minus the grey line in Fig. 2.7). We conclude that, with the current estimate of the orbital period of the binary, we cannot associate all the dips in the K2 photometry with eclipses and rather ascribe

them to unresolved beating of pulsation modes, except perhaps the dip near day 1966. Large beating patterns as the ones seen near days 1946, 1955, and 1964 (Fig. 2.7) have indeed been detected before in multi-periodic massive pulsators, both in high-cadence ground-based (e.g., Handler et al. 2004, 2006) and space photometry (e.g., Pápics et al. 2012). With the long-cadence sampling at 29 min, the unresolved nature of the light curve is not so surprising, because the fastest pulsation mode is sampled only seven times per cycle. While such sampling works fine for the analysis and interpretation of long-duration light curves of months to years, there is a limitation to resolve beating patterns for a data set of only 33 d. The beating between frequencies f_1 and f_4, as well as the one between f_2 and f_5, occurs with a period of 9.1 d and the beating phenomena we measure are separated by roughly this value, occurring near days 1946, 1955, and 1964 (top panel of Fig. 2.7). The nature of the isolated dip in the light curve at day 1966 remains unclear. That decrease in brightness is not accompanied by local increases as one would expect from multi-periodic beating among linear pulsation modes and could therefore still be caused by binarity. Indeed, according to Fig. 2.9, the dip occurs near orbital phase ~ 0.5 and, given the large uncertainty on the current estimate of the orbital period, could be caused by an eclipse. Unfortunately, there are no HIPPARCOS data data available to add to the K2 photometry for this star.

2.4.2 First modelling attempts

The five dominant frequencies listed in Table 2.2 (i.e., f_1, f_2, f_3, f_4 and f_5) have values typical of pressure modes in an O9 main-sequence star as already found for HD 46149 and HD 46202 by Degroote et al. (2010b) and Briquet et al. (2011), respectively. Part of the theoretical radial and zonal dipole or quadrupole p-mode spectrum for O-type stars is shown in Fig. 2.10 for a mass of $35\,M_\odot$ (left panel) and $30\,M_\odot$ (right panel). This figure was constructed from the grid of stellar and pulsational models described in Degroote et al. (2010b), whose input physics is discussed in Briquet et al. (2011), to which we refer for details. The two stellar models whose zonal p modes are shown in Fig. 2.10 have an initial hydrogen fraction of $X_c = 0.715$ and a step-function core overshoot parameter of $\alpha_{\rm ov} = 0.2 H_{\rm p}$. As we have shown in the previous Section, EPIC 202060092 is situated between the two vertical dashed lines. These correspond to ages of 3.53 and 3.51 Myr (hotter temperature limit) and 4.39 and 4.86 Myr (coolest temperature limit), for $35\,M_\odot$ and $30\,M_\odot$, respectively.

Even though relatively large uncertainties occur for the atmospheric parameters of the star, the measurement of $v \sin i$ is fairly robust. It immediately excludes $f_{12} = 0.1123\,{\rm d}^{-1}$ to be the rotational frequency. Indeed, the models with $35\,M_\odot$ and $30\,M_\odot$, whose low-degree p modes were shown in Fig. 2.10, have radii of

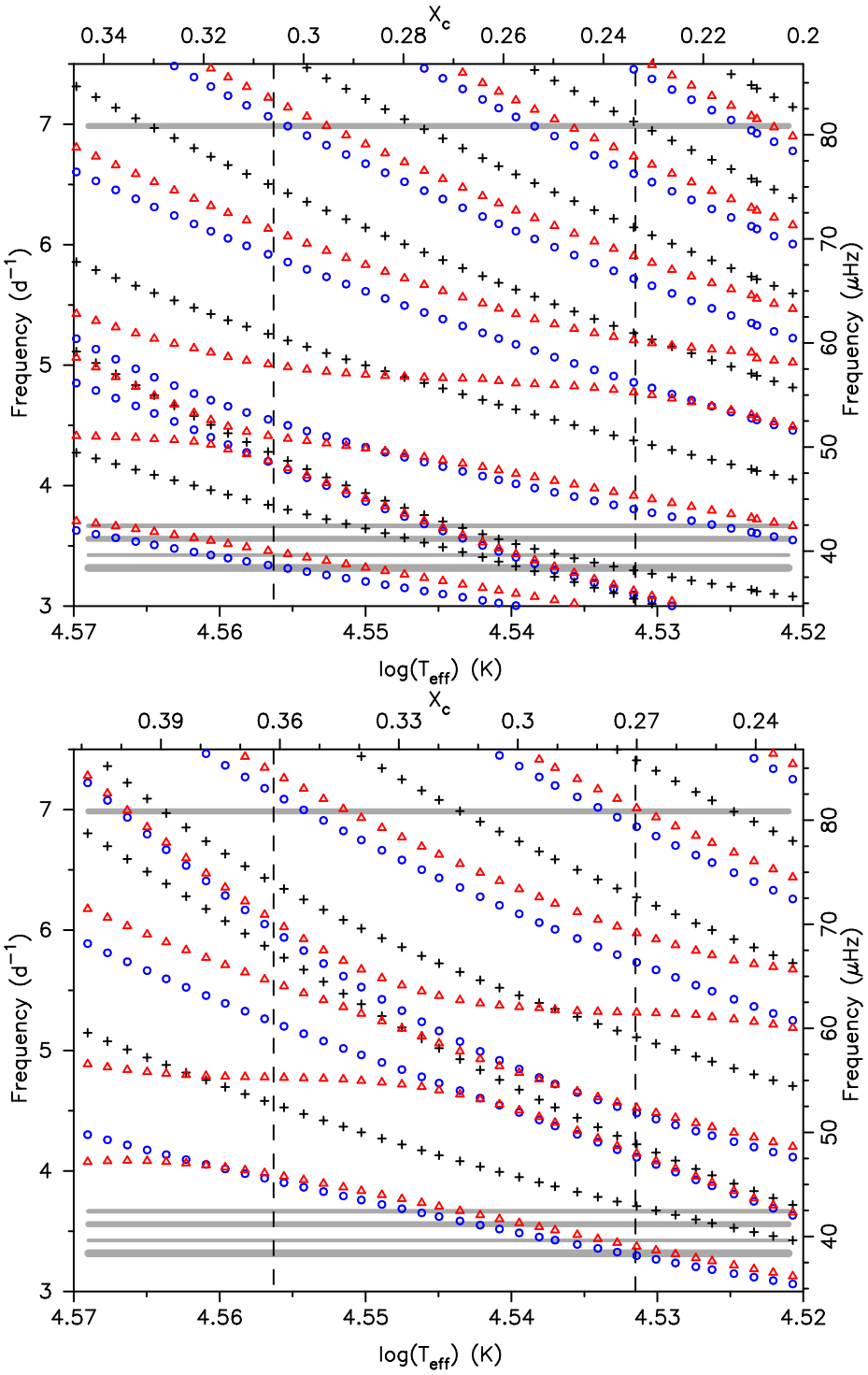

Figure 2.10: Adiabatic pulsation frequencies of radial (blue circles), dipole (black crosses), and quadrupole (red triangles) zonal modes for a stellar model with $M = 35\,\mathrm{M}_\odot$ (*top*) and with $M = 30\,\mathrm{M}_\odot$ (*bottom*). EPIC 202060092 is situated in between the two vertical dashed lines, which indicate the spectroscopic 1σ-range of the measured $T_{\rm eff}$. The top $x-$axes indicate the central hydrogen fraction, where the value at birth was $X_c = 0.715$. The horizontal grey lines indicate the five dominant independent frequencies, where the line thickness represents the frequency resolution.

$15\,R_\odot$ and $12.5\,R_\odot$, respectively, for the measured $T_{\rm eff}$. We find lower limits for the rotational splitting within p mode multiplets of roughly $0.36\,d^{-1}$ and $0.43\,d^{-1}$ for $35\,M_\odot$ and $30\,M_\odot$, respectively, corresponding to the upper limit on the rotation frequency of a $15\,R_\odot$ and a $12.5\,R_\odot$ star, respectively.

Even though the white-light CoRoT photometry of HD 46202 by itself did not lead to mode identification in the absence of multiplets in the frequency spectrum, the same situation as we have here for EPIC 202060092, Briquet et al. (2011) managed to perform forward seismic modelling from frequency matching and pinpointed the four free parameters $(M, X, Z, \alpha_{\rm ov})$ of HD 46202 with high precision, for the input physics that went into their dense grid of theoretical models. Their frequency resolution was much higher, typically between 10^{-4} and $10^{-3}\,d^{-1}$, than what we can deduce from the current long-cadence K2 data. This major accomplishment for HD 46202 was owed to the CoRoT sampling rate of 32 s, which delivered a light curve of more than 80 000 data points rather than only 1 600 for EPIC 202060092 from K2. Despite similar duration of the monitoring, this implies a factor $\sim\sqrt{50}$ better frequency precision. Moreover, their study was based on twice as many spectra of a single star of one magnitude brighter than EPIC 202060092, implying a co-added averaged spectrum of S/N above 500. Finally, the ten times lower $v \sin i = 25 \pm 7\,{\rm km\,s^{-1}}$ of HD 46202 compared to EPIC 202060092 also implied modest rotational splitting values such that forward modelling assuming zonal modes made sense.

For the case of EPIC 202060092, which has a similar pulsation spectrum and hence the same potential, we encounter the limitations of the poor frequency resolution and of not knowing the azimuthal order m of the dominant modes because the fast rotation introduces frequency shifts of at least $0.3\,d^{-1}$ when $m \neq 0$. It can be seen from Fig. 2.10 that, even for only two masses and one set of values $(X, Z, \alpha_{\rm ov})$, several of these models fulfill the requirements of the five measured frequencies, keeping in mind that large yet unknown frequency shifts due to rotational splitting must be allowed for. A similar situation of unknown rotational shifts was encountered in the NGC 884 cluster modelling by Saesen et al. (2013), but in that study some seismic constraints could still be achieved thanks to the demand of an equal age and metallicity of the stars in the cluster.

With the present K2 photometry and HERMES spectroscopy, forward seismic modelling is not possible for EPIC 202060092 due to the unknown mode geometry of all candidate pulsation mode frequencies. We do note that even the identification of (ℓ, m) for just one of its modes would break most of the degeneracy in the seismic grid. As an example, identification of f_4 as a radial mode would imply it is the fundamental, while f_3 is then the third (for $35\,M_\odot$, left panel of Fig. 2.10) or fourth (for $30\,M_\odot$, right panel of Fig. 2.10) radial overtone. At present, however, such inference remains speculative. Nevertheless, the models imply that, if f_1 to f_5 are due to low-degree low-order modes, then

the mass of the star cannot be far below $30\,M_\odot$. While the identification of one of the pressure modes would lead to a constraint on the overall properties of EPIC 202060092 through forward seismic modelling, these p modes do not sufficiently penetrate the radiative layer to obtain stringent constraints on the near-core region. Quantities such as the extent of the convective-core overshooting layer, would still remain ill-defined without detected g modes.

Firm conclusions on the properties of the orbit of EPIC 202060092 and on the nature of its companion require additional and long-term time-resolved high S/N spectroscopy. Given its potential for future seismic modelling, we plan to acquire such data with the aim to pinpoint the orbit and characterise the two components with high precision, as well as to detect and identify the dominant pulsation mode(s). This will require spectral disentangling and the application of sophisticated mode identification methodology (e.g., Tkachenko et al. 2014, for an example of another potentially interesting pulsating massive binary).

2.5 State of affairs of high-precision O-star space photometry

The five O-type stars monitored by K2 so far confirm earlier findings based on high-precision uninterrupted space photometry, i.e., the diversity of the variable character of these stars is large. Table 2.3 provides an overview of all eighteen O-type stars that have been monitored with SMEI, MOST, CoRoT, and K2 and their dominant cause of the photometric variability. For several of the stars, various causes of variability act simultaneously. The secondary of the binary HD 47129 is the only object in the list known to host a magnetic field and this star is variable. Nevertheless, rotational modulation connected with chemical and/or temperature surface inhomogeneities occurs for five of the eighteen stars and is usually due to some level of magnetic activity even though the fields may be too weak or too complex to give detectable longitudinal field components.

From the viewpoint of seismic modelling with the aim to improve the input physics of massive star models, one needs to secure high-precision frequency values of several pulsation modes. While this is not impossible and has been achieved for a rapidly-rotating pulsating Be star (e.g. Neiner et al. 2012b), it turned out hard to achieve so far in the case of internal gravity waves driven by the convective core in O stars (e.g. Aerts & Rogers 2015). The requirement to detect pulsation mode frequencies with high precision of $\sim 0.0001\,d^{-1}$ can best be achieved in the case of self-driven modes caused by an opacity mechanism active in the partial ionisation layers of the iron-group elements, because they have long lifetime. HD 46202 is the only O-type star that has been modelled

Table 2.3: Overview of O-star variability deduced from high-cadence high-precision space photometry with the dominant causes of the variability listed, where IGW stands for "Internal Gravity Waves" (e.g., Rogers et al. 2013). The duration of the longest uninterrupted light curve is listed. **References**: *a*: Blomme et al. (2011), *b*: Howarth & Stevens (2014), *c*: Ramiaramanantsoa et al. (2014), *d*: this work, *e*: Mahy et al. (2011), *f*: Johnston et al. (2017), *g*: Degroote et al. (2010b), *h*: Pablo et al. (2017), *i*: Briquet et al. (2011), *j*: Howarth et al. (2014), *k*: Aerts et al. (2017a), and *l*: Pablo et al. (2015).

HD or EPIC	V mag	SpT	Data Source	Duration of LC (d)	$v \sin i$ $\mathrm{km\,s^{-1}}$	Variability Cause(s)	Reference to Space Photometry
HD 46223	7.28	O4V(f)	CoRoT	34.3	100	IGW	*a*
HD 66811	2.24	O4I(n)fp	SMEI	236	400	Rotation	*b*
HD 46150	6.73	O5V(f)	CoRoT	34.3	80	IGW	*a*
HD 24912	4.06	O7IIInf	MOST	30.0	200	Rotational Modulation	*c*
EPIC 202060098	15.1	O7V	K2	33.1	?	Rotational Modulation	*d*
HD 46966	6.87	O8V	CoRoT	34.3	50	IGW	*a*
HD 47129	6.06	O8 III/I+ O7.5III	CoRoT	34.3	75 & 300	Binarity, Rotation Magnetic secondary	*e*
HD 165246	7.60	O8V+ B7V	K2	29.8	245 & ?	Binarity, Heat-driven modes	*f*
HD 46149	7.61	O8.5V((f))+ B?	CoRoT	34.3	30 & ?	Rotational Modulation & Stochastic p modes	*g*
HD 37043	2.77	O9III+ B1III/IV	BRITE	130+ 110	100 &?	Binarity, Tidal pulsations	*h*
HD 46202	8.19	O9V(f)	CoRoT	34.3	25	Heat-driven p modes	*i*
HD 44597	9.05	O9V	K2	33.1	~ 30	IGW?	*d*

Continued on next page

Table 2.3 – continued from previous page

HD 256035	9.21	O9V:p+?	K2	33.1	270	Heat-driven modes	*d*
HD 255055	9.40	O9V:p(e)	K2	33.1	$\sim$ 40	IGW?	*d*
HD 149757	2.56	O9.5Vnn	WIRE,MOST, SMEI	232	400	Heat-driven p modes	*j*
HD 188209	5.63	O9.5Iab	*Kepler*	1460	75	IGW?	*k*
HD 36486	2.41	O95II+ B +	MOST	21.9	120 & ?	Binarity, Tidal pulsations	*l*
EPIC 202060097	13.7	O9.5V	K2	33.1	?	Rotational Modulation	*d*

seismically so far (Briquet et al. 2011). While this led to the derivation of its fundamental parameters with higher precision than any other method delivered so far, it was not possible to probe its interior structure properties at a level necessary to improve the input physics of the models, due to the too short time base of the space data.

Heat-driven O-type pulsators hold the same potential of deep seismic sounding of their interior structure than was recently achieved by Moravveji et al. (2015) for the B8.3V star KIC 10526294 and by Moravveji et al. (2016) for the rapidly rotating B8V star KIC 7760680. KIC 10526294 is a $3.2\,M_{\odot}$ star providing seismic evidence for diffusive mixing in the stellar envelope at a level of $\log D_{\rm mix}$ between 1.75 and 2.00 dex, in addition to core overshooting $f_{\rm ov} = 0.017 \pm 0.001$ in an exponential description. The seismic modelling of KIC 7760680 indicated $f_{\rm ov} = 0.024 \pm 0.001$ and a diffusive mixing of $\log D_{\rm mix} = 0.75 \pm 0.25$. A major improvement for evolutionary models of massive stars requires the observational calibration of the overall mixing properties in their interior, because theoretical considerations lead to $\log D_{\rm mix}$ values differing by many orders of magnitude and are therefore of limited value for the moment (e.g., Mathis et al. 2004). Asteroseismology of O star pulsators is the best method to make progress for the tuning of models of the most massive stars in the Universe, but it requires long-term high-precision time-resolved photometric and spectroscopic monitoring. As we have shown in this work, the K2 mission has a major role to play here and EPIC 202060092 was an optimal target among the five measured ones, but its complex beating pattern was not sufficiently sampled in terms of cadence, precision, and duration of the photometry achieved during Campaign 0. Moreover, it turned out to be a spectroscopic binary and we need to understand the contributions of each of its components to the detected variability. Requirements for its future seismic modelling are the accurate determination of its orbital properties and of the fundamental parameters of its binary components, along with a higher precision of the pulsation frequencies. Given its potential, spectroscopic monitoring will be continued in the coming years with the aim to unravel the orbital motion and to attempt detection of its pulsation modes in long-term residual spectroscopy.

Following Degroote et al. (2010b) and Briquet et al. (2011), our current work is a successful proof-of-concept study to perform future O-star seismology. *This is possible with the optimised K2 mission in combination with ground-based spectroscopy.* Indeed, as of K2's Campaign 3, the improvement on its performance in terms of pointing and precision of the photometry, as well as in the duration of the campaigns ($\sim$ 80 d, i.e., twice to three times as long as the current study) holds the potential to deliver the appropriate photometric data needed for in-depth modelling of O-star pulsations, whatever their excitation mechanism. A light curve at short cadence during 80 d will deliver some 115 000

data points, which will result in a factor $\sim$ 20 better frequency resolution than for the Campaign 0 data.

Note added at time of PhD print: the K2 mission meanwhile observed additional O stars in Campaign 09; we have not yet studied these stars.

Chapter 3

Investigating a sample of anticipated magnetic Ap/Bp stars

This chapter is currently under revision as

Detection of magnetic fields in chemically peculiar stars observed with the K2 space mission

B. Buysschaert, C. Neiner, A. J. Martin, C. Aerts, M. E. Oksala, D. M. Bowman, and T. Van Reeth

Monthly Notices of the Royal Astonomical Society, 2018, Submitted (17 pages)

Original abstract:

We report the results of an observational study aimed at searching for magnetic pulsating hot stars suitable for magneto-asteroseismology. A sample of sixteen chemically peculiar stars was selected and analysed using both high-resolution spectropolarimetry with ESPaDOnS and K2 high-precision space photometry. For all stars, we derive the effective temperature, surface gravity, rotational and non-rotational line broadening from our spectropolarimetric data. High-quality K2 light curves were obtained for thirteen of the sixteen stars and revealed rotational modulation, providing accurate rotation periods. Two stars show

evidence for roAp pulsations, and one star shows signatures of internal gravity waves or unresolved g-mode pulsations. We confirm the presence of a large-scale magnetic field for eleven of the studied stars, of which nine are first detections. Further, we report one marginal detection and four non-detections. Two of the stars with a non-detected magnetic field show rotational modulation due to surface abundance inhomogeneities in the K2 light curve, and we confirm that the other two are chemically peculiar. Thus, these five stars likely host a weak (undetected) large-scale magnetic field.

3.1 Introduction

Unfortunately, the number of known magnetic and pulsating hot stars with a complete characterization of their large-scale magnetic field and sufficient data to perform asteroseismic modelling remains limited. This is in part due to the brightness limitation for ground-based high-resolution spectropolarimetry ($V = 7 - 10$ mag is the typical limit for moderately rotating hot stars) and in part because few intrinsically bright hot stars were observed by photometric space missions, such as *Kepler* or CoRoT. The K2 space mission (Howell et al. 2014) has partly filled this niche, since its field of view changes on the sky every ∼90 days, and monitors stars that are accessible with modern high-resolution spectropolarimetry. As such, we are able to search for and investigate the periodic variability in photometry caused by oscillations and rotational modulation, while also measuring the strength of the large-scale magnetic field.

For this current study, we selected a sample of candidate magnetic hot stars, based on their peculiar chemical surface composition, to be observed with both K2 and ESPaDOnS, with the aim to find optimal targets for magneto-asteroseismology.

We describe the sample selection in Sect. 3.2. Section 3.4 discusses the observations and their respective data treatments. The periodic variability in the K2 photometry is investigated in Sect. 3.5, estimates on the stellar parameters are determined in Sect. 3.6, and in Sect. 3.7 we examine the high-resolution spectropolarimetry for the presence of a large-scale magnetic field. Section 3.8 discusses the results, and a summary and conclusions are provided in Sect. 3.9.

3.2 Sample selection

For each observing campaign of the K2 space mission, we selected the CP-2 stars (also known as Ap/Bp stars) and the He weak/strong stars from the times theRenson & Manfroid (2009) catalogue, which contains a list of stars known to have peculiar chemical photospheric abundances. The Ap/Bp stars are typically slow rotators with strong large-scale magnetic fields, which cause stratification in their atmospheres and create long-term chemical spots on the stellar surface (e.g., Stibbs 1950; Michaud 1970). The He strong stars are also assumed to host large-scale magnetic fields (e.g., Borra & Landstreet 1979, with σ Ori E as the best studied example, Oksala et al. 2015b). The He weak stars (CP-4 stars) are of a different nature and do not form a homogeneous group (which was already noted by e.g., Sargent 1964; Norris 1971; Jaschek & Jaschek 1974). Some CP-4 stars exhibit intense Si, or Ti and Sr lines, and are considered a hot extension of the magnetic Ap/Bp stars (examples of magnetic He weak stars are 3 Sco (Landstreet et al. 1979), HD 176582 (Bohlender & Monin 2011), and HR 2949 (Shultz et al. 2015a)). Others show overabundances of P and Ga, typically noted for HgMn stars (CP-3 stars), and could thus be related to these non-magnetic HgMn stars.

In total, we have proposed over 60 of these anticipated magnetic stars for observations with the K2 mission. These were subsequently selected by the time allocation committee and monitored by the K2 space mission during campaigns C00 up to C15. From these stars, we selected 16 of the brightest and/or slowest rotating ones to be observed with high-resolution spectropolarimetry, with the aim to confirm the presence of a stable large-scale magnetic field. This sub-sample forms the basis of the work presented here. The individual stars and their properties are presented in Table 3.1. The photometric variability of the complete sample of 60 stars is analysed and presented in Bowman et al. (2018, submitted).

Two stars of the sample are the primary components of long-period binary systems. HD 134759 is part of a hierarchical system, for which the shortest orbital period is 23.42 years (Heintz 1982). HD 158596 has an angular separation of $\sim$0.3 arcsec according to its Hipparcos data (ESA 1997). One star is part of a short-period binary system, namely HD 139160. Levato et al. (1987) indicated an orbital orbit of 5.28 d and an eccentricity of 0.33 ± 0.02. Yet, substantial scatter remains between their spectroscopic observations and orbital solution.

Table 3.1: Ap/Bp stars observed with K2 and ESPaDOnS. Spectral types are retrieved from Renson & Manfroid (2009) and confirmed binary systems in the literature are indicated (see text). Values for the effective temperature $T_{\rm eff}$ and surface gravity $\log g$ were determined in this work by fitting synthetic spectra to the Hβ and Hγ lines. The values for the projected rotational velocity $v \sin i$ and the non-rotational line broadening $v_{\rm NR}$ were determined from a fit to an unblended metal line.

Star	V [mag]	SpT	$T_{\rm eff}$ [K]	$\log g$ [dex]	$v \sin i$ [km s^{-1}]	$v_{\rm NR}$ [km s^{-1}]
HD97859	9.35	B9 Si	13750 ± 300	3.85 ± 0.10	83 ± 1	42 ± 5
HD107000	8.02	A2 Sr	7850 ± 200	3.20 ± 0.15	20 ± 5	41 ± 6
HD134759	4.54	Bp Si + ...	11900 ± 200	3.80 ± 0.10	60 ± 2	33 ± 4
HD139160	6.19	B7 He wk.	13200 ± 400	4.05 ± 0.10	20 ± 5	35 ± 5
HD152366	8.08	B8 Si	10250 ± 450	3.30 ± 0.30	23 ± 2	17 ± 3
HD152834	8.83	A0 Si	10100 ± 500	3.40 ± 0.30	13 ± 1	10 ± 2
HD155127	8.38	B9 Eu Cr Sr	8050 ± 150	3.45 ± 0.15	37 ± 3	35 ± 5
HD158596	8.94	B9 Si + ...	11200 ± 400	3.90 ± 0.20	60 ± 3	40 ± 4
HD164224	8.49	B9 Eu Cr	8850 ± 250	3.45 ± 0.10	22 ± 4	40 ± 7
HD165972	8.96	B9 Si	12700 ± 250	3.85 ± 0.10	29 ± 4	50 ± 5
HD166804	8.88	B9 Si	12900 ± 250	4.00 ± 0.10	45 ± 3	29 ± 4
HD173406	7.43	B9 Si	13150 ± 250	4.05 ± 0.10	38 ± 2	33 ± 5
HD173657	7.41	B9 Si Cr	10750 ± 500	3.80 ± 0.20	91 ± 5	47 ± 15
HD177013	9.04	A2 Eu Cr Sr	11700 ± 400	4.40 ± 0.20	24 ± 6	41 ± 8
HD177562	7.38	B8 Si	12200 ± 300	3.65 ± 0.10	15 ± 1	13 ± 3
HD177765	9.15	A5 Eu Cr Sr	8600 ± 200	4.50 ± 0.10	5 ± 2	8 ± 2

3.3 Previous inference of large-scale magnetic fields

For some of the stars in our sample, the presence of a large-scale magnetic field has been investigated from previous observations. However, in several cases it was not clearly confirmed that the star hosts a large-scale magnetic field. These observations are either from a photometric estimation of the 'surface' magnetic field (e.g., Cramer & Maeder 1980a), medium resolution circular spectropolarimetry of metal or Balmer lines (e.g., Romanyuk et al. 2014), or from the directly observed Zeeman splitting of absorption lines (Mathys et al. 1997).

The photometric Z index based on the Geneva photometric system and calibrated on Kurucz models (Kurucz 1979) can indicate the presence of a (large-scale) magnetic field for hot stars (with a spectral type ranging from B1 to A2; Cramer & Maeder 1979, 1980b). This method was used by Cramer & Maeder (1980a) to indicate that HD 134759 and HD 139160 should host a large-scale magnetic field with a strength of more than 1 kG. North & Cramer

(1984) continued this analysis and determined a magnetic field strength of 1 kG, 2.7 kG, 4.1 kG, 2.4 kG, and 1.2 kG for HD 134759, HD 155127, HD 164224, HD 165972, and HD 173406, respectively.

Low to medium resolution circular spectropolarimetry was utilized to detect and measure the strength of the large-scale magnetic fields of three stars in our sample. Landstreet et al. (1975) investigated HD 134759 and obtained a longitudinal magnetic field value of -600 ± 700 G, which the authors did not claim as a definite detection. HD 97859 was observed and discussed by El'kin (1998), who obtained a longitudinal magnetic field of -400 G. No error bars were provided, but it can be assumed to be of the order of the measured value, as HD 97859 had the largest $v \sin i$ of all stars in their sample, with typical uncertainties ranging from 100 G to 500 G for stars with a $v \sin i < 20\,\mathrm{km\,s^{-1}}$. Finally, HD 107000 was monitored by Romanyuk & Kudryavtsev (2008) and Romanyuk et al. (2014, 2015), who measured longitudinal magnetic field values ranging from -240 ± 30 G up to 320 ± 50 G that vary with a period of about 2.4 d.

Mathys et al. (1997) and Mathys (2017) noted that HD 177765 hosts a sufficiently strong large-scale magnetic field to cause Zeeman splitting of several absorption lines. By measuring the strength of the splitting, the authors determined a mean magnetic field modulus of approximately 3.4 kG, with little variation between the various observations.

Given this overview, we conclude that only HD 107000 and HD 177765 have a firmly detected large-scale magnetic field, albeit not with modern high-resolution spectropolarimetry.

3.4 Observations

3.4.1 K2 photometry

To construct the K2 light curves, we retrieved the target pixel files from the Mikulski Archive for Space Telescopes (MAST). For each (sub)-campaign and each star, we determined custom non-circular apertures from the stacked images. These were sufficiently large to accommodate the pixel drifts due to the thruster fires (Howell et al. 2014) and did not change during a given data set. Next, the mean background per frame was subtracted to create raw background corrected photometry. This was subsequently passed through the K2SC package (Aigrain et al. 2015, 2016, 2017) to correct for the pixel drifts, and their associated instrumental effects, by means of Gaussian processes. Subsequently, an outlier rejection was applied to the corrected photometry of each (sub)-campaign

and another (long-term) instrumental detrending was performed. During this detrending step, we accounted for the high-amplitude rotational modulation signal (see Sect. 3.5.1). Finally, we combined the different (sub)-campaigns for a given star to one light curve. Details on the K2 photometry are given in Table 3.2.

Reduced K2 light curves were constructed for 14 stars of the sample, while reductions for HD 134759 and HD 139160 were still ongoing at the time of writing. A significant fraction of the flux of HD 177562 was lost outside the subraster, causing the light curve to be of poor quality. Therefore, only 13 light curves were used in the remaining of this chapter.

Note added at the time of PhD print: More robust reduction tools and detrending software for the K2 photometry have become available at the time when this research was conducted. This was not yet the case when the O-stars from Chapter 2 were analysed. Hence, the difference in the methodology to obtain high-quality light curves from the target pixel files.

3.4.2 ESPaDOnS spectropolarimetry

Each star was observed at least once by the Echelle SpectroPolarimetric Device for the Observations of Stars (ESPaDOnS, Donati et al. 2006) mounted at the Canada France Hawaii Telescope (CFHT) on Mauna Kea in Hawaii. Standard settings were used for the spectropolarimeter in circular polarisation mode (Stokes V). The spectropolarimetric sequences consisted of four consecutive sub-exposures, for which the exposure times were tailored to the spectral type, brightness, and anticipated $v \sin i$, to be able to detect a dipolar field of 600 G or higher. The observations were reduced with the LIBRE-ESPRIT (Donati et al. 1997) and UPENA softwares available at CFHT. The data span from 3 700 Å to 10 500 Å and have an average resolving power R = 65 000. The spectropolarimetric data were normalized to unity per spectral order with the interactive spline fitting tool SPENT (Martin et al. 2017). Details on the spectropolarimetric observations are given in Table 3.4.

3.5 Photometric variability

3.5.1 Rotational modulation

We computed a Lomb-Scargle periodogram (Lomb 1976; Scargle 1982) for each of the 13 K2 light curves. The dominant variability for all 13 light curves

Table 3.2: Logs of the the K2 photometric observations. We provide the EPIC ID, the K2 campaign number, C, during which observations were taken, the total duration of the observations, and the total number of datapoints in the light curve, N. **Remarks**: *a* Light curve not yet fully reduced at the time of submission. *b* Light curve has a significant time gap in between the two campaigns. *c* Light curve of poor quality due to flux loss outside the sub-raster.

Star	EPIC ID	C	Time length [d]	N	Notes
HD 97859	201777342	01	80.07	3345	
HD 107000	201667495	10	47.89	1907	
HD 134759	249657024	15			*a*
HD 139160	249152551	15			*a*
HD 152366	203749199	02, 11	822.59	4209	*b*
HD 152834	232176043	11	69.43	2925	
HD 155127	232284277	11	69.45	2876	
HD 158596	225990054	09, 11	221.99	5831	*b*
HD 164224	226241087	09	68.64	2824	
HD 165972	224206658	09	68.64	2822	
HD 166804	227373493	09	68.64	2812	
HD 173406	218676652	07	65.79	2624	
HD 173657	213786701	07	81.28	3361	
HD 177013	219198038	07	81.24	3289	
HD 177562	214133870	07	81.80	3494	*c*
HD 177765	214503319	07	78.78	3331	

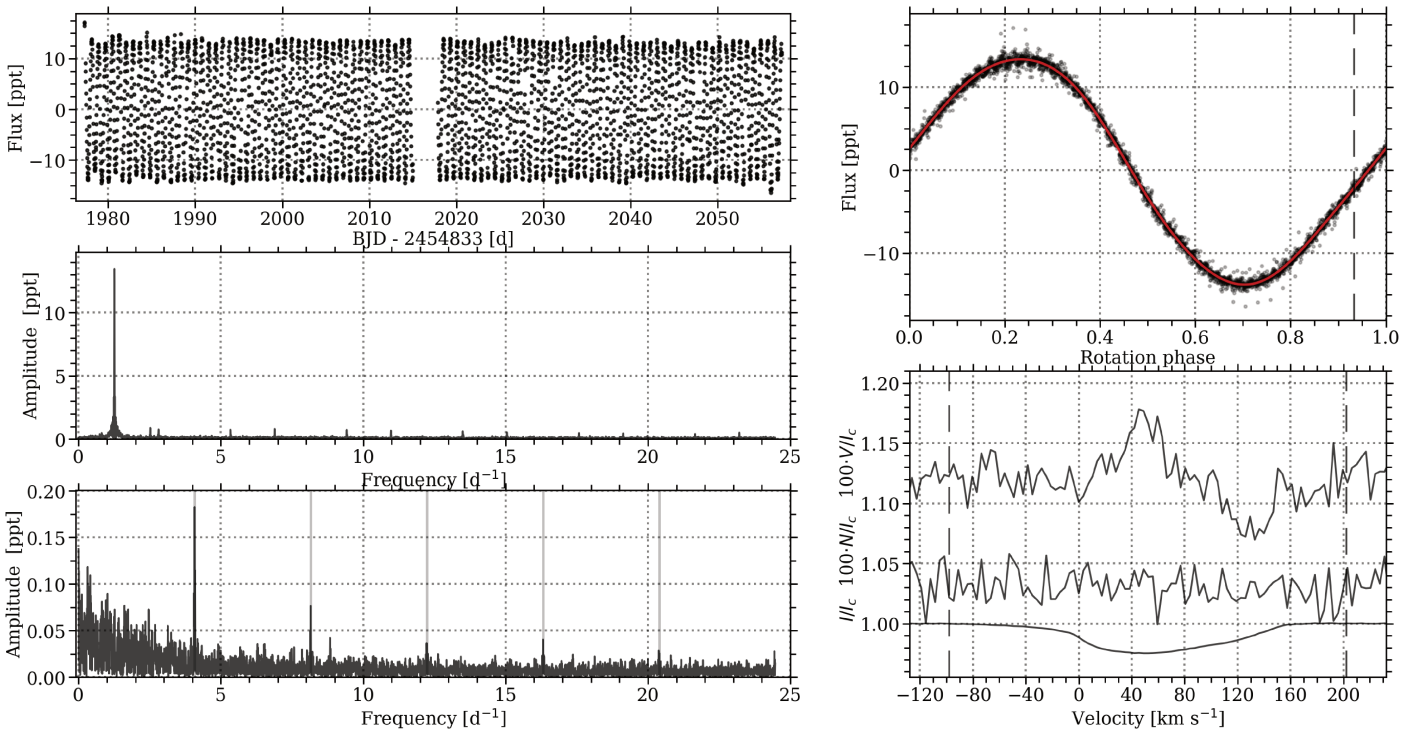

Figure 3.1: The K2 light curve of HD 97859 is shown in the *top left* panel and its corresponding Lomb-Scargle periodogram in the *middle left* panel. *Top right*: K2 photometry (black) phase-folded with the rotation period, as well as a fourth-order sine model (red). Rotation phase where ESPaDOnS spectropolarimetry was taken are marked by the black dashed lines. *Bottom left*: Lomb-Scargle periodogram of the residual K2 photometry, after removal of the rotational modulation signal. Instrumental frequencies related to the thruster firing are indicated by the gray solid lines. *Bottom right*: LSD profiles of the ESPaDOnS spectropolarimetry where the Stokes V, the diagnostic null, and the Stokes I profiles are shown, with an offset for increased visibility. Integration limits for the determination of the FAP and longitudinal magnetic field are indicated by the dashed vertical lines.

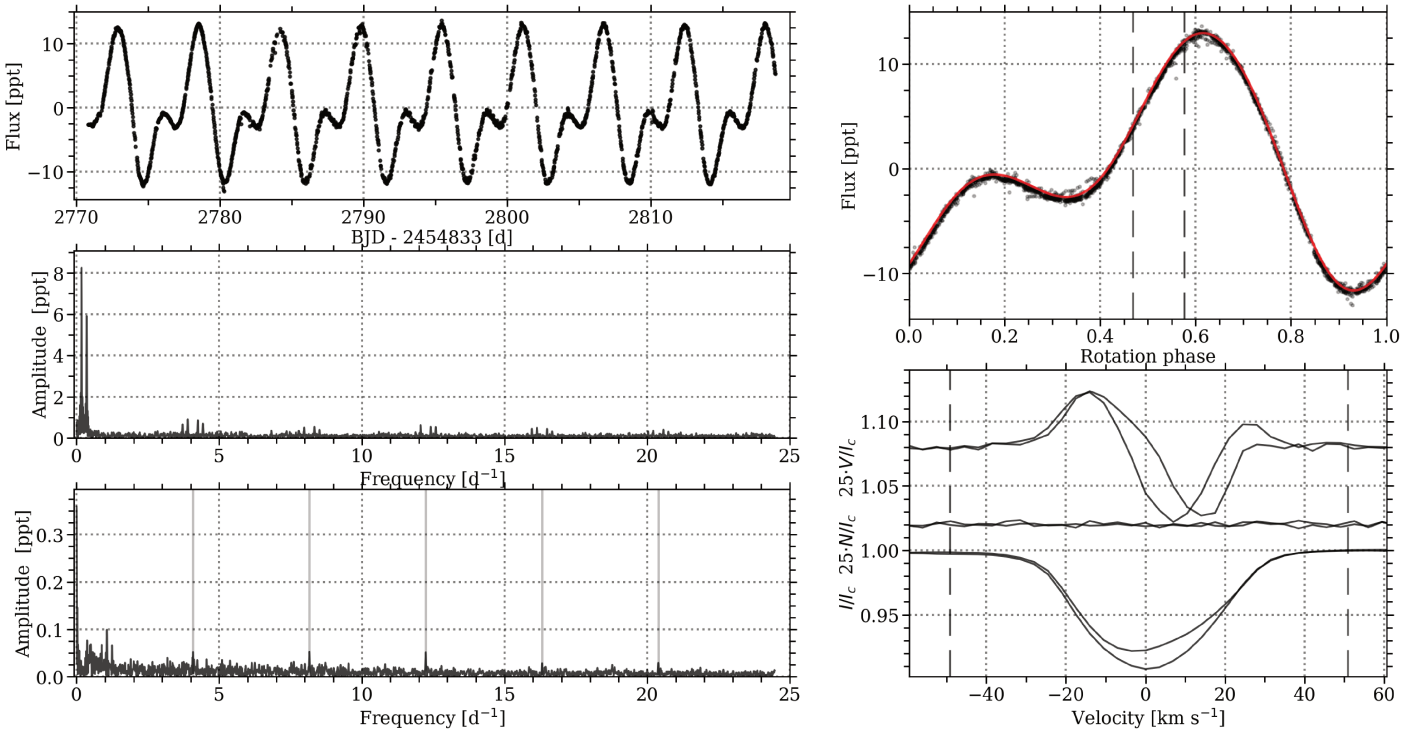

Figure 3.2: Information related to HD 107000, showing the K2 photometry, rotational modulation, and the LSD profiles of the ESPaDOnS data. Same colour coding was applied as Fig. 3.1.

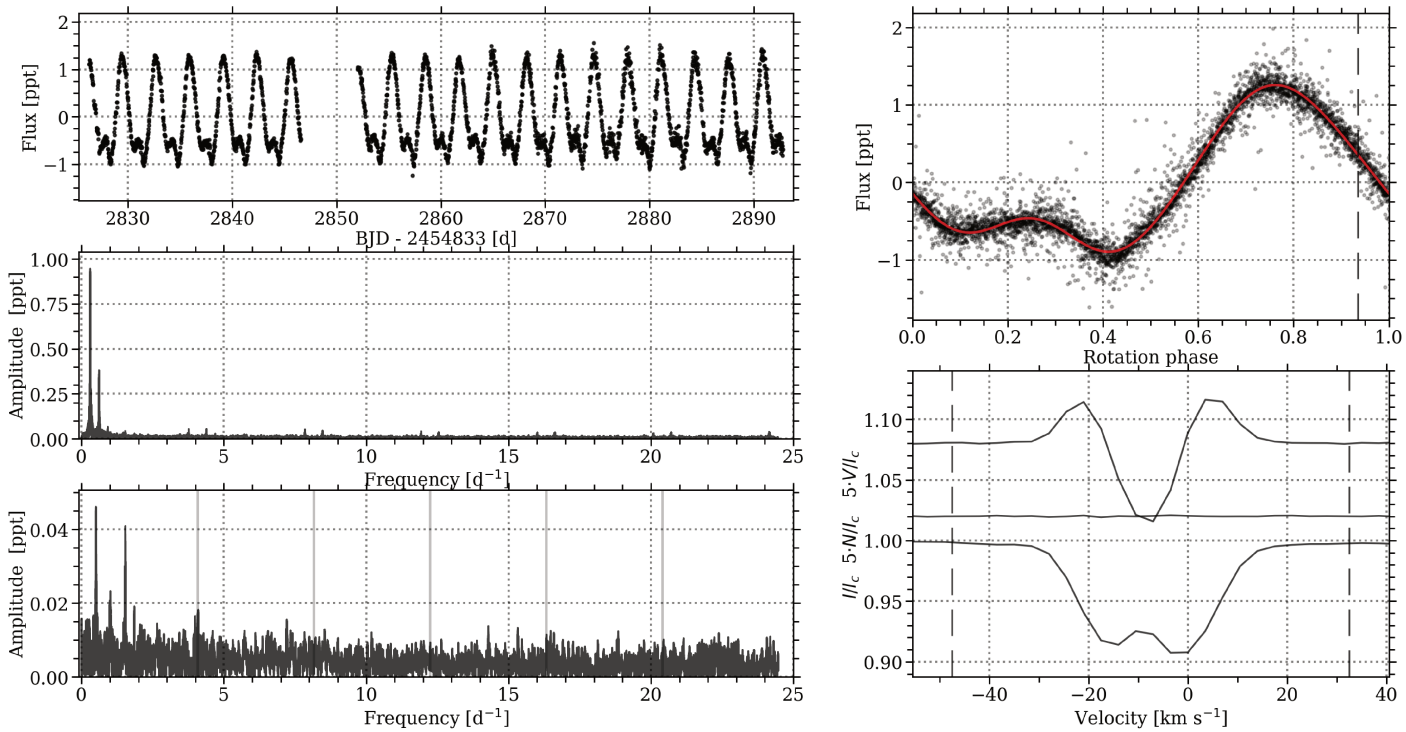

Figure 3.3: Information related to HD 152366, showing the K2 photometry, rotational modulation, and the LSD profiles of the ESPaDOnS data. Same colour coding was applied as Fig. 3.1. Only the photometry of C11 is shown in the *top left* panel, while the complete K2 light curve was used for the rotational modulation, and periodograms.

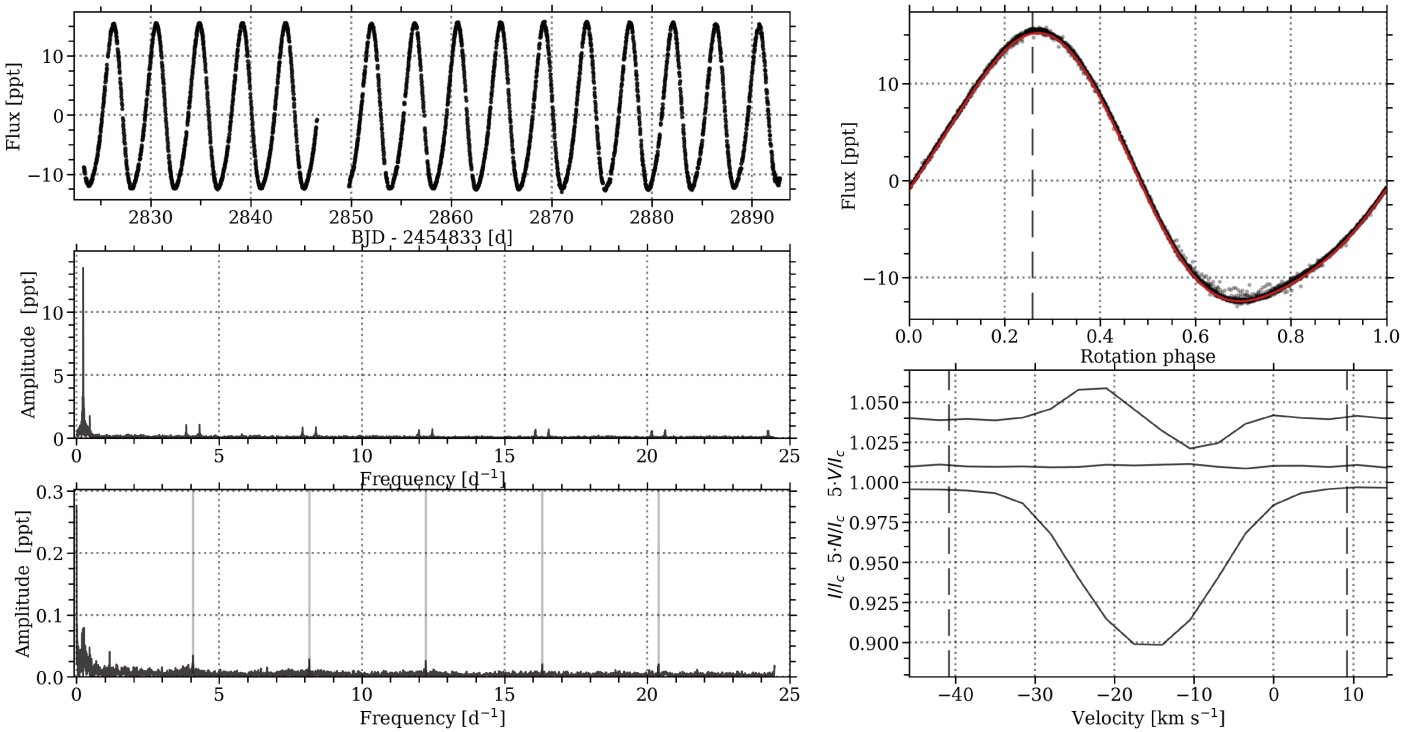

Figure 3.4: Information related to HD 152834, showing the K2 photometry, rotational modulation, and the LSD profiles of the ESPaDOnS data. Same colour coding was applied as Fig. 3.1.

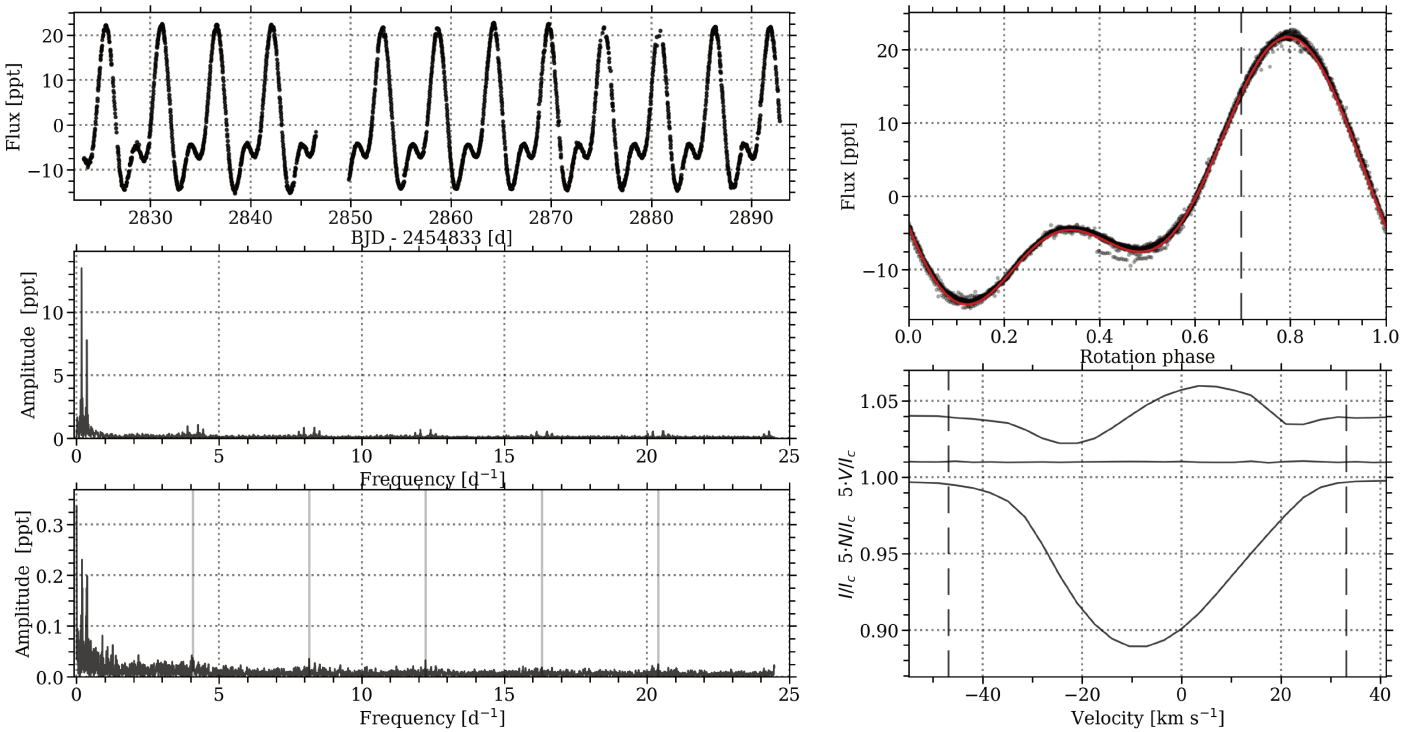

Figure 3.5: Information related to HD 155127, showing the K2 photometry, rotational modulation, and the LSD profiles of the ESPaDOnS data. Same colour coding was applied as Fig. 3.1.

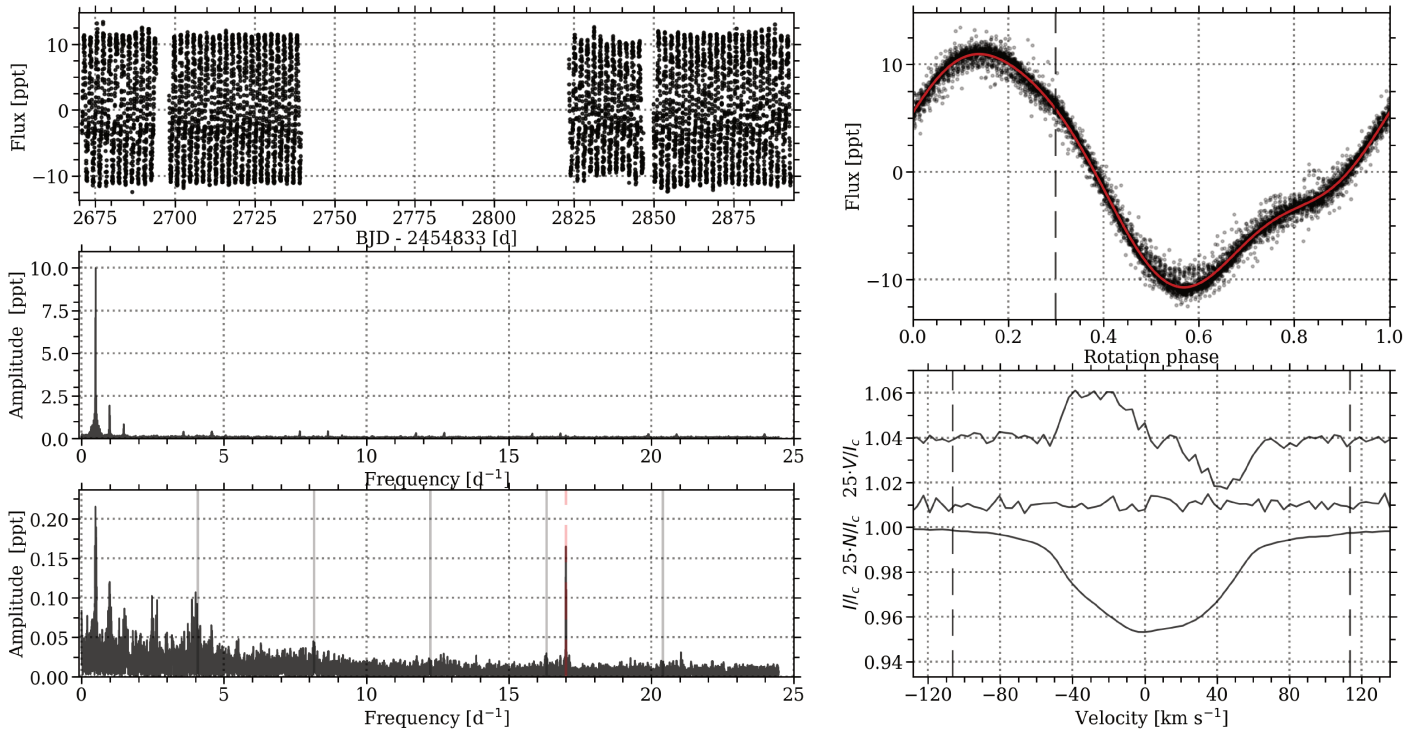

Figure 3.6: Information related to HD 158596, showing the K2 photometry, rotational modulation, and the LSD profiles of the ESPaDOnS data. Same colour coding was applied as Fig. 3.1. The alias frequency of the presumed roAp pulsation is marked by the red dashed line in the *bottom left* panel.

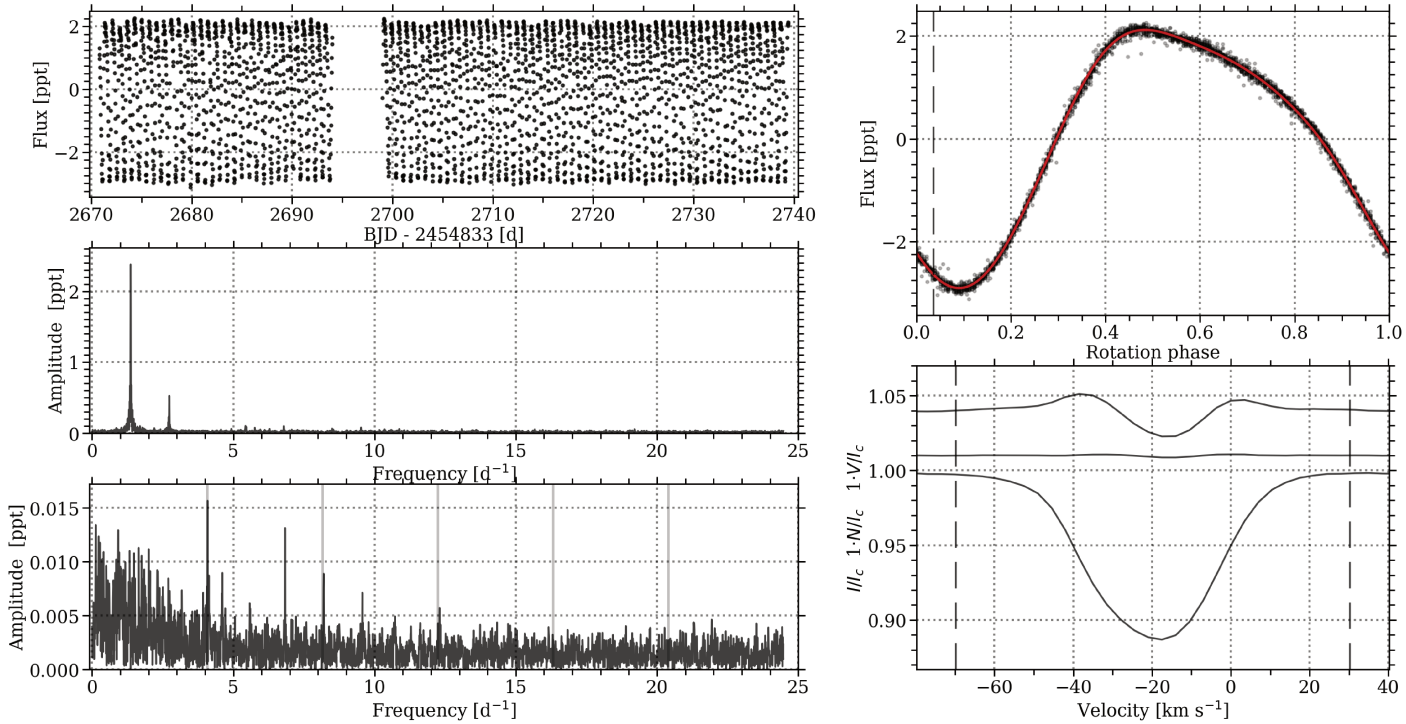

Figure 3.7: Information related to HD 164224, showing the K2 photometry, rotational modulation, and the LSD profiles of the ESPaDOnS data. Same colour coding was applied as Fig. 3.1. Some addition low-frequency power excess remained in the periodogram of the K2 residuals, suggesting unresolved g mode frequencies.

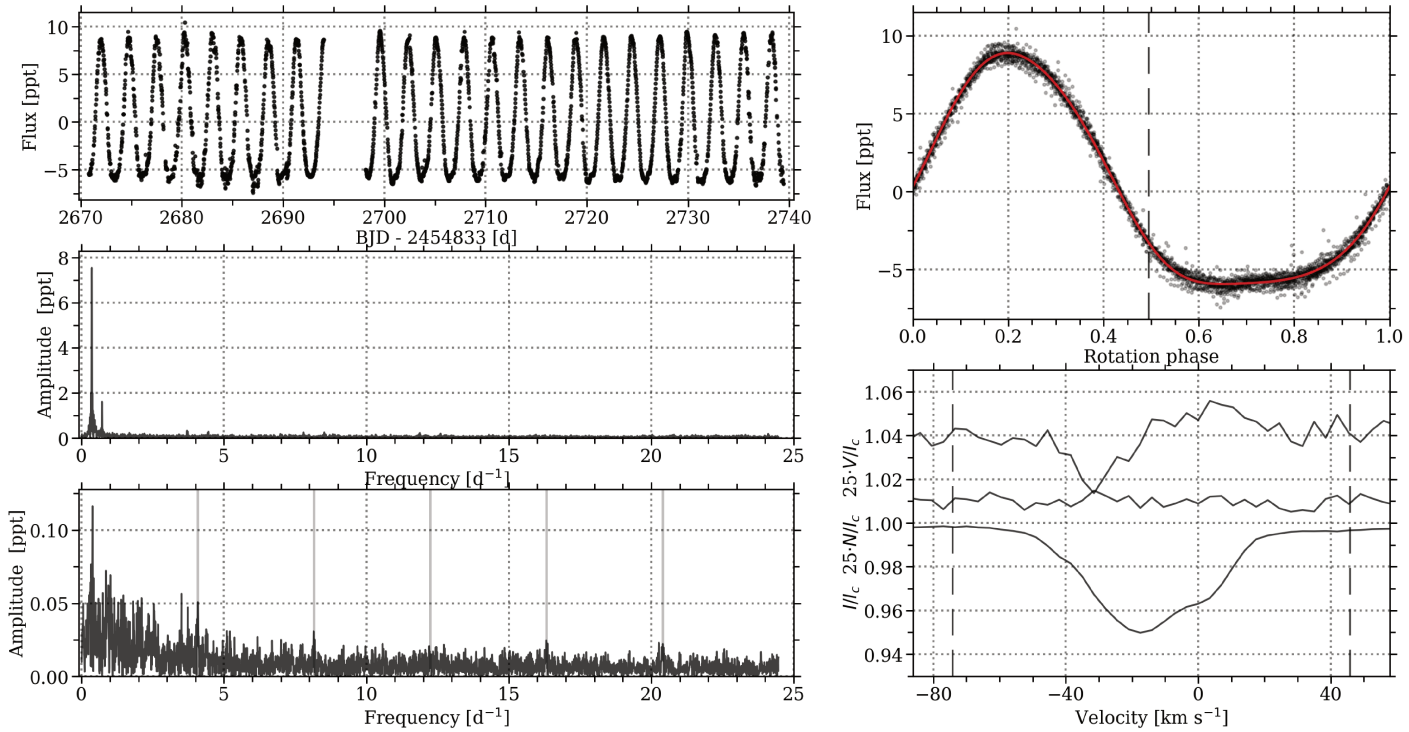

Figure 3.8: Information related to HD 165792, showing the K2 photometry, rotational modulation, and the LSD profiles of the ESPaDOnS data. Same colour coding was applied as Fig. 3.1.

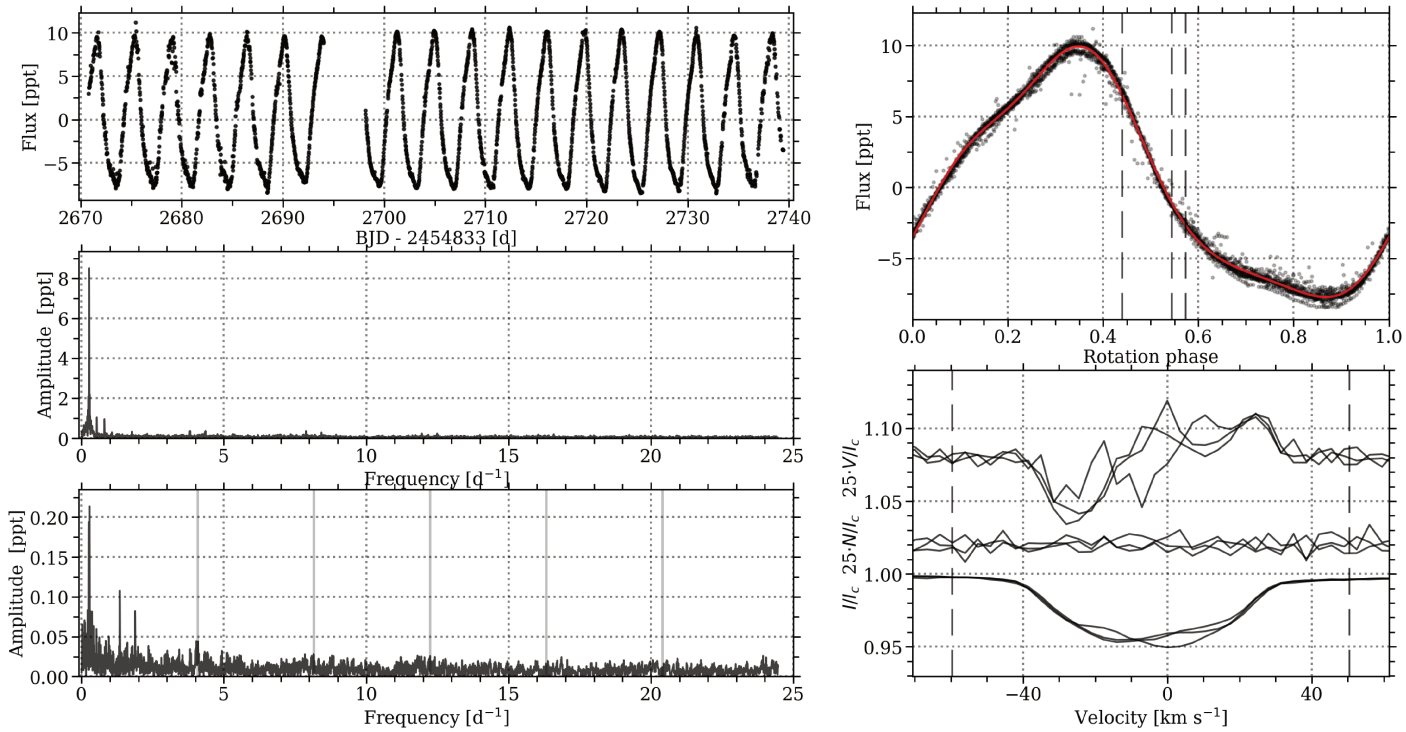

Figure 3.9: Information related to HD 166804, showing the K2 photometry, rotational modulation, and the LSD profiles of the ESPaDOnS data. Same colour coding was applied as Fig. 3.1.

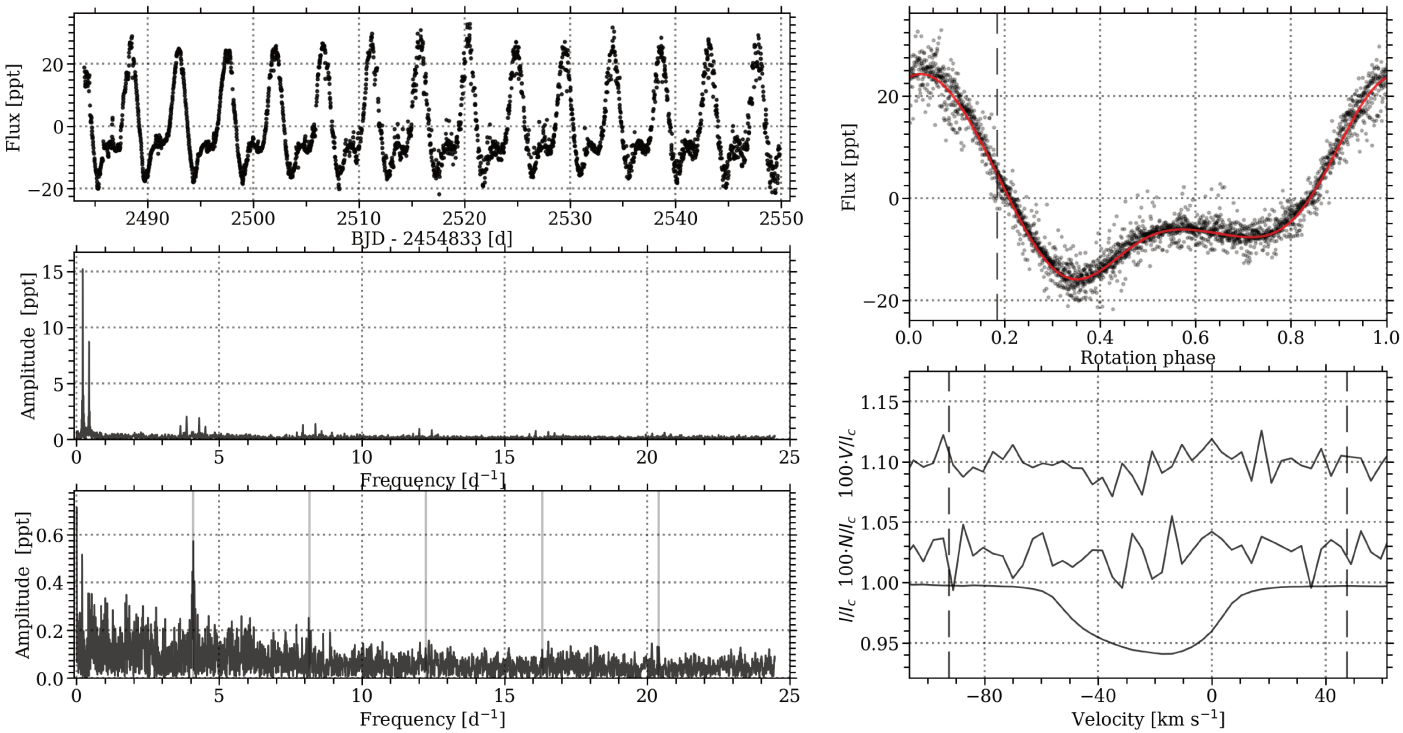

Figure 3.10: Information related to HD 173406, showing the K2 photometry, rotational modulation, and the LSD profiles of the ESPaDOnS data. Same colour coding was applied as Fig. 3.1. No magnetic field was detected in the spectropolarimetry.

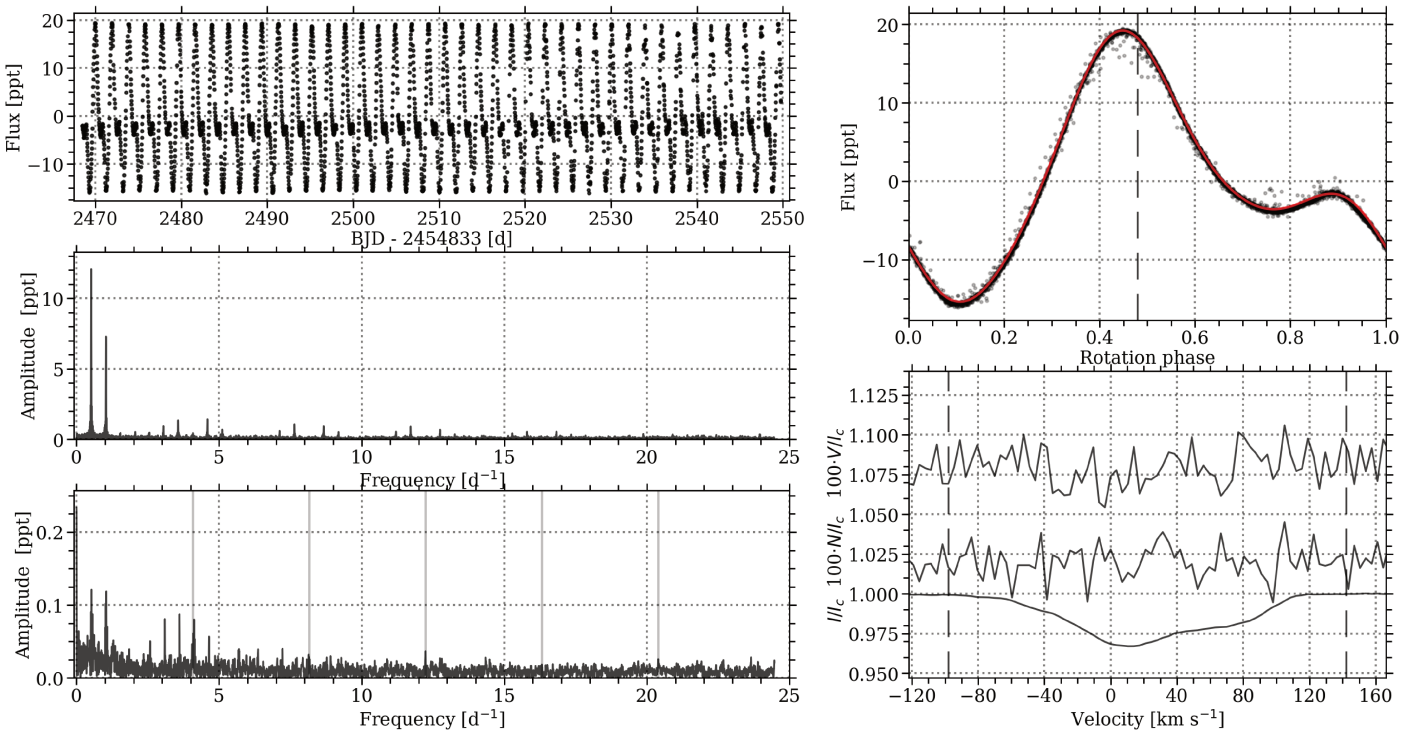

Figure 3.11: Information related to HD 173657, showing the K2 photometry, rotational modulation, and the LSD profiles of the ESPaDOnS data. Same colour coding was applied as Fig. 3.1. No magnetic field was detected in the spectropolarimetry.

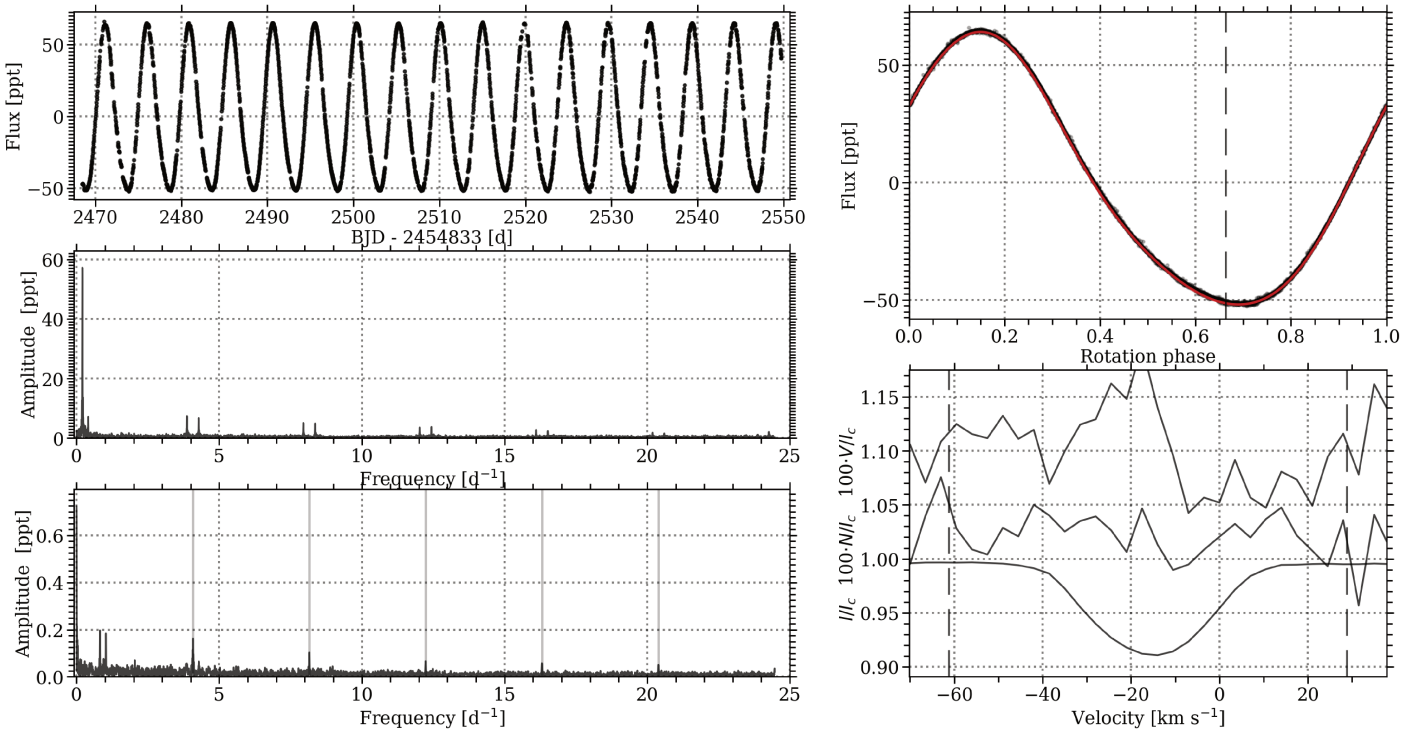

Figure 3.12: Information related to HD 177013, showing the K2 photometry, rotational modulation, and the LSD profiles of the ESPaDOnS data. Same colour coding was applied as Fig. 3.1.

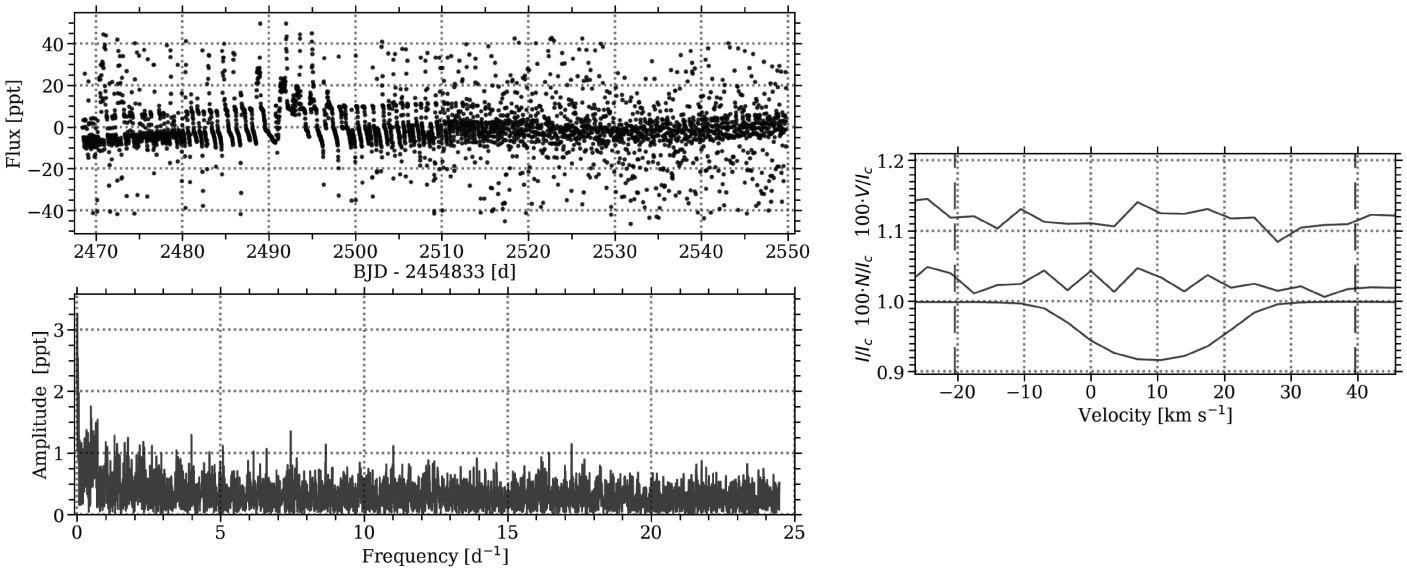

Figure 3.13: Information related to HD 177562, showing the K2 photometry, and the LSD profiles of the ESPaDOnS data. Same colour coding was applied as Fig. 3.1. Since the K2 photometry was of poor quality, we were unable to recover any periodic variability. No magnetic field was detected in the spectropolarimetry.

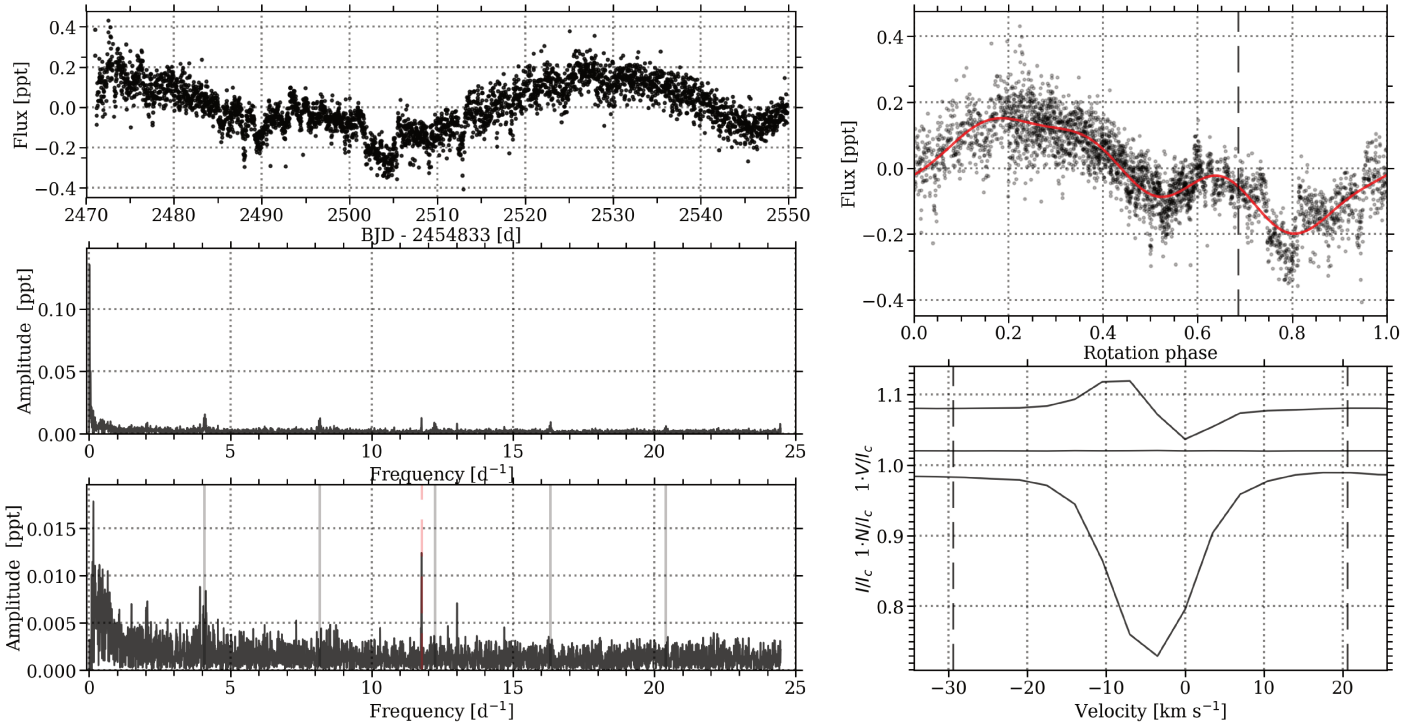

Figure 3.14: Information related to HD 177765, showing the K2 photometry, rotational modulation, and the LSD profiles of the ESPaDOnS data. Same colour coding was applied as Fig. 3.1. The alias frequency of the presumed roAp pulsation is marked by the red dashed line in the *bottom left* panel.

occurs in the low-frequency regime which consists of a few significant frequency harmonics. These periodograms are indicated in the top and middle panels of the left column of Figs. 3.1 – 3.14. We attribute this variability to rotational modulation, due to surface abundance inhomogeneities. Instead of iteratively prewhitening this variability, we performed a Least-Squares (LS) fit to the light curve with a fourth-order sine model:

$$M(t) = C + \sum_{n=1}^{4} A_n \cdot \sin\left(2\pi(n f_{\rm rot} t + \phi_n)\right) , \tag{3.1}$$

where A_n and ϕ_n are the amplitude and phase of the nth harmonic and C is a constant offset. This fitting procedure has the advantage that the exact rotation frequency, $f_{\rm rot}$, and its higher frequency harmonics are simultaneously enforced. We truncated the series at the fourth order, because this was the highest frequency harmonic encountered in the periodograms. The fitting process was a two-step approach. First, $f_{\rm rot}$ was kept fixed to the estimated value from a ten times oversampled Lomb-Scargle periodogram to estimate A_n, ϕ_n, and C. In the second step, all parameters, including $f_{\rm rot}$, were set as free fitting parameters, where $f_{\rm rot}$ was allowed to vary within the Rayleigh resolution limit. We show the final fit to the K2 light curve in the top right panel of Figs. 3.1 – 3.14. We propagated the Rayleigh limit as a conservative uncertainty for each $P_{\rm rot}$.

Several of the stars in our sample have previously been monitored to investigate their periodic variability. We compared the literature values for the rotation period with the values derived in this work (see Table 3.3). Most agreed well with only two exceptions. For HD 107000, we recovered twice the literature value. This may occur if Wraight et al. (2012) performed a frequency extraction instead of fitting a high-order sine model to the STEREO light curve in the time domain. Our value for the rotation period of HD 107000 offers a better fit to the K2 light curve. The other exception is HD 177765, for which Mathys (2017) indicated a rotation period longer than 5 years due to the lack of variability in the mean magnetic field modulus. The variability in the K2 light curve has a small amplitude and does not contain two full cycles of the derived rotation period (56 days). We cannot exclude that this photometric variability has a different (possibly instrumental) origin than rotation.

3.5.2 Remaining periodic variability

By removing the rotation signal from the K2 photometry, we drastically reduced the power in the Lomb-Scargle periodograms (e.g., the bottom left panel of Fig. 3.1). The strongest remaining signal within the periodogram of the residuals falls within one of the following categories:

Table 3.3: Rotation periods from photometric modulation. Values determined in this work were calculated from the K2 photometry. We also indicate the figure summarizing the analysis for that star. **References**: *a*: Watson et al. (2006), *b*: Wraight et al. (2012), *c*: Bernhard et al. (2015), *d*: Hümmerich et al. (2016), *e*: Mathys (2017). **Remarks**: ⋆: Length of the K2 light curve is smaller than twice the rotation period.

Star	$P_{\rm rot}$ [d] This work	$P_{\rm rot}$ [d] Literature	Note	Figure
HD 97859	0.792 ± 0.008	0.7921 ± 0.0002	*b*	3.1
HD 107000	5.6 ± 0.7	2.8187 ± 0.0002	*b*	3.2
HD 134759		3.099 ± 0.001	*b*	
HD 139160		6.62 ± 0.02	*b*	
HD 152366	3.23 ± 0.01			3.3
HD 152834	4.4 ± 0.3	4.2928 ± 0.0003	*d*	3.4
HD 155127	5.5 ± 0.4	5.5243 ± 0.0004	*d*	3.5
HD 158596	2.02 ± 0.02	2.02206 ± 0.00005	*c*	3.6
HD 164224	0.73 ± 0.01			3.7
HD 165972	2.8 ± 0.1	2.7596 ± 0.0001	*d*	3.8
HD 166804	3.7 ± 0.2	3.7035 ± 0.0002	*d*	3.9
HD 173406	4.6 ± 0.3	5.095	*a*	3.10
HD 173657	1.94 ± 0.05	1.93789 ± 0.00005	*d*	3.11
HD 177013	4.9 ± 0.3	4.873	*a*	3.12
HD 177562				
HD 177765	56 ± 40	$\gg 5$ years	*e*,⋆	3.14

- Low-frequency power excess related to imperfectly reduced and corrected K2 photometry. This might have been caused by stitching different K2 (sub)-campaigns together into one light curve or because of an incomplete removal of long-term instrumental variability. HD 152834 and HD 165972 (i.e., Figs. 3.4 and 3.8) show examples of this power excess in the periodogram of the residuals.

- Remaining aliasing structure around the ∼6 h K2 thruster fire frequency (or its harmonics) or at the harmonics of the ∼6 h thruster fire frequency itself. A clear example of the former was observed for HD 173657 (Fig. 3.11).

- Remaining structure around the rotation frequency or its frequency harmonics. This is observed, for example, for HD 155127, HD 158596, or HD 166804 (i.e., Figs. 3.5, 3.6 and 3.9). The surface abundance inhomogeneities are anticipated to be stable over the time scale of the light curves, as they are linked to the stable large-scale magnetic fields.

However, spot migration could have occurred, but is considered to be unlikely.

Three stars are exceptions to these results with significant power, unrelated to instrumental effects, in their residual periodograms. Both HD 158596 and HD 177765 show a clear, isolated frequency peak at $17.001 \pm 0.005\,\mathrm{d}^{-1}$ and $11.76 \pm 0.01\,\mathrm{d}^{-1}$ (visible in Figs. 3.6 and 3.14), respectively. These could be Nyquist aliases of an unresolved, high-frequency pulsation mode in the rare subgroup of roAp stars (e.g., Kurtz 1982). Alentiev et al. (2012) discussed the detection of a $61.01\,\mathrm{d}^{-1}$ roAp pulsation in the spectroscopy of HD 177765, supporting the hypothesis that we may indeed be dealing with an alias frequency in the photometry. We cannot exclude that the frequency peak for HD 158596 originates in the fainter secondary component. Ground-based short-cadence photometry has been requested at the time of the PhD print to confirm that these two stars host roAp pulsations. Finally, we note that HD 164224 reveals a low-frequency power excess, which could be due to unresolved g-mode pulsation frequencies or internal gravity waves, which are predicted in stars with convective cores (e.g., Aerts & Rogers 2015).

We did not find evidence of frequency peaks related to stellar oscillations driven by the κ-mechanism for any of the 13 targets.

3.6 Estimation of stellar parameters

To perform the magnetometric analysis, we required estimates for the effective temperature, $T_{\rm eff}$, and the surface gravity, $\log g$, to construct average spectra with the LSD technique (Donati et al. 1997). This method drastically increases the S/N of a possible Zeeman signature in the (LSD) Stokes V profile.

As a first step, we deduced the projected rotational velocity $v \sin i$ and the radial velocity for each star by fitting a rotation profile (see e.g., Gray 2005) convolved with a Gaussian profile to an unblended Fe or Si line. The Gaussian profile captures the non-rotational broadening $v_{\rm NR}$ acting upon the absorption line, due to macro-turbulence, micro-turbulence, waves, etc. We followed the goodness-of-fit approach by Simón-Díaz & Herrero (2014) to derive the values and confidence intervals for $v \sin i$ and $v_{\rm NR}$ and report the results in Table 3.1, keeping in mind that these two parameters are correlated.

Next, we determined $T_{\rm eff}$ and $\log g$ for each star by fitting pre-computed SYNTV local thermodynamical equilibrium synthetic spectra (Tsymbal 1996) for LLMODELS atmosphere models (Shulyak et al. 2004) using the Grid Search in Stellar Parameters (GSSP, Tkachenko 2015) software to the observations.

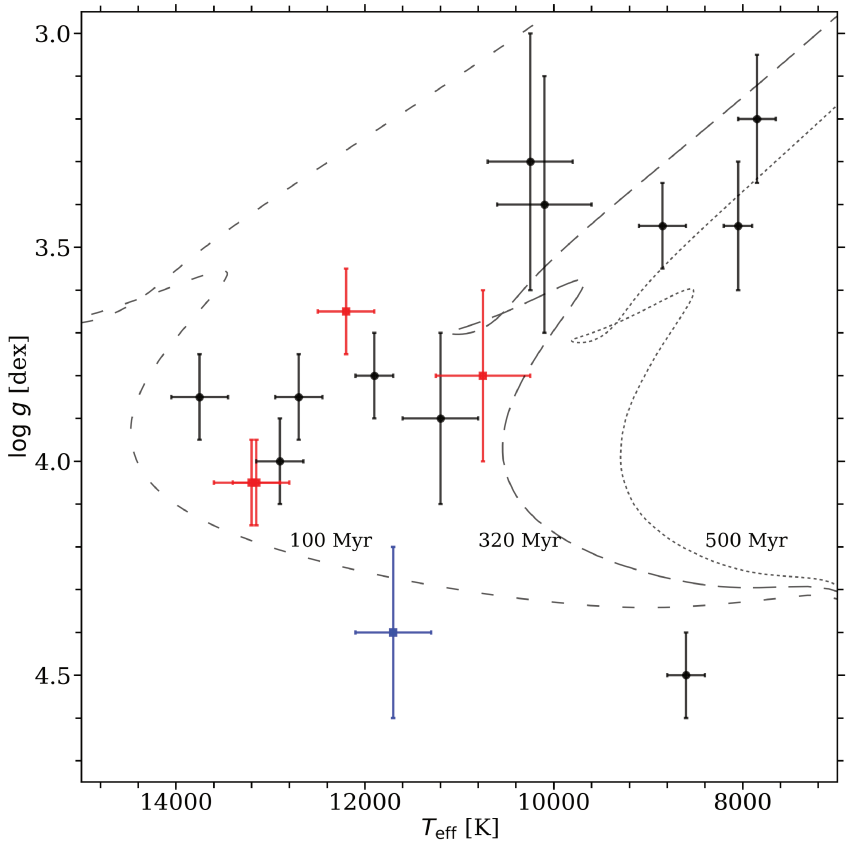

Figure 3.15: Comparison between the derived stellar parameters for the sample of Ap/Bp stars to publicly available MIST isochrones (grey dashed lines, computed with MESA v7503 and retrieved from Choi et al. 2016). Stars for which the detection status of a large-scale magnetic field is a define detection, a marginal detection, or a non-detection are marked in black, blue, and red, respectively.

Because of the significant chemical peculiarities for these stars, we performed the fitting simultaneously to the Hβ and Hγ lines, while keeping the overall metallicity fixed at [M/H] = 0.0 and the micro-turbulent velocity at $v_{\rm micro}$ = 2.0 km s^{-1}. Moreover, both the line broadening and the radial velocity were fixed at the values in Table 3.1. The grid of stellar parameters for GSSP spanned from $T_{\rm eff}$ = 6000 K up to 15000 K, with steps of 500 K, and $\log g$ from 3.0 dex up to 4.5 dex, with a step of 0.1 dex. The determined values for $T_{\rm eff}$ and $\log g$, as well as their statistical uncertainties, are also listed in Table 3.1. These errors on $T_{\rm eff}$ and $\log g$ should be considered as a lower limit of the confidence intervals, because Ap stars are known to have a core-wing anomaly for their hydrogen lines (see e.g., Cowley et al. 2001; Kochukhov et al. 2002). For the stars with unresolved binary components, the values given may have contributions from both stars. However, the difference in $T_{\rm eff}$ as a result of this would not significantly affect our conclusions.

Although the secondary components of HD 134759, HD 139160, and HD 158596 should be well within the fiber area of ESPaDOnS, we did not find a clear indication of the presence of the secondary in the spectra. Therefore, we also fitted their respective observations with a single-star synthetic spectrum to estimate the relevant stellar parameters.

We compare the parameters of each star to publicly available MIST isochrones (Choi et al. 2016) in Fig. 3.15. All stars agree with an age younger than 500 Myr, but we cannot deduce any further evolutionary pattern.

3.7 Magnetometry

To boost the S/N of the possible Zeeman signatures in the Stokes V spectrum, we constructed an average line profile using the LSD technique. A pre-computed VALD3 line mask (Ryabchikova et al. 2015) with parameters close to the estimated stellar parameters was used for each star, and is listed in Table 3.4. All hydrogen lines and all spectral lines blended with hydrogen lines, telluric features, and known diffuse interstellar bands were removed from the line masks. Furthermore, the depths of the lines in the masks were adjusted to match the observations (a process so-called "tweaking", see e.g., Grunhut et al. 2017). The resulting LSD profiles are shown in the bottom right panel of Figs. 3.1 – 3.14 and in Fig. 3.16.

Most of the LSD Stokes I profiles show some sort of distortion. We attributed this profile variability to the surface abundance inhomogeneities, because the corresponding K2 photometry displays rotational modulation.

3.7.1 Zeeman signature

The FAP (Donati et al. 1992, 1997, and Chapter 1) was utilized to determine the presence of a Zeeman signature in the LSD Stokes V profile following the criteria defined in Sect. 1.2.3. Using these criteria, 12 stars have a DD, while 4 have a ND. We mark the detection status in Table 3.4.

For each spectropolarimetric observation, we also determined the longitudinal magnetic field according to Eq. (1.16). The integration range spans the full width of the Zeeman signature and the mean absorption line profile. We report the values for the mean wavelength λ, the mean Landé factor g, the integration range, and the calculated longitudinal magnetic field in Table 3.4.

The determined B_l values are well in line with the expectations for magnetic hot stars with a polar strength of at least several 100 G (where the polar strength

Table 3.4: Magnetometric properties of the sample. We provide the HJD at the middle of the spectropolarimetric sequence, as well as the total exposure time. Furthermore, we indicate the $T_{\rm eff}$ and $\log g$ of the VALD3 line mask, the S/N in the LSD Stokes I profile, the Landé factor g, the mean wavelength λ, the integration range around the line centroid used for the longitudinal field calculation and FAP analysis, the detection status of a Zeeman signature (DD for definite detection, ND for non-detection and MD for marginal detection), and the measured longitudinal magnetic field.

Star	HJD -2450000	$t_{\rm exp}$	$T_{\rm eff}$ line mask	$\log g$	S/N	g	λ	int. range	Det.	B_l
	[d]	[s]	[K]	[dex]			[nm]	[km s^{-1}]		[G]
HD97859	7881.78364	4×1272	14000	4.0	4829	1.192	519.13	$\pm$150	DD	570 ± 122
HD107000	7475.92214	4×338	7750	3.5	2836	1.210	519.94	$\pm$50	DD	250 ± 10
	7497.87935	4×338			3047	1.210	518.95		DD	162 ± 12
HD134759	7799.17433	4×37	12000	4.0	4941	1.183	520.89	$\pm$70	DD	305 ± 30
	7801.17550	4×37			5056	1.183	521.12		DD	364 ± 31
HD139160	7820.00404	8×22	13000	4.0	3133	1.177	520.43	$\pm$45	ND	42 ± 50
primary								$\pm$25	ND	-2 ± 30
secondary								$\pm$35	ND	49 ± 116
HD152366	7818.06147	4×599	10000	3.5	2843	1.196	518.52	$\pm$40	DD	-82 ± 14
HD152834	7818.08468	4×267	10000	3.5	1769	1.188	511.72	$\pm$25	DD	228 ± 20
HD155127	7818.10943	4×676	8000	3.5	1812	1.201	511.06	$\pm$40	DD	-435 ± 7
HD158596	7818.15110	4×1060	11000	4.0	2744	1.182	525.24	$\pm$110	DD	610 ± 46

Continued on next page

Table 3.4 – continued from previous page

HD164224	7817.15008	4×1089	8750	3.5	1373	1.197	515.58	± 50	DD	580 ± 27
HD165972	7905.94729	4×517	13000	4.0	3144	1.185	518.54	± 60	DD	-326 ± 50
HD166804	7883.11294	4×443	13000	4.0	3095	1.180	517.88	± 55	DD	-476 ± 50
	7886.92179	4×443			3066	1.180	518.47		DD	-520 ± 50
	7890.13132	4×443			2468	1.180	519.00		DD	-429 ± 67
HD173406	7500.13798	4×214	13000	4.0	1882	1.174	519.73	± 70	ND	-44 ± 45
HD173657	7554.98727	4×226	11000	4.0	3631	1.164	508.96	± 120	ND	-79 ± 84
HD177013	7905.96915	4×310	12000	4.5	963	1.163	511.23	± 45	MD	217 ± 59
HD177562	7553.02367	4×262	13000	3.5	4572	1.176	524.93	± 30	ND	16 ± 18
HD177765	7554.99870	4×120	8500	4.5	1001	1.204	513.89	± 25	DD	1067 ± 21

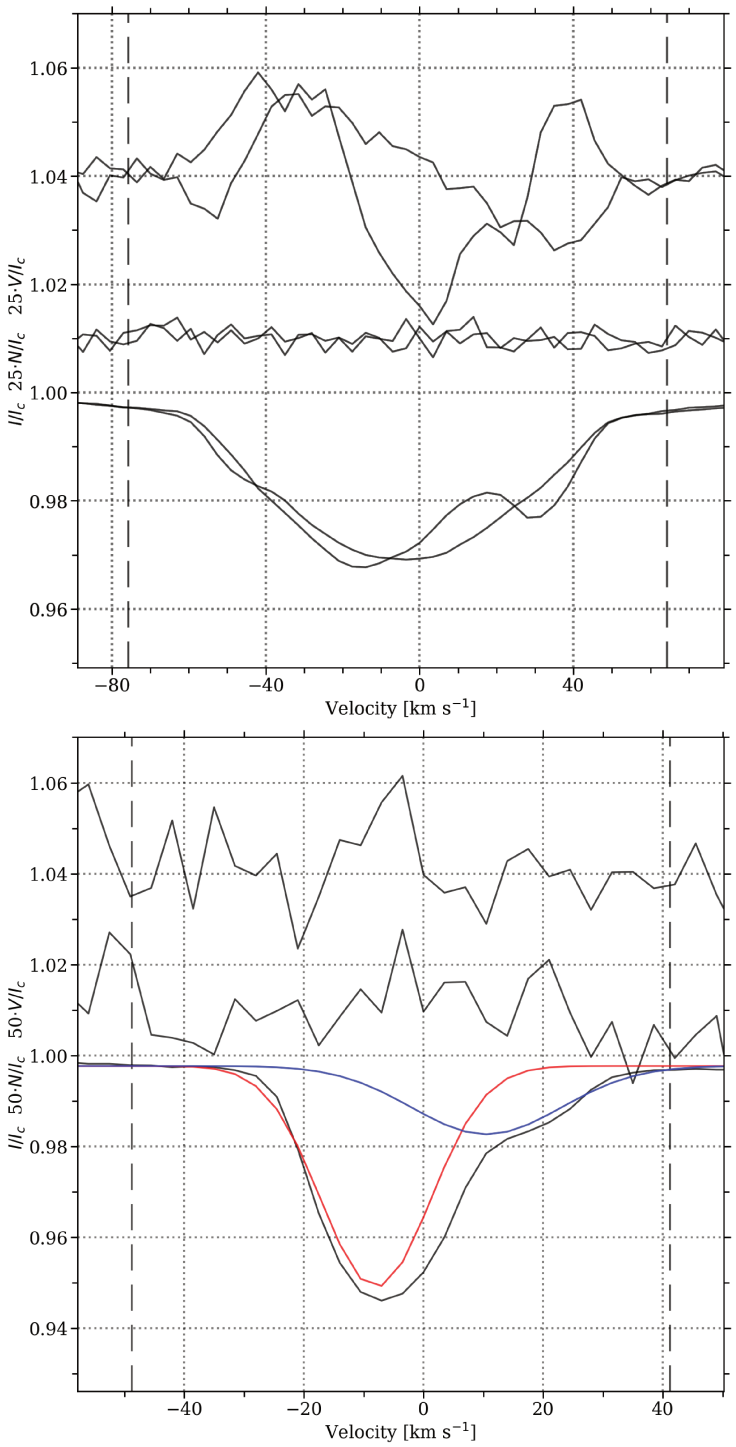

Figure 3.16: LSD profiles of the ESPaDOnS spectropolarimetry for HD 134759 (*top*) and HD 139160 (*bottom*) where the Stokes V, the diagnostic null, and the Stokes I profiles are shown, with an offset for increased visibility. Integration limits for the determination of the FAP and longitudinal magnetic field are given by the black lines. No magnetic field was detected in the spectropolarimetry for HD 139160. In addition, the two individual Gaussian models for the LSD Stokes I for the primary (red) and secondary (blue) component of HD 139160 are indicated.

is at least 3.5 times the measured longitudinal magnetic field, Preston 1967). Stars for which we obtained a ND also have a measured B_l compatible with zero within the 2σ confidence interval. In addition, Zeeman splitting is observed in individual lines (Stokes I) of HD 177765 (as already clearly indicated in Fig. 4 of Mathys et al. 1997), confirming that the star hosts a strong field of several kG. This strong magnetic field agrees with the relatively long rotation period for the star (out of the studied sample) when considering magnetic braking.

Nearly all of the detected Zeeman profiles have a typical appearance for large-scale magnetic fields with a simple geometry (dominantly dipolar), where the exact shape depends on the rotation phase and on the unknown inclination and obliquity angles. Distortions of the Zeeman signature due to the distorted LSD Stokes I profile did occur for several stars, such as HD 166804. However, the signature was sufficiently clear that these distortions did not cause any issues with the detection. Moreover, the rotation periods are sufficiently long compared to the total exposure time of the spectropolarimetric sequence, so that the measured B_l values were not affected by these distortions.

3.7.2 Binary systems

As mentioned earlier, three stars of our sample are part of a binary system. A component of two of these (i.e., HD 134759 and HD 158596) clearly hosts a large-scale magnetic field. The spectropolarimetric sequence of HD 139160, however, led to a ND. Here, we consider several explanations.

- The ND could be caused by the binary nature of HD 139160. The distortions in the LSD Stokes I profile could be due to the presence of the nearby companion, classifying HD 139160 as SB2 system, instead of the previously claimed surface abundance inhomogeneities. By means of LS fitting, we described the LSD Stokes I profile with two Gaussian functions to represent the individual components (see bottom panel of Fig. 3.16). After subtracting either one of the Gaussian profiles, we isolated the individual components in the Stokes I profile. We then used these two profiles to redetermine the FAP for a Zeeman signature (in the LSD Stokes V) and recomputed the longitudinal magnetic field (see Table 3.4). Again, we did not detect a signature of a large-scale magnetic field for the individual components. Hence, the binary nature is probably not the cause of the ND.
- HD 139160 has a rather short orbital period of 5.28 d, according to the modelling efforts of Levato et al. (1987) to the measured radial velocities. As magnetic hot stars seem to be less common in binary systems with

short orbital periods (as inferred from the BinaMIcS results, Alecian et al. 2015), this could explain the ND. Yet, spectropolarimetric data with a much higher S/N are needed to exclude the possibility of a weak magnetic field.

- As indicated earlier, two sub-groups of He-weak stars exist. The He-weak stars related to the HgMn stars do not host a large-scale magnetic field. We compared the Stokes I spectrum with the synthetic ATLAS9 + COSSAM_SIMPLE (with solar abundances) spectrum, but did not find clear evidence of strong P or Ga absorption lines, which would associate HD 139160 to this non-magnetic sub-group of He-weak stars. We did, however, note the substantially weaker He I lines. Thus, HD 139160 may host a large-scale magnetic field, but that is weaker than our detection threshold.

3.8 Discussion

3.8.1 Rotation period

The determined rotation periods indicate that all stars are slow to moderate rotators. This result was expected because of a known bias introduced in the sample star selection since we required to obtain high S/N, high-resolution spectropolarimetry with reasonable exposure times. Nevertheless, rotation periods of a few days are typical of Ap/Bp stars. We compare the determined rotation frequencies with the derived values for $v \sin i$ in Fig. 3.17. No strict relation is present, as expected due to differences in stellar radii and the anticipated random distribution of inclination angles. HD 97859 and HD 164224 seem closer to (rotation) pole-on than the others, as they are situated in the upper part of the diagram. The two probable roAp stars do not reside in a particular region of Fig. 3.17. The variety in the inclination angle i, and the obliquity angle β, is further supported by the different shapes of the rotational modulation in the K2 photometry.

3.8.2 Magnetic detections and non-detections

Out of the 16 expected magnetic stars in our sample, we directly detected the presence of a strong, large-scale magnetic field for 11 stars. This is the first firm detection for 9 of these stars and the first for all 11 stars employing high-resolution spectropolarimetry. We have a 69 % detection rate in our sample, with no obvious correlation with the stellar properties for the detection status.

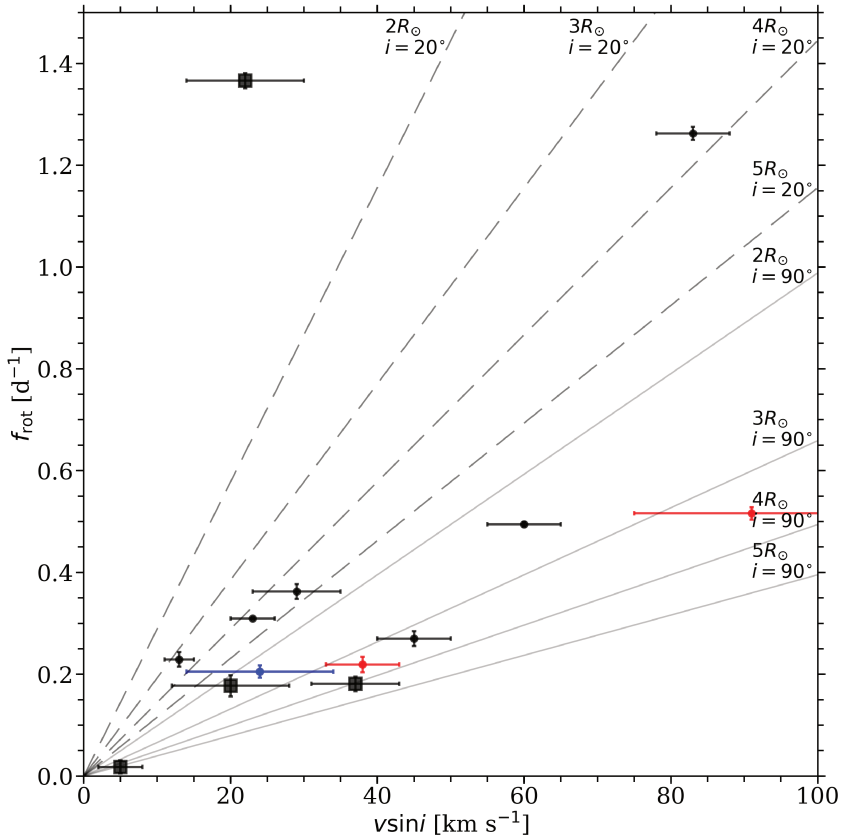

Figure 3.17: Rotation frequency $f_{\rm rot}$ versus $v \sin i$ (dots). The colour of the symbols indicates the magnetic detection (black for a DD, blue for a MD, red for a ND). The symbol relates to the measured $T_{\rm eff}$, with squares for A-type stars and dots for B-type stars. Solid lines represent the anticipated rotation frequency for the labelled stellar radius, inclination angle, and measured $v \sin i$. Solid lines are for $i = 90\,^\circ$ and dashed lines for $i = 20\,^\circ$. Anticipated rotation frequencies at a given $v \sin i$ decrease for increasing model radii ($2R_\odot$, $3R_\odot$, $4R_\odot$, and $5R_\odot$, respectively). We indicate the confidence intervals for both $f_{\rm rot}$ and $v \sin i$, where we added the errors of $v \sin i$ and of $v_{\rm NR}$ in quadrature given the correlated nature of these two parameters.

The spectropolarimetric measurements for the four stars with a ND and the one MD are of similar quality as the other 11 stars with detected magnetic fields. Moreover, it seems unlikely that the NDs/MDs were due to particularly unfavourable rotation phases where the field is seen in a cross-over configuration (see top right panels of Figs. 3.1 – 3.14).

Two of the stars with a ND, namely HD 173406 and HD 173657, show stable rotational modulation over the duration of their K2 light curves. Because of the poor quality light curve of HD 177562, we could not confirm the presence

of rotational modulation for this star with a ND. Yet, the comparison of the ESPaDOnS spectra with their respective synthetic spectra suggests chemical peculiarities, as claimed by the Renson & Manfroid (2009) catalogue. Therefore, it is likely that these three stars are indeed Ap/Bp stars with expected, stable surface abundance inhomogeneities, and thus host a large-scale magnetic field. It may be that these stars host a weaker large-scale magnetic field than what we assumed when computing the expected S/N for the exposure times of the spectropolarimetric observations. Whether or not these weaker magnetic fields are an evolutionary consequence (where the strength of the field is reduced through magnetic flux conservation; see e.g., Landstreet et al. 2008; Fossati et al. 2016) cannot be concluded without additional data. Upcoming accurate DR2 Gaia (Perryman et al. 2001) parallaxes will result in independent estimates on the radius, while additional high-resolution spectropolarimetry will permit the derivation of a more accurate upper limit on the strength of the anticipated large-scale magnetic field.

The distortions of the LSD Stokes I profile of HD 173657 (see bottom right panel of Fig. 3.11) could be due to a resolved SB2 system, instead of surface abundance inhomogeneities. However, this star is not known to be a binary system and we only obtained one observation. More spectroscopic observations are needed to corroborate this hypothesis.

We also did not detect the presence of a large-scale magnetic field for the He-weak star HD 139160. We explored the possibility of a large-scale magnetic field in the individual components of the binary system, but again obtained a ND for both components. Since we did not note any strong P or Ga lines in the spectroscopic observations, HD 139160 is inferred to be unrelated to the non-magnetic HgMn stars. Thus, we anticipate the presence of a large-scale magnetic field that is weaker than what was expected when computing the exposure time for the spectropolarimetric sequences. Further spectropolarimetric observations will be needed to derive a more robust upper-limit on the strength of the anticipated magnetic field.

3.8.3 Lack of heat-driven stellar oscillations

We found no evidence for the presence of stellar oscillations produced by the κ-mechanism in any of the Ap/Bp stars studied in this work. Our target stars do reside in the theoretical κ-driven instability regions (see Fig. 1.6). Although only a small fraction of the stars in these regions are known to have observable oscillations at current detection thresholds, the fact that none of our targets show such pulsations is significant. These results provide supportive evidence

for the theoretical predictions that strong large-scale magnetic fields change the nature of waves and may even completely suppress them (Lecoanet et al. 2017).

Two stars in our sample (HD 158596 and HD 177765) show statistically-significant peaks in their periodograms that are strong evidence for being Nyquist aliases of high-frequency roAp pulsations. Furthermore, HD 164224 shows a significant low-frequency power excess that is unlikely to be explained by instrumental effects and could be caused by unresolved g-mode pulsation modes or internal gravity waves. Extended observations of all these candidate pulsators will be extremely useful in characterising the exact nature of their observed variability in the K2 photometry.

3.9 Summary and conclusions

We observed 16 chemically peculiar hot stars with space-based high-precision photometry to study their periodic variability, and with modern high-resolution optical spectropolarimetry to detect the signatures of a large-scale magnetic field. The investigated stars are all slow to moderate rotators, with large-scale magnetic fields being easier to detect from spectropolarimetry in slowly-rotating stars compared to fast rotators. Although our sample of stars was biased towards slow rotators, the observed rotation periods are typical of Ap/Bp stars. It is known that gravity-mode oscillations are easier to detect in slowly-rotating OB-type stars (Aerts & De Cat 2003; Aerts et al. 2017b). Therefore, our sample bias should favour the detection of such oscillations.

In our sample, 13 stars have a high-quality K2 light curve and all of them show evidence of rotational modulation. We detected a large-scale magnetic field for 69% of our sample stars and found no obvious correlation between this detection and the stellar parameters, such as binarity, rotation rate, or occurrence of possible stellar pulsations. All four non-magnetic stars, HD 139160, HD 173406, HD 173657, and HD 177562 show either rotational modulation, peculiar chemical surface abundances, or both, and therefore likely host an undetected weak large-scale magnetic field.

No κ-driven oscillations were detected in any of the targets in our sample. Two stars, namely HD 158596 and HD 177765, show an isolated high-frequency peak in their periodogram, which we interpret as the Nyquist alias of high-frequency roAp pulsations in these stars. One star, HD 164224, shows a significant low-frequency power excess in its periodogram which could be evidence of unresolved g-mode pulsations or internal gravity waves. Further observations and analysis of these candidate pulsators are needed to fully test these hypotheses, since we are limited by the length and cadence of the K2 space photometry.

Chapter 4

Magneto-asteroseismic study of o Lup

This chapter is currently under revision as

Magnetic characterization and variability study of the magnetic SPB star o Lup

B. Buysschaert, C. Neiner, A. J. Martin, M. E. Oksala, C. Aerts, A. Tkachenko, E. Alecian, and the MiMeS Collaboration

Monthly Notices of the Royal Astonomical Society, 2018, Submitted (19 pages)

Original abstract:

Thanks to large dedicated surveys, large-scale magnetic fields have been detected for about 10 % of early-type stars. We aim to precisely characterize the large-scale magnetic field of the B5IV primary component of the wide binary o Lup, by using high-resolution ESPaDOnS and HARPSpol spectropolarimetry, and by analyzing the variability of the measured longitudinal magnetic field. In addition, we investigate the periodic variability using space-based photometry collected with the BRITE-Constellation by means of iterative prewhitening. The rotational variability of the longitudinal magnetic field indicates $P_{\rm rot} = 2.95333(2)$ d and that the large-scale magnetic field is dipolar, but with a significant quadrupolar contribution. Strong differences in the strength of the measured magnetic field occur for various chemical elements as well as rotational

modulation for Fe and Si absorption lines, suggesting a non-homogeneous surface distribution of chemical elements. Estimates of the geometry of the large-scale magnetic field indicate $i = 27 \pm 10\,^\circ$, $\beta = 74^{+7}_{-9}\,^\circ$, and a polar field strength of 5.25 kG. The BRITE photometry reveals the rotation frequency and several of its harmonics, as well as a dominant g-mode pulsation frequency at $f = 1.106 \pm 0.007\,\mathrm{d}^{-1}$. This g-mode pulsation dominates the line-profile variability of the majority of the spectroscopic absorption lines. We do not find direct observational evidence of the secondary in the spectroscopy. Therefore, we attribute the pulsations and the large-scale magnetic field to the primary of the o Lup system, but we discuss the implications should the secondary contribute to the variability.

4.1 Introduction

o Lup (HD 130807, HR 5528, HIP 72683, B5IV, $V = 4.3$ mag) is an early-type star and a member of the Sco-Cen association, following its Hipparcos parallax (Rizzuto et al. 2011). This region is a site of recent massive star formation at a distance of 118 – 145 pc, with the exact value depending on the sub-group of the association. Isochrone fitting to the Hertzsprung-Russell diagram indicates that the star formation occurred some 5 – 20 Myr ago.

Using interferometry, Finsen (1951) detected a secondary component for o Lup, at an angular separation of 0.115 arcsec. The most recent interferometric measurement indicates that the components have an angular separation of 0.043 arcsec, with a contrast ratio of 0.28 ± 0.06 mag (Rizzuto et al. 2013). From the distance to the Sco-Cen association, the authors deduced that the components are 5.33 au apart with a mass ratio of 0.91. Moreover, the distance to the Sco-Cen association implies that the largest measured angular separation is above 17 au, such that the orbital period of the binary must be longer than 20 years (Alecian et al. 2011).

Within the scope of the MiMeS survey, HARPSpol observations were collected for o Lup. Alecian et al. (2011) concluded that o Lup hosts a large-scale magnetic field, with variability of the measured longitudinal magnetic field indicating a rotation period between one and six days. This agrees well with the small value of the projected rotation velocity, $v \sin i = 27 \pm 3\,\mathrm{km\,s^{-1}}$ (determined by Głębocki & Gnaciński 2005). Moreover, Alecian et al. (2011) determined $T_{\mathrm{eff}} = 18000$ K and $\log g = 4.25$ dex for o Lup from a comparison with synthetic spectra using TLUSTY non-local thermal equilibrium atmosphere models and the SYNSPEC code (Lanz & Hubeny 2007; Hubeny & Lanz 2011). The authors

also noted weaker He I lines and stronger Si II than expected from the solar abundances. Hence, the surface abundance of certain chemical elements seems to be peculiar. Finally, Si, N, and Fe exhibited line-profile variations (LPVs) on a timescale of about one day. Alecian et al. (2011) proposed surface abundance inhomogeneities as the cause of these LPVs.

o Lup has recently been observed by the BRITE-Constellation of nano-satellites to monitor its photometric variability. This space-based photometry could aid in the determination of the rotation period of *o* Lup by observing the rotational modulation caused by surface abundance inhomogeneities due to the large-scale magnetic field. Moreover, it might permit us to determine the precise value and the physical process causing the variability with a period of about one day in the spectral lines. Additional ground-based, high-resolution, optical spectropolarimetric data was collected to characterize the magnetic field of *o* Lup more precisely.

We introduce the various observational data sets in Sect. 4.2, and indicate how these were treated and corrected for instrumental effects when needed. In Sect. 4.3, we estimate the stellar parameters of *o* Lup by fitting synthetic spectra to the observations and we search for evidence of the secondary component in the spectroscopy. The periodic photometric variability is investigated in Sect. 4.4, while Sect. 4.5 covers the analysis of the large-scale magnetic field. The sub-exposures of the spectropolarimetric sequences are used to detect and characterize the LPVs in Sect. 4.6. We end this chapter by discussing the obtained results in Sect. 4.7 and by drawing conclusions and providing a summary in Sect. 4.8.

4.2 Observations

4.2.1 BRITE photometry

The BRITE-Constellation, an international collaboration between Austria, Canada, and Poland, currently comprises of five fully functional and operational nano-satellites. These BRITE nano-satellites aim to monitor stars brighter than $V \approx 5$ mag using two colour pass-bands, over various observing campaigns. Each nano-satellite hosts a 3 cm telescope, providing a wide field of view ($24^\circ \times 20^\circ$) to simultaneously observe up to a few dozen stars (Weiss et al. 2014). Three nano-satellites perform their respective observations through a red photometric filter (550 – 700 nm; UniBRITE (UBr), BRITE Toronto (BTr), and BRITE Heweliusz (BHr)), while two have a blue filter (390 – 460 nm; BRITE Austria (BAb), and BRITE Lem (BLb)). The various BRITE spacecraft have a low-

Earth orbit, with orbital periods of about 100 min ($\sim$0.07 d). Therefore, they cannot continuously monitor targets, and instead, only observe them for a portion of the satellite orbit. The usable fraction of the orbit can be as large as 30 %, depending on the observing conditions, the satellite, and the studied field, before the telescope has to be pointed away (Pablo et al. 2016).

o Lup was observed by three nano-satellites of the BRITE-Constellation during the Centaurus I campaign. The BAb nano-satellite monitored o Lup from 9 April 2014 until 18 August 2014, with a large time gap (of about 76 days) in the middle of the campaign, the UBr nano-satellite performed continuous observations from 31 March 2014 until 27 August 2014, and the BTr nano-satellite had a short campaign from 27 June 2014 until 3 July 2014. Light curves were constructed by the BRITE-team from the raw CCD images using circular apertures (Pablo et al. 2016; Popowicz et al. 2017). These raw light curves were corrected for the intrapixel sensitivity and additional metadata were added, such as aperture centroid position and on-board CCD temperature. We retrieved these publicly available Data Reduction version 2 (DR2) data from the BRITE data archive[1].

The extracted BRITE photometry was further corrected by accounting for known instrumental trends using our in-house tools (see Appendix B.1 for explicit details). Here, we provide a short summary of the applied procedure. As a first step, we converted the timing of the observations to mid-exposure times. Next, we subdivided the light curves according to the temporal variability of the on-board CCD temperature $T_{\rm CCD}$, because strong discontinuities and differences in its variability were noted (see bottom panels of Fig. 4.1). For each of these data subsets, we performed an outlier rejection using the aperture centroid positions $x_{\rm c}$ and $y_{\rm c}$, the on-board temperature $T_{\rm CCD}$, the observed flux, and the number of data points per nano-satellite orbit. Once all spurious data were removed, we recombined the data sets to convert the photometric variability to ppt. The data were then again subdivided into the same subsets to correct for the fluctuating shape of the point-spread-function caused by the varying on-board temperature. The next correction step was a classical decorrelation between the corrected flux and the other metadata (including the nano-satellite orbital phase) whenever the correlation was sufficiently strong. This detrending procedure was performed for the complete UBr data set and for the two BAb observing sub-campaigns (before and after the large time gap). We could not correct the BTr data, since the very short 6 days time span leads to uncertain instrumental correction. Thus, we did not use this BTr photometry in this work. Finally, we applied a local linear regression filter to the corrected BRITE photometry, detrending and suppressing any remaining (instrumental) signal

[1] `https://brite.camk.edu.pl/pub/index.html`

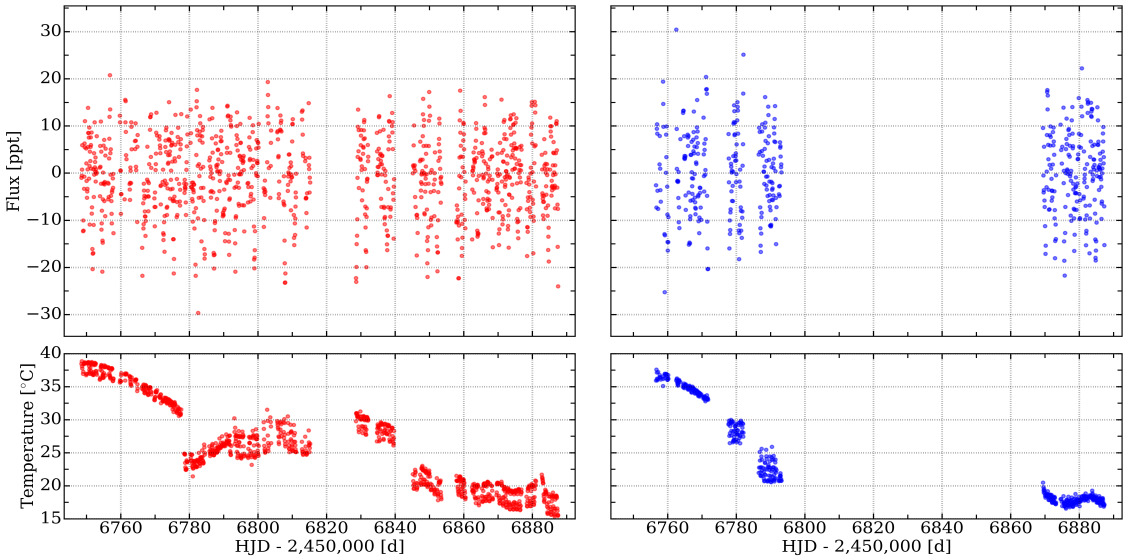

Figure 4.1: *Top*: Satellite-orbit averaged and reduced BRITE lightcurves for *o* Lup, where the UBr photometry is indicated in red (*left*) and the BAb photometry in blue (*right*). *Bottom*: Corresponding satellite-orbit averaged temporal variability of the on-board CCD temperature, showing different and discontinuous behaviour.

Table 4.1: Diagnostics related to the two BRITE light curves of *o* Lup. For each light curve, we provide the rms scatter of the flux before and after correction, the length of the light curve, the length of the largest time gap, and the $D_{\rm sat}$ and $D_{\rm orb}$ duty cycles before and after correction. The number of successful satellite orbits with observations is indicated as well.

		UBr	BAb
$\mathrm{rms}_{\rm raw}$	[ppt]	4.57	3.50
$\mathrm{rms}_{\rm corr}$	[ppt]	2.44	2.33
length	[d]	139.0	130.7
time gap	[d]	13.4	76.3
$D_{\rm sat,raw}$	[%]	70.5	26.3
$D_{\rm sat,corr}$	[%]	53.1	24.0
$D_{\rm orb,raw}$	[%]	17.4	12.8
$D_{\rm orb,corr}$	[%]	15.6	10.3
$N_{\rm orb,corr}$		1058	450

with a period longer than ∼10 days. The last part consisted of determining satellite-orbit averaged measurements.

The final corrected, detrended, and satellite-orbit averaged photometry is given

in Fig. 4.1. To assess the quality of the reduced BRITE photometry, we also provide the values for some diagnostic parameters in Table 4.1. The first of these parameters is the root mean square (rms) of the flux, given as

$$\mathrm{rms} = \sqrt{\frac{1}{N}\sum_{i}^{N}\frac{\sigma_i^2}{k_i}}\,, \tag{4.1}$$

where σ_i and k_i are the standard deviation of the flux and the number of observations within orbital passage i, respectively, and N is the total number of orbital passages for a given BRITE data set. Also listed are the median duty cycle per satellite orbit D_{orb} and the fraction of successful satellite orbits D_{sat}. The former indicates the portion of the satellite orbit used for observations, while the latter parametrizes the amount of successful satellite orbits over the total time span of the light curve.

The two final BRITE light curves (taken with the UBr and BAb nano-satellites) formed the basis of the photometric analysis of the periodic variability of o Lup discussed in Sect. 4.4.

4.2.2 Spectropolarimetry

The HARPSpol polarimeter (Piskunov et al. 2011) was used in combination with the High Accuracy Radial velocity Planet Searcher (HARPS) spectrograph (Mayor et al. 2003) to measure the Zeeman signature indicating the presence of a large-scale magnetic field at the surface of o Lup. This combined instrument is installed at the ESO 3.6-m telescope at La Silla Observatory (Chile) and covers the 3800–6900 Å wavelength region with an average spectral resolution of 110 000. Standard settings were used for the instrument, with bias, flat-field, and ThAr calibrations taken at the beginning and end of each night. In total, 36 spectropolarimetric sequences were obtained during three different observing runs, in May 2011, July 2012, and April 2016. The first two campaigns were part of the Magnetism In Massive Stars (MiMeS) survey (Wade et al. 2016), and the third observing run was performed in the framework of the BRITE spectropolarimetric survey (Neiner et al. 2016). Each spectropolarimetric sequence consists of four consecutive sub-exposures with a constant exposure time ranging between 207 s and 1000 s. An overview of the spectropolarimetric data set is given in Table A.1.

The HARPSpol data were reduced using the REDUCE package (Piskunov & Valenti 2002; Makaganiuk et al. 2011), and resulted in a circular spectropolarimetric observation for each sequence. A minor update to the package enabled us to extract individual spectra for each sub-exposure of

the spectropolarimetric sequence. The spectropolarimetric observations were normalized to unity continuum using the interactive spline fitting procedure SPENT (Martin et al. 2017). This normalization method was performed per spectral order to achieve a smooth overlap between consecutive spectral orders. The spectroscopy of each sub-exposure was normalized using the same procedure for spectral orders of interest.

o Lup was also observed twice with the ESPaDOnS (Donati et al. 2006) mounted at CFHT in April and June 2014[2]. These spectropolarimetric sequences comprise of four consecutive sub-exposures with an exposure time of 85 s. The data were reduced with the LIBRE-ESPRIT (Donati et al. 1997) and UPENA softwares available at CFHT. The resulting ESPaDOnS spectropolarimetric and spectroscopic observations were normalized to unity continuum in the same manner and using the same interactive tool as for the HARPSpol data. Details for the ESPaDOnS spectropolarimetry are provided in Table A.1.

4.3 Comparison with synthetic spectra

An accurate magnetometric analysis (Sect. 4.5) starts from the selection of the appropriate spectral lines (also referred to as the line mask), which depends on the atmospheric parameters of the star. To this aim, we used a grid of synthetic spectra to model the observed Balmer lines (Hα, Hβ, Hγ, and Hδ) and selected metal lines, deriving a value for the effective temperature $T_{\rm eff}$, and the surface gravity $\log g$ of *o* Lup. The selected lines included the He I 4471Å line and the Mg II 4481Å line, since their relative depths are good indicators for $T_{\rm eff}$ and $\log g$. The synthetic spectra produce a (good) first approximation of the stellar parameters, because the fainter secondary component and possible surface abundance inhomogeneities will lead to an uncertain chemical abundance analysis.

A model grid[3] covering a range of $T_{\rm eff}$ spanning from 3500 K to 55000 K and $\log g$ from 0.00 dex to 5.00 dex was calculated using ATLAS9 model atmospheres by Bohlin et al. (2017, retrieved from MAST) and Martin et al. (2017) assuming plane parallel geometry, local thermodynamic equilibrium, and an opacity distribution function for solar abundances (Kurucz 1993). Synthetic spectra were computed with COSSAM_SIMPLE (Martin et al. 2017).

We varied the $T_{\rm eff}$ and $\log g$ of the synthetic spectra, applying various values for the rotational broadening around the literature value of $v \sin i = 27\,{\rm km\,s^{-1}}$, and

[2]Principal investigator of the publicly available ESPaDOnS data: M. Shultz.

[3]As $T_{\rm eff}$ increases, the range of the $\log g$ values covered reduces to values between 4.00 dex and 4.75 dex at 55000 K.

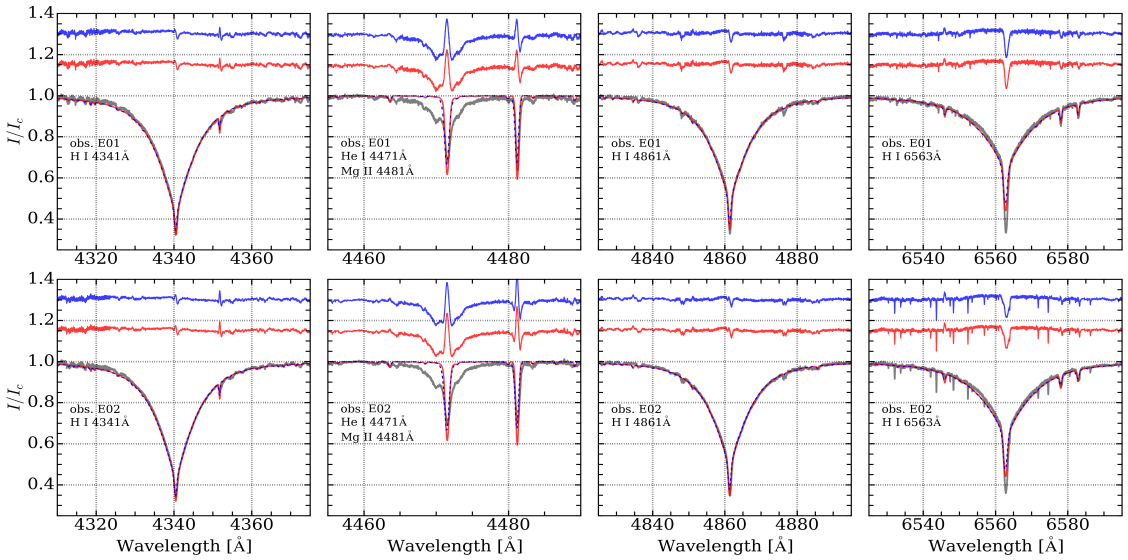

Figure 4.2: Comparison between two ESPaDOnS spectra of o Lup, taken two months apart (shown in black), and synthetic ATLAS9 / COSSAM_SIMPLE spectra (solid black line). The blue line is the synthetic spectra for a single star with $T_{\rm eff} = 15000\,{\rm K}$, $\log g = 3.8\,{\rm dex}$, and $v \sin i = 35\,{\rm km\,s^{-1}}$, and the red line is the synthetic spectra for a binary star with $T_{\rm eff,1} = 17000\,{\rm K}$, $T_{\rm eff,2} = 14000\,{\rm K}$, $\log g_1 = 3.9\,{\rm dex}$, $\log g_2 = 3.8\,{\rm dex}$, $v \sin i_1 = 50\,{\rm km\,s^{-1}}$, $v \sin i_2 = 25\,{\rm km\,s^{-1}}$, $RV_1 = -5\,{\rm km\,s^{-1}}$, $RV_2 = +5\,{\rm km\,s^{-1}}$, and a light fraction of 50 %. Residuals to the fit are indicated with the same colour coding and a small offset for increased visibility. The *top* row corresponds to observation E01 and the *bottom* row to E02 (see also Table A.1).

allowing for a radial velocity (RV) off-set to fit the ESPaDOnS spectra. This resulted in a best fit with $T_{\rm eff} = 15000\,{\rm K}$, $\log g = 3.8\,{\rm dex}$, and $v \sin i = 35\,{\rm km\,s^{-1}}$. The wings of the Balmer lines are generally well described by the model, while the depths of several metal lines, such as Mg II or He I are overestimated. Peculiar surface abundances connected to the large-scale magnetic field can produce such a discrepancy since the grid relies on a solar composition for the synthetic data. We show the ESPaDOnS observations and the best synthetic model in Fig. 4.2, as well as the residuals to the fit.

However, o Lup is a known interferometric binary system. The contrast ratio derived by Rizzuto et al. (2013) implies that about 40 % of the flux should originate from the secondary component. Moreover, the angular separation between the two components of o Lup is sufficiently small that both fall within the fiber of modern spectrographs. However, the secondary has never firmly been detected in spectroscopy. Using the ATLAS9 and COSSAM_SIMPLE synthetic spectra, we investigated whether a binary spectrum describes the observations

better than a single star.

We varied $T_{\rm eff}$ for both components from 13000 K up to 18000 K and $\log g$ from 3.5 dex up to 4.5 dex, allowing various $v \sin i$ values, light fractions from 0 % up to 50 %, and relative RV offsets up to 50 km s^{-1}. The best fit occurs for $T_{\rm eff,1} = 17000$ K, $T_{\rm eff,2} = 14000$ K, $\log g_1 = 3.9$ dex, $\log g_2 = 3.8$ dex, $v \sin i_1 = 50$ km s^{-1}, $v \sin i_2 = 25$ km s^{-1}, $RV_1 = -5$ km s^{-1}, $RV_2 = +5$ km s^{-1}, and a light fraction of 50 %. This model is indicated in Fig. 4.2. While the description of the metal lines improved, the fit to the Balmer lines did not always improve. The binarity has a similar effect on the metal lines as a surface under-abundance, which is often observed for magnetic early-type stars. Moreover, the light fraction of the secondary is higher than determined from interferometry, i.e., the fitting algorithm tries to obtain a better description for the (weaker) metal lines. For these reasons, we rejected the fit with the binary spectrum and argue that, if present, we cannot distinguish both components in the spectroscopy due to similar spectral type, small RV shifts, and expected chemical peculiarities. This is in agreement with the results of Sect. 4.5.1, where we show that the Zeeman signature spans the full width of the average line profiles and Sect. 4.6.3 where we obtain evidence of surface abundance inhomogeneities. Therefore, we adopt $T_{\rm eff} = 15000$ K and $\log g = 3.8$ dex as the starting point for the magnetometric analysis.

Incorrect values for $T_{\rm eff}$ or $\log g$ do impact the analysis of the longitudinal magnetic field as an inappropriate set of lines will be used in the determination of the average line profile in the magnetometric analysis. However, slight discrepancies between the adopted values and the real ones would only have a negligible impact, since the line depth in the line mask will be adjusted to the observations (see also Sect. 4.5.1).

4.4 Periodic photometric variability

Magnetic early-type stars often show periodic photometric variability due to co-rotating surface abundance inhomogeneities that are related to the large-scale magnetic fields. Moreover, Alecian et al. (2011) discussed the possibility of stellar pulsations in *o* Lup, yet attributed the LPVs to surface abundance inhomogeneities. To determine the cause of the LPVs, we investigated the BRITE photometry for coherent periodic variability. We first used an iterative prewhitening approach to determine the frequencies of the periodic variability. To deduce whether the found periodic variability remains constant in frequency and amplitude over the time span of the light curve, we then constructed time-frequency diagrams.

4.4.1 Iterative prewhitening

Iterative prewhitening is typically applied to recover and study the stellar pulsation mode frequencies of massive and early-type stars in both ground-based and space-based photometry (e.g. Degroote et al. 2009b). Adopting this approach, we searched for the significant frequencies in ten times oversampled Lomb-Scargle periodograms (Lomb 1976; Scargle 1982) of the BRITE photometry within the $0-8\,\mathrm{d}^{-1}$ frequency range. No variability was expected at higher frequencies. The significance of frequency peaks was calculated using the S/N criterion (Breger et al. 1993) with a frequency window of $1\,\mathrm{d}^{-1}$ after the extraction of the variability. Frequency peaks were considered significant if they reached the threshold value of 4. The periodograms for each BRITE light curve are shown in Fig. 4.3.

This method resulted in 6 significant frequencies for the UBr photometry and 3 frequencies for the BAb photometry, in the frequency domain of $0-1.5\,\mathrm{d}^{-1}$. We report these in Table 4.2, together with their respective uncertainties within the frequency resolution. It was expected that the analysis of the BAb would result in less clear periodic variability, represented by the smaller amount of significant frequencies, due to the large time gap, which complicates the analysis and the lower number of data points. We note that f_2 is the second frequency harmonic of f_1 and f_5 is the third harmonic of f_1, making it very likely that these three frequencies are related to the rotational modulation of the magnetic component. (We confirm this hypothesis in Sect. 4.5.) Moreover, f_4 is very close to $1.0\,\mathrm{d}^{-1}$, which is a known instrumental frequency for the BRITE photometry, related to the periodic on-board temperature variability (see e.g., Figs. B.2 to B.4).

Periodic variability with the same frequency in both the UBr and BAb photometry had comparable amplitudes (see Table 4.2). The frequency f_3 is likely due to a g-mode pulsation. In this case, the slightly higher amplitude in the blue filter was expected. Yet, without additional and simultaneous time resolved photometry using different bandpass filters, performing mode identification of the stellar pulsation with the amplitude ratio method was impossible (see e.g. Handler et al. 2017, where this method was successfully applied for a pulsating early-type star with BRITE and ground-based photometry).

Once all significant periodic photometric variability was subtracted from the UBr photometry, the frequency diagram of the residuals seems to be nearly constant with amplitudes well below 1 ppt (see black lines in Fig. 4.3). No obvious variability remained in the residual light curve in the time domain. The noise floor in the periodogram of the residual BAb photometry was considerably higher than that of the UBr residuals, caused by a combination of less data points and an unfavorable window pattern due to the time gap in the light

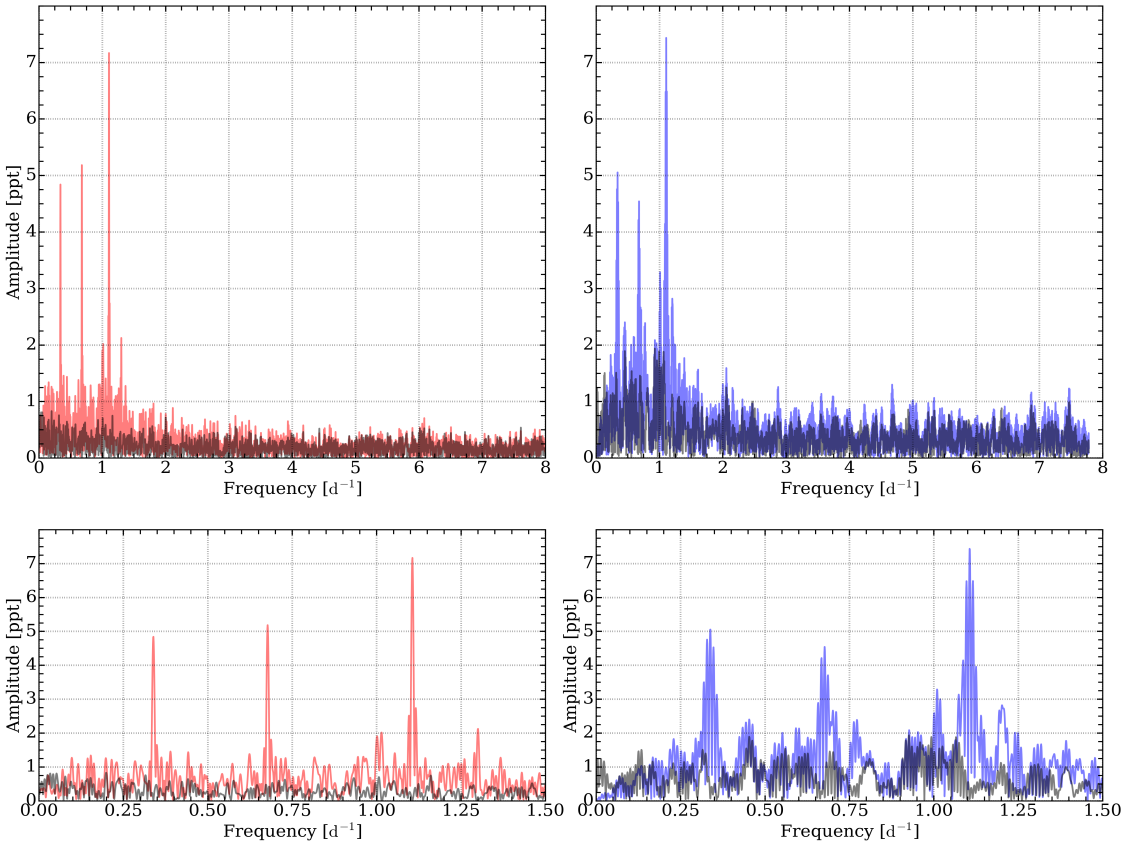

Figure 4.3: Lomb-Scargle periodograms showing the periodic variability for the UBr (*left*) and BAb (*right*) light curves. *Top*: Periodograms covering the full investigated frequency domain. The periodograms of the light curve are given in red (UBr; *left*) and blue (BAb; *right*), while the variability of the residuals after the iterative prewhitening is given in black. *Bottom*: Periodograms covering the frequency domain where significant periodic variability is recovered.

curve.

4.4.2 Time-dependent periodic variability

Periodograms of the complete light curve are not able to indicate if the amplitude of the periodic signal remains constant over the full data set. Therefore, we constructed time-frequency diagrams by determining a Lomb-Scargle periodogram at discrete steps into the light curve. Since we wished to achieve a reasonable frequency resolution for these periodograms, we adopted a 20 d time window (corresponding to a $\delta f_{\rm res} = 0.05\,{\rm d}^{-1}$) and the step size for the window was set to 2 days. To limit the effects of a low number of data points, we did not calculate any periodograms whenever the $D_{\rm sat}$ duty-cycle was less than

Table 4.2: Significant periodic variability seen in the UBr and BAb BRITE photometry of o Lup. We indicate the frequency and corresponding amplitude, A, together with their respective uncertainties, as well as the S/N of the detection in the Lomb-Scargle periodogram during the iterative prewhitening procedure. The resolving power of the frequency is listed as the Rayleigh frequency limit, while the amplitude uncertainty is determined from Montgomery & O'Donoghue (1999). We also indicate the proposed origin of the observed periodic photometric variability.

ID	Origin	UBr			BAb		
		f (d^{-1}) ± 0.007	A (ppt) ± 0.17	S/N	f (d^{-1}) ± 0.018	A (ppt) ± 0.35	S/N
f_1	$\sim f_{\rm rot}$	0.339	4.63	9.6	0.338	5.02	4.7
f_2	$\sim 2f_{\rm rot}$	0.677	5.03	8.5	0.647	4.62	5.0
f_3	g mode	1.106	7.14	10.0	1.106	7.65	5.8
f_4	$f_{\rm inst}$	1.001	1.91	5.9			
f_5	$\sim 3f_{\rm rot}$	1.016	1.29	4.5			
f_6	g mode	1.296	1.40	4.8			

30 % within a given time window. In addition, the amplitudes of f_1, f_2, and f_3 were considerably larger than those of the other three significant frequencies. To show the possible time-dependent effects of the lower-amplitude frequencies, we constructed an additional time-frequency diagram for the residuals of each light curve where the largest-amplitude periodic variability was subtracted. All these time-frequency diagrams are given in Fig. 4.4.

The time-frequency diagrams indicate no amplitude changes for f_1, f_2, and f_3. The only frequency that had a significant amplitude change with time is f_4 (see middle top panel of Fig. 4.4), which we anticipated to be of instrumental origin. To verify this hypothesis, we also constructed a time-frequency diagram for the on-board CCD temperature using the same settings as for the photometry (right panels of Fig. 4.4). Although non-periodic variability was present, this diagram did indeed indicate a similar shift in amplitude around $1.0\,d^{-1}$ for $T_{\rm CCD}$ of the UBr data, confirming the hypothesis that f_4 is instrumental. The variability with f_5 and f_6 has a low amplitude. Indeed, the time-frequency diagram of the residuals (with f_1, f_2, and f_3 subtracted) indicate minor variability at these frequencies, making it impossible to unravel inconsistencies for their amplitudes.

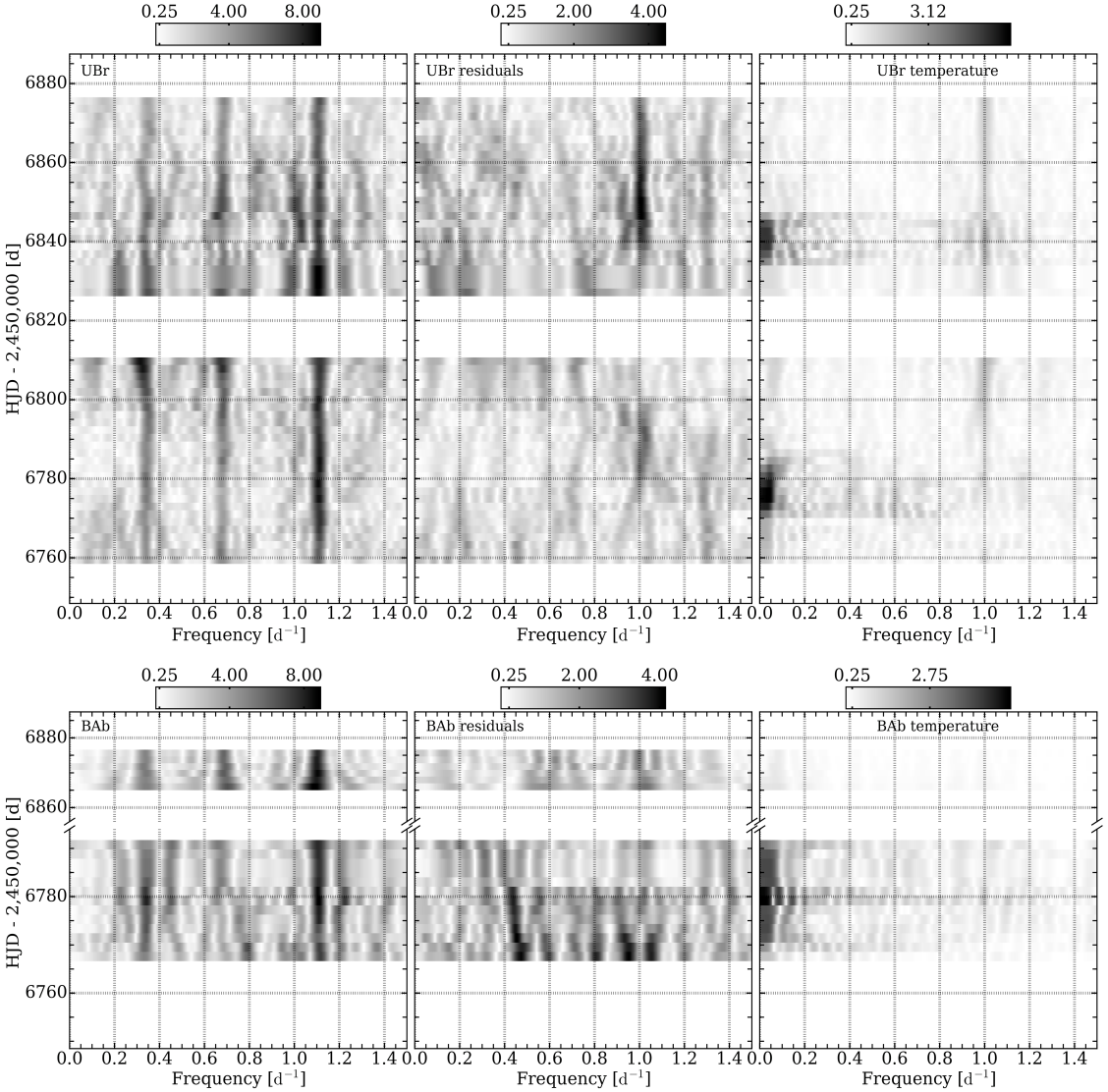

Figure 4.4: Time-frequency diagrams of the UBr (*top*) and BAb (*bottom*) photometry, where the amplitude of the periodic variability is indicated by the grayscale. Periodograms are calculated over a time window of 20 d and the step size between consecutive windows is 2 d. *Left column*: Time-frequency diagrams of the photometry itself. *Middle column*: Time-frequency diagrams of the residual photometry, when the first three frequencies, with the largest amplitude, were subtracted. *Right column*: Time-frequency diagrams of the on-board CCD temperature T_{CCD}, where the grayscale depicts the amplitude in degrees Celsius.

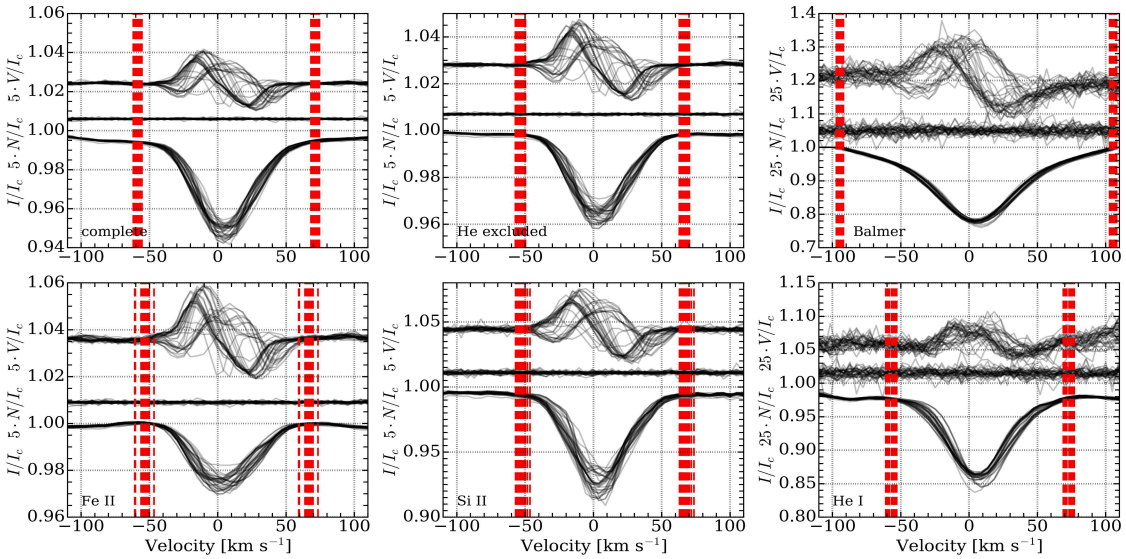

Figure 4.5: Overplotted mean line profiles constructed with the LSD method using various line masks. Each panel shows (from top to bottom) the LSD Stokes V profile, the diagnostic null profile, and the LSD Stokes I profile for the observations, that are off-set for increased visibility. Differences in the line depth of the LSD Stokes I profile, the strength and shape of the Zeeman signature in the LSD Stokes V profile, and the shape of the LPVs in the LSD Stokes I profile are clearly visible. We indicate the integration limits for the computation of the longitudinal magnetic field and the FAP determination by the red dashed lines for each observation. For the Balmer lines, only the cores of the LSD Stokes I profiles were used and shifted upwards to match the integration limits (where the core of the line transitions to the wing) to unity, following the technique of Landstreet et al. (2015, see text).

4.5 Magnetic measurements

4.5.1 Zeeman signatures

To reliably detect the Zeeman signature of a stable large-scale magnetic field at the surface of an early-type star, mean line profiles are constructed from each high-resolution spectropolarimetric observation to boost the S/N of the signature in the Stokes V polarization. We used the LSD technique (Donati et al. 1997) to create these mean line profiles. We started from a pre-computed VALD3 line mask (Ryabchikova et al. 2015) with $T_{\rm eff} = 15000$ K and $\log g = 4.0$ dex, which is the closest match to our results of $T_{\rm eff} = 15000$ K and $\log g = 3.8$ dex (Sect. 4.3), under the assumption that o Lup is a SB1 system. As usual, we removed from the line mask all hydrogen lines and all metal lines that were

blended with hydrogen lines, telluric features, and known diffuse interstellar bands to ensure we only included with metal lines with similar line profiles (the only exception being the He I lines where pressure broadening through the Stark effect is still significant). All metal lines with a depth smaller than 0.01 were also discarded. Finally, the depths of the lines included in the line mask were adjusted to correspond to the observations. This resulted in a final line mask with 893 lines included, each with their respective wavelength, line depth, and Landé factor. An additional line mask (and corresponding LSD profiles) without (blends with) He I lines was also constructed and included 821 metal lines. We show these mean line profiles in Fig. 4.5 for both line masks. The Zeeman signature in the LSD Stokes V profile clearly varies between the various observations. Moreover, the LSD Stokes I profile exhibits clear LPVs, possibly due to the rotational modulation caused by surface abundance inhomogeneities or the stellar pulsation. Fortunately, the diagnostic null profiles (i.e., deconstructively added polarization signal within the sequence, see Donati et al. 1997) suggest that no significant instrumental effects or LPVs have occurred during the spectropolarimetric sequence, as they are flat.

Based on the FAP criteria for a magnetic detection (Donati et al. 1992, 1997, and Chapter 1), all the LSD profiles for *o* Lup indicated a DD, either with the complete line mask or using the He-excluded line mask. Thus, a large-scale magnetic field is clearly detected in the high-resolution spectropolarimetry.

Figure 4.5 further indicates that the Zeeman signature in LSD Stokes V spans the full width of the LSD Stokes I profile, indicating that this full width corresponds to the magnetic component. Hence, we assume for simplicity that the observed large-scale magnetic field comes from the primary. However, in case both components of *o* Lup contribute to the spectrum, we underestimate the strength of the magnetic field through an error in the depth of the Stokes I profile in Eq. (1.16). The LSD Stokes I profiles indicated no significant RV shift between the two binary components of the *o* Lup system. Given their expected similar spectral type and LPVs in one of the components, it is thus not feasible to distinguish which component exhibits the LPVs and which is magnetic.

4.5.2 Longitudinal field measurements

Since the large-scale magnetic fields of early-type stars are expected to be stable over long time scales and inclined with respect to the rotation axis, the measured longitudinal magnetic field (defined as Eq. (1.16)) should exhibit rotational modulation (depending on the orientation). We provide the mean Landé factor g and the mean wavelength λ for the various line masks in Table 4.3 and the determined values for B_l in Table A.2. The integration limits to determine the

Table 4.3: Parameters related to the study of the longitudinal field measurements from various LSD line masks of *o* Lup. We provide the mean Landé factor g and the mean wavelength λ from the LSD calculation, as well as the resulting mean equivalent width (EW) of the LSD Stokes I profiles. The integration range around the line centroid for the calculation of the longitudinal magnetic field (see Eq. (1.16)) and determination of the FAP is given, as well as the resulting parameters of the dipole with a quadrupole contribution model (i.e., Eq. (4.3)) fitted to the measured longitudinal field.

Parameter		Complete	He excluded	Balmer	Fe II	Si II	He I
g		1.1906	1.1877	1.5000	1.1939	1.1446	1.2474
λ	[nm]	505.99	508.79	486.13	516.79	508.46	478.18
$\langle \mathrm{EW} \rangle$	$[\mathrm{km\,s^{-1}}]$	2.96 ± 0.10	1.83 ± 0.11		1.34 ± 0.10	3.41 ± 0.30	8.74 ± 0.21
int. range	$[\mathrm{km\,s^{-1}}]$	± 65	± 60	± 100	± 60	± 60	± 65
B_0	[G]	344 ± 6	821 ± 11	531 ± 32	1679 ± 31	724 ± 22	27 ± 9
B_1	[G]	568 ± 9	1340 ± 15	913 ± 45	2905 ± 43	1053 ± 30	82 ± 14
B_2	[G]	61 ± 8	168 ± 13	64 ± 46	383 ± 37	57 ± 29	-1.4 ± 12

B_l should cover the full LSD Stokes I profile, and thus, also the full Zeeman signature. Following the plateau method (e.g., Fig. 3 of Neiner et al. 2012a), where we investigated the dependency on B_l and $\sigma(B_l)$ with the integration limit for a near magnetic pole-on observation, we determined an integration range of $\pm 65\,\mathrm{km\,s^{-1}}$ and $\pm 60\,\mathrm{km\,s^{-1}}$ around the line centroid to be the most appropriate for the complete and the He-excluded LSD profiles, respectively. These values were considerably larger than the literature $v \sin i = 27\,\mathrm{km\,s^{-1}}$ for o Lup, which was a measurement for the FWHM of the absorption line and did not capture the entire width of the absorption profile or the Zeeman signature.

When the large-scale magnetic field has a pure dipolar geometry, the rotational modulation of the measured longitudinal magnetic field can be characterized by a sine model:

$$B_l(t) = B_0 + B_1 \sin\left(2\pi \left(f_{\mathrm{rot}}(t - T_0) + \phi_1\right)\right) , \tag{4.2}$$

where B_1 and ϕ_1 are the amplitude and phase of the sine, B_0 the constant offset, f_{rot} the rotation frequency, and a zero-point T_0. However, when the large-scale magnetic field has a dipolar component with a non-negligible quadrupolar contribution, the longitudinal magnetic field modulation is given by a second-order sine model:

$$B_l(t) = B_0 + B_1 \sin\left(2\pi \left(f_{\mathrm{rot}}(t - T_0) + \phi_1\right)\right) + B_2 \sin\left(2\pi \left(2 f_{\mathrm{rot}}(t - T_0) + \phi_2\right)\right) . \tag{4.3}$$

Again, B_i and ϕ_i are the amplitude and phase of the individual sine terms. We fitted both models to the longitudinal magnetic field measurements of the He-excluded LSD profiles using a Bayesian Markov Chain Monte Carlo (MCMC) method (using EMCEE; Foreman-Mackey et al. 2013) to determine the rotation period. We adopted the log-likelihood function for a weighted normal distribution:

$$\mathcal{L}(\Theta) = -\frac{1}{2} N \ln(2\pi) - N \sum_{i=1}^{N} \ln\left(\sigma\left(B_l(t_i)\right)\right) - \sum_{i=1}^{N} \left(\frac{\left(B_l(t_i) - \mathcal{M}(\Theta; t_i)\right)^2}{2\sigma\left(B_l(t_i)\right)^2} \right) , \tag{4.4}$$

with ln the natural logarithm, $\mathcal{M}(\Theta; t_i)$ the model of Eq. (4.2) or Eq. (4.3) for a given parameter vector Θ at timestep t_i. The measured longitudinal magnetic field at t_i is given by $B_l(t_i)$, its respective error by $\sigma\left(B_l(t_i)\right)$, and N is the number of observations. We constructed uniform priors in the appropriate parameter spaces for each free parameter describing the models of Eq. (4.2) and Eq. (4.3). For the rotation frequency, this was around f_1 from the BRITE

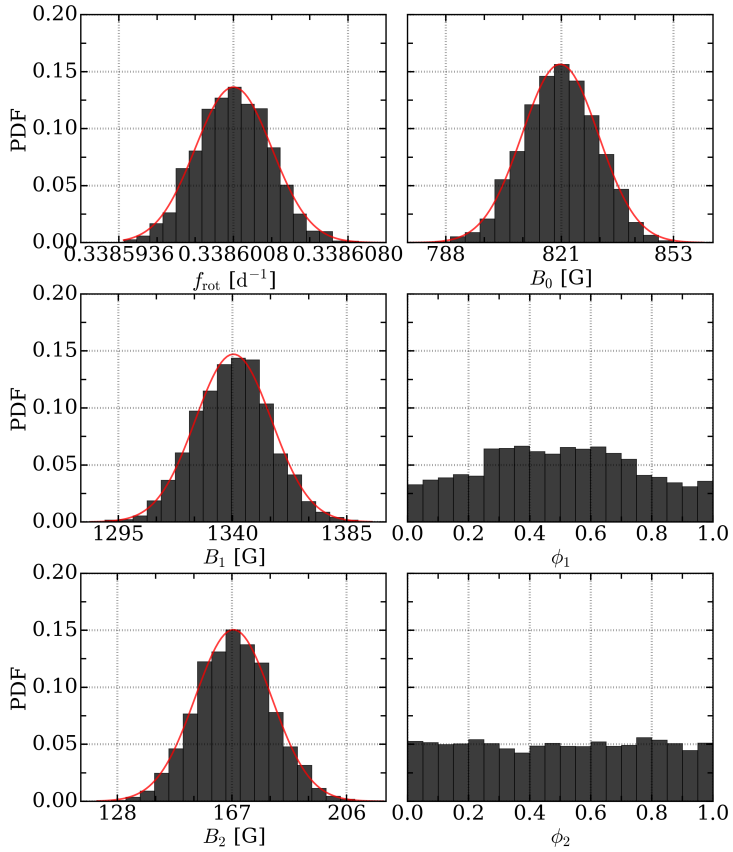

Figure 4.6: Results of the MCMC analysis on the measured longitudinal magnetic field of the He-excluded LSD profiles using the model of Eq. (4.3). The posterior probability distributions (PDF) are indicated for each fitted parameter. When these had a normal distribution, we represent it with the Gaussian description marked in red.

photometry with a range set by the Rayleigh frequency limit using the time length of the spectropolarimetric data set ($\delta f_{\rm ray} = 0.0006\,{\rm d}^{-1}$). Calculations were started at random points within the uniform parameter space with 128 parameter chains and continued until stable frequency solutions were reached.

The posterior probability distribution function (PDF) of the rotation frequency of Eq. (4.3) showed a maximum at $f_{\rm rot} = 0.338601(2)\,{\rm d}^{-1}$, corresponding to a rotation period of $P_{\rm rot} = 2.95333(2)\,{\rm d}$. Also the PDF for the amplitudes B_1 and B_2, and the offset B_0 show a normal distribution. The distributions for the phases ϕ_1 and ϕ_2 are nearly uniform, which is expected from the distribution of $f_{\rm rot}$ as the phase for each given rotation frequency value has a normal distribution. We indicate these PDFs in Fig. 4.6 and list the deduced values for B_0, B_1, and B_2, with their respective uncertainties, in Table 4.3. The fit to the B_l values computed from the He excluded LSD profile resulted in a non-zero

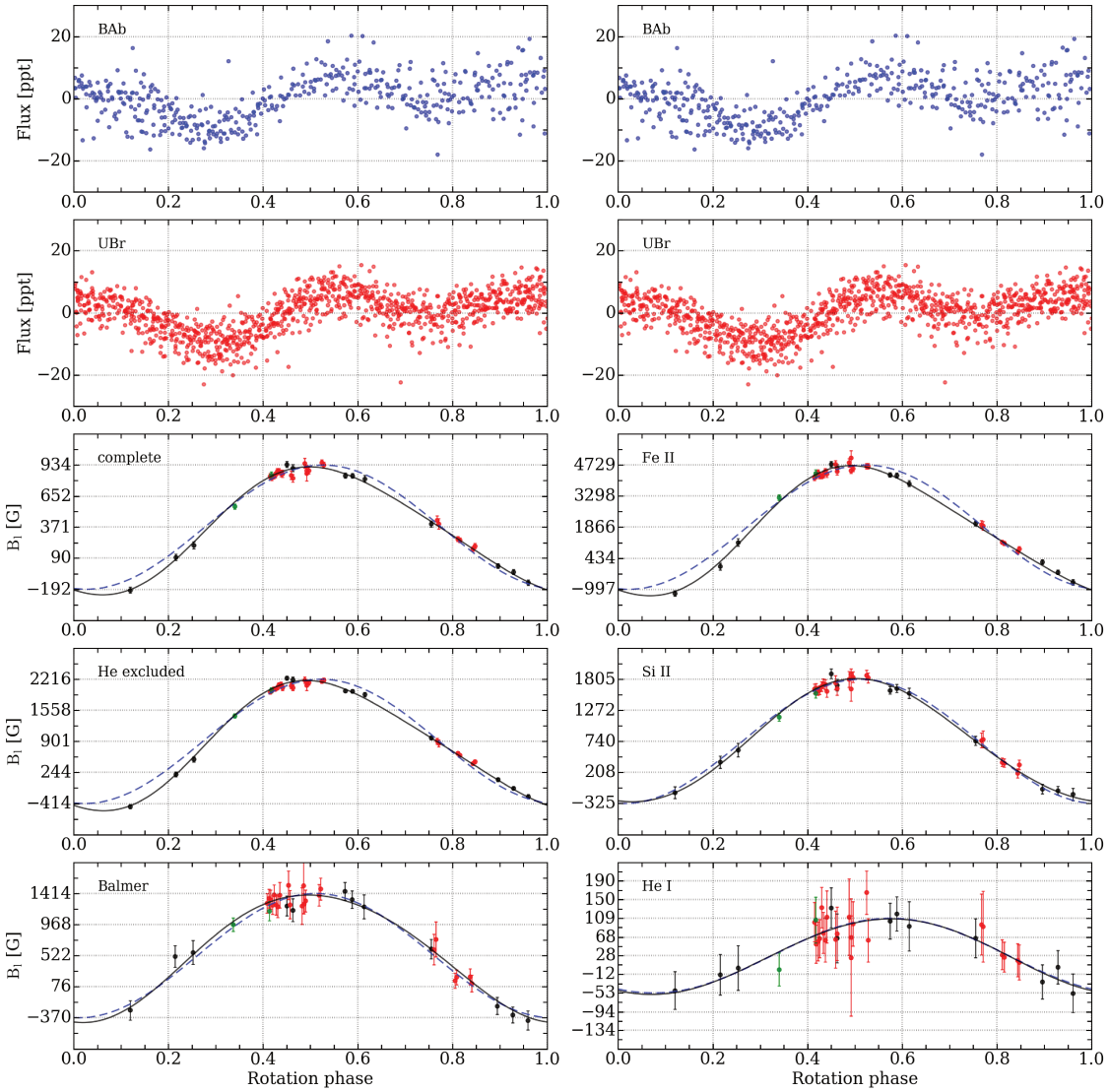

Figure 4.7: Phase folded BRITE light curves (after subtracting the variability with f_3; *upper two rows*) and longitudinal magnetic field measurements from LSD profiles with various line masks, using a $P_{\rm rot} = 2.95333$d and $T_0 =$ HJD 2455702.5, and indicated by the observing campaign (black for MiMeS, red for BRITEpol, and green for ESPaDOnS). The pure dipole model for the geometry of the large-scale magnetic field of Eq. (4.2) is indicated by the dashed blue line and the dipole with a quadrupole contribution of Eq. (4.3) is indicated by the solid black line. Note the differences in strength of the measured B_l values for the various LSD line masks.

value for B_2, indicating that the second-order term of the model is needed, hence the quadrupolar component of the large-scale magnetic field is significant. This was further supported by the Bayesian inference during the fitting process

and model selection.

Assuming that both components of o Lup contribute to the spectrum and that their rotation periods are sufficiently shorter than the length of the spectroscopic time series, we assert that only one component hosts a strong large-scale magnetic field. Indeed, there is a lack of variability in the measured longitudinal magnetic field other than with a period $P_{\rm rot}$. A second magnetic component would severely distort the rotational modulation indicated in Fig. 4.7. Only a binary system with synchronized rotation periods could reproduce this variability, which is highly unlikely for the o Lup binary system given its $P_{\rm orb} > 20$ years. Furthermore, a (close) binary system with multiple magnetic early-type stars is still extremely rare (ϵ Lup is the only known example, Shultz et al. 2015b).

We included the BRITE light curves, phase folded with $P_{\rm rot}$ and with the periodic pulsation variability with f_3 removed, in the top panels of Fig. 4.7 to compare the photometric rotational modulation with that of the longitudinal magnetic field. The peak brightness in the folded BRITE light curves occurs close to the phase where we observed the magnetic field extrema, suggesting that the brighter surface abundance inhomogeneities are located close to the magnetic poles. The remaining photometric variability depends on the inclination angle i, the obliquity angle β, and the position of the abundance inhomogeneities at the stellar surface, which requires tomographic imaging and/or spot modelling and is beyond reach of the current data.

4.5.3 Single-element longitudinal field measurements

While adjusting the line depths of the metal lines used in the LSD line masks, we noted that the Zeeman signature shows different strengths for different chemical species. Therefore, we constructed three different line masks containing only 19 He I, 264 Fe II, or 61 Si II metal lines. Special care was taken to exclude any line blends with metal lines that had a stronger or similar line depth than the considered chemical element. The corresponding mean Landé factors and mean wavelengths are given in Table 4.3, and the LSD profiles themselves are given in Fig. 4.5. Similar to the LSD profiles constructed with the complete line mask, we obtained DDs for all LSD profiles constructed with either Si II or Fe II lines. For the He I LSD profiles, however, we obtained ten NDs, and 26 DDs, most likely caused by the lower S/N, as fewer lines were included in constructing the mean line profile. Indeed, the S/N in the LSD Stokes V and Stokes I profiles of the He I line mask was typically three times lower than that of the Fe II LSD profiles (see Table A.1). Again, we noted strong LPVs for the LSD Stokes I profiles of all single-element LSD line masks, while the diagnostic null profiles indicated that no LPVs or instrumental effects have

occurred during the spectropolarimetric sequence. We study these LPVs in more detail in Sect. 4.6.

We used the single-element LSD line masks to measure the longitudinal magnetic field associated with the large-scale magnetic field. Again, we used the plateau method to determine the integration range for the computations. This resulted in an integration limit of $65\,\mathrm{km\,s^{-1}}$, $60\,\mathrm{km\,s^{-1}}$, and $60\,\mathrm{km\,s^{-1}}$ around the line centroid for the He I, Fe II, and Si II line masks, respectively. Keeping the rotation frequency fixed to the previously derived value, we performed an MCMC fit to model the rotational modulation of the measured longitudinal magnetic field. These models and the measured values are shown in Fig. 4.7.

The rotational modulation of the measured B_l values from the LSD profiles constructed with only Fe II lines favored the model of a dipolar magnetic field with a quadrupolar contribution. This is in agreement with the results for the complete LSD line masks derived in Sect. 4.5.2. For the analysis of the measured longitudinal magnetic field of *o* Lup with only Si II lines, we obtained a less clear distinction between both models for the rotational modulation of the measured B_l values. Both models agree with the measurements, within the derived uncertainties on the B_l values. Yet, the fit with the model of dipolar magnetic field and a quadrupolar component was preferred from Bayesian inference. Finally, the B_l values measured from the He I LSD line mask were much smaller. This caused the rotational modulation of the measured B_l values to be minimal, leading to a comparable description by both models. Since the deduced errorbars on the measured B_l values for the He I remained comparable to those derived from the other LSD line masks, it seemed likely that the noted differences are (astro)physical. Surface abundance inhomogeneities structured to the geometry of the large-scale magnetic field at the stellar surface could be an explanation. Elements that are concentrated at the magnetic poles will lead to larger B_l values, while elements located close to the magnetic equator will result in smaller B_l values. Such features should be noted during tomographic analyses (such as Zeeman Doppler Imaging), but require a spectropolarimetric data set which is more evenly sampled over the rotation period than the current observations.

We tried to model the Zeeman signature of the large-scale magnetic field, seen in the LSD Stokes V profile, using a grid-based approach (see e.g., Alecian et al. 2008, for further details). However, we were unable to accurately model the changing Zeeman profile with varying rotation phase. This was likely caused by the insufficient sampling of the rotation period at key phases.

4.5.4 Balmer lines longitudinal field measurements

The magnetometric analysis of single-element LSD profiles exhibited a strong scatter in the strength of the measured B_l values, suggesting surface abundance inhomogeneities for certain chemical elements (e.g., He, Si, and Fe). To measure the rotational modulation of the longitudinal magnetic field for an element that should be homogeneously distributed over the stellar surface we analyzed the hydrogen lines. The wavelength regions around the Balmer lines in the spectropolarimetric observations were normalized with additional care, using only linear polynomials, so as to not influence the depth of the line core or the broad wings.

We constructed a mean line profile for the Balmer lines, including Hα, Hβ, and Hγ in the LSD line mask. Three of these profiles indicated a ND and one a MD of a Zeeman signature in the observations (see Table A.1), most likely due to the lower S/N in the Stokes V profiles for these observations. We then followed the method of Landstreet et al. (2015) to measure the B_l values. This method uses only the core of the line and ignores the broad wings. Moreover, to scale the measurements more in line with those from the metal lines, the (LSD) Stokes I profile was not integrated from unity, but instead from the intensity level I_w, where the core transitions into the wings. As the Zeeman signature in the LSD Stokes V profile is slightly wider than the core of the Stokes I profile, we used this width to set the integration range to $100\,\mathrm{km\,s^{-1}}$ around the Stokes I line centroid. We present these LSD profiles in Fig. 4.5, where the indicated Stokes I profile is shifted upwards to place I_c at unity. While fixing the rotation frequency, we performed an MCMC fit to determine the fitting parameters for the description of the rotational modulation of the measured B_l values. The fit of both models to the measured B_l values is given in Fig. 4.7, with the parameters in Table 4.3.

The rotational modulation of the measured longitudinal magnetic field from the Balmer lines was more accurately represented by the model for a dipolar magnetic field and a quadrupolar component. This result agreed with those of the other LSD profiles according to Bayesian inference. Yet, the discrepancies between this model and that of a dipolar magnetic field were small at most of the rotation phases, due to large uncertainties in B_l caused by the low S/N in the LSD Stokes V profiles of the Balmer lines.

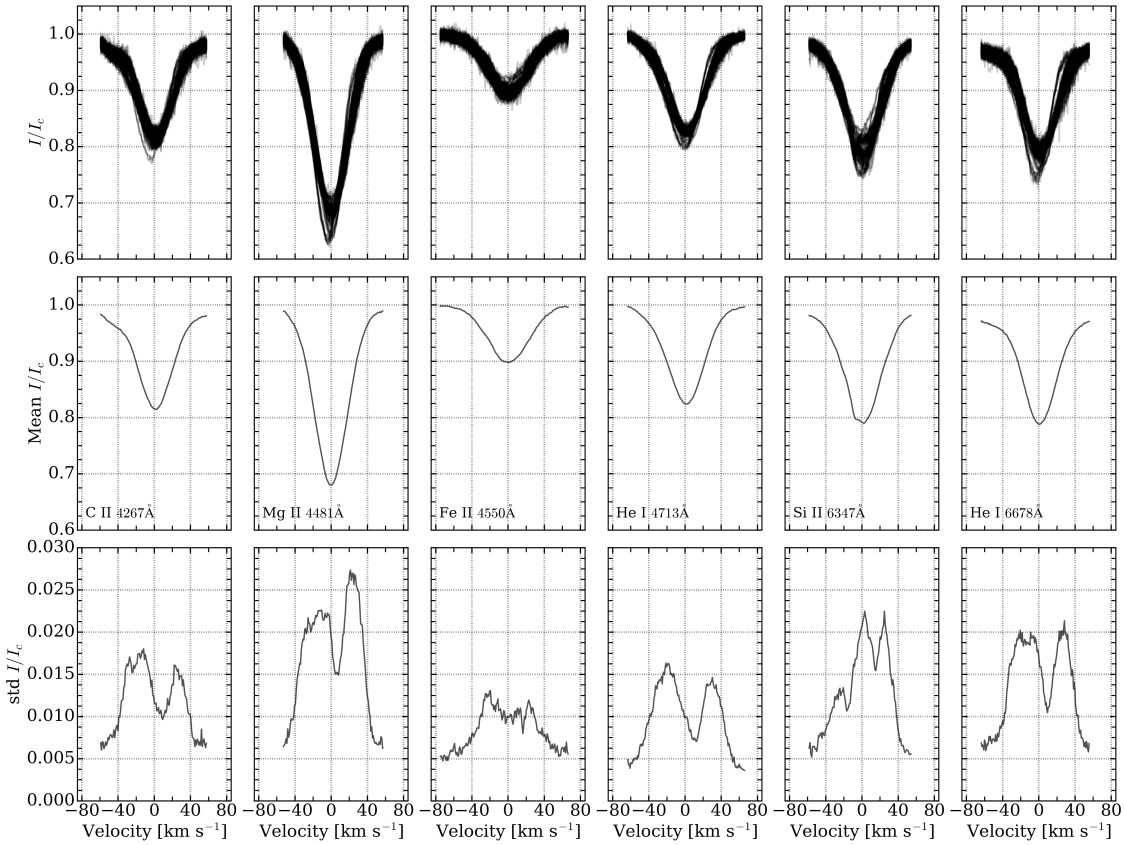

Figure 4.8: LPVs for various selected absorption lines. *Top row*: all observations of the given line overlayed to illustrate the LPVs. As an additional diagnostic, we indicate the mean profile (*middle row*) and standard deviation (std; *bottom row*) of all observations. The standard deviation, particularly, shows strong differences when comparing the selected absorption lines.

4.6 Line profile analysis

Pulsating early-type stars and magnetic early-type type stars are both known to exhibit LPVs. Alecian et al. (2011) already noted such behaviour for *o* Lup. Therefore, we investigated the zeroth and first moment of selected absorption lines for periodic variability using FAMIAS (Zima 2008). The analysis of six absorption lines, using the sub-exposures of the spectropolarimetric sequences, is presented in Sect. 4.6.1. We also investigated the Hα line for variability in Sect. 4.6.2, to try to diagnose the presence of a magnetosphere. Finally, we examined the possibility of co-rotating surface abundance inhomogeneities by analyzing the zeroth line moment of six absorption lines in Sect. 4.6.3.

4.6.1 Individual lines

To analyze the LPVs of stellar pulsations in absorption lines, it is preferred to work with deep and unblended absorption lines. This remains valid when investigating the signatures caused by the rotational modulation of surface abundance inhomogeneities. During the analysis of the Zeeman signature in the LSD Stokes V profile, we noted differences between different chemical species. Therefore, we selected absorption lines from various elements. For He, we selected and analyzed the He I 4713.2 Å and the He I 6678.2 Å lines, which are close multiplets of several He lines. In addition, the Mg II 4481.1 Å line fulfilled the set criteria. At an effective temperature of 15000 K, there are not many strong and suitable Si lines. Therefore, we opted for the Si II 6347.1 Å, although it is blended with the weaker Mg II 6347.0 Å line. Similarly, we selected the Fe II 4549.5 Å line, which blends with a weak Ti II line. Finally, we chose the C II 4267.3 Å line, which is actually a multiplet. The spectroscopy used during the LPV analysis was the individual sub-exposures of the spectropolarimetric sequences. We removed the last two sub-exposures of the observation H25 (see Table A.1), since they did not contain any flux due to bad weather. This resulted in a total of 142 spectroscopic observations taken over ∼1780 days, with large time gaps in between each observing campaign. We show the selected spectroscopic lines in Fig. 4.8, together with their mean line profile and the standard deviation of all observations of a given absorption line. The latter indicated a different shape for the LPVs for the Fe II and Si II lines compared to the other selected absorption lines, such as the He I or C II lines. This might indicate a different dominant variability, and hence a different origin or cause for the LPVs. The standard deviation of the selected Mg II line also looked slightly different, yet it seemed to be an intermediate profile between the two studied He I lines.

For each line selected, we set appropriate limits for the calculation of the line moments. These limits were set at similar flux levels for a given spectral line, close to the continuum level, unless strong pressure broadening (e.g. He I 6678.2 Å) or asymmetries in the line wings (e.g., C II 4267.3 Å) were noted, resulting in a more narrow range. We determined the zeroth, $\langle v^0 \rangle$, first, $\langle v \rangle$, and second moment, $\langle v^2 \rangle$, (representative of the equivalent width, radial velocity, and skewness, respectively) for each selected line with the software package FAMIAS (Zima 2008). Here we continue the discussion of the coherent periodic variability in the first line moment. The zeroth line moment is analyzed in Sect. 4.6.3. From the BRITE photometry and the rotational modulation of the longitudinal magnetic field, two periods were already known to cause periodic variability. These are the rotation period ($P_{\rm rot} = 2.95333\,{\rm d}$) and the g-mode pulsation frequency ($f_3 = 1.106\,{\rm d}^{-1}$). For the rotation period, we kept the period fixed and fit a second order sine function (similar to Eq. (4.3)) to

$\langle v \rangle$ of each selected spectroscopic line. Such a model is preferred since the surface abundance inhomogeneities do not always produce a sinusoidal signal, although it heavily depends on the inclination angle i and the distribution of the inhomogeneities. The quality of the fit was determined by the loglikelihood function for a (non-weighted) normal distribution:

$$\mathcal{L}(\Theta) = -\frac{1}{2} N \ln(2\pi) - N \ln\left(\sigma\left(\langle v \rangle\right)\right) - \frac{\sum_{i=1}^{N} \left(\langle v \rangle(t_i) - \mathcal{M}(\Theta; t_i)\right)^2}{2\sigma\left(\langle v \rangle\right)^2} \,, \qquad (4.5)$$

where $\sigma\left(\langle v \rangle\right)$ is the error on $\langle v \rangle$, of the order of $1\,\mathrm{km\,s^{-1}}$. Again, 128 parameter chains were used during the MCMC fitting, starting from random positions within the uniform priors, and computations continued until stable solutions were reached. The computed $\mathcal{L}(\Theta)$ for the fits are given in Table 4.4, and the phase-folded $\langle v \rangle$ are shown in Fig. 4.9. For the fits with the g-mode pulsation frequency, we followed a similar MCMC fitting approach, but used a sine function with the frequency as a free parameter (starting from the value delivered by the Fourier analysis) as the model description. The fit to the $\langle v \rangle$ of the Mg II line resulted in $f = 1.105711(8)\,\mathrm{d^{-1}}$, agreeing well with the value derived from the UBr light curve ($f_3 = 1.1057 \pm 0.0070\,\mathrm{d^{-1}}$). Subsquently, we fixed the frequency while performing the MCMC fitting to the $\langle v \rangle$ of the remaining spectral lines. We also report the $\mathcal{L}(\Theta)$ of these fits in Table 4.4 and show the phase-folded $\langle v \rangle$ values with $f = 1.105711\,\mathrm{d^{-1}}$ in Fig. 4.9.

For all selected absorption lines, except the Fe II line, the $\mathcal{L}(\Theta)$ favors periodic variability with the g-mode pulsation frequency. Scatter in the phase folded $\langle v \rangle$ suggests that additional periodic variability is present for several absorption lines. The scatter is different for the MiMeS data (depicted in black in Fig. 4.9) and the BRITEpol data (indicated in red in Fig. 4.9), pointing to a different beating pattern in those two data sets.

The dominant variability in the Fe II line is caused by the rotation, as revealed by both the $\mathcal{L}(\Theta)$ in Table 4.4 and a visual inspection of Fig. 4.9. The latter also confirms the presence of the first harmonic of the rotation frequency to describe the variability. A comparison with the phase folded BRITE light curves or longitudinal magnetic field measurements (cf. Fig. 4.7) does not reveal an obvious correlation. Future tomographic analyses should indicate the distribution of the surface abundance inhomogeneities more clearly.

4.6.2 Balmer lines

Magnetic early-type stars can host a magnetosphere in their nearby circumstellar environment (see also Sect. 1.2.2). The interactions of wind matter within

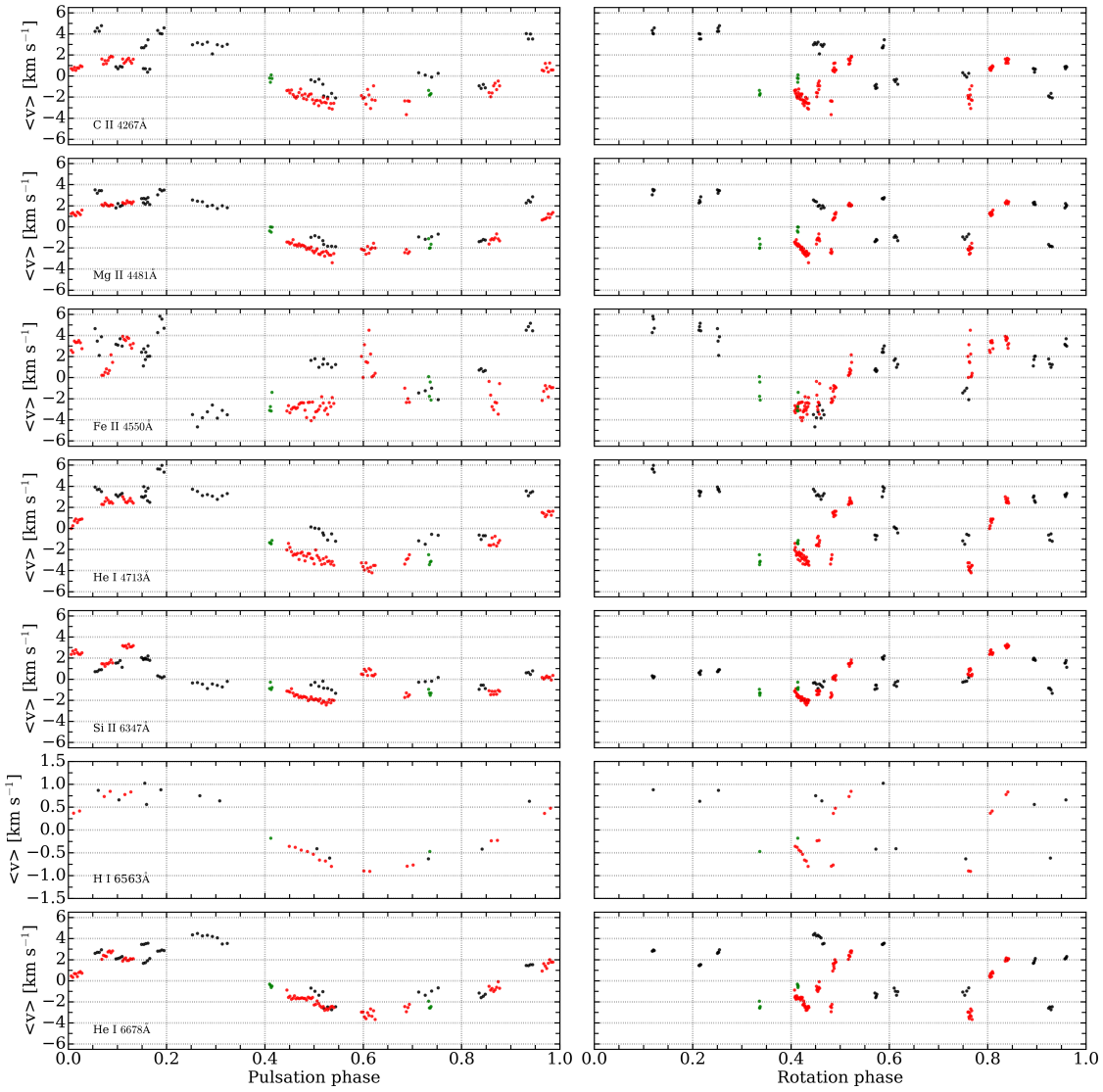

Figure 4.9: Phase folded $\langle v \rangle$ for selected absorption lines with the g-mode pulsation period $1/f = 1/1.105711 = 0.904346\,\mathrm{d}$ (*left*) and the rotation period ($P_{\mathrm{rot}} = 2.95333\,\mathrm{d}$ and $T_0 = \mathrm{HJD}\,2455702.5$; *right*). The same colours for the observations as Fig. 4.7 is used.

this magnetosphere could, cause rotationally modulated variability in certain spectroscopic lines, with periodic variable emission features in Hα the easiest to identify. For o Lup, we did not observe such emission profiles, however, we did note variability in the core of the Hα line. We thus repeated the analysis of the line moments, where we restricted their computation to the core of the line, fixing the integration limits where the broad line wing starts.

We performed the same analysis as for the other absorption lines for the cores

Table 4.4: Loglikelihood values for the fits to the first moment $\langle v \rangle$ of selected absorption lines, revealing the time scale of the LPVs. Fits were performed with either the rotation frequency and a second order sine function to indicate rotational modulation caused by surface abundance inhomogeneities or with the g-mode pulsation frequency and a sine function.

line		$\mathcal{L}(\Theta)$ $f = f_{\rm rot}$	$\mathcal{L}(\Theta)$ $f = 1.105711\,{\rm d}^{-1}$
C II	4267.3 Å	-382.2	-161.3
Mg II	4481.1 Å	-371.5	-227.2
Fe II	4549.5 Å	-388.5	-490.7
He I	4713.2 Å	-513.2	-218.4
Si II	6347.1 Å	-220.8	-202.0
H I	6562.2 Å	-39.3	-33.4
He I	6678.2 Å	-440.0	-177.0

of the Hα line of each complete spectropolarimetric sequence. The loglikelihood according to Eq. (4.4) results in the phase folded $\langle v \rangle$ in Fig. 4.9. The Hα variability did not correspond to rotational modulation, therefore, we did not detect a signature of the potential magnetosphere. Similar to the majority of the lines of the previous section, the MCMC fit indicated that the g-mode pulsation frequency is the dominant source for the LPVs. The significantly lower $\mathcal{L}(\Theta)$ for the fit to the core of Hα is the result of using only 36 spectropolarimetric sequences compared to the 142 spectroscopic observations.

4.6.3 Surface abundance inhomogeneities

The equivalent width or zeroth line moment can be used as a first approximation to follow the change in the surface abundance of chemical species. This has been used before to confirm the presence of co-rotating surface abundance inhomogeneities for magnetic stars (e.g., Mathys 1991). We phase fold the derived $\langle v^0 \rangle$ of the six selected absorption lines with $P_{\rm rot} = 2.95333\,{\rm d}$ and the determined g-mode pulsation frequency. No clear and coherent variability was obtained when we phase folded $\langle v^0 \rangle$ with the g-mode pulsation frequency. This is not entirely unexpected, as most non-radial pulsation modes distort the shape of the line instead of strongly altering the equivalent width of the line. In contrast, the abundance of the Si II and the Fe II lines did indicate coherent variability with the rotation period. We show these phase folded $\langle v^0 \rangle$ measurements in Fig. 4.10.

The variability of $\langle v^0 \rangle$ of the Fe II line can be described by a second order sine

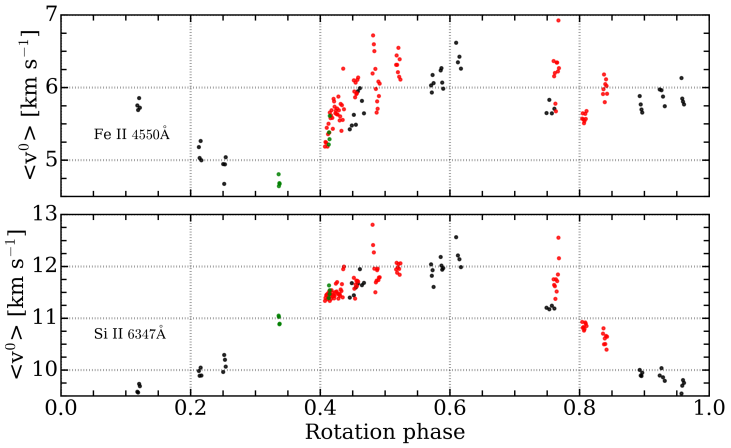

Figure 4.10: Phase folded $\langle v^0 \rangle$ for the Fe II and the Si II absorption lines with the rotation period ($P_{\rm rot}$ = 2.95333 d and T_0 = HJD 2455702.5). The same colours for the observations as Fig. 4.7 is used.

function, but heavily relies on the scarce measurements between rotation phase 0.20 and 0.35. Moreover, the phase folded $\langle v^0 \rangle$ of the Fe II line seems to be coherent with the phase folded BRITE photometry (see top panels of Fig. 4.7). The simplest explanation for the LPVs in this Fe line, thus, is the presence of surface abundance inhomogeneities that are located close to the magnetic poles. Such a geometrical configuration agrees with the stronger measured longitudinal magnetic field from LSD profiles with only Fe lines (Fig. 4.7) and is often encountered for magnetic Ap/Bp stars.

A different profile was obtained for the rotational modulation of the $\langle v^0 \rangle$ of the Si II line. We recall that the $\langle v \rangle$ of this Si II line did not show clear variability with neither the g-mode pulsation frequency nor the rotation period. These results indicate that the Si surface abundance inhomogeneities have a different location on the surface of *o* Lup than the Fe surface abundance inhomogeneities.

For the four other investigated absorption lines, the measured $\langle v^0 \rangle$ followed a profile in between that of the Fe II line and the Si II line, albeit with a smaller amplitude. The measured abundances of these lines are most likely following the changes in the local atmosphere caused by the Si and Fe surface abundance inhomogeneities.

4.7 Discussion

Comparison between the ESPaDOnS spectroscopy and synthetic spectra did not indicate *o* Lup was an SB2 system, despite the interferometric results (Rizzuto

et al. 2013). Either the secondary component is not visible in the spectroscopy, or the RV shifts were too small to detect due to two components of similar spectral type. Therefore, we continue this section under the assumption that only the primary component contributes to the variability and the large-scale magnetic field. We do comment, where applicable, what the implication would be in case of an indistinguishable secondary component.

4.7.1 Geometry of the magnetic field

The rotational modulation of the measured longitudinal magnetic field favored the model of a dipolar magnetic field with a quadrupolar contribution. The strength of the quadrupolar term in the model varied with the used LSD line mask, but it was typically about 10 % of the strength of the dipolar term (see Table 4.3).

Assuming a typical stellar radius of $3 - 4\,R_\odot$ for a B5IV star with $T_{\rm eff} = 15000\,\mathrm{K}$ (e.g., Fig. 1 of Pápics et al. 2017) and using the measured rotation period of $2.95333(2)\,\mathrm{d}^{-1}$ and the literature $v \sin i = 27 \pm 3\,\mathrm{km\,s^{-1}}$ (Głębocki & Gnaciński 2005), we estimated the inclination angle to be $27 \pm 10\,^\circ$ (corresponding to an equatorial velocity of $v_{\rm eq} = 60 \pm 9\,\mathrm{km\,s^{-1}}$). These assumptions lead to an obliquity angle $\beta = 74^{+7}_{-9}\,^\circ$, following the scaling relation of Shore (1987) for a purely dipolar large-scale magnetic field (see also Eq. (1.17)). The quadrupolar contribution needed for the description of the modulated longitudinal magnetic field will only have a minor effect on this estimated value. Moreover, this value does not depend strongly on the LSD line mask used for the measurements of the longitudinal magnetic field.

A conservative lower limit for the polar strength of the large-scale magnetic field (when the geometry is a pure dipole) is 3.5 times the maximal measured longitudinal magnetic field value (Preston 1967); this also follows from the mean factor for Eq. (1.18). Using the measurements of the LSD profiles from the Balmer lines, since these were not influenced by the surface distribution of the chemical elements, we obtained a lower limit of 5.25 kG for the polar strength of the magnetic field. This value is typical for magnetic Bp stars.

Detailed modelling of the Zeeman signatures or successful ZDI mapping of the stellar surface is required to verify the values derived from simple assumptions. However, the current spectropolarimetric data set is not sufficient to do so, because of missing observations at several key rotation phases.

In case the secondary significantly contributes to the spectropolarimetric data, we underestimated the strength of the detected large-scale magnetic field, since the total Stokes I profile was used for the normalization of the B_l values. For a

40 % contribution of a secondary, the actual strength of the magnetic field will be underestimated by 40 % or 60 %, depending on which component is hosting the large-scale magnetic field.

We consider it unlikely that both components of the o Lup binary system host a large-scale magnetic field with the published light ratio and the similar values for $v \sin i$. In case both hosted a large-scale magnetic field, the similar light contributions would lead to two overlapping Zeeman signatures in the LSD Stokes V profiles, resembling a highly complex magnetic field geometry. The similar values for the $v \sin i$ (and light ratio) would suggest a similar rotation period, causing the longitudinal magnetic field to vary with two superimposed periods. This would lead to a strong beating effect. None of the above was observed (see Figs. 4.5 and 4.7). Only if both stars would rotate with exactly the same period could they pollute the observations unnoticed, and perhaps result in the necessity of the high-order fit to the measured B_l values. However, the synchronization time scale of a binary system with an orbital period of at least 20 years is sufficiently long to exclude this possibility.

4.7.2 Discrepancies in the measured magnetic field strength

Strong differences in the strength of the measured longitudinal magnetic field from different chemical elements are not often noted for magnetic early-type stars. They are, however, observed here. Surface abundance inhomogeneities are likely the cause of these differences. We support this hypothesis with the analysis of the LPVs, since the chemical species having a stronger longitudinal magnetic field are also the same species that indicated the rotation frequency as the dominant variability for the first line moment (i.e., Fe II). Moreover, the zeroth line moment of some studied lines suggested that the measured equivalent width changes with the rotation phase, implying a non-uniform surface distribution for these chemical elements. A similar conclusion was obtained by Yakunin et al. (2015) for the magnetic helium-strong B2V star HD 184927. The larger measured B_l values for LSD profiles with just Fe II lines would indicate that their surface abundance inhomogeneities are located close to the magnetic pole, while the weaker fields retrieved from the He I would locate their respective surface abundance inhomogeneities close to the magnetic equator. In addition, the weaker longitudinal magnetic field measurements for the He I lines could also be related to a contribution in the LSD Stokes I profile coming from the secondary of the o Lup system, which is suggested to have a similar spectral type.

We do not anticipate that the stellar pulsation is causing these severe differences in the measured longitudinal magnetic field strength. It would rather produce

additional systematic offsets out of phase with the rotation period, as the pulsation frequency is not a harmonic of the rotation frequency. For the secondary component to cause these differences, it must have a different spectral type, leading to different contributions to spectral lines of different chemical species. This is in contradiction to the binary fitting process, that suggested a similar spectral type for both components. Also, the interferometry indicated a relatively similar spectral type for the secondary and a mass ratio of 0.91 (Rizzuto et al. 2013).

4.7.3 Magnetosphere

The detected large-scale magnetic field for the primary component of *o* Lup is sufficiently strong to create a magnetosphere. However, the star is not sufficiently massive to have a considerable mass-loss rate, producing only a limited amount of wind matter to fill the magnetosphere. Therefore, no observational evidence of the magnetosphere is expected. Indeed, no rotational modulation, nor emission features were noted for the Balmer lines. No X-ray observations are available for *o* Lup to diagnose the interactions between wind matter coming from both magnetic hemispheres.

Petit et al. (2013) determined the star may host a centrifugal magnetopshere, using the magnetic properties derived by Alecian et al. (2011). Repeating these computations for a $4.7\,M_\odot$ star with a $3.5\,R_\odot$ radius, the updated $P_{\rm rot} = 2.9533\,\mathrm{d}$, and a polar magnetic field strength of 5.25 kG (and assuming a mass-loss rate described by Vink et al. 2001), we obtained a Keplarian co-rotation radius $R_{\rm K} = 4.2\,R_\star$ and an Alfvén radius $R_{\rm A} = 26.5\,R_\star$ (and a mass-loss rate $\log \dot{M} = -10.42\,\mathrm{dex}$ with $\dot{M}$ given in $M_\odot\,\mathrm{yr}^{-1}$). This confirms the results of Petit et al. (2013) that the magnetic component of *o* Lup hosts a centrifugal magnetosphere. Yet, as previously indicated, the mass-loss rate is too low, particularly compared to the extend of the magnetosphere ($R_{\rm A} \gg R_{\rm K}$), to produce sufficient observational evidence of magnetospheric matter. In addition, the binary orbit of *o* Lup is too wide to cause effects in the circumstellar matter of the magnetic component.

4.7.4 Stellar pulsations

The BRITE photometry indicated that two frequencies, namely $f_3 = 1.106\,\mathrm{d}^{-1}$ and $f_6 = 1.296\,\mathrm{d}^{-1}$, were not explained as a frequency harmonic of the rotation frequency or as instrumental variability due to the spacecraft. Furthermore, we recovered one of these frequencies (i.e., f_3) as the dominant periodicity in the first line moment of the C II 4267.3 Å, Mg II 4481.1 Å, He I 4713.2 Å, and

the He I 6678.2 Å lines, as well as from the core of Hα. The frequency value and the stellar parameters of the magnetic primary suggest that this frequency is a g mode. The majority of stars exhibiting such pulsation modes show a rich frequency spectrum, with sectoral dipole modes that are quasi-constantly spaced in the period domain (e.g., Pápics et al. 2014, 2017; Kallinger et al. 2017). We only find two pulsation mode frequencies due to the limited BRITE and ground-based data sets compared to the *Kepler* capacity in terms of aliasing.

The shape of the LPVs of the aforementioned spectral lines, seen in the standard deviation of the lines, suggests a dominant low-degree mode (likely a dipole mode). Yet, detailed mode identification with FAMIAS did not produce conclusive results on the mode geometry. Furthermore, the frequency $f_6 = 1.296\,\mathrm{d}^{-1}$ is also within the appropriate frequency domain for g-mode pulsations. In the absence of the secondary in the spectroscopy, we assume that the g-mode pulsations originate from the magnetic component, as the majority of the LPVs are explained by f_3. However, if the secondary contributes to the total flux, the periodic variability with f_3 or f_6 could be produced by the companion since its anticipated similar spectral type would place it within the SPB instability strip as well.

Without at least several detected pulsation modes, the magnetic and pulsating component of o Lup is not a suitable candidate for magneto-asteroseismology, and so does not provide the opportunity to investigate the influence of the large-scale magnetic field on the structure and evolution of the stellar interior.

4.8 Summary and conclusions

We combined HARPSpol and ESPaDOnS spectropolarimetry to study and characterize the large-scale magnetic field of o Lup. Using the variability of the measured longitudinal magnetic field, we determined the rotation period to be $P_{\mathrm{rot}} = 2.95333(2)\,\mathrm{d}$, which agrees with earlier estimates that the rotation period would be of the order of a few days (Alecian et al. 2011). We assumed that the primary component of the o Lup system hosts the large-scale magnetic field, given the lack of firm detection of a secondary component in the spectroscopic data set.

Comparing the strength of the measured B_l for various chemical elements, we noted large differences, indicative of chemical peculiarity and abundance structures at the stellar surface. The largest values were obtained for Fe, while the smallest values were derived from He I lines. This suggests that Fe surface abundance inhomogeneities are located closer to the magnetic poles, while those for He are present near the magnetic equator. Yet, we cannot fully exclude

a possible contamination by the secondary component of o Lup in the LSD Stokes I profiles. Tomographic imaging is needed to confirm the locations of the suggested surface abundance inhomogeneities in detail. However, this is not feasible with the current spectropolarimetric data set, as we are lacking observations at several necessary rotational phases.

Fitting models to the rotational variability of the measured B_l values favors a description of a dipolar magnetic field with a quadrupolar contribution. This remains valid for the LSD profiles constructed with all metal lines, averaging out the effects of the surface abundance inhomogeneities, as well as for the LSD profiles from the Balmer lines. Typically, the strength of the quadrupolar contribution is about 10 % of that of the dipolar contribution. Using simple approximations, we estimated the inclination angle of the magnetic component of o Lup to be $i = 27 \pm 10\,^\circ$, which then leads to an obliquity angle $\beta = 74^{+7}_{-9}\,^\circ$. A conservative lower limit on the polar strength of the large-scale magnetic field, measured from the LSD profiles of the Balmer lines, would be 5.25 kG.

The BRITE photometry for o Lup shows up to six significant frequencies, indicating periodic photometric variability. Three of these frequencies (f_1, f_2, and f_3) correspond to the rotation frequency, and the second and third frequency harmonics. One frequency (f_4) is confirmed to be of instrumental origin, due to periodic variability of the satellite on-board temperature that was not perfectly accounted for during the correction process. The remaining two frequencies (f_3 and f_6) fall in the frequency domain of SPB pulsations. In case f_3 and f_6 originate from the magnetic component, o Lup A would be classified as a magnetic pulsating early-type star. However, the few detected pulsation mode frequencies are not sufficient for detailed magneto-asteroseismic modelling.

Investigating selected absorption lines in the individual sub-exposures of the spectropolarimetric sequences indicates the presence of LPVs. The first line moment of these lines almost always indicate f_3 as the dominant frequency, except for the Fe II line where $f_{\rm rot}$ was the dominant frequency. This is, again, suggestive of surface abundance inhomogeneities for Fe. Moreover, the equivalent width of the studied Fe II and Si II lines did change significantly with the rotation phase, demonstrating non-uniform surface abundances for these chemical species. The shape of the LPVs for the other selected absorption lines, where f_3 is dominant, agrees with a zonal or sectoral dipole mode, confirming that f_3 is a pulsation mode frequency.

Chapter 5

Investigating the magnetic supergiant ζ Ori for stellar pulsations

This chapter was originally published as

Studying the photometric and spectroscopic variability of the magnetic hot supergiant ζ Orionis Aa

B. Buysschaert, C. Neiner, N. D. Richardson, T. Ramiaramanantsoa, A. David-Uraz, H. Pablo, M. E. Oksala, A. F. J. Moffat, R. E. Mennickent, S. Legeza, C. Aerts, R. Kuschnig, G.N. Whittaker, A. Popowicz, G. Handler, G. A. Wade, and W. W. Weiss

Astronomy & Astrophysics, 2017, 602, A91 (20 pages)

Original abstract:

Massive stars play a significant role in the chemical and dynamical evolution of galaxies. However, much of their variability, particularly during their evolved supergiant stage, is poorly understood. To understand the variability of evolved massive stars in more detail, we present a study of the O9.2Ib supergiant ζ Ori Aa, the only currently confirmed supergiant to host a magnetic field. We have obtained two-colour space-based BRITE photometry for ζ Ori Aa during two observing campaigns, as well as simultaneous ground-based, high-

resolution optical CHIRON spectroscopy. We perform a detailed frequency analysis to detect and characterize the star's periodic variability. We detect two significant, independent frequencies, their higher harmonics, and combination frequencies: the stellar rotation period $P_{\rm rot} = 6.82 \pm 0.18$ d, most likely related to the presence of the stable magnetic poles, and a variation with a period of 10.0±0.3 d attributed to circumstellar environment, also detected in the Hα and several He I lines, yet absent in the purely photospheric lines. We confirm the variability with $P_{\rm rot}/4$, likely caused by surface inhomogeneities, being the possible photospheric drivers of the discrete absorption components. No stellar pulsations were detected in the data. The level of circumstellar activity clearly differs between the two BRITE observing campaigns. We demonstrate that ζ Ori Aa is a highly variable star with both periodic and non-periodic variations, as well as episodic events. The rotation period we determined agrees well with the spectropolarimetric value from the literature. The changing activity level observed with BRITE could explain why the rotational modulation of the magnetic measurements was not clearly detected at all epochs.

5.1 Introduction

Massive supergiants undergo strong mass loss through line driven winds (e.g., Kudritzki & Puls 2000, for a thorough review). The properties of the wind and the associated mass loss were studied for many massive supergiant stars by investigating the P Cygni profiles of the Si IV and N V lines observed by the International Ultraviolet Explorer (IUE; e.g., Prinja et al. 2002). These observations indicated the presence of time-variable absorption structures, known as discrete absorption components (DACs), inferred to exist for most massive OB stars (e.g., Howarth & Prinja 1989; Kaper et al. 1996). Such structures start as broad low-velocity components close to the stellar surface and evolve to narrow high-velocity components. The recurrence timescale and the acceleration timescale of these structures both correlate with the rotation velocity of the star, yet the strength between consecutive rotation cycles varies, as does their coherence on longer timescales. Such variations are defined to be cyclic rather than periodic, since the amplitude of the variations differs on a timescale of several stellar rotations.

Mullan (1984, 1986) proposed that co-rotating interaction regions (CIRs), i.e., spiral-shaped wind structures in co-rotation with the star, lay at the origin of DACs. Theoretical work by Cranmer & Owocki (1996) showed that localized perturbations at the stellar surface, such as bright surface

inhomogeneities, produce CIRs in the star's circumstellar environment, and that slowly propagating discontinuous velocity plateaus in the wind located ahead of the compressed CIR arms cause the DACs, instead of the CIRs themselves. Recent high-precision photometric monitoring of the mid-O-type giant ξ Per by MOST (Walker et al. 2003) shows evidence of signatures of co-rotating bright surface inhomogeneities at the surface of the star, with a potential link to its DAC behavior (Ramiaramanantsoa et al. 2014). Still, the origin of the surface inhomogeneities remains uncertain; magnetic fields (e.g., Henrichs et al. 1994) and non-radial pulsations (e.g., Willson 1986; Castor 1986) have been proposed as scenarios.

Large-scale magnetic fields continue to be the preferred pathway to produce local surface anisotropies, since they can cause chemical stratification or lower the optical depth, due to magnetic pressure at the magnetic poles, commonly leading to bright surface inhomogeneities. Moreover, they also naturally explain differences in the wind velocity, aiding the formation of CIRs. However, a recent study by David-Uraz et al. (2014) detected no large-scale magnetic fields for a sample of mainly OB supergiants having a well-studied DAC behavior. Their derived upper limits on non-detected polar fields was typically larger than 50 G. These limits are larger than the typical field strengths expected under the assumption of magnetic flux conservation for the increased stellar radius during the supergiant phase (Bagnulo et al. 2006; Landstreet et al. 2007, 2008; Fossati et al. 2016), which only reaches up to a few tens of gauss. Additionally, the determined upper limits on the strength of the magnetic dipole do not reach the critical strength needed to significantly perturb the wind.

Some hot supergiants also exhibit stellar pulsations. These prove to be crucial ingredients to unraveling the internal properties of such objects. Different types of pulsations are theoretically expected and commonly classed as periodically variable supergiants (see also Fig. 1.6), yet only scarcely detected in massive evolved stars (see Aerts et al. 2010, and Chapter 1).

SPB oscillations are expected to occur in OB supergiants. Such pulsations are driven by the κ-mechanism acting on the iron opacity bump at $T \sim 2 \times 10^5$ K. However, an intermediate convective layer just above the hydrogen burning shell is needed to prevent the gravity modes from propagating into the core (Gautschy 2009; Godart et al. 2009). These SPB supergiants have low-degree, high-order g modes, with a period of several days (e.g., Saio et al. 2006; Lefever et al. 2007).

Oscillatory convection (non-adiabatic g^-) modes have been theoretically predicted to occur at the stellar surface of massive supergiants, with periods ranging from about 1.5 days to hundreds of days (Saio 2011). Low-degree oscillatory convection modes are driven at the convective envelope associated

with the iron-group opacity peak. Yet, high-degree convection modes can also become overstable when non-adiabatic computations are performed for high-luminosity stars (e.g., Shibahashi & Osaki 1981). These modes are believed to cause some of the variability seen in massive supergiants, e.g., ζ Pup (O4I(n)fp; Howarth & Stevens 2014). The discovered single 1.78 d periodicity in this star has recently been interpreted as caused by evolving rotating bright surface inhomogeneities instead of stellar pulsations (Ramiaramanantsoa et al. 2018).

Moravveji et al. (2012) invoked gravity modes driven by fluctuations in the energy generation rate ϵ (i.e., the ϵ-mechanism; Unno et al. 1989) to describe the longest variability periods determined for Rigel (B8Ia). This mechanism occurs when the heat exchange reaches a maximum. For massive supergiants, such as Rigel, these fluctuations take place in the hydrogen burning shell partly located in the radiative zone, just below the intermediate convection layer.

Finally, strange-mode pulsations are theoretically expected for the most luminous massive supergiants (Saio et al. 1998; Saio 2009; Glatzel 2009; Godart et al. 2011). They are produced by the opacity mechanism on Fe and He II ionization stages (Saio 2011). However, none have yet been firmly detected.

Different types of stellar pulsations are thus theoretically expected, and on many occasions observed. However, no firm link between these stellar pulsations and the origin of DACs has currently been noted. As such, neither of the proposed photospheric driving mechanisms is clearly supported or disproved. Therefore, it is possible that various processes produce bright surface inhomogeneities leading to DACs, for example non-radial pulsations or large-scale magnetic fields. The recent discoveries of gravity waves in space photometry of hot supergiants is also worth mentioning. From Aerts et al. (2017a) and Simón-Díaz et al. (2017), it was found that the O9Iab star HD 188209 and the B1Ia star HD 2905 reveal photospheric variability due to waves and rotational modulation in the wind.

Variability on a much shorter timescale, on the order of several minutes, has been noted for some supergiants (e.g., Hubrig et al. 2014; Kholtygin et al. 2017). The exact mechanism, however, remains uncertain, but it might be related to a stochastic process.

In this work, we study ζ Ori Aa, the only confirmed magnetic O-type supergiant to date. The star has previously shown complex behavior and variability, making it a very interesting object. We collected two-colour space-based BRITE photometry as well as simultaneous ground-based high-resolution optical CHIRON spectroscopy, to study both the photometric and spectroscopic periodic variability of ζ Ori Aa by means of a detailed frequency analysis. The frequency domain $0 - 10\,\mathrm{d}^{-1}$ is investigated since the signal of any periodic or cyclic magnetic, wind, circumstellar or stellar variability is expected in this frequency

Table 5.1: Stellar parameters for the three main components of ζ Ori, determined by Hummel et al. (2013) unless noted differently. Stellar masses and radii were determined from the photometric distance. **References**: *a*: Sota et al. (2014); *b*: Simón-Díaz & Herrero (2014); *c*: Blazère et al. (2015); *d*: Bouret et al. (2008).

	Aa	Ab	B
m_V (mag)	2.08	4.28	4.01
SpT	O9.2Ib Nwk [a]	B1IV	B0III
M ($M_\odot$)	33 ± 10	14 ± 3	–
R ($R_\odot$)	20 ± 3.2	7.3 ± 1.0	–
$v \sin i$ (km/s)	127 [b]	< 100 [c]	350
$T_{\rm eff}$ (kK)	29.5 ± 1.0 [d]	29 [c]	–
$\log g$ (dex)	3.25 ± 0.10 [d]	4.0 [c]	–

domain.

We first introduce ζ Ori Aa and the current understanding of the object in Sect. 5.2. Next, we describe the photometric observations and present a detailed frequency analysis in Sect. 5.3. Section 5.4 contains the spectroscopic measurements and analysis. Our results are discussed in detail in Sect. 5.5. Finally, we summarize our conclusions on the variability of ζ Ori Aa and make remarks for future studies in Sect. 5.6.

5.2 ζ Orionis

ζ Ori (Alnitak, V = 1.79) is part of the Orion OB association (e.g., Blaauw 1964; Kubiak et al. 2017), which comprises of several regions of active star formation. More specific, ζ Ori is part of the Orion OB Ib and Orion OB Ic regions. Furthermore, the star is also surrounded by the NGC 2023 and NGC 2024 H II regions (see e.g., Bron et al. 2018). Both the Orion OB association and the H II regions lead to an increased background level around ζ Ori, but the star is sufficiently bright to outshine their respective contributions.

5.2.1 Multiplicity of ζ Ori

ζ Ori is a wide visual binary system consisting of ζ Ori A (HR 1948) and ζ Ori B (HR 1949), currently separated by ∼2.4 arcsec. The changes in common proper motion listed in the *Washington Double Star Catalog* led to an orbital solution with a period longer than several hundred years (Mason et al. 2001; Turner

et al. 2008). Since the components have such a large separation, it is assumed that they have not had any significant influence on each other's evolution.

More recently, Hummel et al. (2000) utilized optical interferometry and showed that ζ Ori A is itself a binary system, composed of the massive supergiant ζ Ori Aa and an additional hot companion ζ Ori Ab 40 mas away. The intensive spectroscopic and interferometric monitoring campaign permitted Hummel et al. (2013) to deduce the orbital solution of the Aa+Ab system, together with some of the physical properties of both components. The system is moderately eccentric, $e = 0.338 \pm 0.004$, with an orbital period of 2687.3 ± 7.0 d (~ 7.4 years). The long orbital period and eccentricity indicate a low probability of tidal interaction between the two components. However, such interaction cannot be fully excluded, because of the large radius of ζ Ori Aa and the presence of a third component (ζ Ori B), which could hamper circularization of the system (Correia et al. 2012).

Finally, a much fainter fourth component, ζ Ori C, is located about 57 arcsec away from ζ Ori Aa. Because of the large brightness difference (>7 mag) and its considerable separation, we ignore ζ Ori C for the remainder of this work. The physical parameters of the other three components are given in Table 5.1.

5.2.2 Magnetism

Bouret et al. (2008) detected the possible presence of a weak magnetic field for the primary ζ Ori A. Using the Narval spectropolarimeter (Aurière 2003), the authors estimated the approximate rotation period of the star, and determined the geometrical configuration of the magnetic field. However, this study did not account for the component ζ Ori Ab, which at that time had not yet been explored (Hummel et al. 2013). More recently, Blazère et al. (2015) determined the rotation period and the magnetic configuration more precisely, by combining archival and new Narval spectropolarimetry, while accounting for the presence of ζ Ori Ab by performing spectral disentangling of the two components. This analysis led to a rotation period of 6.83 ± 0.08 d for ζ Ori Aa (Blazère, private communication), and the confirmation of a dipolar magnetic field with a polar strength of about 140 G. This rotation period is clearly visible in the 2007–8 magnetic measurements, but less clear in the 2011–12 data, because the latter was affected by additional unexplained variability. No magnetic field was detected for the companion ζ Ori Ab, with an upper limit for the polar field strength of 300 G.

Furthermore, the presence of a weak dynamical magnetosphere was considered by Bouret et al. (2008) and Blazère et al. (2015), because of the locked Hα emission with the rotation period, an indication of magnetically confined circumstellar

material. A compatible result was obtained by Morel et al. (2004), although they observed a lower harmonic of the rotation period. The large uncertainty on the mass-loss rate and the terminal wind speed makes a qualitative calculation of the Alfvén radius, and thus the precise confinement of the magnetosphere, difficult (see Blazère et al. 2015).

The studied X-ray observations of ζ Ori Aa are inconclusive, as different works favor (Waldron & Cassinelli 2001) or argue against (Cohen et al. 2014; Nazé et al. 2014) the influence of the magnetic field on the X-ray variability of ζ Ori Aa. Since ζ Ori Aa hosts a weak magnetic field during a turbulent evolutionary stage, it is indeed likely that the weak magnetosphere only very weakly contributes to the X-ray variability, and that the emission instead originates from wind shocks generated through other mechanisms. This stellar wind may have violent epochs; significant X-ray flux increases have been observed for ζ Ori Aa (Berghofer & Schmitt 1994), although such variability is not always reported (e.g., Nazé et al. 2014).

5.2.3 Discrete absorption components

Like most massive stars, ζ Ori A shows evidence of wind variability, manifested by DACs, in their UV resonance lines. Kaper et al. (1996, 1999) studied this variability, using 29 UV spectra taken by IUE over a time span of 5.1 days. The authors reported the presence of DACs for ζ Ori A, visible in both the Si IV 1393.8Å, 1402.8 Å and N V 1238.8Å, 1242.8 Å doublets with a recurrence timescale of $t_{\rm rec} = 1.6 \pm 0.2$ d. Unlike most stars with identified DACs, the recurrence timescale for ζ Ori A is roughly one-quarter of the inferred rotation period instead of the more typical one-half period. Considering the bright surface inhomogeneities paradigm as the possible photospheric origin of the CIRs (as in the canonical model of Cranmer & Owocki 1996), this means that four surface inhomogeneities would be needed to create the accompanying CIRs in ζ Ori Aa, instead of two. Moreover, Kaper et al. (1999) state that the DACs are relatively weak for a supergiant, indicating there might indeed be something fundamentally different in the physical process for ζ Ori A. Finally, the authors observed a strong peak at a period of ~ 6 d in the Fourier analysis of their UV time series observations of ζ Ori A, but the interpretation of that periodicity was hampered by the fact that their observations only spanned 5.1 d. This ~ 6 d period can probably be associated with the rotation period (6.83 ± 0.08 d) determined from spectropolarimetry.

5.3 BRITE photometry

5.3.1 Observations

ζ Ori was first observed by the two Austrian BRITE nano-satellites (BAb and UBr) as part of the commissioning field of the mission. This commissioning field is now known as the Orion I field. In total, the observations lasted ∼130 d, starting in early December 2013 and ending in mid March 2014: both BRITE nano-satellites studied the field with a high observing cadence whenever the satellites orbital phase permitted. The second visit by the BRITE-Constellation to ζ Ori occurred from late September 2014 until mid March 2015, lasting ∼170 d in total. During this Orion II observing campaign, approximately the first 40 % of the observations were taken by BAb and BTr, and then the two Polish BRITE nano-satellites, BLb and BHr, took over. For some satellites, tests were performed to investigate whether on-board stackings of multiple, consecutive CCD images improved the data quality (Pablo et al. 2016). This led to various observing cadences being adopted throughout the Orion II campaign, although each individual observation occurred with an exposure time of 1.0 s. Table 5.2 lists the various BRITE observations of ζ Ori, taken during the Orion I and Orion II campaigns[1]. The individual components of ζ Ori are not separately monitored by the BRITE-Constellation, since the pixel size (27 ") is larger than the angular separation. Hence, the light curve contains all of its components, of which ζ Ori Aa is the brightest (see Table 5.1). With the average size of 10 pixels for the PSF for ζ Ori (see Fig. B.3), we deduce a photometric aperture of about 4 arcmin. Only a limited contribution of the nearby H II regions to the BRITE light curve is expected.

To limit telemetry usage, no full CCD images are downloaded from the spacecrafts. Smaller CCD sub-rasters, with a size of 32×32 pixels, are instead used for each star. Once the observing campaign finishes, light curves are extracted from the CCD frames for all stars in the studied field, using circular apertures (Popowicz et al. 2017). The raw light curve files have been corrected for intrapixel sensitivity, and provide additional metadata such as CCD centroid positions and CCD temperature. We then start from these data files and correct for any remaining instrumental effects in the photometry.

[1]The BRITE-Constellation returns yearly to the Orion field. Two additional BRITE light curves are now available at the time of the PhD print.

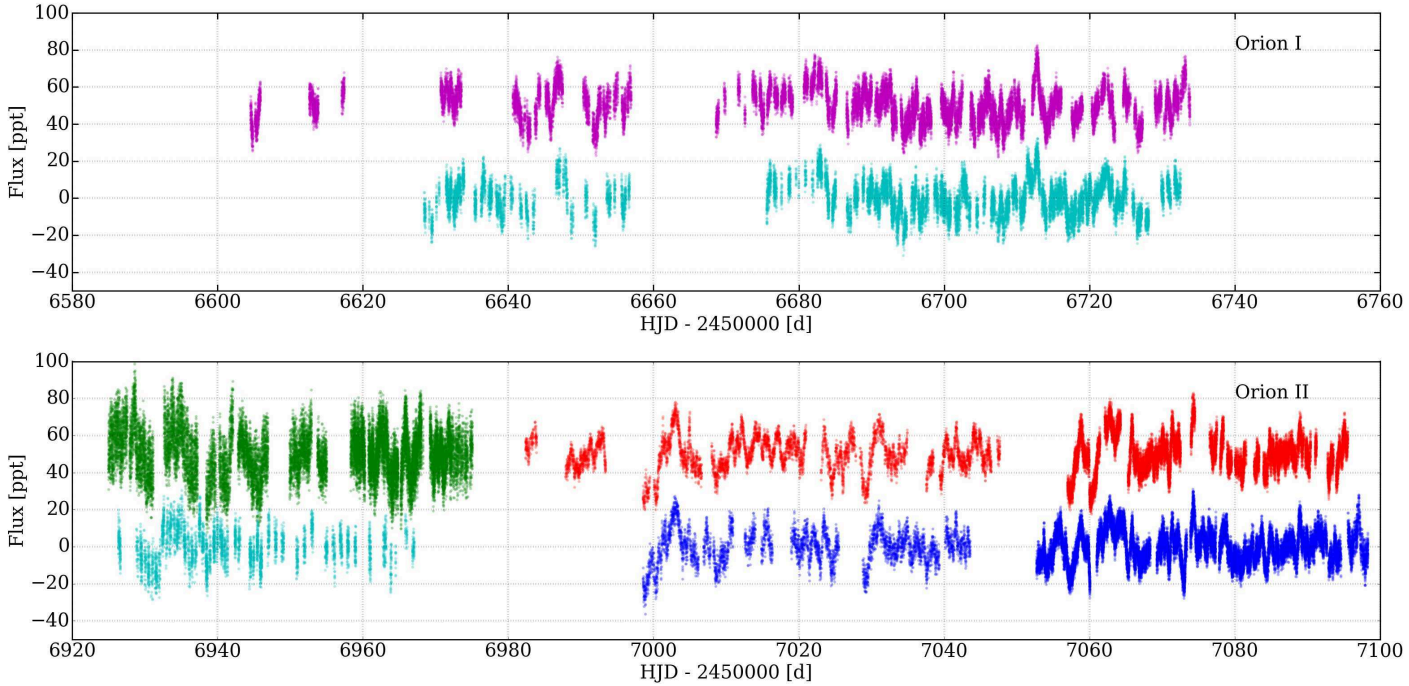

Figure 5.1: All available BRITE photometry for ζ Ori, fully detrended and corrected for instrumental effects for the Orion I (*top*) and Orion II (*bottom*) observing campaigns. The colour represents which nano-satellite of the BRITE-Constellation monitored ζ Ori: magenta for UBr, cyan for BAb, green for BTr, red for BHr, and blue for BLb. Observations taken by a red nano-satellite (UBr, BTr, BHr) have an offset of 50 ppt for increased visibility.

5.3.2 Data reduction summary

The extracted BRITE photometry reveals the presence of several instrumental effects. Therefore, we constructed a data processing package to remove spurious signals and correct any remaining trends with instrumental variables. This package is now publicly available on Github[2], and is based on our own experience with space-based photometry and the BRITE Data Analysis Cookbook[3] (see also Pigulski et al. 2016; Pigulski 2018).

The first step of the reduction process consists of a conversion of the timing of the measurements to mid-exposure times. This permits a clearer connection between BRITE light curves with different on-board image stackings. Next, we remove spurious signals, i.e., outliers, from both the metadata and the measured photometry, while accounting for their fluctuations with respect to time. The metadata provided with the BRITE data consists of the on-board CCD temperature $T_{\rm CCD}$, and the CCD centroid positions x_c and y_c. Once the data preparation is completed, we correct the BRITE photometry for the time- and temperature-dependent point spread function (PSF) by means of iterative B-spline fitting between flux and centroid positions within discrete subsets of the data based upon the temperature variability. Finally, we account and correct for any significant correlation between the flux and $T_{\rm CCD}$, x_c, y_c, and ϕ_s, the orbital phase of the satellite. For a more detailed description of the various decorrelation steps, we refer to Appendix B.1.

This data preparation and correction process was repeated for each data file provided. In addition to correcting for the instrumental signal, it also decreased the (instrumental) noise on the photometry, which we describe as the rms of the flux (see Eq. (4.1)). Finally, duty cycles for the different BRITE data sets were calculated, two of which have the most diagnostic value. One is the median duty cycle per satellite orbit $\mathrm{D_{orb}}$, which indicates the fraction of the satellite orbit spent taking observations. The other is $\mathrm{D_{sat}}$, which marks the portion of total satellite orbits used to successfully monitor the target.

The rms values of the raw and the corrected photometry, as well as the duty cycles for the corrected light curves, are provided in Table 5.2. The various corrected light curves are shown in Fig. 5.1. However, even after correction, differences remain in the data quality for ζ Ori between the various BRITE nano-satellites (Pablo et al. 2016).

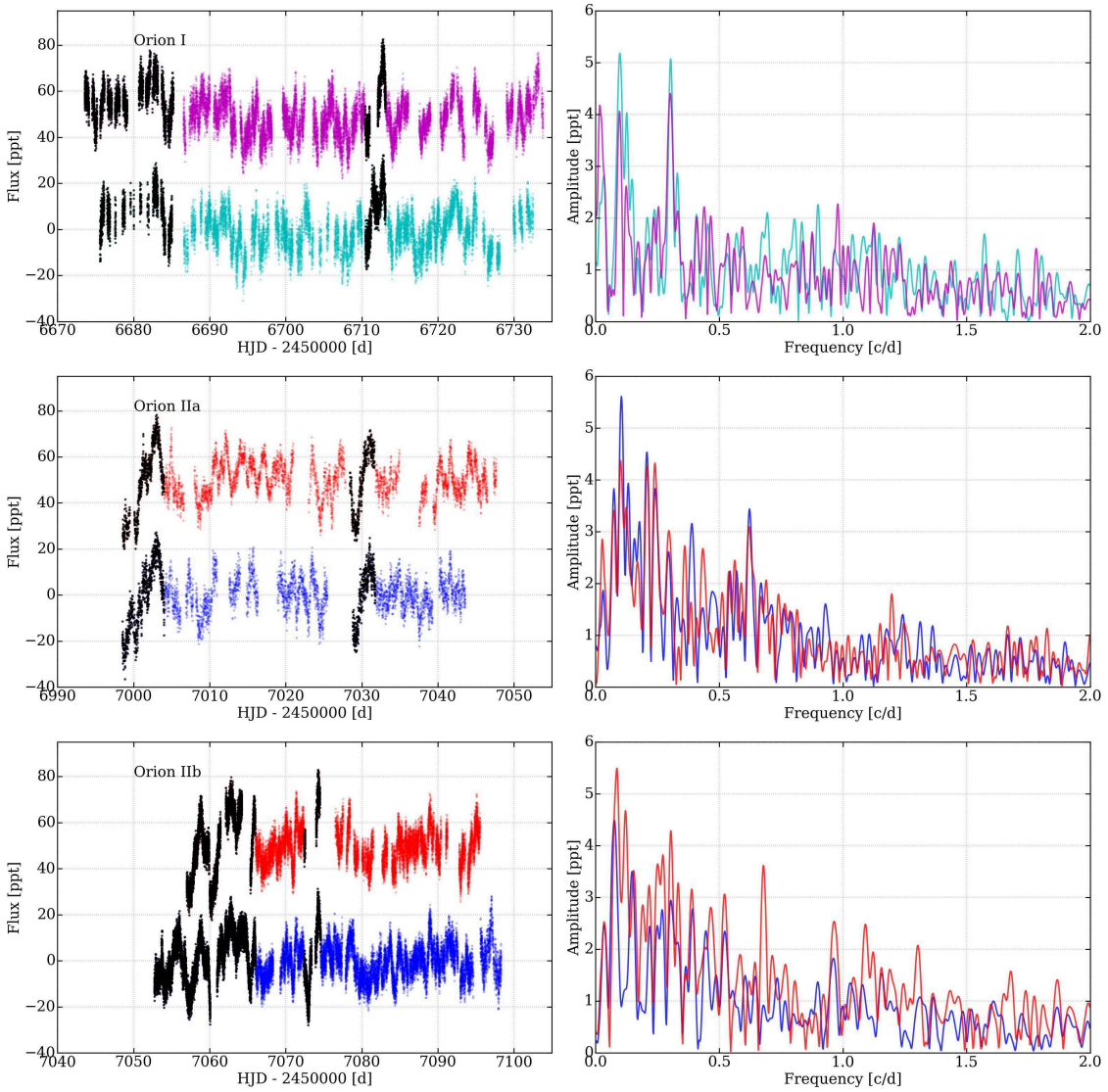

Figure 5.2: *Left*: BRITE photometry of ζ Ori during the three distinct epochs, used for the time series analysis. The colour represents which nano-satellite of the BRITE-Constellation monitored ζ Ori: magenta for UBr, cyan for BAb, red for BHr, and blue for BLb. The regions having non-periodic events, which were excluded for a dedicated analysis, are marked in black (see text). *Right:* Corresponding Lomb-Scargle periodograms of the full light curves. No significant periodic variability was found outside the region of 0 to $1\,\mathrm{d}^{-1}$.

Table 5.2: Diagnostics related to the BRITE observations of ζ Ori. For each setup, the cadence, start time and length of the data set, rms flux within an orbit passage before and after correction, median duty cycle per satellite orbit D_{orb}, and duty cycle of orbit passages where data were successfully taken D_{sat} are indicated. Duty cycles are determined for the corrected light curves. **Remarks**: *a*: Significant time length reduction due to strong outliers after processing. We report the length of the corrected photometry. *b*: Observations were discarded because of i) the strong irregular temperature variability, and ii) the mismatch between the aperture and the CCD sub-raster. *c*: Observations were not used due to strong charge-transfer-inefficiency effects.

Satellite	Run	Setup Set	Stacked Observ.	T_{start} [HJD-2450000]	Length [d]	rms_{raw} [ppt]	rms_{corr} [ppt]	D_{orb} [%]	D_{sat} [%]
BAb	Orion I	3	1	6628.43	74.01	1.76	0.86	11.7	32.2
BAb	Orion I	4	1	6702.51	29.99	1.37	0.72	13.5	66.5
UBr	Orion I	7	1	6603.61	129.28	1.00	0.64	14.2	40.6
BAb	Orion II	2	1	6926.35	10.75	1.85	1.50	6.0	50.6
BAb	Orion II	3	1	6937.37	7.55	1.36	1.16	5.8	40.6
BAb	Orion II	4	1	6945.39	21.64	3.81	1.08	6.7	21.3
BTr	Orion II	1	1	6924.72	47.14	1.85	1.42	16.6	70.8
BTr [a]	Orion II	2	3	6972.17	2.88	2.00	1.64	24.8	89.9
BTr [b]	Orion II	3	3	6987.61	7.99	1.51	–	–	–
BLb	Orion IIa	3	5	6998.52	45.04	1.45	1.19	12.1	75.8
BLb	Orion IIb	6	1	7052.75	45.53	1.20	0.55	17.0	89.2
BHr [a]	Orion II	2	3	6972.24	11.01	0.89	0.81	7.6	59.4
BHr	Orion IIa	5	5	6998.56	49.06	1.05	0.85	12.5	78.1
BHr [c]	Orion II	6	1	7049.56	7.30	12.22	–	–	–
BHr	Orion IIb	7	1	7056.99	38.53	1.10	0.52	18.8	67.7

5.3.3 Time series analysis of individual BRITE photometry

Once all the BRITE observations were corrected, we adopted two different techniques to perform a time series analysis to study the periodic photometric variability of ζ Ori. First, we performed an iterative prewhitening approach to determine the periodicity of the dominant fluctuations (see e.g., Degroote et al. 2009b). Second, we determined the time-frequency diagrams of the data sets, calculating the periodogram within a moving window with a given time window and time step. In this way, we studied the changes in both power and frequency of the periodic variability over time.

It became immediately apparent that the character of the variability of ζ Ori during the two BRITE observing campaigns is fairly different (see right panels of Fig. 5.2). Therefore, we studied the data from each campaign independently. In addition, we only considered the observations with the highest data quality (i.e., lowest rms flux variability; see Table 5.2) and the best duty cycle for the time series analysis. The considered Orion II data were further subdivided into two independent sub-sets, because of the inconsistent number of on-board stacked images, which caused issues in the weighting of the frequency analysis, and because of differences in the observed variability. Thus, we investigated data for three different epochs, namely Orion I, Orion IIa, and Orion IIb. For each epoch, we have a red and a blue photometric data set of almost equal length, which agree quite well once corrected for the instrumental effects. We show these six investigated light curves in Fig. 5.2, with their corresponding Lomb-Scargle periodograms indicating their periodic variability.

Each individual BRITE light curve underwent separate iterative prewhitening to determine the significant periodic variability, using a ten-times oversampled Lomb-Scargle periodogram (Lomb 1976; Scargle 1982). We calculated the significance of a frequency peak in the periodiogram using a S/N criterion. We considered it significant when a S/N larger than four was reached (Breger et al. 1993) within a frequency window of $4.0\,\mathrm{d}^{-1}$ after prewhitening. Such a large window was chosen because all detected variability is present in the low-frequency regime ($< 2.0\,\mathrm{d}^{-1}$) of the periodogram; therefore, the full window is not effectively used for the S/N calculation. Finally, only the frequency domain below $10\,\mathrm{d}^{-1}$ was considered for investigation because the satellite orbital frequency produces a forest of very strong alias peaks every 14.3 – $14.8\,\mathrm{d}^{-1}$; the exact value depends on which of the nano-satellite is used.

The extracted frequencies from the various light curves were examined via a pairwise comparison between the two colours of the same epoch, and also over

[2] `http://github.com/bbuysschaert/BRITE_decor`

[3] `http://brite.craq-astro.ca/doku.php?id=cookbook`

Table 5.3: Extracted frequencies for the BRITE photometry of . The first column of each data set presents the extracted frequencies for the full data set and the second column is for the non-periodic-event excluded photometry (these events are marked in black in Fig. 5.2). Uncertainties on the frequencies were determined using the Rayleigh frequency limit, and are thus conservative. All frequencies are given in cycles per day.

	Combined	Orion I				Orion IIa				Orion IIb			
Frequency		Blue		Red		Blue		Red		Blue		Red	
$\delta f_{\rm ray}$	0.003	0.02	0.02	0.02	0.02	0.02	0.03	0.02	0.02	0.02	0.03	0.03	0.03
$f_{\rm rot}$	0.147	0.15					0.14			0.15	0.16	0.16	
$2f_{\rm rot}$	0.292	0.30	0.30	0.30	0.30	0.30		0.30	0.30	0.31		0.30	0.31
$3f_{\rm rot}$								0.43	0.44	0.45		0.47	
$4f_{\rm rot}$		0.58		0.60		0.62	0.62	0.62	0.61		0.59		
$f_{\rm env}$	0.100	0.10	0.09	0.10	0.09	0.10		0.10				0.09	
$2f_{\rm env}$					0.21	0.21		0.21		0.22	0.22		
$4f_{\rm env}$				0.41		0.38	0.37			0.39			
$f_{\rm x}$	0.036	0.03		0.03			0.04	0.03	0.02			0.03	
$f_{\rm rot} + f_{\rm env}$	0.248	0.24				0.23	0.24	0.24					
$3f_{\rm rot} + f_{\rm env}$						0.54	0.54	0.54		0.53			
$4f_{\rm rot} + f_{\rm env}$									0.68			0.68	0.68
$f_{\rm env} + f_{\rm x}$	0.118	0.12	0.12	0.13		0.13							
$f_{\rm env} + f_{\rm x}$	0.130												
$f_{\rm env} + f_{\rm x}$	0.135												
$f_{\rm env} - f_{\rm x}$	0.068							0.07	0.07	0.08	0.06	0.07	0.06
$f_{\rm rot} - f_{\rm x}$	0.109												
$2f_{\rm rot} + f_{\rm x}$	0.320	0.33		0.34									
$2f_{\rm rot} - f_{\rm x}$	0.276							0.27	0.27	0.27		0.26	

the three observing epochs. When we did not retrieve the same frequency in at least two data sets, within the confidence interval, that frequency was discarded for the model light curve. We list the final set of extracted frequencies for each of the six data sets in Table 5.3. Because of the moderate duty cycle and because of the presence of gaps within the BRITE observations, we used the Rayleigh frequency limit for the confidence interval of the extracted frequencies. The conservative uncertainty for a frequency is thus $\delta f_{\rm ray} = 1/T$, where T is the total time span of the data.

While investigating the individual BRITE light curves, the phase-folded photometry with the dominant periodicities, and the residual light curves of the detailed frequency analysis, we identified peculiar time regions in the light curves. These regions stand out through their pronounced deviations to the iterative prewhitening model, as the observed brightness differs substantially from the model for the periodic variations. As such, we assumed that these time regions are influenced more strongly by non-periodic or non-cyclic variability than the remainder of the BRITE photometry. To define these time regions more accurately, we used an iterative approach to study the simultaneous blue and red residual light curves to the iterative prewhitening model. These new light curves were then subjected to a new detailed frequency analysis. We continued to exclude observations until no obvious deviations from the periodic variability model were noted. The final rejected time domains are marked in black in Fig. 5.2. An independent frequency analysis was then performed on these alternative light curves, for which we provide the deduced periodic variability in Table 5.3. The particular regions of more pronounced non-periodic variability are further discussed in Sect. 5.5.3.

In total, we extracted 16 different frequencies in the frequency domain $0 - 1\,{\rm d}^{-1}$ (see Table 5.3). The majority of these 16 frequencies are understood to originate from three independent frequencies, which construct through harmonics and simple frequency combinations most of the extracted periodic variability. The three independent frequencies are $f_{\rm rot} = 0.15 \pm 0.02\,{\rm d}^{-1}$, $f_{\rm env} = 0.10 \pm 0.02\,{\rm d}^{-1}$, and $f_{\rm x} = 0.04 \pm 0.02\,{\rm d}^{-1}$. We append this reasoning for each frequency in Table 5.3. All of these fundamental frequencies, and some particular ones, are discussed in more detail in Sects. 5.4 and 5.5.

The variations with the largest detected amplitudes correspond to $2f_{\rm rot}$ and $f_{\rm env}$ (see Table B.1), and are clearly distinguishable in the right panel of Fig. 5.2. Differences in amplitudes are noted between the various epochs. In particular $4f_{\rm rot}$, which is related to (the photospheric origin of the) DACs, is stronger in the red data. However, these differences are likely related to the non-periodic variability, since amplitudes are altered when the regions strongly affected by the non-periodic variability are excluded (marked in black in Fig. 5.2). Moreover, owing to the considerable amount of corrections applied, we expect our formal

uncertainty on the determined amplitude to be strongly underestimated. In addition, different responses between the various nano-satellites could occur. Hence, we refrain and warn against overinterpreting the possible differences in amplitude between the simultaneous red and blue photometry.

For each individual BRITE light curve we also investigated the time-frequency diagram. To be able to study the low-frequency regime of these periodograms, a sufficient frequency resolution needed to be achieved. Hence, the chosen time window spanned 20 days, corresponding to a frequency resolution of $0.05\,\mathrm{d}^{-1}$. The stepsize was set to be 4 d, because if it were too small it would smear out variability over time, while if too large it would hamper the interpretation of the observed variations. If the $\mathrm{D_{sat}}$ duty cycle of the data within the time window did not reach 50 %, no periodogram was determined for that time step. The calculated periodograms were ten-times oversampled Lomb-Scargle periodograms. We show the final time-frequency diagrams in Fig. 5.3, organized per observing epoch, including the regions marked in black in Fig. 5.2.

While the constraint on the duty cycle $\mathrm{D_{sat}}$ inhibits the determination of a Lomb-Scargle periodogram at each step, the analysis of the time-frequency diagrams is still able to confirm the differences between each studied epoch of BRITE photometry. These differences are compatible with the results from the iterative prewhitening approach. Moreover, within each epoch, the amplitude of prominent frequencies varies with respect to time, and often increases whenever regions with strong non-periodic variability occurred (marked in black in Fig. 5.2), indicating the presence of non-periodic photometric variability for ζ Ori. Typically, the most pronounced variability of the iterative prewhitening analysis can be linked to certain regions of the data set, with $2f_{\mathrm{rot}}$ the general exception, as indicated by the time-frequency diagrams (see Fig. 5.3). Minor shifts in frequency for certain variability can be noted with respect to time, yet still fall within the determined frequency resolution dictated by the adopted time window of the time-frequency diagrams (i.e., $\delta f_{\mathrm{ray}} = 0.05\,\mathrm{d}^{-1}$).

Once all periodic variability corresponding to the significant frequencies was extracted from the BRITE photometry of ζ Ori using the iterative prewhitening approach, we again calculated the residuals to this model. Although the periodogram of these residuals did not indicate any remaining significant periodic variability, the residual flux did still contain visible variability (see left panels of Fig. 5.4). When comparing the residuals of each light curve to the version of the same light curve with the earlier discarded regions, we noted that more variability remains within the discarded regions in the residuals of the original light curve. This, again, confirmed the need for the separate analysis, where the strongest non-periodic (and non-cyclic) variability was excluded.

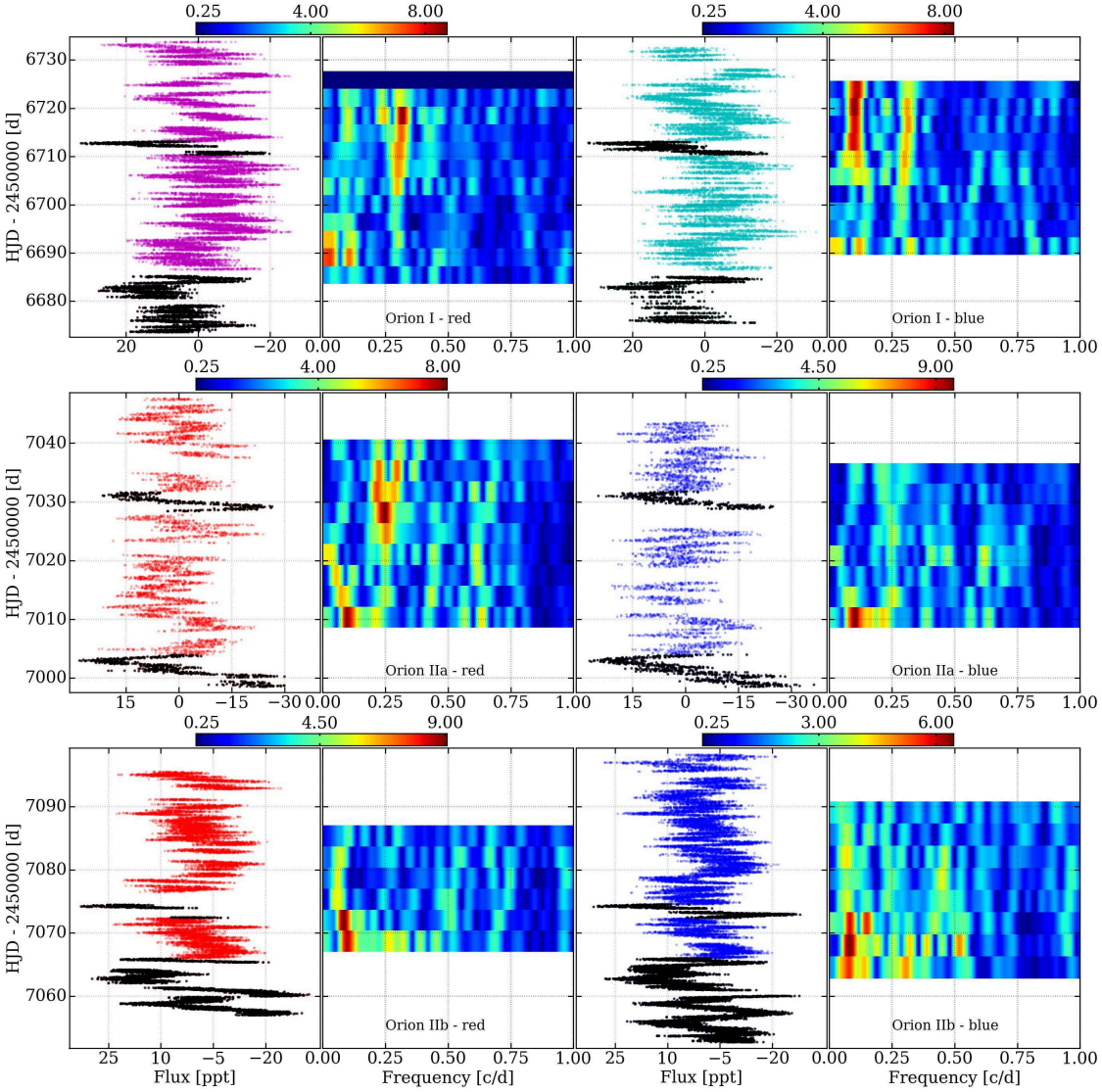

Figure 5.3: Studied light curves of ζ Ori during the various epochs (*first* and *third* panels from left), compared to their respective time-frequency diagrams (*second* and *fourth* panels). Observations are indicated by a colour representing the nano-satellite: magenta for UBr, cyan for BAb, red for BHr, and blue for BLb. The amplitude of a given frequency in the sliding Lomb-Scargle periodogram is given by the colour scale (in ppt; marked above each panel). The time-frequency diagrams were calculated with a time window of 20 d and a time step of 4 d.

5.3.4 Time series analysis of combined BRITE photometry

Aiming to increase the frequency resolution and decrease the noise level, we merged various BRITE observations to one long-baseline light curve. This

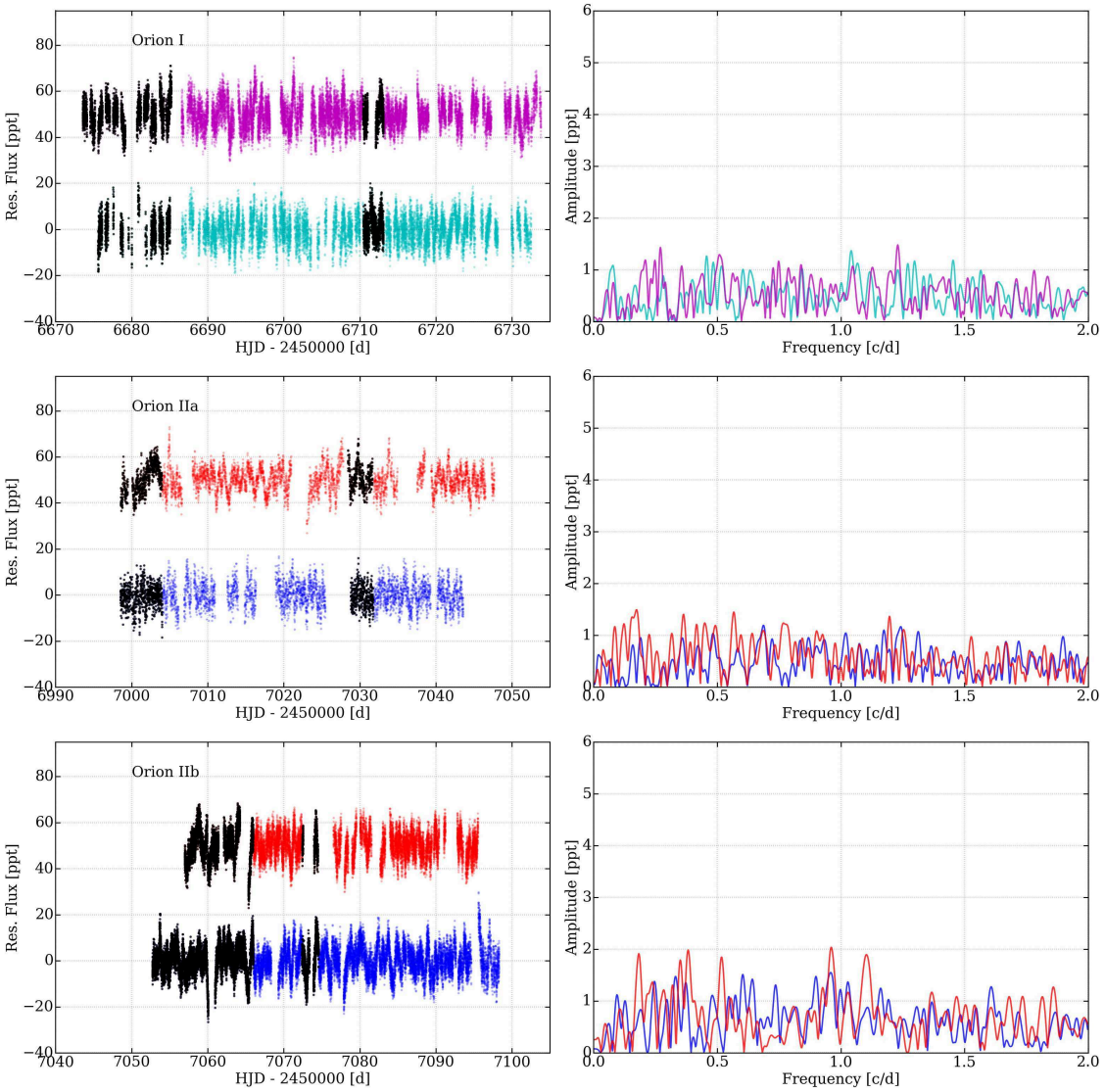

Figure 5.4: *Left*: Residual BRITE photometry of ζ Ori during three distinct epochs after all significant periodic variability was removed through iterative prewhitening. The same colour-coding as in Fig. 5.2 has been applied. *Right:* Corresponding Lomb-Scargle periodograms of the residual light curves, represented with the same scale as in Fig. 5.2. The flux residuals contain some remaining variability, which is not significant in the Lomb-Scargle periodogram.

was only possible with the increased comprehension of the individual BRITE photometry for ζ Ori. Studying the duty cycles and data quality of the respective BRITE light curves, we opted to include all red and blue data from all three epochs, i.e., Orion I, Orion IIa, and Orion IIb, as well as the BRITE Toronto-1 data (see Table 5.2). As a first step, we averaged and rebinned the observations to one single measurement per satellite orbit passage, permitting

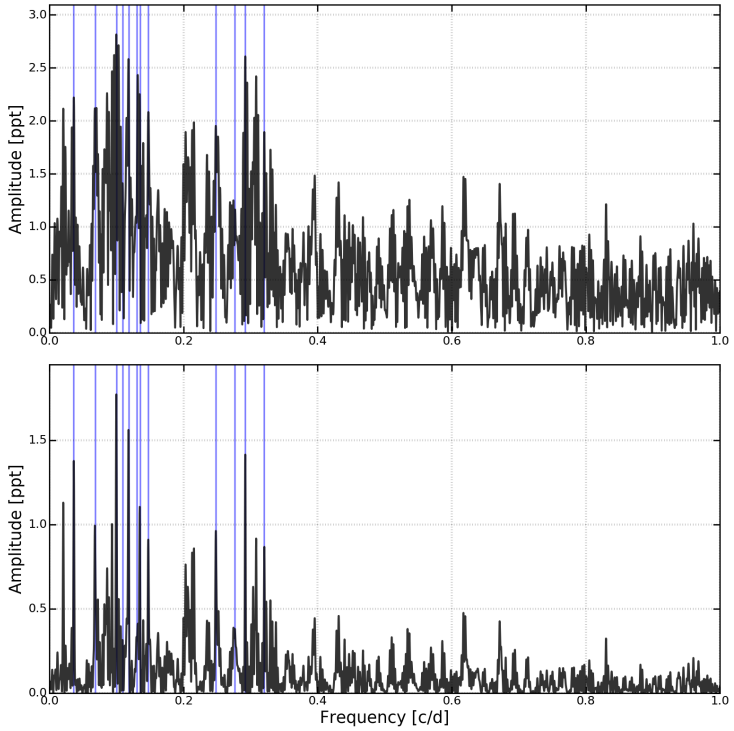

Figure 5.5: Different periodograms of the combined BRITE light curve for ζ Ori. *Top*: Regular Lomb-Scargle periodogram, significantly influenced by the spectral window of the combined data set. *Bottom*: CLEAN periodogram, using ten iterations and a gain of 0.5, showing the variability more clearly. Extracted significant periodic variability is marked in blue.

an easier connection between data sets with a different number of on-board image stackings. Next, we merged all these rebinned data, ignoring the colour information from the observations. Although minor differences between the two colours are present, as we show later, the individually studied light curves agree rather well. Moreover, we increased the duty cycle of the full light curve significantly by combining the simultaneous light curves, since minor differences for the orbital period of the BRITE nano-satellites lead to observations being taken at different times. This new, combined light curve spans 493.7 days, over both the Orion I and Orion II BRITE observing campaigns, with a 191.2 day time gap between the two parts.

Similar to the study of the individual BRITE data sets, we prewhitened significant periodic variability of the combined BRITE photometry of ζ Ori, using an iterative approach on a ten-times oversampled Lomb-Scargle periodogram. Again, we used the S/N criterion to determine the significance of a given frequency, using a frequency window of $2\,\mathrm{d}^{-1}$, and only investigated the frequency domain below $10\,\mathrm{d}^{-1}$. We show this periodogram in Fig. 5.5; we

also show a CLEAN periodogram (Roberts et al. 1987), because the large time gap in the data set influences the spectral window of the periodogram considerably. In total, we determined and extracted 12 significant frequencies, which are given in Table 5.3. Because of the large time gap present in the combined photometry, the Rayleigh frequency limit might be a too optimistic value for the frequency uncertainty. Therefore, we only used the time span when BRITE observations for ζ Ori Aa were actually taken (about 300 days). This leads to an altered frequency resolution of $\delta f_{\rm ray} = 1/T_{\rm obs} = 0.003\,{\rm d}^{-1}$.

Several of the 12 retrieved frequencies agree with values we determined from the individual data, albeit determined with a higher precision. However, some of the previously determined frequencies were not recovered, e.g., $0.60\,{\rm d}^{-1}$ and $0.68\,{\rm d}^{-1}$, since they appear to be much more prominent in the red data of Orion IIb, and fairly weak in the Orion I photometry. Thus, these became less significant when we combined the red and blue BRITE photometry of the various epochs.

5.4 CTIO 1.5 m/CHIRON échelle spectroscopy

5.4.1 Observations

ζ Ori A was observed 60 times between 2015 February 6 and 2015 March 16 (typically twice per night) with the CHIRON échelle spectrograph mounted on the CTIO 1.5-m telescope (Tokovinin et al. 2013). This fiber-fed spectrograph was used in slicer mode, yielding an effective resolving power of $R \sim 80000$, and covers the region from 4 590 to 7 600 Å. All spectra were corrected for bias and flat-field effects and wavelength calibrated through the CHIRON pipeline. Each visit consisted of two consecutive spectra with an individual exposure time of 8 seconds. These extracted spectra were combined into a single spectrum, resulting in individual visits having a S/N per resolving element of at least 75 in the continuum near Hα. The spectra were blaze-corrected and normalized to a unity continuum. Several telluric features are present in the Hα region. To remove these lines, we used a telluric template spectrum convolved to the instrumental response in the region surrounding Hα, as measured from the full width at half maximum of isolated H_2O lines. The depth of the template lines was adjusted interactively until the residual spectrum was smooth. A log of the different spectroscopic observations is given in Table B.4.

The fiber going to CHIRON has a diameter of 2.7 arcsec on the sky, which is sufficiently small to exclude ζ Ori B, which is currently ~ 2.4 arcsec away. the nearby H II regions are excluded during the observations. Therefore, the

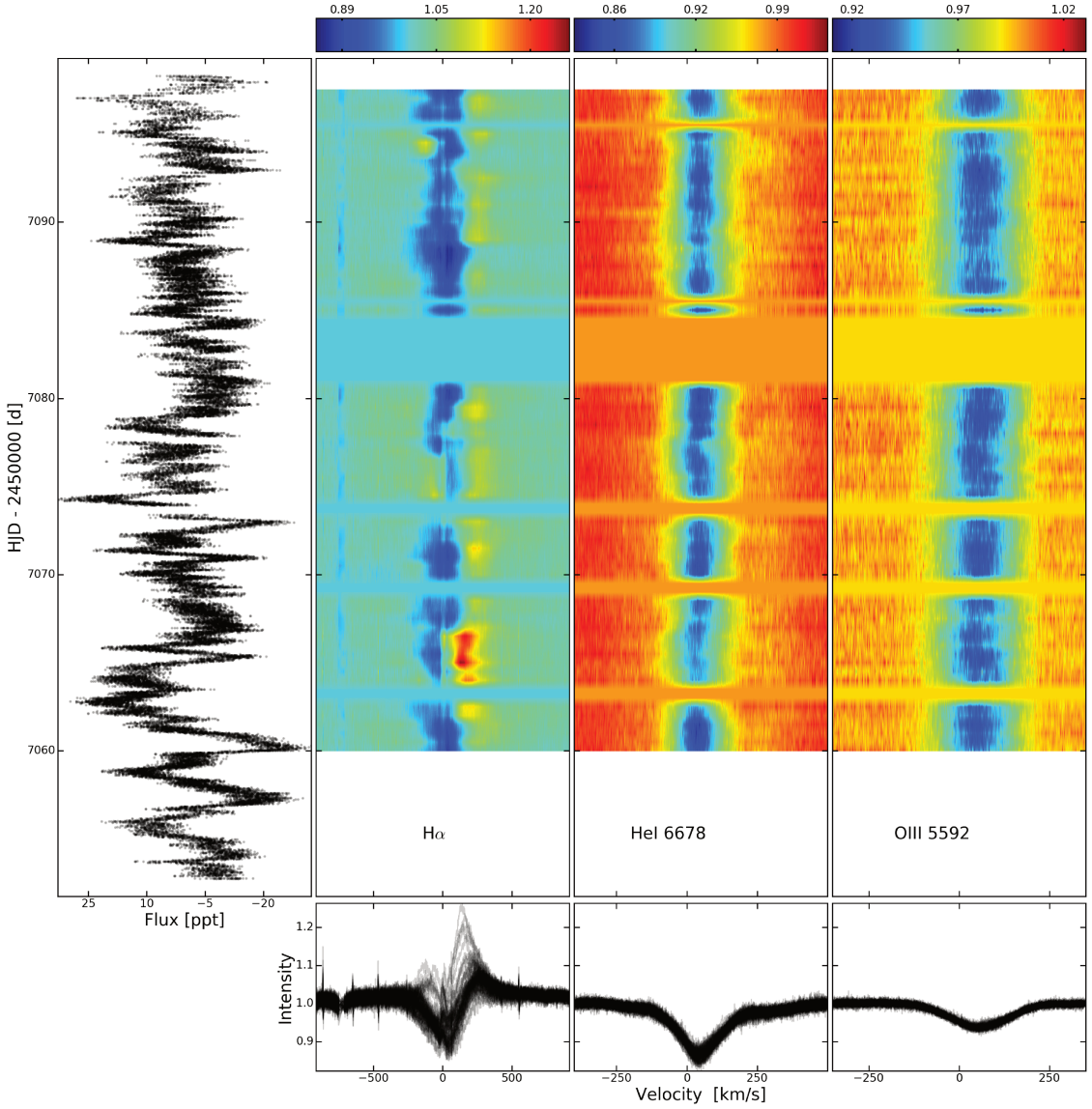

Figure 5.6: Comparison between the simultaneous CHIRON spectroscopy and the BRITE photometry during the Orion IIb campaign. *Left*: Superimposed red and blue BRITE photometry during the Orion IIb campaign. *Right*: Dynamical representation of different lines from the CHIRON spectroscopy taken simultaneously with the Orion IIb BRITE campaign. *Bottom*: Overlayed profiles of the spectroscopic lines.

CHIRON data only contain spectral features of ζ Ori Aa and ζ Ori Ab, albeit with different contributions. The short time span and especially the quality of the CHIRON data leads to a very uncertain spectral disentangling. Including archival spectroscopy to cover the full (inner) orbit would most likely only add to that uncertainty because of differences in the optical design of the instruments.

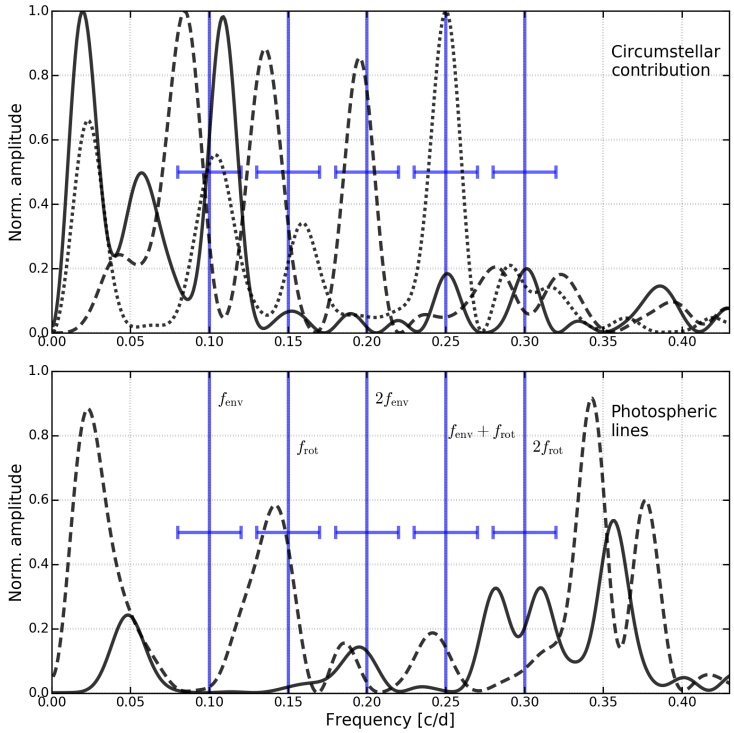

Figure 5.7: CLEAN periodograms for EWs of various spectroscopic lines. *Top*: Periodograms for lines being influenced by the circumstellar environment (solid - Hα; dashed - He I 6678.2 Å; dotted - He I 4921.9 Å). *Bottom*: Periodograms for purely photospheric lines (solid - O III 5592.3 Å; dashed - C IV 5801.3 Å). Dominant frequencies found in the individual BRITE photometry are marked in blue (from left to right: $f_{\rm env}$, $f_{\rm rot}$, $2f_{\rm env}$, $f_{\rm env} + f_{\rm rot}$, and $2f_{\rm rot}$).

In the remainder of this paper, we consider that any spectral variability in the studied frequency regime originates from the magnetic supergiant ζ Ori Aa, first because the short time span of the CHIRON data does not contain significant radial velocity variations from the binary motions, and because ζ Ori Ab is fainter, leading to a respective contribution of at most 10 % (as noted from earlier spectral disentangling attempts by Blazère et al. 2015), so that any mild spectral variability in ζ Ori Ab will have an effect comparable to the noise level.

5.4.2 Analysis of the Hα spectra and He I lines

We limited the investigation of the spectral lines with a circumstellar contribution (i.e., in the near-vicinity around the star) to Hα, which is the Balmer line most influenced by the circumstellar environment, and two of the strongest He I lines, i.e., He I 6678.2 Å and He I 4921.9 Å.

In Fig. 5.6, we show the dynamical representation of the Hα and He I 6678.2 Å lines and compare them to the simultaneous BRITE photometry of the Orion IIb epoch. As expected for a massive star, these lines vary with time, and the variation is most pronounced for the P Cygni profile of Hα. To study the periodic component of this variability, we measured the net equivalent width (EW) of the lines. For Hα we integrated over both the absorption and emission features. The integration limits for the measurements spanned from $v = -1000$ to $1000\,\mathrm{km\,s^{-1}}$ for Hα, and was typically from $v = -500$ to $500\,\mathrm{km\,s^{-1}}$ for the He I lines, with v being the radial velocity. Next, we calculated and investigated the periodograms of the EWs to determine the most dominant periodic behavior. Since the data were taken from Earth and have limited coverage, they have an unfavorable spectral window. Therefore, we resorted to CLEAN periodograms, since these limit the influence by the spectral window, using ten iterations, a gain of 0.5, and ten times oversampling. Only a limited frequency regime from 0 to $0.5\,\mathrm{d^{-1}}$ was investigated, because of the presence of very strong $1\,\mathrm{d^{-1}}$ aliasing effects and a strong reflection effects. These normalized periodograms of the EW are shown in the top panel of Fig. 5.7.

The scarce sampling of the data did not permit a detailed frequency extraction and analysis. Instead, we compared the periodogram with that of the BRITE photometry to determine which known frequencies are needed to explain the variability of the spectral lines. For all lines, we retrieved prominent variability at $0.09 - 0.11 \pm 0.03\,\mathrm{d^{-1}}$, corresponding to f_{env}. In addition, the EWs of the He I lines also exhibit fluctuations interpreted as the rotation at f_{rot}, while we only marginally retrieve this variability for Hα. Different combinations between independent frequencies are again observed, similar to the BRITE photometry. We refrain from further interpreting the power below $0.05\,\mathrm{d^{-1}}$ in Fig. 5.7, because additional testing showed that these amplitudes are severely altered by the upper frequency limit of the CLEAN routine. Increasing this upper limit decreases the power below $0.05\,\mathrm{d^{-1}}$, by moving it towards the $\sim 1\,\mathrm{d^{-1}}$ area, indicating the uncertain origin and nature of this variability and possibly influenced by the CLEAN routines. Finally, the power around $0.32 - 0.38\,\mathrm{d^{-1}}$ should be treated with care, since it is likely a combination of reflections of power in the $0.60 - 0.68\,\mathrm{d^{-1}}$ region around the $1\,\mathrm{d^{-1}}$ alias, and variations with $2f_{\mathrm{rot}}$.

5.4.3 Analysis of photospheric lines

Following Bouret et al. (2008) and Martins et al. (2015), we selected O III 5592.3 Å and C IV 5801.3 Å as photospheric absorption lines for further investigation, because they are not influenced (or only weakly) by the stellar winds and the circumstellar environment. The same method as in Sect. 5.4.2

was used to study the periodic variations of the EW of these lines, which was typically determined in the velocity region spanning $v = -400$ to $400\,\mathrm{km\,s^{-1}}$. We show the normalized determined CLEAN periodograms for these lines in the bottom panel of Fig. 5.7.

The most striking result for the periodograms of the purely photospheric lines is the strong difference with their corresponding periodograms of the Hα and He I lines. Indeed, the frequency region around f_{env} appears to be absent of any significant power for the purely photospheric lines. Instead, the strongest power is present below $0.05\,\mathrm{d^{-1}}$ and in the $0.32 - 0.38\,\mathrm{d^{-1}}$ region, which should be treated with care, similar to the periodograms for the lines with a circumstellar contribution. Some power around f_{rot} is also present for the C IV line.

5.5 Discussion

According to the V magnitudes determined by Hummel et al. (2013) for all three components, and their similar temperature of about 29000 K, we deduce that 77 % of the received flux in the BRITE photometry originates from ζ Ori Aa, 10 % from ζ Ori Ab, and 13 % from ζ Ori B. These values are compatible with the contribution of ζ Ori Ab to the Narval data, as determined from the spectral disentangling by Blazère et al. (2015). Therefore, throughout the discussion of the extracted frequencies from the BRITE photometry, we expect that all detected variability is caused by the magnetic supergiant ζ Ori Aa and its circumstellar environment. In the same way, variations observed in the CHIRON spectroscopy are likely related to ζ Ori Aa (see Sect. 5.4.1). Moreover, the possible high-degree β Cep pulsations of the B component (Hummel et al. 2013) would fall in a different frequency regime ($> 2\,\mathrm{d^{-1}}$) than that of the currently determined periodic variability. In addition, high-degree pulsation modes are not often visible in photometry due to partial cancellation effects. Yet, it cannot be fully excluded that strong variability in ζ Ori Ab or ζ Ori B could produce weak frequency peaks in the data presented here.

5.5.1 Rotation

In each and every studied BRITE light curve, we determined periodic variability related to half the literature rotation period, corresponding to a frequency of $0.30 \pm 0.02\,\mathrm{d^{-1}}$ (see Table 5.3). However, the amplitude corresponding to this variation differs from one epoch to the next, most likely due to non-periodic photometric events happening in the light curve altering the determined amplitudes of the periodic variability. Excluding the regions of the light curve

where the non-periodic signals occur the strongest has no considerable effect on the extraction of this frequency: we still recover it for four out of six light curves. The only exception is the blue Orion II data. Using the combined BRITE photometry, we retrieve a similar frequency: $0.292 \pm 0.003\,\mathrm{d}^{-1}$.

The presence of photometric variability with exactly half the rotation period is often observed for hot or massive magnetic stars (e.g., σ Ori E; Oksala et al. 2015b), and is related to the dipolar structure of the large-scale magnetic field, coming into and leaving the observer's line of sight. Indeed, the conditions at the magnetic poles are fairly different from the rest of the star, both at the stellar surface and in its very close circumstellar proximity. It was not possible to accurately verify the phase difference between the rotational modulation of the BRITE photometry of ζ Ori Aa and the longitudinal field measurements of Blazère et al. (2015) because of the substantial errorbar on the derived rotation period.

In addition to the frequency corresponding to half of the rotation period, we also extracted f_{rot}, $3f_{\mathrm{rot}}$, or $4f_{\mathrm{rot}}$ for some of the BRITE light curves. Of these, the anomalous variability is related to $3f_{\mathrm{rot}}$, as it would indicate the presence of three surface inhomogeneities. Such a geometrical magnetic configuration is considered highly unlikely. Yet, a strong bias to favor a small number of (equidistant) surface inhomogeneities exists: the effect of more than a few individual inhomogeneities on the stellar surface of ζ Ori Aa on the light curve would be merged, effectively masking their presence and mimicking the variability of only a few inhomogeneities. However, detailed modelling of the location of the surface inhomogeneities is currently beyond the scope of this work, since it requires a higher precision of P_{rot} that is not achievable with the current data set. We discuss the fourth harmonic in more detail in Sect. 5.5.2, as it is likely related to DACs.

Combining measurements of the frequencies believed to be f_{rot} and its higher harmonics from the individual BRITE photometry to increase the precision, we obtain $P_{\mathrm{rot}} = 6.65 \pm 0.28\,\mathrm{d}$. Doing this for the combined BRITE photometry, yields $P_{\mathrm{rot}} = 6.82 \pm 0.19\,\mathrm{d}$. These values are consistent within the error bars with the rotation period of Blazère et al. (2015, i.e., $6.83 \pm 0.08\,\mathrm{d}$). A more precise measurement of the rotation period will be difficult without a detailed understanding of the variability of the supergiant ζ Ori Aa, in particular, of its circumstellar environment.

Because of the limited temporal resolution of the spectroscopic data set, we could not perform a detailed frequency analysis of the spectroscopic variability to accurately determine the rotation period from spectroscopy.

5.5.2 DACs

Most of the studied BRITE photometry indicated that ζ Ori Aa is variable with $P_{\rm rot}/4$. This periodicity coincides with the DAC recurrence timescale derived by Kaper et al. (1999) for ζ Ori Aa. Indeed, our derived value of $t_{\rm rec} = 1.67 \pm 0.06$ d agrees with the literature value of 1.6 ± 0.2 d (i.e., $f_{\rm rec} = 0.625 \pm 0.075\,{\rm d}^{-1}$). During our analysis, both the time-frequency diagrams and the prewhitening of the individual BRITE light curves indicated that the amplitude of this frequency varies with time (e.g., Table B.1 and Fig. 5.3). Under the assumption that DACs are related to surface inhomogeneities, the description of four (transient) enhanced brightness regions evenly distributed in longitude over the stellar surface is the most likely. However, with the current knowledge of this object, we were unable to corroborate or disprove the exact mechanism that creates the hypothetical enhanced brightness regions leading to the CIRs. Higher quality observations, having a high duty cycle and long baseline, are needed to explore the origin of these inhomogeneities and study their stability over time.

Variability with a similar timescale seems to be present in the studied spectroscopic lines. Yet, the limited cadence and poor spectral window, mainly related to reflection effects over $1\,{\rm d}^{-1}$, did not permit us to exclude a purely instrumental origin.

Finally, red Orion IIb data show evidence of photometric brightness variations with a frequency of $0.68 \pm 0.02\,{\rm d}^{-1}$. We consider this power to be related to the four surface inhomogeneities, yet slightly distorted to a higher frequency because of a frequency combination with $f_{\rm env}$. This timescale also matches, within the uncertainty, the Hipparcos periodicity of 1.407 d discussed by Morel et al. (2004).

5.5.3 Circumstellar environment

Comparing the variability of the CHIRON spectroscopy with that of the BRITE photometry results in a particular agreement and discrepancy. Both the BRITE photometry and spectroscopic lines with a circumstellar contribution (i.e., Hα and He I lines) show variability with $f_{\rm env} = 0.100 \pm 0.003\,{\rm d}^{-1}$, while it is strikingly absent in the photospheric lines. Therefore, we conclude that the BRITE photometry contains a contribution from the circumstellar environment of ζ Ori Aa, and that this environment is periodically (or possibly cyclically) variable with $f_{\rm env}$, and additionally indicates non-periodic variability. Studying the individual BRITE light curves without these strong non-periodic events, we no longer recover this frequency for the Orion IIa and Orion IIb data. We therefore consider these parts of the BRITE photometry to be dominated by

non-periodic variability originating at the circumstellar environment. Figure 5.6 indeed shows that these regions of the light curve are correlated with strong changes in shape and power of the P Cygni profile of the Hα line, which probes the variability within the circumstellar environment.

We deem it therefore probable that the circumstellar environment causes the observed differences in variability between the three BRITE epochs, either by decreasing the detected flux by obscuring parts of the stellar surface or temporarily increasing the brightness. An example of the effect of such an increase in brightness can be seen in the Orion I data, where the rotational variability with $2f_{\rm rot}$, coming from ζ Ori Aa itself, is still visible during the event (i.e., top left panel of Fig. 5.2 at HJD = 2456714).

Since ζ Ori Aa hosts a large-scale magnetic field at the stellar surface, the circumstellar environment would also be influenced by it. Previous studies have shown that the dynamical magnetosphere of ζ Ori Aa is rather weak (Blazère et al. 2015). We do not find strong evidence for rotational variability in Hα, compatible with a very weak or absent magnetosphere. If the magnetosphere were causing periodic photometric and spectroscopic variability, it would relate with $f_{\rm rot}$ instead of $f_{\rm env}$. Thus, the magnetosphere is unlikely to produce the found variability.

Periodic (increased) mass loss could also lead to periodic circumstellar variability. Various processes could lead to increased mass loss, yet only a limited amount would do this in a periodic manner. Beating effects between the frequencies of non-radial pulsations would be such a process, similar to the mass-loss mechanism proposed for the Be phenomenon (e.g., Rivinius et al. 1998, 2003; Neiner et al. 2013; Baade et al. 2016). However, we did not detect any stellar pulsations for ζ Ori Aa.

5.5.4 Remaining variability

In addition to variability related to the stellar rotation or the circumstellar environment, we also extracted several other frequencies. These do not seem to fall in a particular frequency domain with a straightforward interpretation, and show some sort of relation through (simple) combinations. We investigated these frequencies and chose $f_{\rm x} = 0.036 \pm 0.003\,{\rm d}^{-1}$ to be an independent frequency, because it explains the majority of the remaining frequencies. However, since the origin of this periodic variability is not understood, a different frequency of the combinations might be the proper, independent one. Nevertheless, to produce frequency combinations, the fundamental frequencies (and their combinations) need to originate from the same component, i.e., ζ Ori Aa. Therefore, our assumption that all variations arise from ζ Ori Aa is likely correct.

Since ζ Ori Aa is undergoing a rather turbulent stage of its evolution, it is also possible that parts of the non-periodic variability are produced by the star itself. A possible mechanism could then be related to the subsurface convective layer. However, the highly variable Hα line, used as one of the diagnostics for the circumstellar environment, does not seem to support this. Additional (spectroscopic) measurements are needed to find observational support for the origin of the non-periodic photometric variability.

5.6 Summary and conclusions

We performed a detailed time series analysis on the individual red and blue BRITE photometry of the magnetic, massive supergiant ζ Ori Aa, which we subdivided into three distinct epochs based on both observational evidence and data characteristics. In addition, we also performed a frequency analysis of the combined BRITE photometry, ignoring the colour information of the observations. In total, we extracted 16 different frequencies, which were present in at least two of the six studied light curves. These 16 frequencies can be explained by three independent frequencies, their higher harmonics or combinations. For two of the independent frequencies, we understand their stellar origin, stellar rotation ($f_{\rm rot}$) and the cirumstellar environment ($f_{\rm env}$). A third independent frequency ($f_{\rm x}$) is necessary to explain the remaining variability as frequency combinations.

One family of frequencies corresponds to the rotation period of ζ Ori Aa, most likely related to two or four bright surface inhomogeneities, evenly distributed in longitude over the stellar surface. Therefore, we were able to determine the rotation period, $P_{\rm rot} = 6.82 \pm 0.19\,{\rm d}$, compatible with the literature value of $6.83 \pm 0.08\,{\rm d}$ (Blazère et al. 2015), within the error bars. We cannot fully exclude that a large number of inhomogeneities is present at the stellar surface of ζ Ori Aa, mimicking a few (equidistant) inhomogeneities. However, the presence of a dipolar magnetic field often implies a simple geometry for the surface inhomogeneities related to the magnetic poles.

The presence of the fourth harmonic of $f_{\rm rot}$ supports the recurrence timescale for DACs, $t_{\rm rec} = 1.67 \pm 0.06\,{\rm d}$, consistent with that of Kaper et al. (1999), i.e., four CIRs are related to enhanced brightness regions evenly distributed in longitude. The mechanism that creates and sustains these inhomogeneities is still unknown, a beating effect between the frequencies of non-radial pulsations or a quadrupolar component to the stable dipolar magnetic field being the preferred pathways. If they are created by a stable magnetic field, a significant quadrupolar component, marginally compatible with the results of Blazère et al.

(2015), is needed. Moreover, we did not detect any non-radial pulsations for ζ Ori Aa, making it impossible to corroborate this mechanism as the source for the four regions.

Thanks to the combination of the BRITE photometry and the simultaneous ground-based, high-resolution optical CHIRON spectroscopy of Hα and He I lines, we linked the 10.0 ± 0.3 d variability to the circumstellar environment. This period is more pronounced during certain regions of the BRITE light curves dominated by the variation of the circumstellar environment. In addition, it explains the noted differences between the three observing epochs during the two BRITE monitoring campaigns. This periodic or cyclic variability of the circumstellar environment is unlikely to be related to the weak magnetosphere of ζ Ori Aa since the confined magnetosphere variability would instead be related to the stellar rotation. Periodically enhanced mass loss similar to Be stars, through beating effects of non-radial pulsations, might be an alternative driving mechanism for the observed variability. Finally, the strong variability of the circumstellar environment might be an explanation for the discrepancies between the 2011–12 Narval spectropolarimety and the dipolar fit of Blazère et al. (2015).

For the presence of enhanced brightness regions, leading to DAC variability, and for periodic mass loss, explaining the circumstellar variability, a beating between non-radial pulsations is proposed as a driving mechanism. However, we do not identify pulsations in the BRITE photometry of ζ Ori Aa.

A high-cadence detailed UV and visual spectropolarimetric campaign, simultaneously with high-precision, long-baseline photometry will be necessary to fully unravel the origin of the variability of ζ Ori Aa, and to determine the possible effects on its circumstellar environment and its magnetic field. Only then, will it be possible to investigate ζ Ori Aa for possible non-radial stellar pulsations or gravity waves as found in the hot supergiants HD 188209 and HD 2905 from combined space-based photometry with long-term ground-based high-resolution optical spectroscopy.

Part III

Seismic modelling of a magnetic star

Chapter 6

Magnetic characterization of HD 43317

This chapter was originally published as

Magnetic characterization of the magnetic SPB/β Cep hybrid pulsator HD 43317

B. Buysschaert, C. Neiner, M. Briquet, and C. Aerts

Astronomy & Astrophysics, 2017, 605, A104 (16 pages)

Original abstract:

Large-scale magnetic fields at the surface of massive stars do not only influence the outer-most layers of the star, but also have consequences for the deep interior, only observationally accessible through asteroseismology. We performed a detailed characterization of the dipolar magnetic field at the surface of the B3.5V star HD 43317, a SPB/β Cep hybrid pulsator, by studying the rotationally modulated magnetic field of archival and new Narval spectropolarimetry. Additionally, we used a grid-based approach to compare the Zeeman signatures with model profiles. By studying the rotational modulation of the He lines in both the Narval and HARPS spectroscopy caused by co-rotating surface abundance inhomogeneities, we updated the rotation period to 0.897673(4) d. The inclination angle between the rotation axis and the observer's line of sight remains ill-defined, because of the low level of variability in Stokes V and deformations in the intensity profiles by stellar pulsation modes. The obliquity

angle between the rotation and magnetic axes is constrained to $\beta \in [67, 90]\,^{\circ}$, and the strength of the dipolar magnetic field is of the order of 1 kG to 1.5 kG. This magnetic field at the stellar surface is sufficiently strong to warrant a uniformly rotating radiative envelope, causing less convective core overshooting, which should be visible in future forward seismic modelling.

6.1 The pulsating magnetic hot star HD 43317

HD 43317 has a B3.5V spectral type and has no detected binary companion (Pápics et al. 2012). Its chemical surface abundances agree with the solar abundances, but with some co-rotating He abundance spots at the stellar surface. By studying a ∼150 d CoRoT (Baglin et al. 2006) light curve, Pápics et al. (2012) detected gravity mode frequencies, making HD 43317 a SPB pulsator, with rotational modulation. Several of the detected pulsation frequencies fall into one of two frequency series with a constant period spacing of either 6339 s or 6380 s. The derived rotation period from the CoRoT photometry is 0.8969 ± 0.0053 d. Similar results were obtained by Pápics et al. (2012) from the detailed frequency analysis of selected spectral lines of simultaneous HARPS spectroscopy (Mayor et al. 2003), spanning approximately 25 d. High-frequency pulsation modes were detected in the selected Mg II 4481Å line, while the He I lines dominantly vary with twice the determined rotation frequency indicative of rotational modulation.

Since many of the extracted pulsation-mode frequencies from the CoRoT light curve fall below twice the deduced rotation frequency, these pulsation modes are unstable coherent internal gravito-inertial modes (Mathis et al. 2014, and references therein) possibly excited by the κ-mechanism, but perturbed by the Coriolis force, instead of regular gravity modes in a non-rotating non-magnetic star. Such modes, as well as internal gravity waves (IGWs) are highly efficient at transporting angular momentum to the stellar surface (e.g., Rogers & Glatzmaier 2005; Rogers et al. 2013; Townsend et al. 2018). On the other hand, convection-driven IGWs are linked to the stochastic motion by the convective plumes escaping the convective core (e.g., Goldreich & Kumar 1990; Samadi et al. 2010; Shiode et al. 2013; Mathis et al. 2014). Such stochastic IGWs have only recently been observed for massive stars (e.g Blomme et al. 2011; Neiner et al. 2012b; Aerts et al. 2017a; Simón-Díaz et al. 2017). In addition, it has become clear from *Kepler* data that gravito-inertial modes in B- and F-type pulsators with period spacings are dipole modes (Van Reeth et al. 2015; Pápics et al. 2017).

Savonije (2013) attempted to explain the detected pulsation-mode frequencies of HD 43317 detected with CoRoT as unstable oscillations in a rapidly rotating star using numerical simulations. Many of the high-visibility axisymmetric gravity modes fall in the correct frequency regime and nearly coincide with the observations by Pápics et al. (2012). However, these unstable modes are not able to explain the observed period spacings, making it difficult to corroborate the assumption of unstable oscillations. Moreover, during the analysis of Savonije (2013), HD 43317 was not yet known to host a large-scale magnetic field.

Following the detection of rotational modulation, especially for the He absorption lines, and the strong X-ray flux (Berghoefer et al. 1996), a spectropolarimetric monitoring campaign for HD 43317 was performed to look for the possible presence of a polarization signature due to a magnetic field. This anticipated magnetic field was detected by Briquet et al. (2013). Enforcing the rotation period found in the CoRoT light curve by Pápics et al. (2012) on the variation of the longitudinal field measurements provided a good sinusoidal fit with the rotation period and indicated a dipolar configuration for the magnetic field. The estimated field strength at the magnetic poles was about 1 kG. Less strong constraints were obtained on the orientation of the field. By using the inclination angle to the stellar rotation axis determined by Pápics et al. (2012), namely $i \in [20, 50]\,^\circ$, Briquet et al. (2013) obtained the obliquity angle of the magnetic field to the rotation axis $\beta \in [70, 86]\,^\circ$. These weak constraints are in part due to the limited rotation phase coverage and the long duration of the nightly averaged exposures of Briquet et al. (2013) with respect to the rotation phase. Finally, the authors did not find any rotational modulation of emission lines indicating the presence of a magnetosphere, but the determined value for the magnetic confinement parameter $\eta_\star$ implies that HD 43317 has a centrifugal magnetosphere.

We have taken additional spectropolarimetric observations of HD 43317 to increase the coverage over the rotation phase. The goal is to improve the observational constraints on the strength and orientation of the large-scale magnetic field. This updated characterization of the field will be used to perform detailed (magneto-)asteroseismic modelling in Chapter 7.

The obtained data, the studied observations, and the treatment thereof are discussed in Sect. 6.2. First, we investigated how strongly the stellar pulsation modes and the rotational modulation influenced the Narval spectropolarimetry, and what the possible implications are (Sect. 6.3). In addition, we used the rotational modulation to update the rotation period of HD 43317. Sections 6.4 and 6.5 are dedicated to the characterization of the large-scale magnetic field of HD 43317, by analyzing the longitudinal magnetic field and modelling the Zeeman signatures with synthetic profiles of an oblique dipolar field, respectively. The obtained results and their implications are discussed in Sect. 6.6 and

conclusions are summarized in Sect. 6.7.

6.2 Observations

6.2.1 Spectropolarimetry

To detect the Zeeman signature of the magnetic field of HD 43317, we have obtained spectropolarimetric observations with Narval (Aurière 2003) mounted at Télescope Bernard Lyot (TBL) at Pic du Midi in France. These observations measure the circular polarization (Stokes V), and span from 3 700 Å to 10 500 Å with an average resolution of ∼65 000. Standard settings were used, with bias, flat-field, and ThAr calibration images taken at both the beginning and end of each night. We combined these new data, taken between November 2015 and January 2016, with the publicly available Narval spectropolarimetry discussed in Briquet et al. (2013), obtained with the same settings between September 2012 and November 2012. Some of the earlier observations of Briquet et al. (2013) are single sequences of four sub-exposures with an exposure time of 1000 s per sub-exposure. Otherwise, the obtained spectropolarimetry consists of three consecutive sequences of four sub-exposures, each with an 800 s integration time. The full duration of an individual spectropolarimetric sequence was carefully tailored to avoid strong LPVs between the consecutive sub-exposures. In total 34 sequences are available for HD 43317, with an average S/N between 100 and 325. The complete overview of the data is given in Table 6.2.2.

All Narval data were reduced with the LIBRE-ESPRIT software (Donati et al. 1997), available at the TBL. A spectropolarimetric observation was deduced per sequence, as well as a spectroscopic measurement for each of the individual Narval sub-exposures. The spectropolarimetric data were rectified to unity continuum using interactive spline fitting tools with IRAF[1]. The spectroscopic observations were rectified and normalized per spectral order as in Pápics et al. (2012).

The obtained Narval spectropolarimetry forms the basis for the characterization of the large-scale magnetic field at the stellar surface of HD 43317 (Sect. 6.4).

[1]IRAF is distributed by the National Optical Astronomy Observatory,which is operated by the Association of Universities for Research in Astronomy (AURA) under a cooperative agreement with the National Science Foundation.

Table 6.1: Observing log of the Narval observations. The exposure time of the full sequence, as well as the mid-exposure HJD, are indicated. The rotation phase, $\phi_{\rm rot}$ is determined with $P_{\rm rot} = 0.897673$d and $T_0 = $ HJD 2456185.8380. The provided S/N is that of the LSD Stokes I profile calculated with various line masks. In addition, the magnetic detection status for each observation is indicated (DD = Definite Detection, MD = Marginal Detection, and ND = Non Detection). **Remarks**: *a*: These observations were used in Sect. 6.4.2 together with the rotation phase-binned measurements from Table 6.3 to fully cover the rotation period. *b*: This observation was excluded during the analysis, since two of the sub-exposures were particularly noisy, leading to issues in the corresponding Stokes V profile with a very low S/N.

ID	HJD [d]	$t_{\rm exp}$ [s]	$\phi_{\rm rot}$	all		He only		He excluded	
	-2450000			S/N	Detect.	S/N	Detect.	S/N	Detect.
1	6185.66197234	4×1000	0.803874	2067	DD	297	ND	1597	ND
2	6203.61791407	4×1000	0.806639	2075	DD	291	MD	1666	MD
3	6206.64674915	4×1000	0.180735	2111	DD	288	DD	1662	MD
4	6214.58370424	4×1000	0.022434	2032	ND	290	ND	1647	ND
5	6230.56793210	4×800	0.828727	2083	DD	288	DD	1650	MD
6	6230.60771309	4×800	0.873043	2052	DD	284	MD	1657	MD
7	6230.64747616	4×800	0.917338	2032	DD	280	MD	1654	MD
8	6232.54916364	4×800	0.035802	1972	MD	284	MD	1624	ND
9	6232.58891699	4×800	0.080087	2018	MD	284	ND	1634	MD
10	6232.62864977	4×800	0.124349	2012	DD	283	DD	1643	ND
11[a]	6244.56044152	4×800	0.416262	1964	MD	286	MD	1590	ND
12	6244.60021716	4×800	0.460572	2018	MD	286	ND	1620	ND
13	6244.64000450	4×800	0.504894	2050	MD	288	ND	1611	ND
14	6245.63552455	4×800	0.613895	1734	ND	287	ND	1454	ND
15	6245.67535221	4×800	0.658263	1703	ND	288	ND	1412	ND
16[a]	6245.71511288	4×800	0.702556	1753	ND	289	ND	1485	ND

Continued on next page

Table 6.1 – continued from previous page

17	6254.51437756	4×800	0.504861	1488	ND	275	ND	1277	MD
18	6254.55412207	4×800	0.549136	1959	MD	288	ND	1571	ND
19	6254.59394714	4×800	0.593501	1873	ND	287	ND	1510	ND
20	7326.61890886	4×800	0.820086	1991	MD	296	ND	1506	ND
21	7326.66079329	4×800	0.866745	1987	MD	294	ND	1515	MD
22	7326.70220134	4×800	0.912874	1906	ND	292	ND	1468	DD
23	7337.61241188	4×800	0.066754	1914	MD	276	MD	1458	MD
24	7337.65343636	4×800	0.112455	1911	DD	275	MD	1461	ND
25	7337.70094841	4×800	0.165383	1929	MD	281	MD	1488	ND
26^a	7339.61360976	4×800	0.296071	1938	DD	278	MD	1541	ND
27^a	7339.65460177	4×800	0.341736	1872	ND	273	ND	1482	ND
28^b	7339.69683246	4×800	0.388781	1401	ND	247	ND	1475	ND
29	7412.46045929	4×800	0.446835	1907	MD	281	ND	1513	ND
30	7412.50162638	4×800	0.492695	1934	ND	287	ND	1536	ND
31	7412.54282594	4×800	0.538591	1927	ND	292	ND	1513	MD
32	7413.45749773	4×800	0.557527	1923	MD	285	MD	1554	ND
33	7413.49866839	4×800	0.603391	1864	ND	290	ND	1511	ND
34	7413.53974771	4×800	0.649153	1942	MD	293	ND	1558	ND

6.2.2 Spectroscopy

We also downloaded the publicly available and fully reduced HARPS spectroscopy (Mayor et al. 2003) of HD 43317, taken in the 'EGGS' configuration with the ESO 3.6-m telescope in La Silla in Chile. The HARPS spectra were acquired within the framework of the ground-based observations of CoRoT asteroseismic targets and are available in the SISMA database (Rainer et al. 2016). These observations cover the wavelength range 3 780 – 6 910 Å with a resolving power of about 80 000. The exposure times of the HARPS spectroscopy vary between 240 and 600 s, leading to an average S/N between 150 and 300. In total, 191 measurements were obtained, taken over a time span of 25 days in December 2009. These observations were rectified and normalized to unity continuum using the same tools as for the Narval spectroscopy. However, this time, the normalization process was performed on the complete wavelength range, because the consecutive spectral orders were accurately merged.

The Narval and HARPS spectroscopic data sets were used to study the LPVs of several spectral lines in Sect. 6.3.

6.3 Line profile analysis

6.3.1 Line profile variability

As discussed by Pápics et al. (2012), HD 43317 shows obvious periodic LPVs. These variations are in part due to the stellar pulsation modes and in part due to the rotational modulation through co-rotating surface abundance inhomogeneities. We selected both the Mg II 4481Å and the He I 6678Å lines, similarly to Pápics et al. (2012), to investigate the stellar pulsation modes and the rotational modulation, respectively.

The left panel of Fig. 6.1 shows the individual and average line profiles for each sequence for the Mg II 4481Å line, organized by rotation phase (determined in Sect. 6.3.2). From this visualization, we note that a few sub-exposures exhibit mild variations during a given polarimetric sequence. However, for almost all observations, these effects of the LPVs are comparable to the noise level, with intensity changes only up to 1 %.

Comparing the mean profiles for various sequences clearly shows the variability of the star. One sequence taken on November 12, 2015 shows a poor S/N. We have excluded this sequence for the remainder of the analyses (and Fig. 6.1). Similar results on the extent of the LPVs during each sub-exposure were obtained

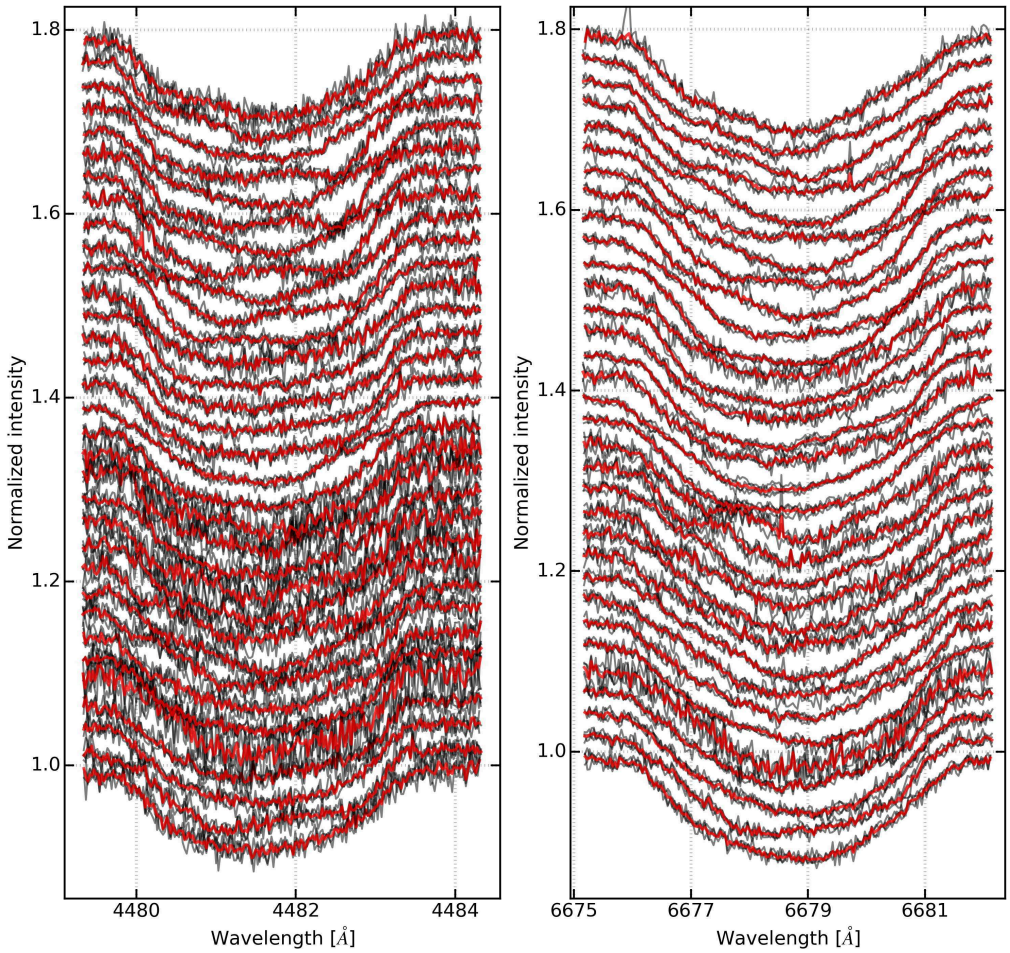

Figure 6.1: Profiles of the Mg II 4481Å (*left*) and He I 6678Å (*right*) lines for each Narval spectropolarimetric sequence in red (for which the four individual sub-exposures are given in black). The profiles are organized according to rotation phase, with a constant offset (independent of the phase difference) for visibility.

when comparing the mean profiles for the He I 6678Å line, given in the right panel of Fig. 6.1.

Because the stellar pulsation periods and the rotation period are expected to remain constant over the time span of a decade, we performed a detailed frequency analysis on the LPVs of the full Narval data set. For this analysis, we used the FAMIAS software package (Zima 2008) and determined the discrete Fourier periodogram for the pixel-by-pixel method (e.g., Mantegazza 2000). FAMIAS computes the discrete Fourier periodogram at each velocity step within the absorption line and averages this to a mean periodogram capturing the periodic LPVs. These discrete Fourier periodograms are shown in Fig. 6.2

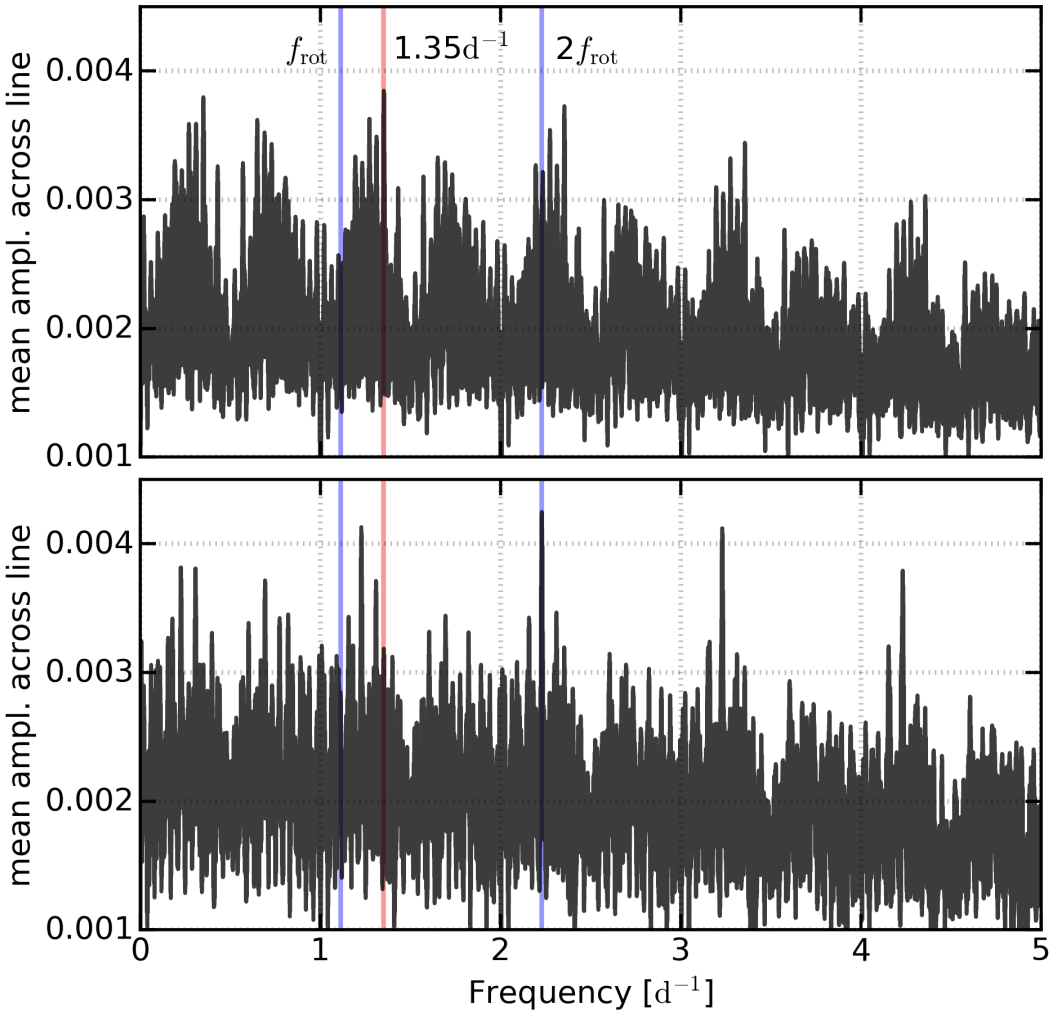

Figure 6.2: Mean discrete Fourier periodograms over the full line profile variations for the Mg II 4481Å (*top*) and the He I 6678Å (*bottom*) absorption lines in the Narval spectroscopy, determined with the pixel-by-pixel method. The rotation frequency and the second harmonic of the rotation frequency are indicated in blue. The found pulsation-mode frequency in the Mg II line is indicated in red. Strong $1\,\mathrm{d}^{-1}$ aliasing frequency peaks are present in the periodograms.

for both the Mg II 4481Å and He I 6678Å lines. For the Mg II 4481Å line, we retrieved variability with the known pulsation mode at $f = 1.35\,\mathrm{d}^{-1}$ from Pápics et al. (2012). However, the amplitude of the frequency did not pass the S/N threshold of four, calculated over a $1\,\mathrm{d}^{-1}$ frequency domain, following the typical S/N criterion for significance used during detailed frequency extractions (Breger et al. 1993). For the He I 6678Å line, we recovered the known rotational modulation with $2f_{\rm rot} \approx 2.23\,\mathrm{d}^{-1}$, which was determined to be significant

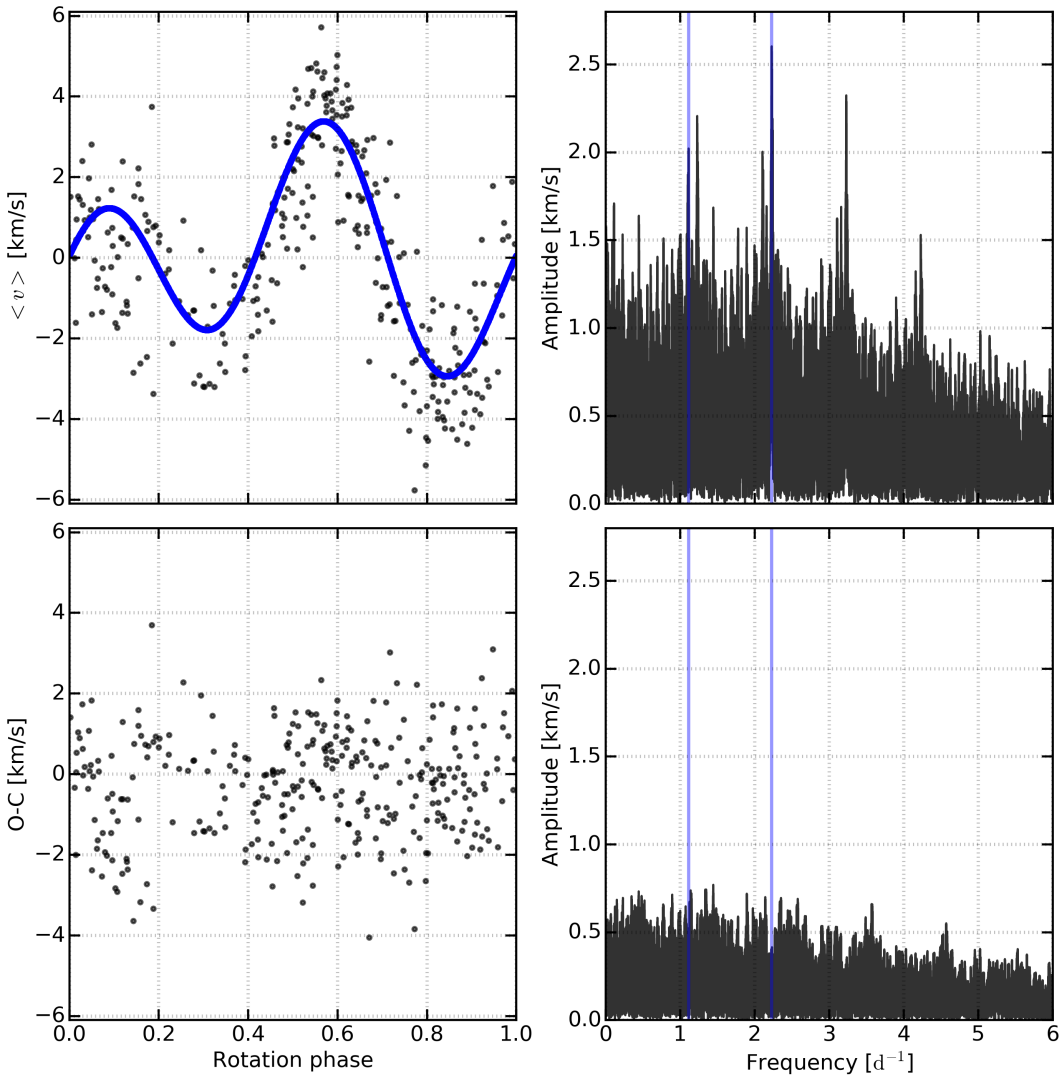

Figure 6.3: The first moment $\langle v \rangle$ of the He I 6678Å line from the combined Narval and HARPS spectroscopy (*top left*). The model for the rotational modulation (see Eq. (6.1)) for $P_{\rm rot} = 0.897673\,\mathrm{d}$ and $T_0 = \mathrm{HJD}\,2456185.8380$ is given as a solid blue line and the observations as black dots. *Bottom left*: residuals of $\langle v \rangle$ after the subtraction of the model. *Right*: Computed Lomb-Scargle periodograms of $\langle v \rangle$ (*top*) and the residuals (*bottom*), with $f_{\rm rot}$ and $2f_{\rm rot}$ marked as vertical blue lines.

following the S/N criterion. Adopting a prewhitening approach, we removed the above mentioned variability using the pixel-by-pixel method. Subsequent frequency extractions did not indicate clear results, most likely because of the poor temporal coverage of the Narval data with respect to the stellar pulsation-mode frequencies.

6.3.2 Determining the rotation period

Pápics et al. (2012) have indicated that the abundance inhomogeneities at the stellar surface of HD 43317 cause rotational modulation of certain spectral lines, especially the He lines. In the previous sub-section, we have shown that this is also observed in the Narval spectroscopy. We assume that these LPVs, seen in the He I lines of both data sets, are predominantly caused by surface abundance inhomogeneities (as suggested by Pápics et al. 2012). For early-type stars, such surface abundance inhomogeneities are known to be related to the dominantly dipolar magnetic field (see the discussion in Sect. 1.2.2). They typically manifest themselves at two locations, one per magnetic hemisphere. Because these large-scale magnetic fields are stable over several decades, the location of the abundance inhomogeneities on the stellar surface is not expected to have changed between the HARPS and Narval data sets. Thus, by combining the HARPS and Narval spectroscopy, we obtained a data set with 325 measurements spanning 6.13 years distributed over three observing campaigns. From this data, we can constrain the rotation period with great accuracy.

Using FAMIAS, we isolated the He I 6678Å, which exhibits clear rotational modulation, and deduced the first moment of the line, $\langle v \rangle$. When phase-folding $\langle v \rangle$ with the rotation period, the modulation should follow a second-order sine function:

$$\mathcal{M}(t) = A_1 \sin(2\pi(f_{\rm rot} t + \phi_1)) + A_2 \sin(2\pi(2 f_{\rm rot} t + \phi_2)) + C \,, \tag{6.1}$$

with A_i and ϕ_i being the amplitudes and phases of the individual sine terms, C a constant offset, and $f_{\rm rot}$ the rotation frequency. As an initial estimate, we performed a LS minimization fit to the observed $\langle v \rangle$ of the He I 6678Å line of HD 43317. In a subsequent step, a Bayesian MCMC approach (using EMCEE; Foreman-Mackey et al. 2013) was adopted to obtain a more reliable result for the rotation period. Uniform priors were considered in the appropriate parameter spaces, and we adjusted the log-likelihood from Duvall & Harvey (1986) and Anderson et al. (1990) to include individual weights:

$$\mathcal{L}(\Theta) = \sum_{i=1}^{N} \left\{ w_i \left(\ln\left(|\mathcal{M}(\Theta; t_i)|\right) + \frac{|\langle v \rangle(t_i)|}{|\mathcal{M}(\Theta; t_i)|} \right) \right\} \,, \tag{6.2}$$

with ln being the natural logarithm, $\mathcal{M}(\Theta; t_i)$ the model of Eq. (6.1) for a given parameter vector Θ, $\langle v \rangle(t_i)$ the observed first moment at t_i, and w_i the weight for that particular observation deduced from the S/N of the corresponding spectroscopic observation. Calculations with the Bayesian MCMC were started in a Gaussian ball around the LS result using 500 parameter chains and continued until the full parameter space was sampled and stable solutions were obtained.

The posterior probability distribution for the rotation period indicated $P_{\rm rot} = 0.897673(4)$ d as the most likely period causing the rotational modulation of $\langle v \rangle$ of the He I 6678Å line. No clear posterior probability distributions were obtained for the remaining model parameters. Hence, we accepted the rotation period from the MCMC and updated the remaining parameters in Eq. (6.1) by means of a LS minimization fit to $\langle v \rangle$. The final model for the variability of the measured $\langle v \rangle$ is shown in Fig. 6.3, as well as the residuals to the fit. Some scatter remains for the residuals, yet the Lomb-Scargle periodogram (Lomb 1976; Scargle 1982) of the residuals indicates no remaining periodic variability. The adopted value for $P_{\rm rot}$ agrees well with the literature rotation period determined from the CoRoT photometry (Pápics et al. 2012). Enforcing this literature value for $P_{\rm rot}$ on $\langle v \rangle$, however, resulted in a worse LS minimization model for $\langle v \rangle$ than our derived solution. The zeroth moment of the absorption lines $\langle v^0 \rangle$ (i.e., the equivalent width) and the second moment $\langle v^2 \rangle$ (i.e., the skewness), were also investigated for periodic variability related to the stellar rotation. However, these two diagnostics show a much larger scatter compared to the first moment and no strong amplitude peaks in their respective periodograms. Thus, we were unable to accurately determine $P_{\rm rot}$ from either $\langle v^0 \rangle$ or $\langle v^2 \rangle$, possibly due to the stellar pulsation modes.

With the rotation period now firmly established, we investigate the co-rotating surface inhomogeneities themselves. In particular, we wish to provide some constraints on their position on the stellar surface. Therefore, we constructed a dynamical spectrum with both the Narval and HARPS spectroscopy of the He I 6678Å line, indicating the residual absorption line to the mean line profile at a given rotation phase (right panel of Fig. 6.4). We considered 50 rotation phase bins and constructed the residuals from a weighted average spectrum for all observations falling within that phase bin. Two obvious features travel in velocity and rotation phase through the line profile, typical for co-rotating surface inhomogeneities. Since the two features are separated about 0.5 in rotation phase, they are expected to reside at opposite sides of the star. Both features show a slightly different duration with respect to the rotation phase, indicating that they are not located at the rotation equator, irrespective of the inclination angle to the rotation axis. Moreover, the surface inhomogeneities are not located too close to the (rotation) poles, otherwise only one feature would have been visible (except when $i \approx 90\,^\circ$). As such, we anticipate that the co-rotating He surface patches are located at a considerable obliquity angle $\beta_{\rm spot}$ with respect to the rotation axis, most likely $\beta_{\rm spot} \in [60, 80]^\circ$.

Finally, two additional features are present at the rotation phase of $\sim$0.7 with positive velocity and at the rotation phase of $\sim$0.95 with negative velocity (marked as dark gray in Fig. 6.4). Since it is not clear whether these travel over the full spectral line, their origin is difficult to identify. Detailed spot

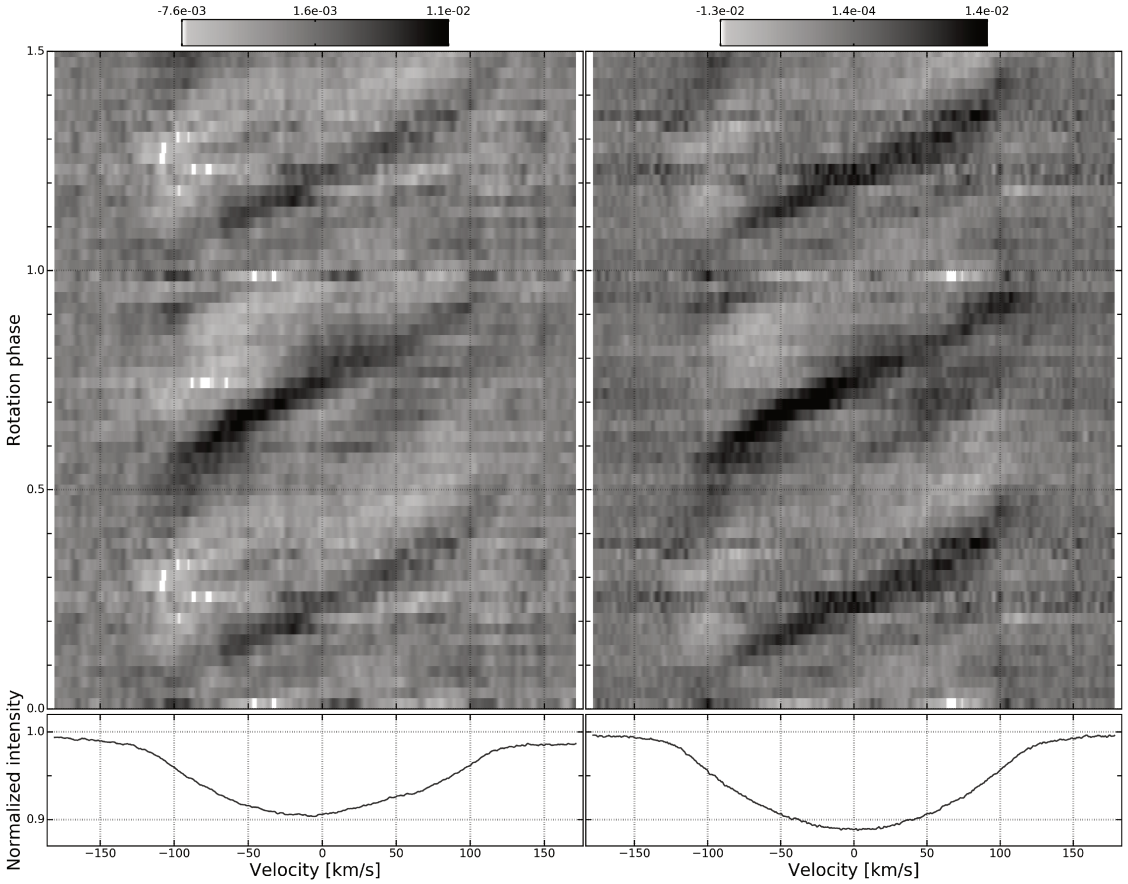

Figure 6.4: *Top*: Dynamical spectra of the residual He I 5016Å (*left*) and He I 6678Å (*right*) lines to their respective median profile, phase folded with the rotation period $P_{\rm rot} = 0.897673\,{\rm d}$ and $T_0 = {\rm HJD}\,2456185.8380$, and smoothed slightly with a Gaussian filter for increased visibility. The variability corresponds to at least two co-rotating surface inhomogeneities at the stellar surface, causing the rotational modulation. The amplitude of the residuals to the mean profile is indicated by the gray-scale. We indicate from rotation phase 0 up to a phase of 1.5. *Bottom*: Mean line profile of both He I absorption lines.

modelling, while accounting for the stellar pulsation modes, or tomographic imaging could aid in the characterization of this feature, but requires higher S/N spectroscopy covering the pulsational beating cycles. This would also demonstrate whether the surface inhomogeneities are located close to the poles of the large-scale magnetic field, as observed for various magnetic early-type stars (see also Sect. 1.2.2.)

We obtain similar conclusions when studying the rotational modulation of the He I 5016Å line (left panel of Fig. 6.4).

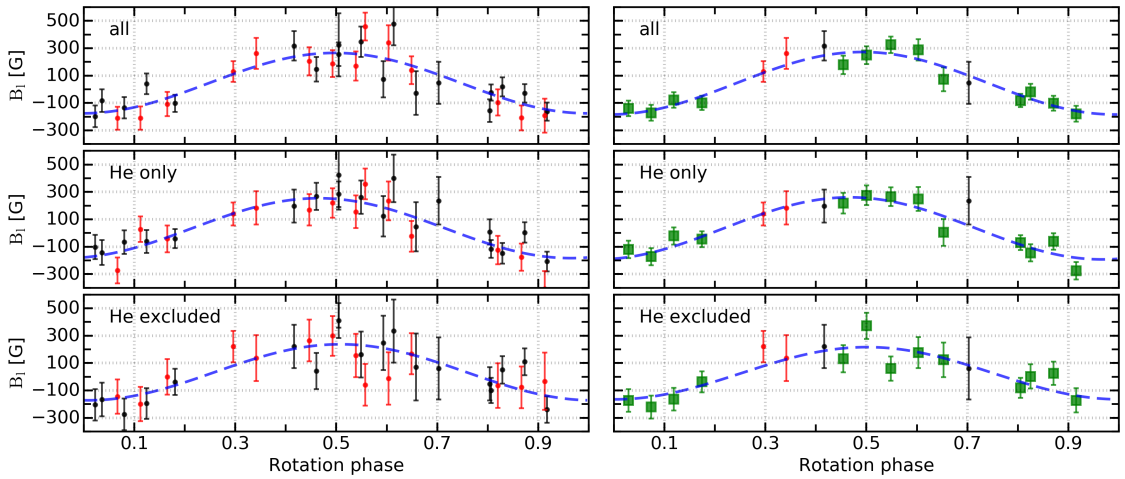

Figure 6.5: Longitudinal field measurements for HD 43317 for various LSD line masks. *Left*: Deduced values from the individual Narval spectropolarimetric sequences. The archival spectropolarimetry (Briquet et al. 2013) is indicated in black, while the additional data presented here are indicated in red. The optimal LS minimization fit, representing the rotational modulation of a dipolar field, is given by the dashed blue line. We assumed $P_{\rm rot} = 0.897673\,$d and $T_0 = \text{HJD}\,2456185.8380$. *Right*: Using the phase-binned data, indicated by the green squares.

6.4 Magnetic field measurements

6.4.1 Zeeman signature

To study the Zeeman signature of the magnetic field of HD 43317, we constructed a mean line profile with the usual LSD technique (Donati et al. 1997). As such, the S/N of the polarization signature is greatly improved. To perform the LSD method, we started from a pre-computed VALD3 line mask (Ryabchikova et al. 2015) for a star of 17000 K and a $\log g = 4.0\,$dex, compatible with the literature values for HD 43317 (Pápics et al. 2012). Hydrogen lines as well as all metal lines blended with hydrogen lines, strong telluric features, and diffuse interstellar bands were removed from the line mask. Finally, the depths of the lines in the mask were adjusted to match the observations. In addition, any lines with a depth smaller than 0.01 were discarded. The final line mask includes 449 lines, with their wavelength, depth, and Landé factor, used in the LSD method. We further subdivided the line mask into a version excluding all (blends with) He lines (containing 396 lines) and a version only containing the 17 He lines.

For each observation, the FAP (Donati et al. 1992, 1997, and Chapter 1) was computed, indicating the detection probability of a Zeeman signature in the LSD Stokes V spectrum. Using the full line mask, 9 observations are DDs, 12 are NDs, and 13 are MDs (Table 6.2.2). Such a low number of (clear) detections was expected, since the exposure times were tailored to avoid influence of the stellar variability, instead of reaching a high S/N.

As indicated in Sect. 6.3.1, a few of the spectropolarimetric observations are distorted by the LPVs. Since the effect of stellar pulsation and rotational modulation is slightly different for each spectral line, the LSD method averages out any strong variability. The diagnostic null profile can indicate the effects of LPVs between these sub-exposures. These null profiles show some scatter, yet the level of the scatter is similar to what is found outside the lines (see Figs. 6.6 – 6.8). The amount of scatter is rather large, because of the limited S/N of the observations, but no obvious evidence of strong distortions by the LPVs during a spectropolarimetic sequence was noted. These results agree with the conclusions from the LPVs in the individual exposures (we refer to Sect. 6.3.1).

6.4.2 Longitudinal field measurements

The large-scale fossil magnetic fields of early-type stars are known to be stable over a timescale of at least a decade. As the star rotates, the line-of-sight component of these magnetic fields, integrated over the stellar surface, varies with the rotation phase. The mean Landé factor used to compute the longitudinal magnetic field value (see Eq. (1.16)) is 1.2072, 1.1567, and 1.2095 for the LSD profiles constructed with the complete line mask, the He-only line mask, and the He-excluded line mask, respectively. The corresponding mean wavelengths are 506.98 nm, 494.04 nm, and 511.58 nm, respectively. The integration limits should span the full Stokes I profile. Overly large integration limits, however, will artificially increase the uncertainty on the measured B_l. We opted for an integration limit of $200\,\mathrm{km\,s^{-1}}$, $115\,\mathrm{km\,s^{-1}}$, and $240\,\mathrm{km\,s^{-1}}$ around the line center for the LSD profiles with the full line mask, He-excluded, and He-only line masks, respectively. These limits differ from the literature $v \sin i = 130 \pm 16\,\mathrm{km\,s^{-1}}$ (Głębocki & Gnaciński 2005) or $v \sin i = 115 \pm 9\,\mathrm{km\,s^{-1}}$ (Pápics et al. 2012) whenever He lines are included. These larger integration limits for the determination of the longitudinal magnetic field were needed to fully cover the LSD Stokes profiles. This additional non-rotational broadening is most likely due to the pressure broadening of the He lines through the Stark effect (e.g., Dimitrijevic & Sahal-Brechot 1984).

For a centered dipolar magnetic field, the rotationally modulated longitudinal field follows a sinusoidal pattern (i.e., Eq. (4.2)). We performed an LS

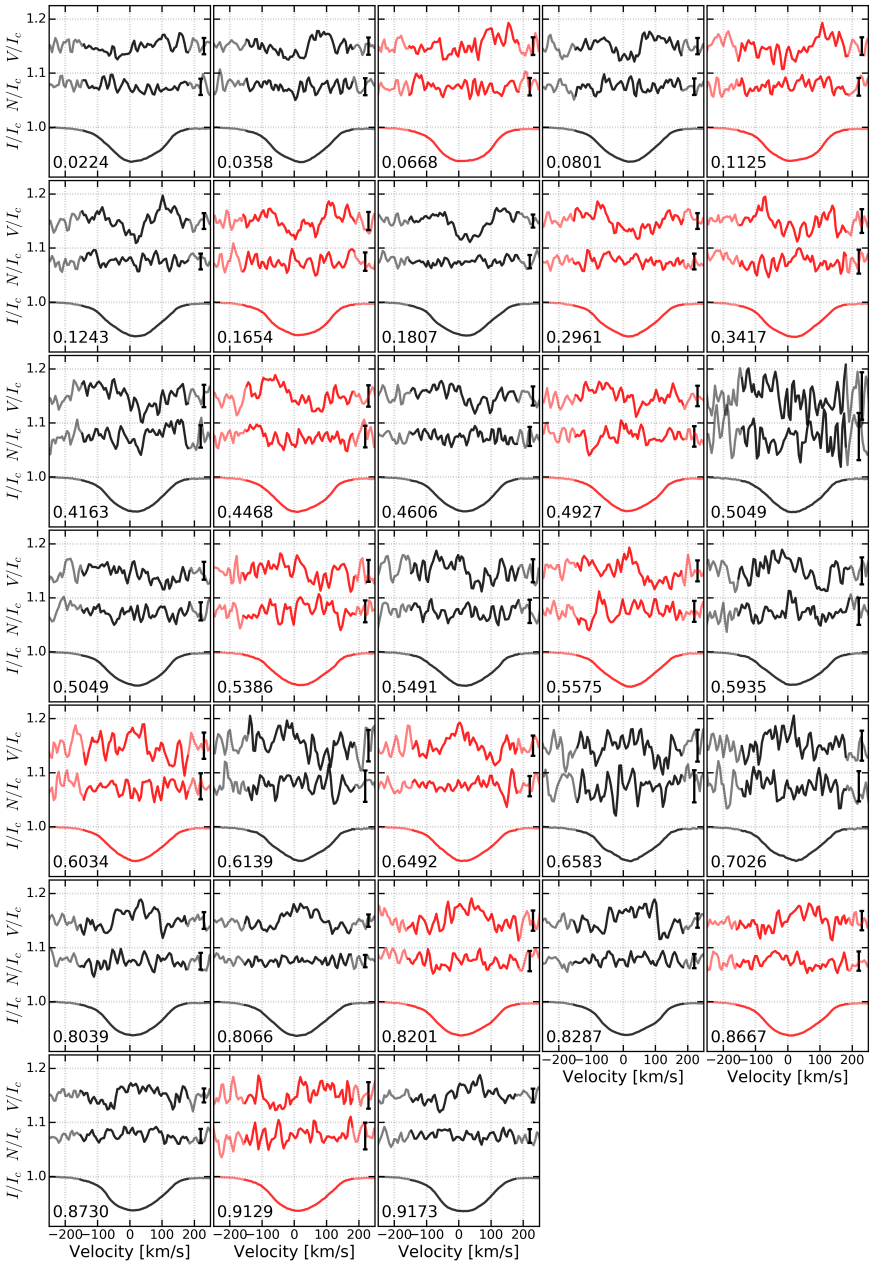

Figure 6.6: LSD profiles determined with the full linemask for HD 43317 (Sect. 3.7). Each panel is organized according to the rotation phase and contains the observed intensity profile (I/I_c; *bottom*), the null profile (N/I_c; *middle*), and the Stokes V (V/I_c; *top*) profiles. Both the null and Stokes V profiles are multiplied by a factor 100 and smoothed with a Gaussian filter with width 6 km/s for increased visibility. Their respective error bars are indicated on the right. Narval data discussed in Briquet et al. (2013) is marked in black, and the more recent Narval spectropolarimetry presented in this work is indicated in red.

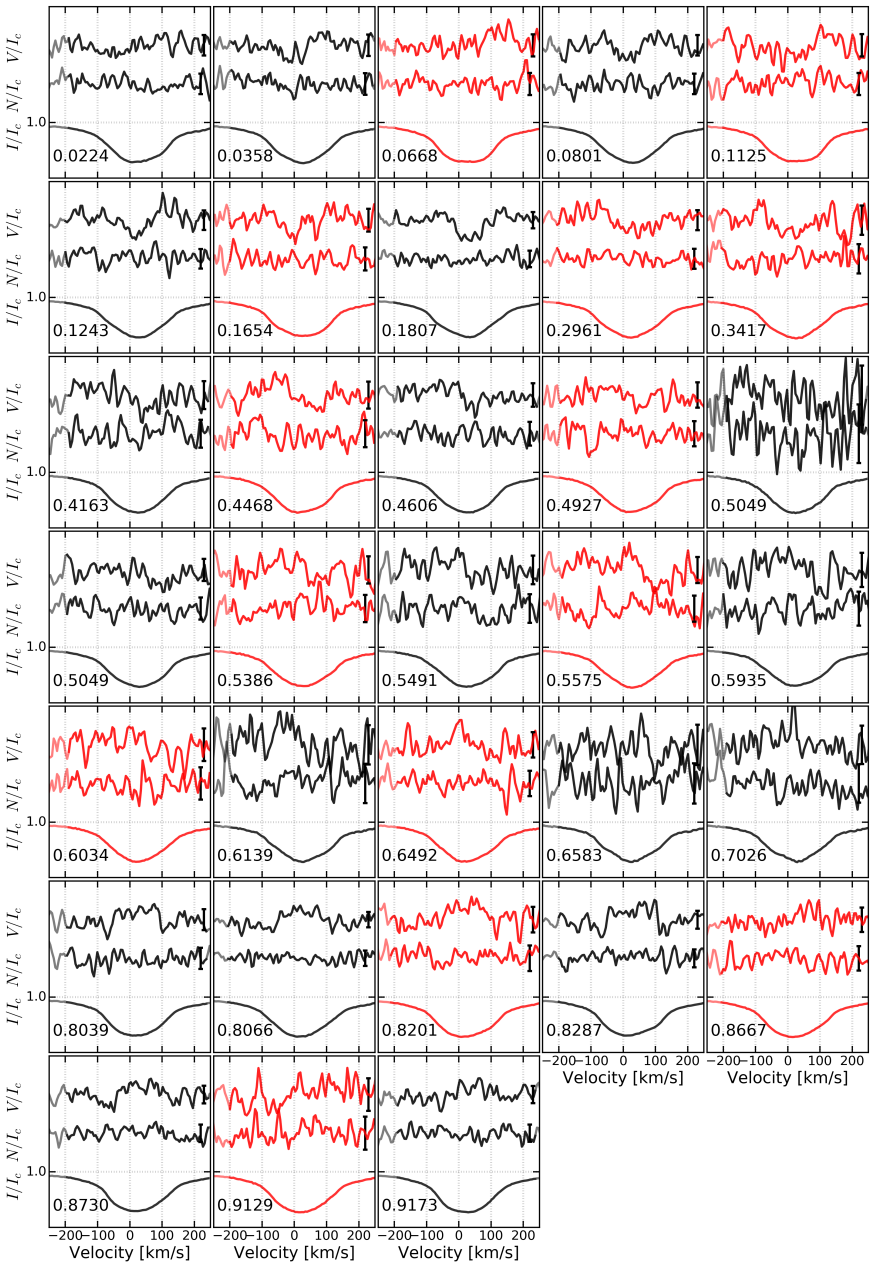

Figure 6.7: As in Fig. 6.6, but for the LSD profiles determined with only the 17 He lines for HD 43317.

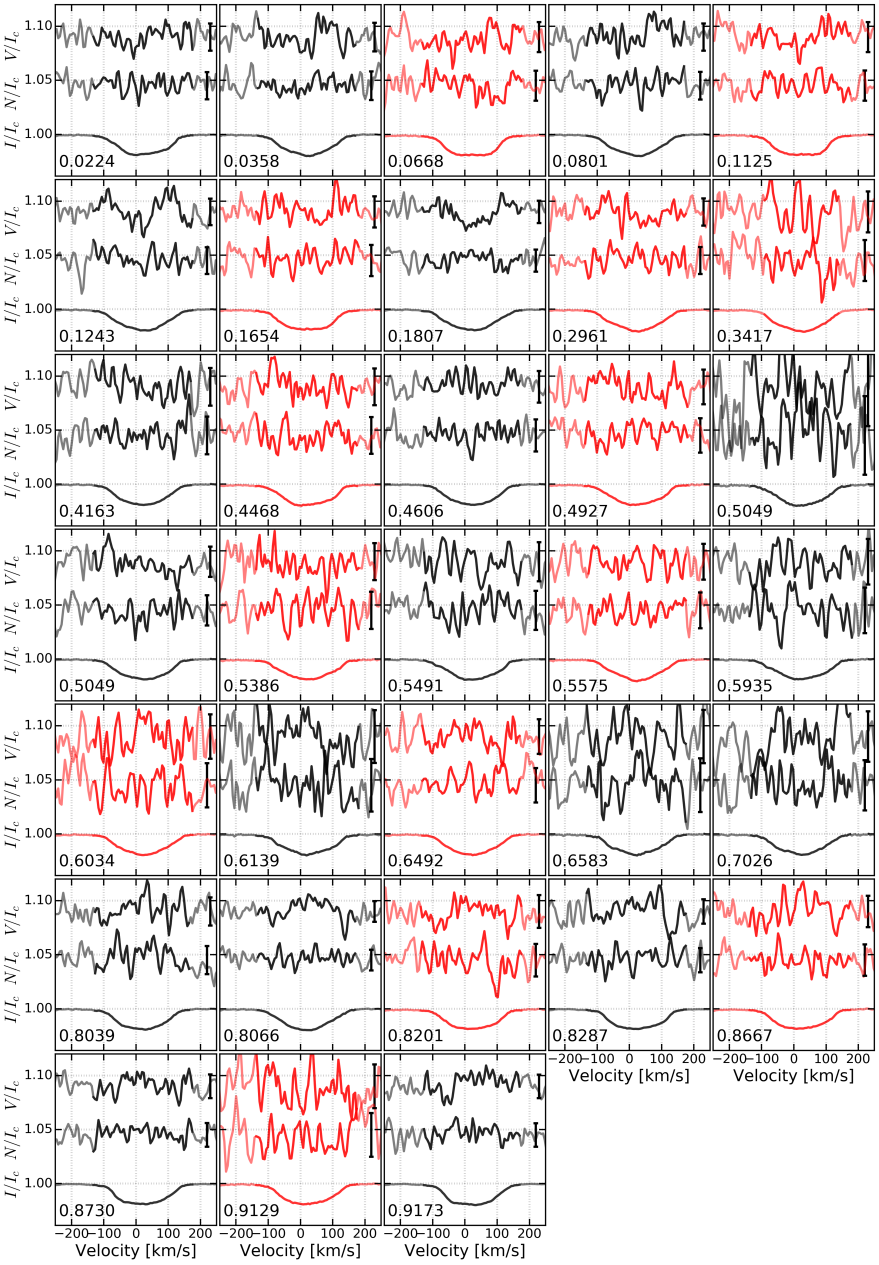

Figure 6.8: As in Fig. 6.6, but for the LSD profiles determined with all significant metallic lines except the (blends with) He lines for HD 43317.

Table 6.2: Obtained parameters from the dipolar fits to the longitudinal field measurements for HD 43317. The estimated obliquity angle, β, is provided, assuming $i \in [20, 50]^\circ$ from Pápics et al. (2012). Using these values, we deduced the limits on the strength of the dipolar magnetic field $B_{\rm dip}$.

mask	B_0 [G]	$B_{\rm amp}$ [G]	β [deg]	$B_{\rm dip}$ [G]
all	45 ± 16	221 ± 22	$[69, 88]$	$[1013, 2300]$
He only	35 ± 18	219 ± 24	$[70, 90]$	$[1003, 2312]$
He excl.	33 ± 25	205 ± 34	$[67, 87]$	$[723, 2150]$
bin: all	44 ± 17	228 ± 23	$[69, 89]$	$[1051, 2403]$
bin: He only	34 ± 19	227 ± 25	$[71, 90]$	$[1045, 2373]$
bin: He excl.	26 ± 24	191 ± 32	$[68, 88]$	$[657, 1960]$

minimization fit to the measured B_l values assuming $P_{\rm rot} = 0.897673$ d and $T_0 =$ HJD 2456185.8380 (T_0 was determined from the subsequent Stokes V modelling in Sect. 6.5.1). These models for the longitudinal magnetic field are given in the left panel of Fig. 6.5. Despite the uncertainties on the B_l values, we obtain a relatively good description of the modulation thanks to the sufficient phase coverage. In addition, we investigated the possibility of a quadrupolar contribution to the large-scale magnetic field by fitting a second order sine function (i.e., Eq. (4.3)) to the measured B_l. These fits all indicate that a quadrupolar contribution is negligible with the accepted rotation period. The values for the amplitude of the dipolar model are given in Table 6.2.

To decrease the uncertainty on the B_l measurements, we phase-binned the Narval data according to their determined rotation phase. When multiple observations differed by less than 2 % in rotation phase, we averaged their spectropolarimetric observations, using the S/N determined in the LSD Stokes V profile as weighting. These average observations were then again converted to LSD profiles, using the same line masks to redetermine the corresponding B_l values. In total, we constructed 13 average spectropolarimetric observations from 30 original measurements (see Table 6.3) and kept the four remaining measurements (observations 11, 16, 26, and 27; see Table 6.2.2) to adequately cover the full rotation period. These phase-folded B_l values are given in the right panels of Fig. 6.5. Phase-binning the spectropolarimetric measurements was only possible because of the precise knowledge of the rotation period, determined independently from the magnetic measurements. As an additional bonus to the increased S/N and smaller uncertainties on the B_l values, the LPVs due to the stellar pulsation modes will be smeared out, since the spectra correspond to different pulsation phases (while having the same rotation phase). Statistically, one can thus assume that the effects of the LPVs on the phase-binned magnetic

Table 6.3: Observing log of the rotationally phase-binned Narval observations, for which the original observation identifications $\mathrm{ID_{exp}}$ from Table 6.2.2 are indicated. The rotation phase ϕ_{rot} is determined with $P_{\mathrm{rot}} = 0.897673$d and $T_0 = \mathrm{HJD}\,2456185.8380$. The provided S/N is that of the LSD Stokes I profile calculated with various line masks. In addition, the magnetic detection status for each rotation phase-binned observation is indicated.

ID	$\mathrm{ID_{exp}}$	ϕ_{rot}	all		He only		He excluded	
			S/N	Detect.	S/N	Detect.	S/N	Detect.
bin-1	4,8	0.028952	2118	MD	294	MD	1735	ND
bin-2	9,23	0.073682	2184	DD	293	MD	1711	MD
bin-3	10,24	0.118743	2151	DD	291	DD	1702	MD
bin-4	3,25	0.174297	2123	DD	288	DD	1689	MD
bin-5	12,29	0.454140	2092	DD	289	ND	1710	ND
bin-6	13,17,30	0.500143	2080	MD	281	ND	1660	MD
bin-7	18,31,32	0.548531	2088	MD	282	MD	1668	ND
bin-8	14,19,33	0.603092	2142	MD	287	MD	1689	ND
bin-9	15,34	0.652713	2095	DD	285	ND	1676	ND
bin-10	1,2	0.805048	2116	DD	290	DD	1687	MD
bin-11	5,20	0.825148	2107	DD	290	DD	1686	MD
bin-12	6,21	0.870397	2059	DD	293	MD	1663	MD
bin-13	7,22	0.915811	2028	DD	296	MD	1630	MD

measurements are smaller, but it is also possible that we add a systematic distortion or artificially widen the spectral lines. Yet, the Stokes I profiles of the phase-binned data remained rather Gaussian, indicating that most LPVs were indeed cancelled out (see Fig. 6.9). The LSD Stokes V profiles of these phase-binned data showed a much clearer Zeeman signature with nine DD and four MD for the full line mask. Some NDs remain for the other LSD line masks, because of the lower S/N of these LSD profiles.

We repeated the fitting process of a sine and second order sine function (i.e., Eqs. (4.2) and (4.3)) to the determined B_l of these 13 phase-binned and 4 original observations. Similar results as with the original data were obtained. The variability agreed with a dipolar field (i.e., a sine function) with a negligible quadrupolar contribution. The determined fits also agreed well with those of the individual data (see Fig. 6.5). We do note that some scatter to the modelled B_l variations remained, possibly indicating that not all LPVs are completely cancelled out.

In case either the inclination angle i or the obliquity angle β is constrained, the other is automatically known through Eq. (1.17). From the dipolar fit to the B_l values of the full line mask, we obtained $B_{l,\mathrm{max}} = 272 \pm 28\,\mathrm{G}$ and

$B_{l,\min} = -184 \pm 28$ G. Pápics et al. (2012) constrained the inclination angle on HD 43317 using their derived $P_{\rm rot}$, $v \sin i$, and the radius of an approximate CLÉS model (Code Liégeois d'Évolution Stellaire; Scuflaire et al. 2008) to $i \in [20, 50]^\circ$. Our minor update to $P_{\rm rot}$ does not alter this assumption. Using these limits for the inclination angle and the modulation of the longitudinal magnetic field for the full line mask and no phase-binning, we obtain $\beta \in [69, 88]^\circ$. The estimates for the other models are given in Table 6.2, and these are all compatible with the estimates of Briquet et al. (2013).

We derived the limits on the dipolar magnetic field $B_{\rm dip}$ with Eq. 1.18 and from the fit to the varying longitudinal magnetic field, assuming the inclination angle provided by Pápics et al. (2012) using the pulsation mode identification (i.e., $i \in [20, 50]^\circ$), the obtained $B_{l,\max}$, the computed β, with their respective uncertainties for each of the six different fits, and the limb-dark coefficient $u = 0.3$ (which is appropriate for a B3.5V star; see e.g., Claret 2000). The derived values are provided in Table 6.2. Typically, they range from 1.0 to 2.4 kG, whenever He lines were included in the line mask. When no He lines were considered, the field could be slightly weaker (0.6 to 2.2 kG). Our results for $B_{\rm dip}$ agree well with those of Briquet et al. (2013), who deduced 0.65 – 1.75 kG and had a slightly smaller value for the amplitude of the sinusoidal fit.

6.5 Stokes V modelling

In an attempt to constrain the geometry of the large-scale magnetic field of HD 43317 more accurately, especially the inclination and obliquity angles, we resorted to modelling the Zeeman signatures with a grid-based approach (for full details, see Alecian et al. 2008). For each observation, a (de)-centered dipolar magnetic field is described and characterized by i, β, the strength of the dipolar field $B_{\rm dip}$, a reference date T_0 for the rotation phase of the maximal amplitude of $B_{\rm dip}$, and the off-centering factor of the field ψ. The latter varies between zero and one, with zero being a centered dipolar field. For each gridpoint in this five-dimensional grid, the Stokes V profiles were integrated over the (θ, ϕ) stellar surface mesh. The routine, then, deduced the best solution by simultaneously minimizing the reduced χ^2 for every observation to their respective Stokes V model within the velocity range of $[-350, 350]\,{\rm km\,s^{-1}}$.

To accurately represent the linewidth of the modelled profiles, we provided the assumed limb-darkening coefficient $u = 0.3$, and a description of the LSD Stokes I profile, parametrized by the radial velocity shift, the depth of the profile, the rotational broadening $v \sin i$, and the non-rotational broadening $v_{\rm NR}$, to the modelling tool. The description was obtained by performing a LS minimization

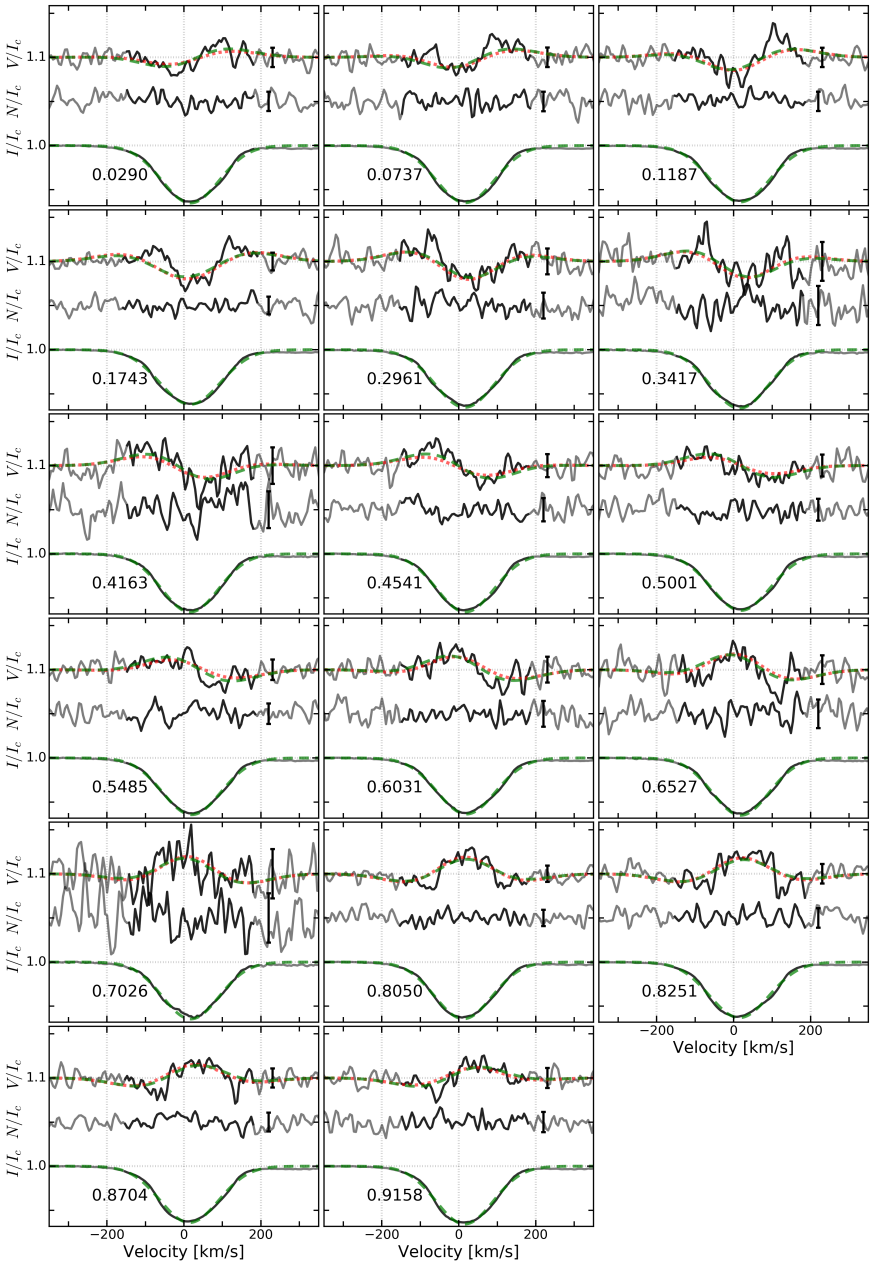

Figure 6.9: Observed LSD profiles compared with the results from the Stokes V modelling. Panels are organized according to the rotation phase and contain the observed intensity profile (I/I_c; *bottom*), the null profile (N/I_c; *middle*), and the Stokes V (V/I_c; *top*) profiles given in black. Both the null and Stokes V profiles are multiplied by a factor 100 and smoothed with a Gaussian filter with a width of $6\,\mathrm{km\,s^{-1}}$ for increased visibility. Their respective error bars are indicated on the right side of each panel. The centered dipole model of Sect. 6.5.1 is indicated by the green dashed lines, while that of Sect. 6.5.2 by the red dotted lines.

fit of the convolution product of two Gaussian functions to the observed LSD Stokes I profiles, for which one Gaussian had a fixed full width at half maximum (FWHM) equal to the literature value for $v \sin i$ derived by Pápics et al. (2012), and the other Gaussian has $v_{\rm NR}$ as a fitting parameter for its FWHM. This indicated $v_{\rm NR} = 110\,{\rm km\,s^{-1}}$, which was not surprising given the wide LSD Stokes I profiles due to various broadening effects, coming from the different included spectroscopic lines. This non-rotational broadening comprises of, at least, the macroturbulent broadening, the pressure broadening of the He lines, the combined amplitudes of the stellar pulsation modes, seen at various optical depths (through the different spectroscopic lines), and possible line broadening due to the magnetic field itself.

Because the S/N in Stokes V for the phase-binned data is substantially higher, we performed the Stokes V modelling to this data set. Moreover, we only modelled the LSD profiles constructed with the complete line mask, since i) it has the highest S/N of the LSD profiles constructed with the different line masks, ii) the LSD Stokes I profiles of the He-only line mask start to differ from a strict Gaussian profile (see Fig. 6.7), iii) no DD were obtained with the He-excluded line mask, and iv) the effects of the LPVs should be minimal.

6.5.1 Full parameter search

Because we did not want to enforce any values for the parameters or restrict the parameter space, we left i and β to vary between 0 and 90 °, $B_{\rm dip}$ between 100 and 2500 G, and T_0 in the range of 2456185 d and 2456185+$P_{\rm rot}$ d. We compare the final, returned model with a centered dipole ($\psi = 0$) to the LSD profiles in Fig. 6.9. These models indicate $i = 55.6 \pm 6.4\,^\circ$, $\beta = 77.0 \pm 4.5\,^\circ$ with $B_{\rm dip} = 982 \pm 45$ G and $T_0 = {\rm HJD}\,2456185.8380 \pm 0.0059$. The provided uncertainties here are 3σ confidence intervals, compared to the 68 % (1σ) confidence intervals throughout the work. When setting ψ as a free parameter during the Stokes V modelling, the models with $\psi = 0$ described the observations most accurately, hence a centered dipolar magnetic field was always favored. This result is compatible with those of the longitudinal magnetic field study, indicating no significant quadrupolar contribution to the dipolar magnetic field.

Comparing the modelled Stokes V profiles with those observed, we noted that the agreement is good but not perfect (a reduced $\chi^2 = 1.13$). While the rotational variability of the Zeeman signature is adequately described, differences compared to the individual observations remain visible, yet fall within the uncertainty on the observed LSD Stokes V profiles. These differences seem to be more substantial when the magnetic field was not observed close to pole-on. In some cases, differences most likely arose because of the considerable noise level of these

observations, reflected by the variable diagnostic null profile. Other observations showed that a minor distortion by the LPVs still occurred when comparing the intensity profiles with the Gaussian approximation. The differences between the Stokes V model and the polarization signature increases whenever the LSD Stokes I profile differs from the anticipated Gaussian approximation (for example at $\phi_{\rm rot} = 0.6527$ or $\phi_{\rm rot} = 0.8704$). We, therefore, assume that the combination of both aforementioned issues causes the differences between models and observations.

6.5.2 Restricted parameter search

The inclination angle determined from the Stokes V modelling differs from the seismic estimate of Pápics et al. (2012). The grid-based approach indicates $55.6 \pm 6.4°$, which is only marginally compatible with the limits derived by Pápics et al. (2012), that is, $i \in [20, 50]°$. Consequently, this larger inclination angle would imply a lower equatorial velocity, when keeping $v \sin i$ constant. Hence, to obtain the same rotation period, HD 43317 needs to have a substantially smaller stellar radius, of about $2.5\,{\rm R}_\odot$. Such a radius is much smaller than what is typically determined and expected for a B3.5V star (i.e., about $4\,{\rm R}_\odot$) or is obtained for the forward modelling of HD 43317 in Chapter 7. Therefore, we rejected the obtained modelling solution on secondary physical arguments, implying that the inclination angle cannot be precisely determined from the Stokes V modelling.

We repeated the Stokes V modelling with the inclination angle fixed at $30\,°$, close to the estimate of Pápics et al. (2012). The resulting parameters for the determined model (with i, ψ, and T_0 fixed) were $\beta = 85 \pm 2\,°$ and $B_{\rm dip} = 1100 \pm 43\,{\rm G}$. β is now artificially better constrained because the correlation between i and β was not accounted for by keeping i fixed. A larger $B_{\rm dip}$ was needed to correctly model the amplitudes of the Zeeman signature. This additional model is indicated in Fig. 6.9 for a visual comparison with the model of Sect. 6.5.1.

The resulting reduced χ^2 of the new model, $\chi^2 = 1.15$, is only slightly worse than the model obtained in Sect. 6.5.1. Hence, we were unable to reliably constrain the inclination angle i from Stokes V modelling. The LPVs in combination with the mediocre S/N are most likely providing an overly large challenge for the standard techniques. In case HD 43317 is seen from a low inclination angle, as anticipated, the star is rotating at a significant fraction of its critical rotation velocity. This could provide an additional observational obstacle for the study of the spectropolarimetric data. Fortunately, we did not note any evidence in the LSD Stokes I profiles of a strong oblate stellar deformation.

6.6 Discussion

6.6.1 Magnetic dipole configuration

Using both the fit to the varying longitudinal magnetic field, together with the corresponding analytical equations, and the Stokes V modelling, we have tried to characterize the large-scale magnetic field at the surface of HD 43317 as a dipolar magnetic field and have attempted to determine the inclination angle of the stellar axis with respect to the observer. The applied methods had varying degrees of success, but always favored a dipolar geometry for the large-scale magnetic field. A minor quadrupolar contribution to the dipolar field is still plausible, but not needed with the current spectropolarimetric data set and accepted rotation period. Hence, we continue to treat the large-scale magnetic field at the stellar surface of HD 43317 as a pure dipolar magnetic field.

The Stokes V modelling, often a strong technique to constrain i, was not able to reliably determine the inclination angle of HD 43317, since the best fit led to a non-physical stellar radius for a B3.5V star. Moreover, enforcing the inclination angle from Pápics et al. (2012) during the modelling resulted in only a slightly worse description of the Zeeman signatures. Therefore, to reliably constrain the inclination angle, we will need to follow a seismic approach by modelling the observed stellar pulsation-mode frequencies, while assuming the pulsation axis coincides with the rotation axis. We test if this is feasible in Chapter 7.

Although i can span a wide range of values, we have a relatively good handle on the obliquity angle between the magnetic axis and the rotation axis. Both the Stokes V modelling and Eq. (1.17) (defined in Sect. 1.2.3) used in Sect. 6.4.2 indicated that β should be large ($> 67\,^\circ$), yet be smaller than $90\,^\circ$. A similar conclusion was reached for the location of the co-rotating He patches (i.e., $\beta_{\rm spot} \in [60, 80]^\circ$ from Sect. 6.3.2). Therefore, it seems that these two surface abundance inhomogeneities are located very close to the magnetic poles, as is often found for magnetic stars.

Finally, from the longitudinal field measurements, the derived limits on the inclination angle and obliquity angle (see Sects. 1.2.3 and 6.4.2), we obtained $B_{\rm dip}$ ranging from 1.0 to 2.4 kG, while the Stokes V modelling indicated $\sim$1 kG. It is not the first time that Stokes V modelling provides a lower amplitude for the field. In the particular case of HD 43317, we note at least two reasons. First, the value derived from the Stokes V modelling relies heavily on the considered value for the non-rotational broadening $v_{\rm NR}$, where a larger $v_{\rm NR}$ corresponds to a larger $B_{\rm dip}$. Accurately deriving $v_{\rm NR}$ is not trivial for early-type stars that host stellar pulsation modes or show rotational modulation (see e.g., Aerts et al. 2014). As such, the uncertainty on $B_{\rm dip}$ is larger than what the Stokes V

Table 6.4: Derived values needed for the study of the magnetosphere of HD 43317, assuming two different inclination angles. Both computations indicate HD 43317 hosts a centrifugal magnetosphere.

	$i = 20\,^\circ$	$i = 50\,^\circ$
$R_\star$ $(R_\odot)$	5.966	2.664
$\log \dot{M}$ $(M_\odot\,\mathrm{yr}^{-1})$	-8.945	-10.493
$\eta_\star$	130.5	7367.8
R_A $(R_\odot)$	21.964	25.48
R_K $(R_\odot)$	6.87	6.87

modelling has indicated. Second, the upper limits for B_dip derived from the longitudinal magnetic field (i.e., $> 2\,\mathrm{kG}$) occurs only under the assumption of the low inclination angle limit, that is, $i = 20\,^\circ$, and thus comes from the uncertainty on i derived by Pápics et al. (2012). Using the averaged longitudinal field measurements for the complete LSD line mask (top right panel of Fig. 6.5) and assuming $i = 30\,^\circ$ for Eq. (1.18), we obtain a $B_\mathrm{dip} = 1.4\,\mathrm{kG}$, which is closer to the Stokes V modelling results. Because of the uncertain v_NR, the large interval for i, and the fast rotation, we, therefore, conclude that the magnetic dipolar field at the stellar surface of HD 43317 likely has a strength between approximately 1.0 and 1.5 kG.

6.6.2 Circumstellar environment

The presence of a magnetosphere around magnetic stars is often noted by the rotationally modulated Hα emission. No such variability was found from the new Narval data, in agreement with the conclusions of both Pápics et al. (2012) and Briquet et al. (2013), using the HARPS spectroscopy and the 2011–2 Narval spectropolarimetry, respectively. This, however, does not necessarily imply that a magnetosphere is absent for HD 43317, since the strength of the variability caused by the magnetosphere depends on the viewing angle upon it. Under the oblique rotator model (Stibbs 1950), this viewing angle depends on i, β, and the rotation phase, resulting in limited variability when either the inclination angle or the obliquity angle is small ($< 20\,^\circ$) while the other one is large ($> 70\,^\circ$). A similar conclusion was reached by Townsend (2008), when studying the effect of the viewing angle upon the photometric variability when using a torus model for the magnetosphere. This unfavorable geometrical configuration is compatible with the current confidence intervals on i and β for HD 43317. Moreover, the mass-loss rate for a B3.5V star is rather small (compared to more massive stars), so only a limited amount of wind matter is able to fill the magnetosphere.

To determine whether HD 43317 hosts a dynamical or centrifugal magnetosphere, we determine the magnetic confinement parameter $\eta_\star$ (using Eq. (7) of ud-Doula & Owocki 2002), considering the adopted 1 kG dipolar magnetic field and the escape velocity $v_\infty = 150\,\mathrm{km\,s^{-1}}$ from Briquet et al. (2013). We computed the theoretical mass-loss rate $\dot{M}$ using Eq. (25) of Vink et al. (2001), because no accurate observed $\dot{M}$ is available for HD 43317. To be compatible with the large confidence interval on the inclination angle, we performed the calculations for two different inclination angles, namely $i = 20\,^\circ$ and $i = 50\,^\circ$, leading to different stellar radii, while assuming the literature $v \sin i$ and the adopted rotation period. Using the computed $\eta_\star$, we determined the Alfvén radius R_A for both cases. The Keplerian corotation radius R_K was derived assuming HD 43317 has a mass of $M = 5.4\,M_\odot$, following the CLÉS model of Pápics et al. (2012), and the adopted rotation period. These values for the different parameters are given in Table 6.4. In both cases, we obtained $R_\mathrm{A} \gg R_\mathrm{K}$, indicating HD 43317 hosts a centrifugal magnetosphere, compatible with the results of Briquet et al. (2013). This result remains valid when HD 43317 has a stronger dipolar magnetic field than the assumed 1 kG.

6.6.3 Implications for the stellar interior

Since HD 43317 is a magnetic early-type pulsator with many detected stellar pulsation-mode frequencies, it will be a prime target to observationally inspect the implications of the large-scale magnetic field for the stellar interior. In Chapter 7, the observed pulsation modes will be used to constrain the stellar structure through forward modelling (as done in, e.g., Degroote et al. 2010a; Pápics et al. 2015; Van Reeth et al. 2016; Moravveji et al. 2016). At this stage, however, we can already utilize several theoretical criteria to study whether or not the large-scale magnetic field at the stellar surface of HD 43317 is sufficiently strong to imply solid-body rotation.

The first criterion is Eq. (3.6) of Zahn (2011), based on the magnetic field description by Mathis & Zahn (2005):

$$B_\mathrm{crit}^2 = 4\pi\rho\frac{R_\star^2\Omega}{\tau_\mathrm{AM}}\,. \tag{6.3}$$

Here, $R_\star$, ρ, and Ω are the stellar radius, the mean density, and the surface velocity, respectively. τ_AM is the time spent by the star on the main sequence. Until better estimates have been derived, we used the radius and mass of the CLÉS model of Pápics et al. (2012) to estimate ρ. To calculate the surface velocity, we adopted $i = 30\,^\circ$ and $v \sin i = 115\,\mathrm{km\,s^{-1}}$, again following Pápics et al. (2012). For the age of HD 43317, we used the result determined by Tetzlaff et al. (2011), who derived $\tau_\mathrm{AM} = 26.0 \pm 5.6\,\mathrm{Myr}$ by fitting HD 43317 to various

evolutionary models. This lead to a $B_{\rm crit} \approx 114\,{\rm G}$ in the radiative zone to suppress differential rotation. Using the ratio between the internal and surface magnetic fields from Braithwaite (2008), that is, a ratio of 30, we obtained a $B_{\rm crit,surf} \approx 4\,{\rm G}$. The derived magnetic field of HD 43317 is substantially stronger than this limit, implying that under the Zahn-criterion, the magnetic field will influence the internal stellar structure by enforcing uniform rotation and inhibiting mixing. In case HD 43317 is older than the assumed 26 Myr, the derived $B_{\rm crit,surf}$ will decrease even further. Moreover, HD 43317 needs to be younger than about 1 Myr, conflicting with the results of Tetzlaff et al. (2011), to significantly challenge the derived $B_{\rm crit,surf}$ and its implications.

An alternative criterion was derived by Spruit (1999), who calculated the minimal initial field strength for uniform rotation when assuming a non-axisymmetric magnetic field:

$$B_{\rm crit,init} = r(4\pi\rho)^{1/2}\left(\frac{\eta\Omega q^2}{3r^2\pi^2}\right)^{1/3}, \tag{6.4}$$

while only considering the radiative zone. We used similar approximations to those of Briquet et al. (2012, for the magnetic pulsator V2052 Oph), and assumed $i = 30°$. This leads to a $B_{\rm crit,init} \approx 1400\,{\rm G}$, corresponding to a $B_{\rm crit,init,surf} \approx 140\,{\rm G}$ using the ratio (10) between the surface field and that in the radiative zone (Braithwaite 2008). Again, the measured dipolar field at the surface of HD 43317 passes this threshold field, implying uniform rotation.

This anticipated uniformly rotating radiative layer should cause a decrease in the size of the convective core overshooting layer, leading to less available fuel for the core-hydrogen-burning phase compared to a non-magnetic star with the same stellar parameters as HD 43317. From forward seismic modelling, it should be possible to observationally parametrize the extent of this overshooting layer (see Chapter 7).

Since the inclination angle is currently ill-defined, we investigate what happens to the critical values if we assume $i = 55.6\,°$, following the result of the Stokes V modelling, while keeping $R_\star$ constant (conflicting with the observed $v \sin i$) or while keeping $v \sin i$ constant (leading to the non-physical $R_\star = 2.5\,R_\odot$). In the first case, both critical values would decrease, due to the slower surface velocity, to $B_{\rm crit,surf} = 3\,{\rm G}$ and $B_{\rm crit,init,surf} \approx 100\,{\rm G}$. The inverse behavior is noted for the second case, as the critical values increase to $B_{\rm crit,surf} = 5.5\,{\rm G}$ and $B_{\rm crit,init,surf} \approx 310\,{\rm G}$. Nevertheless, the determined polar strength between approximately 1.0 and 1.5 kG for the fossil field of HD 43317 remains sufficiently large, compared to the derived critical values to warrant a uniformly rotating radiative envelope.

6.7 Summary and conclusions

Using archival and recent Narval spectropolarimetry, we studied the large-scale magnetic field of HD 43317 and the LPVs, due to stellar pulsation modes and co-rotating surface abundance inhomogeneities.

Thanks to the carefully tailored exposure times of the individual polarization sub-exposures, variations of the line profiles during the complete sequences were minimal. However, the LPVs cause periodic distortions of the spectral lines over longer timescales. By combining the individual Narval sequences with the HARPS spectroscopy, assuming two surface abundance inhomogeneities, and fitting the variability of the first moment of the He I 6678 Å line, we updated the rotation period of HD 43317 to $P_{\rm rot} = 0.897673(4)$ d. Our value for the rotation period is compatible with the value determined by Pápics et al. (2012), derived from the CoRoT photometry.

Using the LSD technique, we constructed mean intensity and polarization line profiles for each Narval sequence using three line masks. The rotational modulation of the derived values for the longitudinal magnetic field agreed with a dipolar magnetic field and did not indicate that any substantial quadrupolar contribution was needed to describe the current spectropolarimetric data set. Thanks to the precisely derived rotation period, we were able to bin and average spectropolarimetric observations with a similar rotation phase. The longitudinal field measurements of these phase-binned data also agreed with a dipolar magnetic field. Small differences are seen for the derived model and may be caused by the LPVs due to the stellar pulsation modes. The results obtained from the various characterizations agree with those derived by Briquet et al. (2013).

We also attempted to characterize the geometry of the dipolar field by comparing each LSD profile of the phase-binned Narval spectropolarimetry to a grid of synthetic polarization profiles produced by a (de)-centered dipolar magnetic field at the stellar surface. The resulting description of the large-scale magnetic field represented the variability of the Zeeman signature with the rotation phase relatively well, but failed to accurately characterize each observed Stokes V profile. The differences are comparable with the noise level of the LSD Stokes V profiles. We assume that these differences were due to a combination of the mediocre S/N level, the rather small variability of the Stokes V profiles, and the LPVs distorting the LSD Stokes I profiles. Moreover, the derived inclination angle ($i = 55.6 \pm 6.4\,^\circ$) from the model led to an overly small stellar radius for HD 43317. An alternative model with the inclination angle fixed to the value of Pápics et al. (2012) ($i = 30\,^\circ$) resulted in only a slightly worse description of the observed polarization profiles. Hence, constraining the inclination angle

from the spectropolarimetric data only seems to be difficult. The obliquity angle of the magnetic field to the rotation axis seems to be substantial, but less than 90 °, irrespective of the technique used. Similar constraints were obtained for the co-rotating He patches at the stellar surface of HD 43317, placing them close to the magnetic poles.

We deduced that the dipolar magnetic field of HD 43317 is between approximately 1.0 and 1.5 kG from the analytical equations for the longitudinal magnetic field measurements and from the Stokes V modelling. Small discrepancies for the field strength between the two methods occur due to the uncertain inclination angle and the uncertain line broadening. Comparing the derived strength for the magnetic field with theoretical criteria indicates that the surface magnetic field of HD 43317 is sufficiently strong to influence the structure of the stellar interior by imposing uniform rotation in the radiative layer of the star. We attempt to confirm these implications by performing forward seismic modelling in Chapter 7.

Chapter 7

Forward seismic modelling of HD 43317

This chapter is currently under revision as

Forward seismic modelling of the magnetic B-type pulsator HD 43317

B. Buysschaert, C. Aerts, D. M. Bowman, C. Johnston, T. Van Reeth, M. G. Pedersen, S. Mathis and C. Neiner

Astronomy & Astrophysics, 2018, Submitted (16 pages)

Original abstract:

The large-scale magnetic fields detected at the surface of about 10 % of hot stars extend into the stellar interior, where they may alter the structure. Deep inner regions of stars are only observable using asteroseismology. Here, we investigated the pulsating magnetic B3.5V star HD 43317, inferred its interior properties and assessed whether the dipolar magnetic field with a surface strength of B_p=1312 ± 332 G caused different properties compared to those of non-magnetic stars. We analysed the latest version of the star's 150 d CoRoT light curve and extracted 35 significant frequencies, 28 of which were determined to be independent and not related to the known surface rotation period of $P_{\rm rot}$=0.897673 d. We performed forward seismic modelling based on non-magnetic, non-rotating 1D MESA models and the adiabatic module of the pulsation code GYRE, utilizing a grid-based approach. Our aim was to estimate the stellar mass, age, and convective core overshooting. The GYRE calculations

were done for uniform rotation with $P_{\rm rot}$. This modelling was able to explain 16 of the 28 frequencies as gravity modes belonging to retrograde modes with $(\ell, m) = (1, -1)$ and $(2, -1)$ period spacing patterns and one distinct prograde $(2, 2)$ mode. The modelling resulted in a stellar mass $M_\star = 5.8^{+0.1}_{-0.2}\,{\rm M}_\odot$, a central hydrogen mass fraction $X_c = 0.54^{+0.01}_{-0.02}$, and exponential convective core overshooting parameter $f_{\rm ov}$=$0.004^{+0.014}_{-0.002}$. The low value for $f_{\rm ov}$ is compatible with the suppression of near-core mixing due to a magnetic field but the uncertainties are too large to pinpoint such suppression as the sole physical interpretation. We assessed the frequency shifts of pulsation modes caused by the Lorentz and the Coriolis forces and found magnetism to have a lower impact than rotation for this star. Including magnetism in future pulsation computations would be highly relevant to exploit current and future photometric time series spanning at least one year, such as those assembled by the *Kepler* space telescope and expected from the TESS (Continuous Viewing Zone) and PLATO space missions.

7.1 Introduction

We selected the B3.5V star HD 43317 for detailed forward seismic modelling, because it has a well characterized large-scale magnetic field (Briquet et al. 2013, and Chapter 6), and, most importantly, its CoRoT light curve (Convection Rotation and planetary Transits; Baglin et al. 2006) shows a rich frequency spectrum of many g-mode frequencies (Pápics et al. 2012). The spectroscopy of HD 43317 suggested it to be a single star and the spectroscopic analysis indicated a solar-like metallicity, an effective temperature $T_{\rm eff} = 17350 \pm 750\,{\rm K}$ and a surface gravity $\log g = 4.0 \pm 0.1\,{\rm dex}$ (Pápics et al. 2012). Furthermore, the measured rotation velocity is $v \sin i = 115 \pm 9\,{\rm km\,s^{-1}}$ (Pápics et al. 2012) and the rotation period is $P_{\rm rot} = 0.897673(4)\,{\rm d}$ (see Sect. 6.3.2). From the study in Chapter 6, it was also found that the dipolar magnetic field at the surface of HD 43317 has a strength of $1.0 - 1.5\,{\rm kG}$, which should be strong enough to result in uniform rotation in the radiative layer according to theoretical criteria (see Sect. 6.6.3). We note that most studied B- and F-type g-mode pulsators with asteroseismic core-to-envelope rotation rates rotate nearly uniformly. The studied sample with such measurements contains stars that rotate up to about half their critical rotation rate but magnetic measurements are not available for them (Aerts et al. 2017b and Van Reeth et al. submitted).

In this Chapter, we assess the interior properties of HD 43317 from its g modes. Since the CoRoT data underwent a final end-of-life reduction to produce the

version of the light curves in the public data archive, we performed a new frequency extraction in Sect. 7.2 to obtain a conservative list of candidate pulsation mode frequencies. Section 7.3 treats the detailed forward modelling of HD 43317 by coupling 1D stellar structure models with pulsation computations, adopting various hypotheses as explained in the text. We discuss the results and implications of the forward modelling in Sect. 7.4, and summarize and draw conclusions in Sect. 7.5.

7.2 Frequency extraction

7.2.1 CoRoT light curve

CoRoT observed HD 43317 during campaign LRa03 from 30/09/2009 until 01/03/2010, producing high-cadence, high-precision space-based photometry (see Auvergne et al. 2009, for explicit details on the spacecraft and its performance). The total light curve spanned 150.49 d with a median observing cadence of 32 s and was retrieved from the CoRoT public archive[1]. An earlier version of the light curve was analysed by Pápics et al. (2012) to study the photometric variability of HD 43317.

We re-processed the CoRoT light curve by removing obvious outliers indicated by non-zero status flag. We also removed the so-called "in-pasted" observations added by the CoRoT data centre to fill observing gaps. Further, we performed a correction for the (likely instrumental) long-term variability through application of a local linear regression filter, removing all signal with a frequency below $0.05\,\mathrm{d}^{-1}$. We ensured that the periodic variability detected in the data was well above this value and that the amplitudes of the frequencies were not significantly altered by the applied correction. Finally, we converted the flux to parts-per-million (ppm). This corrected light curve is shown in the top panel of Fig. 7.1. Its Rayleigh frequency resolution amounts to δf_{ray}=1/150.49=$0.00665\,\mathrm{d}^{-1}$).

7.2.2 Iterative prewhitening

We utilized the corrected CoRoT light curve to determine the frequencies and amplitudes of the periodic photometric variability by means of iterative prewhitening. This approach is appropriate for intermediate- and high-mass pulsators (e.g., Degroote et al. 2009b). To deduce the significance of a frequency

[1] Available at `http://idoc-corot.ias.u-psud.fr/sitools/client-user/COROT_N2_PUBLIC_DATA/project-index.html`.

Table 7.1: Significant frequencies in the CoRoT light curve of HD 43317 ordered and labelled by increasing frequency. For each frequency, we provided the amplitude and its signal-to-noise level (S/N) after the iterative prewhitening. We also provided the formal errors computed by a non-linear least-squares (NLLS). The global amplitude error is approximate and was not used in the forward modelling. When applicable, we indicate the identification of the frequency following Sect. 7.2.3 and 7.3.

	Frequency Value $[\mathrm{d}^{-1}]$	Formal δf from NLLS $[10^{-4}\mathrm{d}^{-1}]$	Amplitude [ppm] ± 1	S/N	Identification
f_1	0.22323	0.14	228	8.8	
f_2	0.39059	0.39	83	4.5	
f_3	0.52900	0.33	98	5.0	
f_4	0.69162	0.50	65	4.2	g mode
f_5	0.75289	0.23	140	6.2	g mode
f_6	0.82781	0.41	80	4.7	g mode
f_7	0.87523	0.28	115	5.2	g mode
f_8	0.92786	0.24	135	5.8	g mode
f_9	0.99541	0.32	1013	20.7	g mode
f_{10}	1.07137	0.24	136	6.0	
f_{11}	1.10039	0.02	1456	21.3	g mode
f_{12}	1.11457	0.18	196	6.3	f_{rot}
f_{13}	1.17536	0.05	672	16.9	g mode
f_{14}	1.22798	0.39	82	4.9	g mode
f_{15}	1.34244	0.17	209	7.2	g mode
f_{16}	1.35291	0.40	86	4.9	g mode
f_{17}	1.50345	0.20	165	8.3	
f_{18}	1.64825	0.43	75	5.2	$2f_6$
f_{19}	1.68418	0.08	427	13.5	
f_{20}	1.70454	0.14	232	8.6	g mode
f_{21}	1.81560	0.07	457	11.8	g mode
f_{22}	2.09539	0.19	168	7.9	$f_9 + f_{11}$
f_{23}	2.15501	0.25	131	9.2	
f_{24}	2.17658	0.21	155	8.7	$f_9 + f_{13}$
f_{25}	2.22787	0.24	139	9.5	$2f_{\mathrm{rot}}$
f_{26}	2.26314	0.21	156	8.8	
f_{27}	2.74964	0.29	112	10.2	
f_{28}	3.31881	0.27	121	11.0	$3f_{\mathrm{rot}}$
f_{29}	3.49578	0.26	125	10.4	g mode
f_{30}	3.57826	0.40	82	9.6	
f_{31}	4.33105	0.06	557	34.0	g mode
f_{32}	5.00466	0.45	72	8.2	g mode
f_{33}	5.02538	0.50	66	8.1	
f_{34}	5.49930	0.34	95	11.1	$2f_{27}$
f_{35}	6.35786	0.45	71	12.5	

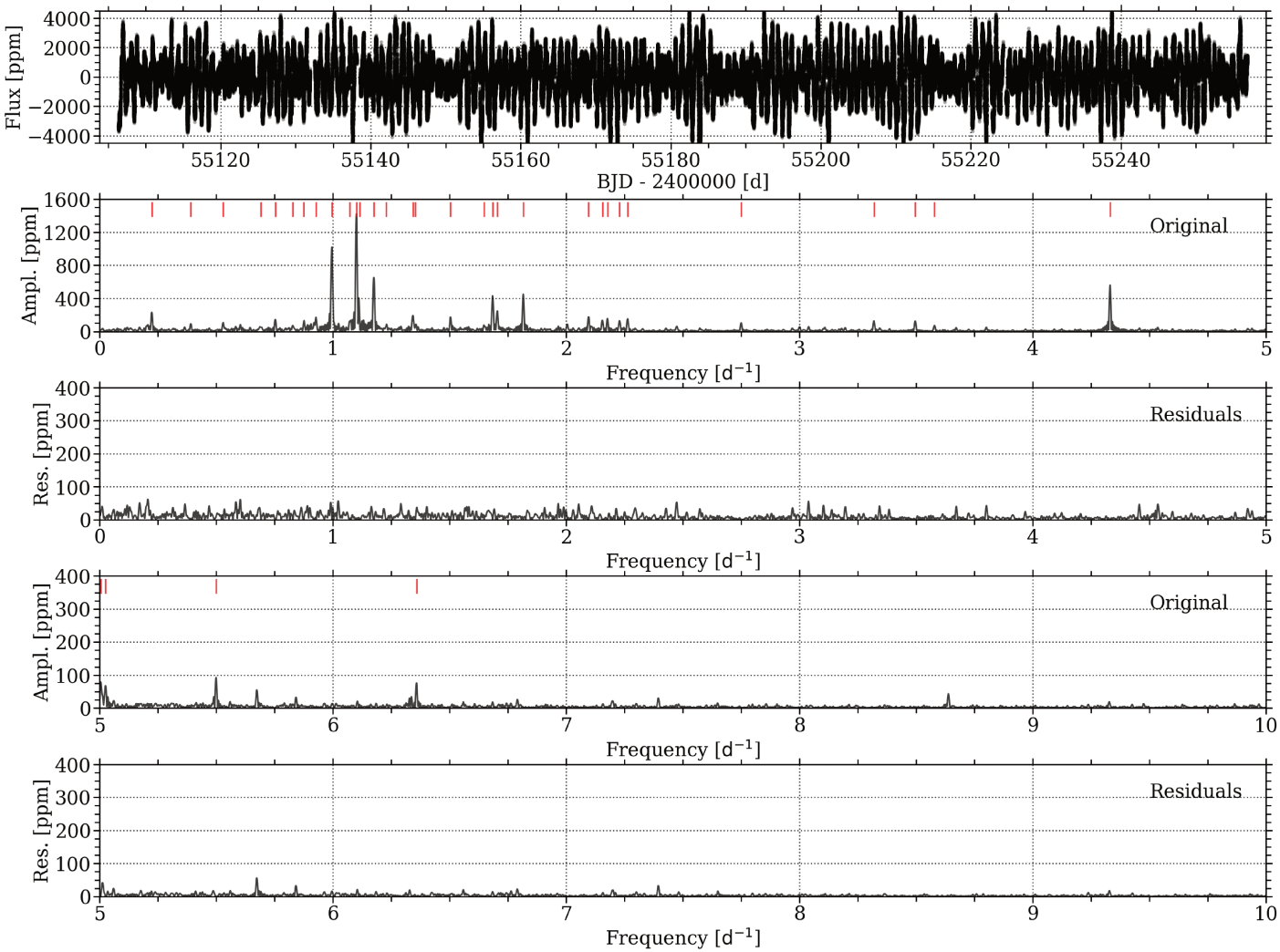

Figure 7.1: CoRoT light curve (*top*) and the corresponding Lomb-Scargle periodograms (*2nd* and *4th row* for increased visibility) of HD 43317. The 35 significant frequencies are indicated by the red tick marks in the upper parts of the periodogram panels. Corresponding periodograms of the residual light curve are given in panels on the *3rd* and *5th row*.

in the ten times oversampled Lomb-Scargle periodogram (Lomb 1976; Scargle 1982), we relied on its signal-to-noise (S/N) level. A frequency was accepted if it had a S/N$\leq$ 4 in amplitude (Breger et al. 1993), where the noise level was computed in a frequency window of $1\,\mathrm{d}^{-1}$ centered at the frequency peak after its corresponding variability was prewhitened. It has been demonstrated (see e.g., Degroote et al. 2009b; Pápics et al. 2012; Degroote et al. 2012) that such a S/N criterion is more appropriate over the false alarm probability (i.e., p-criterion) due to the correlated nature and the noise properties of CoRoT data. The narrow frequency window of $1\,\mathrm{d}^{-1}$ was chosen over wider frequency windows to have a conservative frequency list for the subsequent modelling procedure.

We performed the iterative prewhitening in the frequency domain spanning from $0 - 10\,\mathrm{d}^{-1}$. No significant pulsation frequencies occurred at higher values, and aliasing structure due to the satellite-orbit frequency at $f_{\mathrm{sat}} = 13.97\,\mathrm{d}^{-1}$ is not of interest for the interpretation of the modes. In total, we deduced 35 independent significant frequencies with values ranging from $0.2232\,\mathrm{d}^{-1}$ up to $6.3579\,\mathrm{d}^{-1}$. We provide the optimised frequency and amplitude values after non-linear least-squares fitting in the time domain in Table 7.1, as well as their corresponding S/N values. We also mark these frequencies in the periodogram of the CoRoT light curve, together with the periodogram of the residual light curve, in Fig. 7.1. The formal frequency and amplitude errors following the method of Montgomery & O'Donoghue (1999) were calculated, and these formal errors are also listed in Table 7.1. We recall that amplitudes were not used in the subsequent in the modelling. It is well known that such formal error estimates grossly underestimate the true errors, because of the simplistic assumption of uncorrelated data with white Gaussian noise. This underestimation is particularly prominent in the case of CoRoT data for g-mode pulsators, as these are highly correlated in nature and are subject to heteroscedastic errors (see Degroote et al. 2009b). Correcting for these two properties is far from trivial but leads to at least one and possibly two orders of magnitude increase for the frequency errors given in Table 7.1.

7.2.3 Selecting the individual mode frequencies

Forward seismic modelling is commonly done by fitting the frequencies of independent pulsation modes. Hence, the frequencies extracted from the CoRoT photometry of HD 43317 by the iterative prewhitening needed to be filtered for combination frequencies. For this reason, we limited the frequency list to values that could not be explained by frequency harmonics or low-order (2 or 3) linear combinations of the five highest amplitude frequency peaks (following the method of e.g., Kurtz et al. 2015; Bowman 2017). Low-order combination

or harmonic frequencies typically have a smaller amplitude than the individual parent mode frequencies. Thus, we identified a frequency as a combination frequency if it had a smaller amplitude than the parent frequencies. We also excluded frequencies that corresponded to the known rotation frequency of the star, $f_{\rm rot} = 1.113991(5)\,{\rm d}^{-1}$ (see Sect. 6.3.2), and its harmonics.

By using these various criteria, we removed a total of seven frequencies from the list (see Table 7.1) and identified the remaining 28 as candidate pulsation mode frequencies for the forward seismic modelling.

7.3 Forward seismic modelling

7.3.1 Setup

To determine the stellar structure of HD 43317, we computed a grid of non-rotating, non-magnetic 1D stellar structure and evolution models employing MESA (v8118, Paxton et al. 2011, 2013, 2015). For each MESA model in the grid, we computed linear adiabatic pulsation mode frequencies of dipole and quadrupole geometries using the pulsation code GYRE (v4.1, Townsend & Teitler 2013). These theoretical predictions for the pulsation mode frequencies were then quantitatively compared to the frequencies extracted from the CoRoT light curve to deduce the best fitting MESA models. Such a grid-based modelling approach has been successfully used earlier to interpret the pulsation mode frequencies of g-mode pulsations in rotating stars based on *Kepler* space photometry (e.g., Van Reeth et al. 2016 for γ Dor pulsators and Moravveji et al. 2016 for SPB stars). A good grid set up requires appropriate evaluation of the effect of the choices for the input physics of stellar models on the predicted pulsation frequencies. For g modes in stars with a convective core, a global assessment for non-magnetic pulsators was recently offered by Aerts et al. (submitted). These authors showed that typical uncertainties for the theoretical predictions of low-degree g-mode pulsation frequencies range from 0.001 to $0.01{\rm d}^{-1}$, depending on the specific aspect of the input physics that is being varied. The grid of MESA models in this paper was constructed accordingly.

Compared to the forward modelling of rotating g-mode pulsators based on *Kepler* space photometry, the case of HD 43317 is hampered by two major limitations: i) the ten times poorer frequency resolution of the data that led to fewer significant frequencies and prevented mode identification from period spacing patterns; ii) the unknown effect of a magnetic field in the theoretical prediction of the pulsation frequencies. For this reason, the MESA grid was limited to the minimum number of free stellar parameters to be estimated for meaningful

seismic modelling: the stellar mass $M_\star$, the central hydrogen mass fraction X_c (as a good proxy for the age), and the convective core overshooting. For the latter, we used an exponential overshooting description with parameter $f_{\rm ov}$. Each of these three parameters were allowed to vary in a sensible range appropriate for B-type g-mode pulsators and using discrete steps. The stellar mass ranged from $4.0\,{\rm M}_\odot$ to $8.0\,{\rm M}_\odot$, with a step of $0.5\,{\rm M}_\odot$. For each of these masses, MESA models were evolved from the zero-age main-sequence (ZAMS), corresponding to $X_c{\sim}0.70$, to the terminal-age main-sequence (TAMS), defined as $X_c{=}0.001$; we saved the stellar structure models at discrete X_c steps of 0.01. The parameter for the exponential convective core overshooting, $f_{\rm ov}$, is a dimensionless quantity expressed in units of the local pressure scale height; it was varied from 0.002 up to 0.040, with a step of 0.002. We refer to Freytag et al. (1996), Herwig (2000) and Pedersen et al. (2018) for explicit descriptions of this formulation of core overshooting. We followed the method of Pedersen et al. (2018) to set the exponential overshooting in MESA, where we employed a $f_0 = 0.005$. All other aspects of the input physics were kept fixed following the guidelines in Aerts et al. (submitted). In particular, a solar initial metallicity was adopted according to the spectroscopic results based on a NLTE abundance analysis by Pápics et al. (2012). The chemical mixture was taken to be the solar one from Asplund et al. (2009). We used the opacity tables from Moravveji (2016). Further, we relied on the Ledoux criterion to determine the convection boundaries and adopted the mixing length theory by Cox & Giuli (1968), with mixing length parameter $\alpha_{\rm mlt}{=}2.0$ based on the solar calibration by Christensen-Dalsgaard et al. (1996). We fixed the semi-convection parameter $\alpha_{\rm sc}{=}0.01$ and included additional constant diffusive mixing in the radiative region $D_{\rm ext}{=}10\,{\rm cm}^2\,{\rm s}^{-1}$ following Moravveji et al. (2016). The MESA computations were started from pre-computed pre-main-sequence models that come with the installation suite of the code.

For each of the MESA models in the grid, we computed the adiabatic pulsation frequencies for dipole ($\ell{=}1$) and quadrupole ($\ell{=}2$) g modes with GYRE, given that recent *Kepler* data of numerous rotating F-and B-type g-mode pulsators all revealed such low-degree modes (e.g., Van Reeth et al. 2016; Pápics et al. 2017; Saio et al. 2017). The effects of rotation on the pulsation mode frequencies were included in the GYRE calculations by enabling the traditional approximation (see e.g., Eckart 1960; Townsend 2003). While doing so, we assumed that the star is a rigid rotator with $f_{\rm rot}{=}1.113991\,{\rm d}^{-1}$, as determined from the magnetometric analysis (at the stellar surface; see Sect. 6.3.2) and following the findings by Aerts et al. (2017b) and Van Reeth et al. (submitted). We computed all dipole and quadrupole g modes with radial orders from $n_g{=}-1$ to $n_g{=}-75$.

We adopted a quantitative frequency matching approach and compared the GYRE pulsation mode frequencies with the observed CoRoT frequencies, as

is common practice in forward seismic modelling. As such, we determined the closest model frequency to an observed frequency, and used these to compute the reduced χ^2 value of the fit. While doing so, any predicted model frequency was allowed to match only one observed frequency. The reduced χ^2 values were defined as:

$$\chi^2 = \frac{1}{N-k-1} \sum_{i=1}^{N} \left(\frac{f^i_{\rm obs} - f^i_{\rm mod}}{\delta f_{\rm ray}} \right)^2 , \tag{7.1}$$

with $N > 4$ the total number of frequencies included in the fit, $k = 3$ the number of free parameters to estimate (i.e., the three input parameters of the MESA grid), $f^i_{\rm obs}$ the considered detected frequency in the CoRoT data, $f^i_{\rm mod}$ the theoretically predicted GYRE pulsation mode frequency, and $\delta f_{\rm ray}$ the Rayleigh frequency resolution of the CoRoT light curve. The square of the latter was taken to be a good overall estimate of the variance that encapsulated the frequency resolution of the CoRoT data and the errors on the theoretical frequency predictions by GYRE, given that the formal errors in Table 7.1 were unrealistically small and the theoretical predictions were of similar order of magnitude than the Rayleigh limit for the data set of HD 43317. Moreover, due to lack of an *a priori* mode identification and evolutionary status of the star, it was recommendable to give equal weight to each of the detected frequencies in the fitting procedure because the mode density varies considerably during the evolution along the main sequence. We discuss this issue further in the following sections.

During the forward modelling of HD 43317, the χ^2 value of the fit to the GYRE frequencies of a given MESA model was not the only diagnostic. We also considered the location of the best MESA models (i.e., those with the lowest χ^2 value) in the Kiel diagram to investigate how unique the best solution was. In case the parameters of the MESA models were well constrained by the fitting process, we anticipated the best models to lie within the same location in the Kiel diagram representing a unique χ^2 valley in the 3D parameter space of the MESA grid, which then allowed us to create simplistic confidence intervals for the free parameters, as explained below. This method was a necessary complication compared to the modelling of *Kepler* stars because no obvious independent period spacing pattern spanning several consecutive radial orders could be identified for HD 43317. Hence the straightforward method for mode identification using the technique employed by Van Reeth et al. (2015, 2016) was not possible for our CoRoT target star.

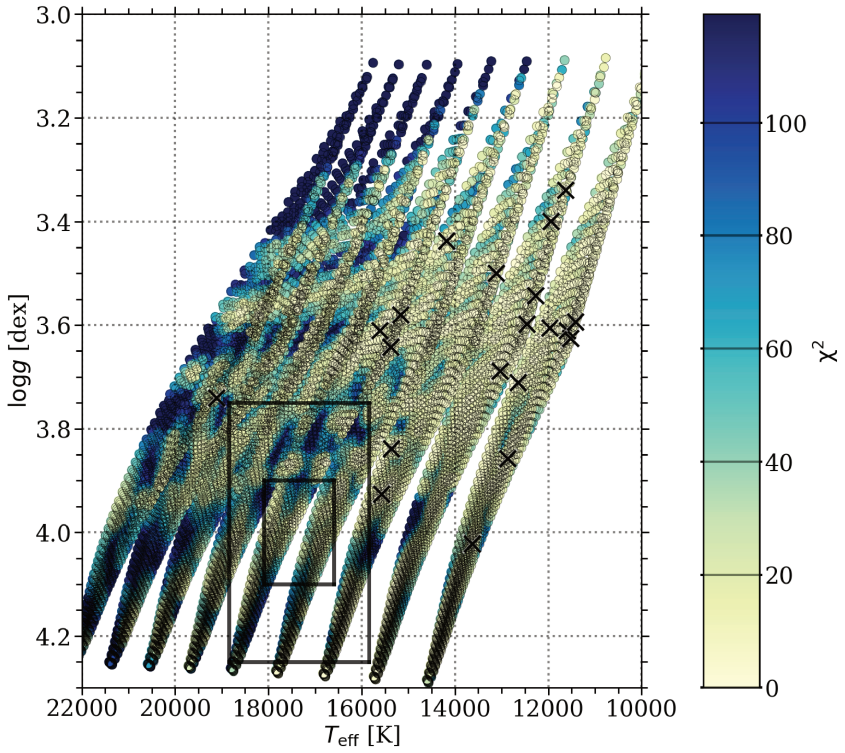

Figure 7.2: Kiel diagram showing the results of blind forward modelling based on all 28 pulsation mode frequencies. The colour scale indicates the χ^2 level and the black crosses represent the location of the 20 best fitting MESA models. The 1σ and 2σ confidence intervals for the derived spectroscopic parameters by Pápics et al. (2012) are shown by the black boxes.

7.3.2 Blind forward modelling

Although the CoRoT data were sufficient to detect g modes in B-type stars, the relatively large Rayleigh frequency resolution did not allow for unambiguous mode identification in the case of HD 43317 due to its fast rotation. This is different from the case of the CoRoT ultra-slow rotator HD 50230, whose g-mode periods constituted the first discovered period spacing pattern that led to mode identification for a main-sequence star thanks to the absence of a slope in its pattern (Degroote et al. 2010a). However, although not available for HD 43317, the ten times longer light curves observed by the *Kepler* mission for tens of g-mode pulsators meanwhile provided critical information on the types of modes expected in such rapidly rotating pulsators (e.g., Van Reeth et al. 2015; Pápics et al. 2017; Saio et al. 2017, for sample papers with B- and F-type stars). This led these authors to the conclusion that almost all detected g modes were dipole or quadrupole modes, irrespective of the rotation rate of the g-mode pulsator. We relied on this knowledge from *Kepler* to guide and perform our modelling of

HD 43317.

Without a period spacing pattern to identify (some of) the 28 candidate pulsation mode frequencies, we first permitted the observed frequencies to match with any of the theoretical frequencies of the predicted dipole or quadrupole mode geometries for a given MESA model, without taking the constraints from spectroscopy into account. The locations of the 20 models with the lowest χ^2 value resulting from such "blind" modelling in the Kiel diagram are shown in Fig. 7.2. These models corresponded to various stellar masses, spanning the entire MESA grid. Moreover, the lowest $\chi^2 < 1$ were reached for models with a low X_c value, corresponding with the lower $\log g$ values in the grid. This result is a common feature of such unconstrained forward modelling without any restriction on the identification of the modes or on the evolutionary stage. Indeed, the mode density in the frequency region of interest is much higher for models near the TAMS than for less evolved stages (see Fig. 7.3). Hence, the χ^2 values will always be artificially smaller for evolved models near the TAMS than for less evolved models in absence of mode identification. Moreover, the majority of these best models relied on zonal mode frequencies, while many of these are unresolved in the CoRoT data (see Fig. 7.3).

This exercise illustrated that blind forward modelling without spectroscopic constraints is not a good strategy in the absence of mode identification. Indeed, the spectroscopic parameters of these best models did not agree with the observationally derived 2σ confidence intervals by Pápics et al. (2012), i.e., $T_{\rm eff} = 17350 \pm 1500$ K and $\log g$=4.0 $\pm$ 0.25 dex. Therefore, a dedicated strategy for the forward seismic modelling of HD 43317 was required.

7.3.3 Conditional forward modelling

We adopted various hypotheses in the best model selection for the estimation of the three stellar parameters ($M_\star, X_c, f_{\rm ov}$). The first hypothesis was that any selected MESA model should comply with the spectroscopic properties of the star. Thus, the effective temperature, $T_{\rm eff}$, and the surface gravity, $\log g$, were demanded to be consistent with those derived from high-precision spectroscopy. As such, we excluded any MESA models that did not agree with the 2σ confidence intervals of the combined spectroscopic analysis done by Pápics et al. (2012). This assumption resulted in the exclusion of MESA models near the TAMS, leaving only models with comparable mode density.

The next assumption was that any appropriate MESA model should be able to explain several of the highest-amplitude frequencies as pulsation mode frequencies. Indeed, it did not make sense to accept models that explained low-amplitude modes while they did not lead to a good description of the dominant

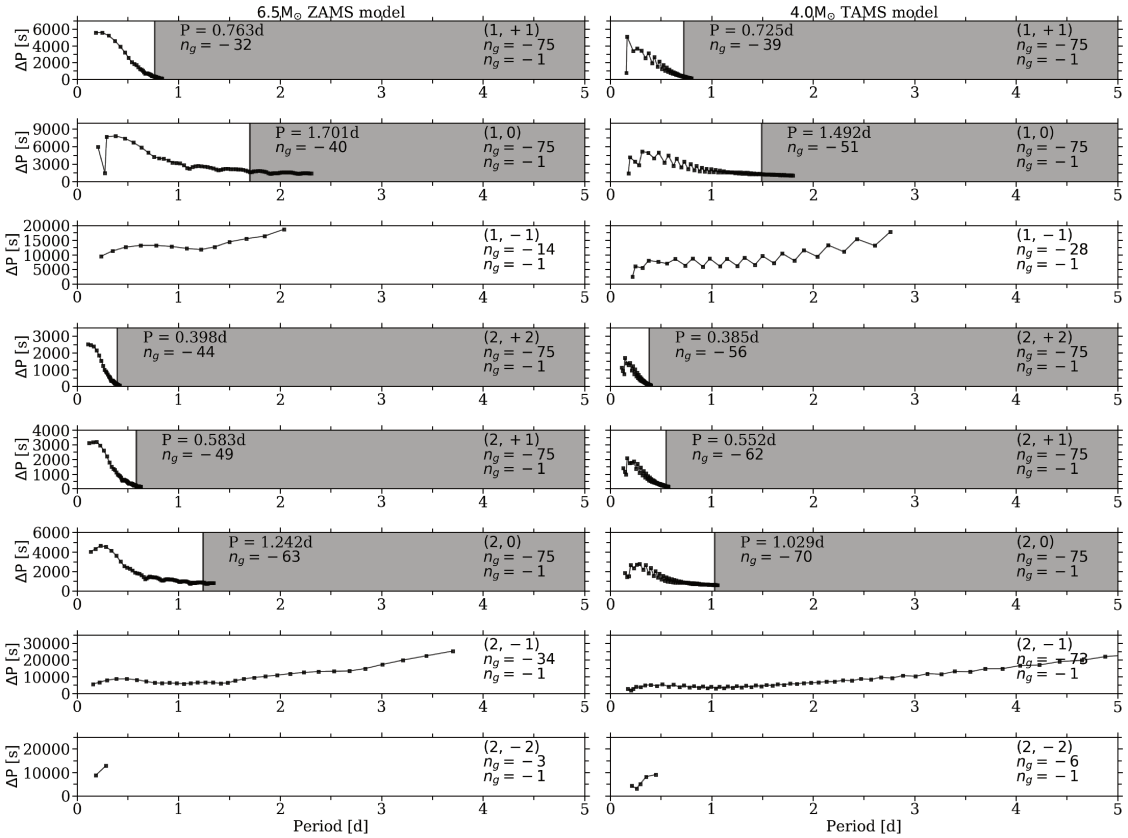

Figure 7.3: Period spacing patterns, as computed by GYRE and accounting for rigid rotation at the rate of HD 43317, using the traditional approximation, for two demonstrative MESA models. *Left:* a $6.5\,M_\odot$ MESA model at the ZAMS; *right:* a $4.0\,M_\odot$ model close to the TAMS. Each row represents the theoretical period spacing pattern for a given mode geometry, with the range of radial orders as listed. Grey boxes correspond to regions where the frequency difference between theoretical frequencies of modes with consecutive radial order is smaller than the Rayleigh frequency resolution of the CoRoT data; these ranges thus cannot be used. The corresponding pulsation period and radial order for the limiting theoretical mode to be used in the modelling for that given MESA model and mode geometry is listed in each upper left corner.

modes. We (arbitrarily) placed the cut-off limit at an amplitude of 500 ppm, thus requiring that f_9, f_{11}, f_{13}, and f_{31} were matched. Using spectroscopic mode identification techniques, Pápics et al. (2012) identified f_{31} to be a prograde (ℓ, m)=$(2, +2)$ mode[2]. We thus fixed the mode identification of this particular frequency during the modelling process. The other three dominant modes in the CoRoT photometry were not detected in the spectroscopy. This is not so

[2]We defined modes with $m > 0$ as prograde modes and $m < 0$ as retrograde modes.

surprising, given that photometric and spectroscopic diagnostics are differently affected by mode geometries (see Chapter 6 in Aerts et al. 2010) and that we have no information on the intrinsic amplitudes of excited modes. Hence, we were not able to use the identification of f_{31} to place constraints on the degree of the other highest-amplitude modes. However, given the dominance of a sectoral mode in the spectroscopy, we excluded a pole-on view of the star, because it would correspond to an angle of complete cancellation for such a mode (at $i = 0\,^{\circ}$; see e.g., Aerts et al. 2010). As such, Pápics et al. (2012) constrained the inclination angle to be $i \in [20^{\circ}, 50^{\circ}]$.

We considered different hypotheses on the identification of the modes, as described in the following sections. These hypotheses followed from comparison of the theoretical period spacing patterns with those from the detected frequencies (comparing Table 7.1 to Fig. 7.3). For most of the $m > 0$ modes, the frequency difference between modes of consecutive radial order was smaller or comparable to the Rayleigh limit of the CoRoT data. The same is true for most zonal modes, especially for the (ℓ, m)=$(2, 0)$ modes. As such, creating a period spacing pattern spanning consecutive radial orders for such modes from the observed frequencies was not meaningful with the frequency resolution of the CoRoT data. Therefore, we assumed that the observed frequencies were $m = -1$ modes, unless explicit evidence was available (e.g., for f_{31} from spectroscopy). We then included additional observed frequencies under the made hypotheses.

With this piece-wise conditional modelling, we intended to constrain both the parameters of HD 43317 and the mode geometry of the detected frequencies. The theoretical period spacing patterns of the best models at any given step denoted which observed frequency could be additionally included in the frequency matching. Detected frequencies were considered for inclusion if they were sufficiently close to a theoretical frequency predicted by the best models. Ideally, this modelling scheme should lead to a well clustered group of MESA models in the Kiel diagram for a large number of the 28 detected frequencies, leading to an estimate on their mode geometry. To ensure robustness and reproducibility of a hypothesis during the forward seismic modelling, we defined the following criteria for any good solution:

- At least five detected frequencies must be accounted for in the use of Eq. (7.1).
- The location of the 20 best MESA models in the Kiel diagram must remain consistent with the 2σ spectroscopic error box.

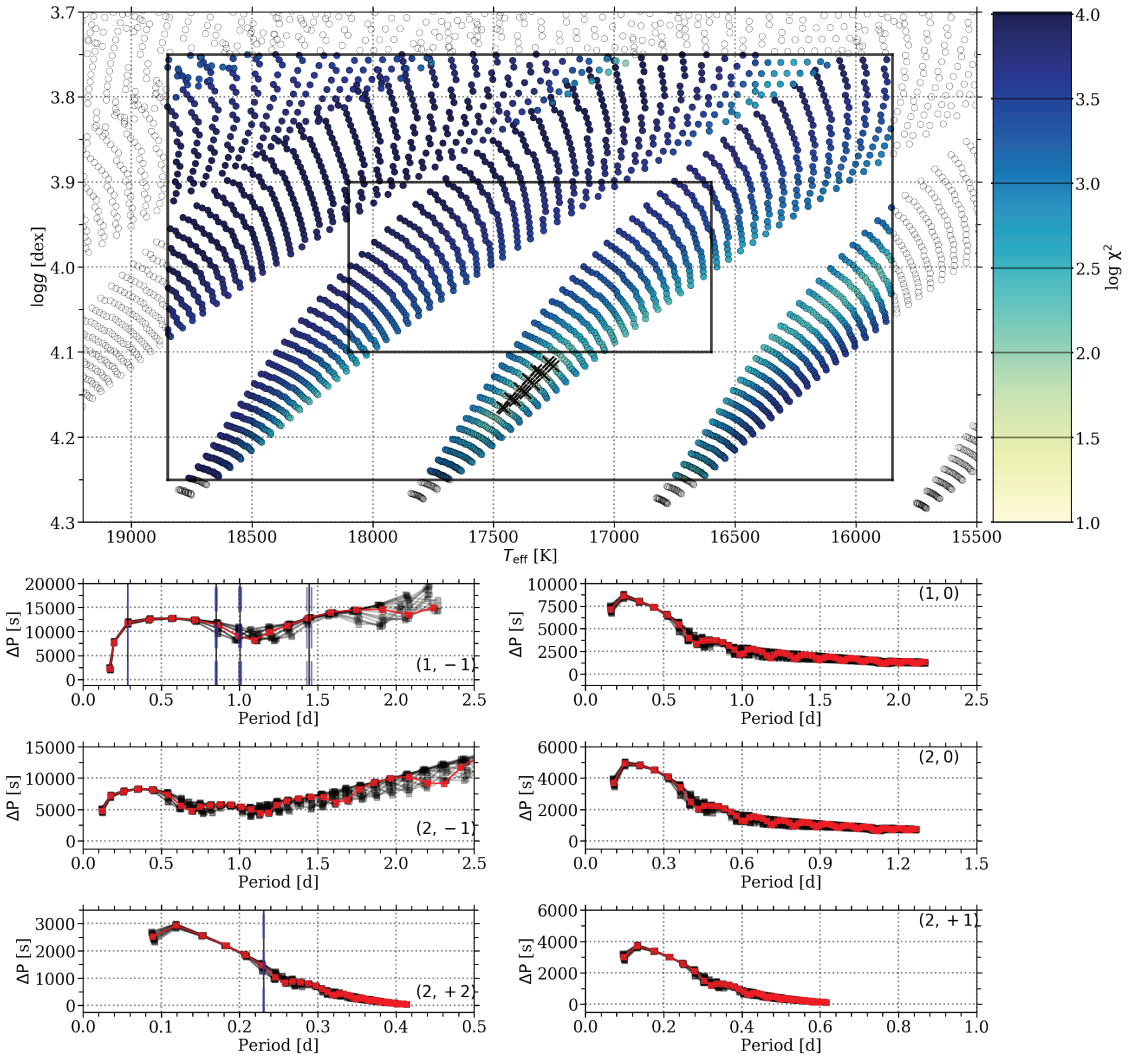

Figure 7.4: Summary plot for the results of the forward modelling of HD 43317 based on the dipole mode hypothesis (see text). *Top*: Kiel diagram showing the location of the MESA models whose GYRE frequencies come closest to the detected frequencies. The color scale represents the χ^2 value (see Eq. (7.1)), the open symbols indicate MESA models outside the spectroscopic limits of the star deduced by Pápics et al. (2012, with the 1σ and 2σ limits indicated by the black boxes), and the black crosses represent the location of the 20 best fitting MESA models. *Bottom panels*: period spacing patterns of the 20 best fitting MESA models for various mode geometries (black lines and squares). Those of the best description are shown in red. The observed pulsation mode periods used in the χ^2 are indicated by the vertical grey lines, while the vertical blue regions indicate the observed period range taking into account the Rayleigh limit of the data. Only $(1, -1)$ modes (i.e., f_4, f_9, f_{13}, and f_{29}, as well as the f_{31} as a $(2, +2)$ mode) were relied upon to achieve the frequency matching.

7.3.4 Dipole retrograde mode hypothesis

As a first hypothesis, we considered the case that the three dominant pulsation mode frequencies f_9, f_{11}, f_{13} corresponded to dipole retrograde modes. Dipole modes were by far the most frequently detected ones in space photometry of g-mode pulsators (e.g., Pápics et al. 2014; Moravveji et al. 2016; Van Reeth et al. 2016). At the measured $v \sin i$ and $f_{\rm rot}$ of HD 43317, most of the detected g-mode frequencies in pulsators with *Kepler* photometry would belong to a series of $(1, -1)$ modes (Van Reeth et al. 2016). As such, it was reasonable to assume that f_9, f_{11}, f_{13} were $(1, -1)$ modes.

Using these three frequencies and f_{31} constrained by spectroscopy,the forward modelling led to models with a mass ranging from $5.0\,{\rm M}_\odot$ up to $6.5\,{\rm M}_\odot$. A comparison of the observed frequencies with the model frequencies suggested that f_{11} was likely not a $(1, -1)$ mode. We thus dropped the requirement on this frequency and repeated the forward modelling with only f_9 and f_{13} as (ℓ, m)=$(1, -1)$ modes and f_{31} as a $(2, +2)$ mode. This returned two families of solutions in the Kiel diagram, namely a group with $M_\star$=$5.0\,{\rm M}_\odot$ with $X_c \approx 0.50$, and a stripe of models with a mass of $5.5\,{\rm M}_\odot$, while X_c decreases from 0.63 to 0.52 and $f_{\rm ov}$ from 0.038 to 0.022. All these models resulted in similar theoretical $(1, -1)$ frequencies and identified f_{29} to have this mode geometry as well. We thus included this observed frequency in the hypothesis and repeated the forward modelling.

The modelling converged to only one family of solutions in the Kiel diagram that corresponded with $M_\star$=$5.5\,{\rm M}_\odot$, $X_c = 0.53 - 0.58$ and $f_{\rm ov}$ ranging from 0.016 to 0.022. These models indicated that the observed frequencies f_3, f_4, f_5, f_6, f_{16} and f_{20} should be part of the $(1, -1)$ period spacing pattern. We included only f_4, because it was the closest match and repeated the modelling with the updated hypothesis.

We recovered the same set of 20 best MESA models with f_4 included in the hypothesis and noted that five additional observed frequencies agreed with the theoretical predictions. Hence, we satisfied our defined criteria. The conclusion of the modelling with this hypothesis is represented in Fig. 7.4. The top panel shows the Kiel diagram with the location of the 20 best MESA models, as well as the χ^2 values of the fitting process to the theoretical GYRE frequencies. The model period spacing patterns of the 20 best fitted models (and the corresponding observed frequencies in the assumption) are given in the bottom panels of Fig.7.4.

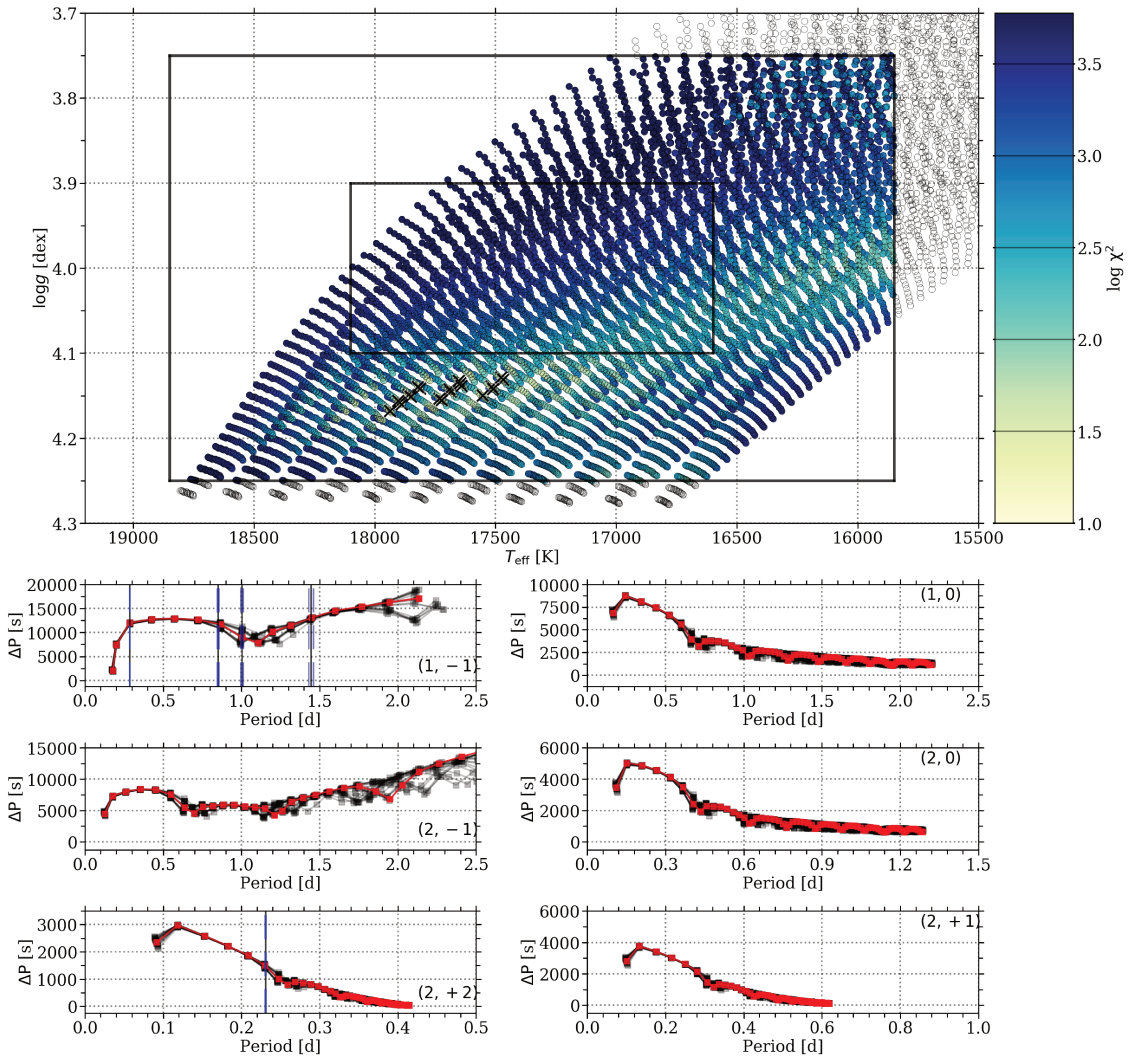

Figure 7.5: Summary plot for the overall forward modelling of HD 43317 using the dipole mode hypothesis on the refined grid of MESA models. The same colour scheme as Fig. 7.4 is used.

7.3.5 Increasing the mass resolution of the MESA grid

To investigate the robustness of our obtained solution shown in Fig. 7.4, we created a new grid of MESA models that had a finer mass resolution. This new grid had the same settings for the micro- and macro-physics as before, but the stellar masses ranged from $5.0\,\mathrm{M}_\odot$ up to $6.0\,\mathrm{M}_\odot$ with a step size of $0.1\,\mathrm{M}_\odot$. We repeated the frequency matching of the five observed frequencies to the GYRE frequencies of the finer grid of models and summarized the result in Fig. 7.5. The 20 best MESA models corresponded to slightly different values for the stellar mass and exponential overshooting factor. These values were unavailable in the coarser grid.

The theoretical frequencies for the already identified $(1, -1)$ modes of the now 20 best models did not alter appreciably compared to those of the solution in the coarse grid, nor did the radial orders change. We included additional identifications as dipole modes, namely f_5, f_6, f_8, f_{16}, f_{20} and f_{32}. The result of the modelling with these ten $(1, -1)$ and one $(2, +2)$ mode is illustrated in Fig. 7.6.

We noted that the location of the 20 best MESA models now moved to slightly lower X_c values when using this more extended frequency list. However, the confidence intervals of these solutions for the different hypotheses still overlapped at a 2σ level, i.e., the location of the best solutions did not move outside the range of their variance. Here, the $\alpha\,\%$ confidence interval is defined by the upper limit on the χ^2 value as

$$\chi^2_\alpha = \frac{\chi^2_{\alpha,k} \cdot \chi^2_{\min}}{k}\,, \tag{7.2}$$

where $\chi^2_{\min}$ is the χ^2 value for the best fit and $\chi^2_{\alpha,k}$ the tabulated value for an $\alpha\,\%$ inclusion of the cumulative distribution function of a χ^2 distribution with $k = 3$ degrees of freedom.

A local minimum in the χ^2 landscape occurred for models with a stellar mass of $5.3\,\mathrm{M}_\odot$ and $X_c \approx 0.40$ (i.e., $T_{\mathrm{eff}} = 16000\,\mathrm{K}$ and $\log g = 4.0\,\mathrm{dex}$), but their χ^2 values were larger than the upper limit of the 2σ confidence interval of the best solutions in the minimum dictated by the spectroscopic limits. This family of second-best models were only compatible at a 3σ level (cf. Fig. 7.8.)

7.3.6 Adding modes with other mode geometry

At this stage, the theoretical frequencies of the best MESA models were able to explain eleven of the 28 observed frequencies of HD 43317. We studied

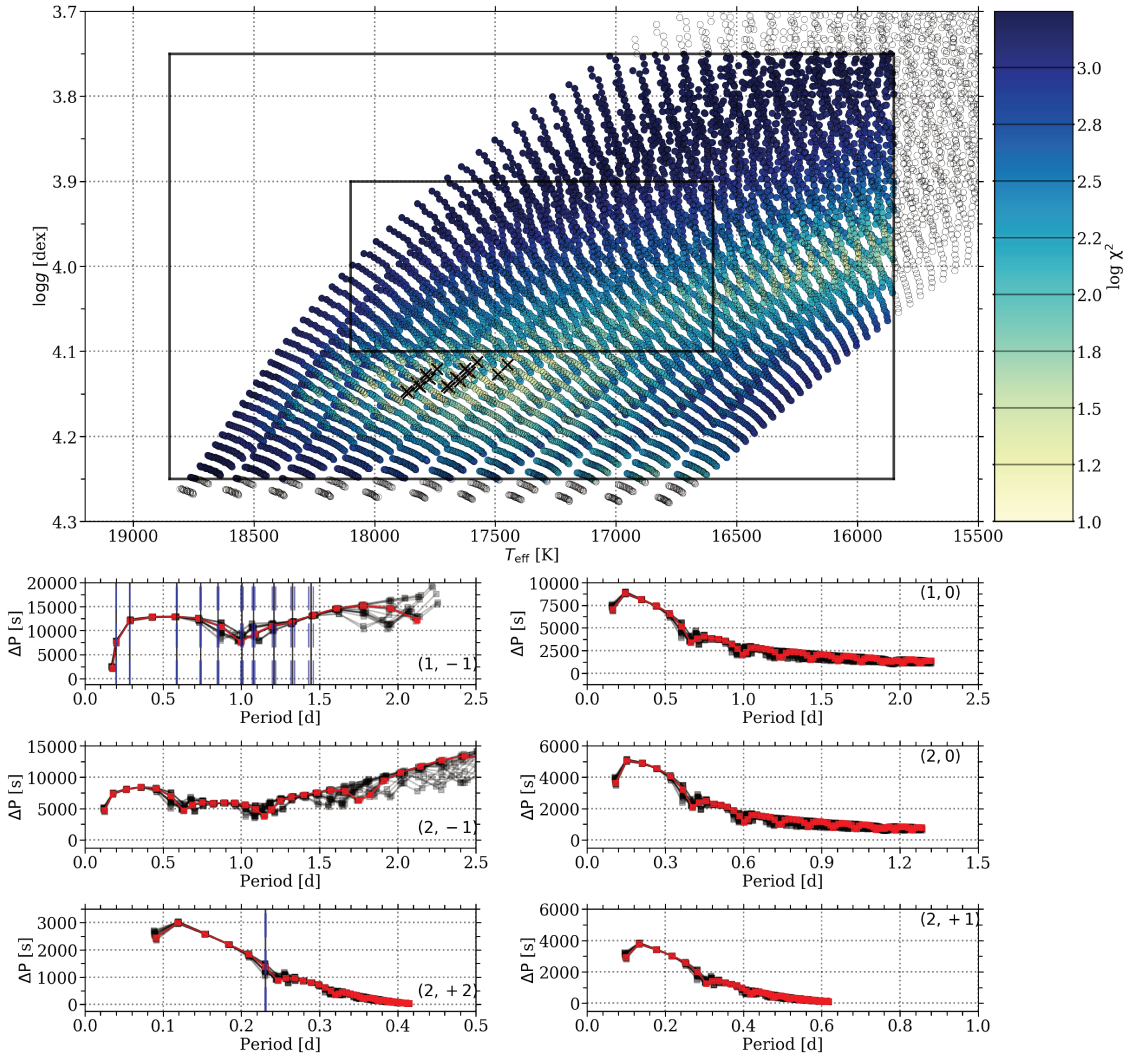

Figure 7.6: Summary plot for the overall forward modelling of HD 43317 using the extended dipole mode hypothesis on the refined grid of MESA models. The same colour scheme as Fig. 7.4 is used.

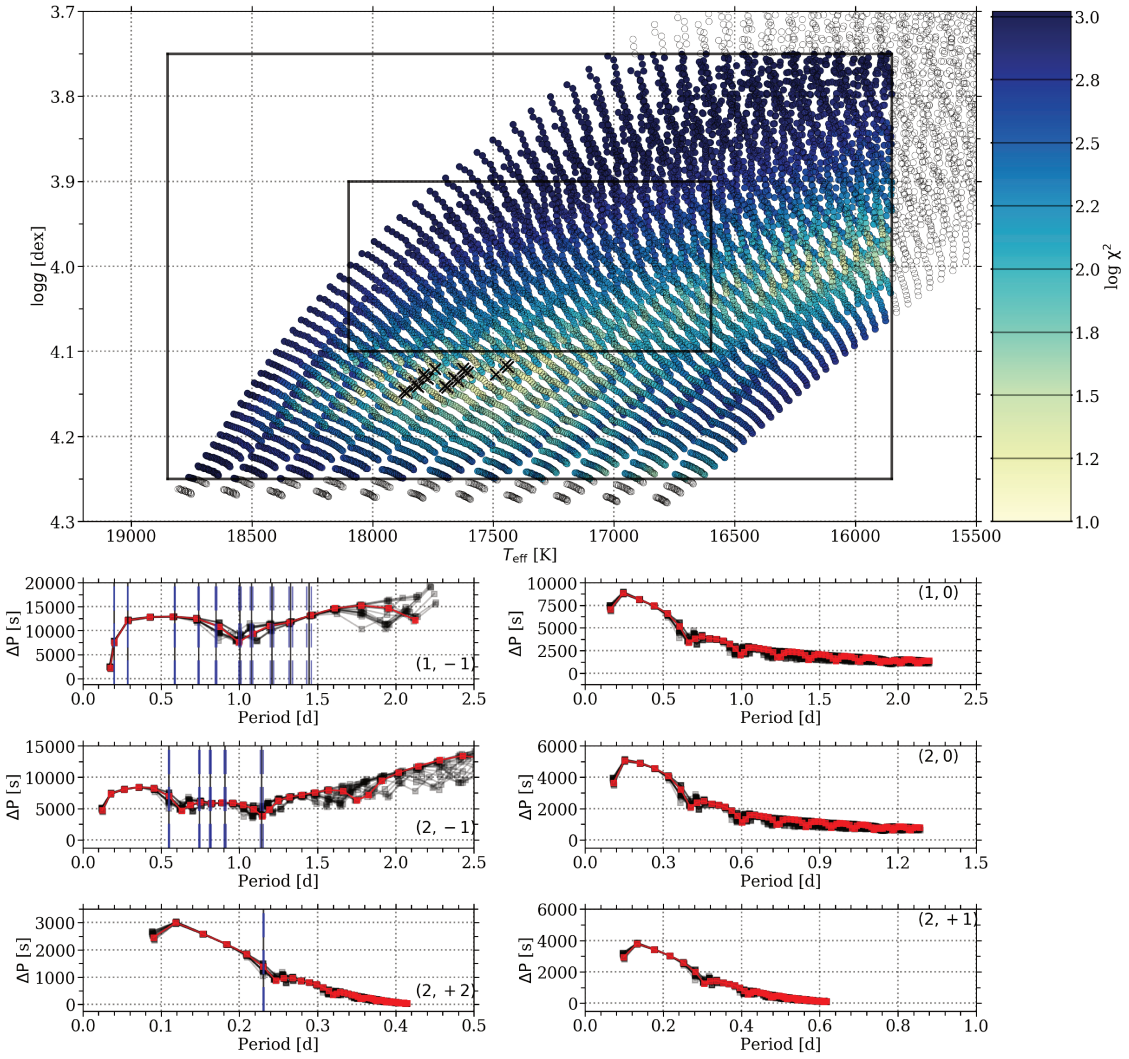

Figure 7.7: Summary plot for the overall forward modelling of HD 43317 using the combined dipole mode hypothesis on the refined grid of MESA models. The same colour scheme as Fig. 7.4 is used.

whether yet unexplained detected frequencies could be associated to pulsation mode frequencies with a different geometry than $(1, -1)$ modes. The frequency density argument made in Sect. 7.3.2 and indicated in Fig. 7.3, showed that it was impossible to resolve zonal and most $m > 0$ modes with the frequency resolution of the CoRoT data set. Hence, we investigated whether theoretically predicted $(\ell, m) = (2, -1)$ modes could explain the additional detected frequencies. Such modes have an angle of least cancellation at 45° (Aerts et al. 2010). This was close to the updated value for the inclination angle $i = 37 \pm 3\,^\circ$ derived in Sect. 7.4.1, validating this assumption. We identified five matches between theoretically predicted $(2, -1)$ mode frequencies and the so far unused frequencies of HD 43317, namely f_7, f_{11}, f_{14}, f_{15} and f_{21}. These were subsequently included in the hypothesis and the modelling was repeated.

The result of this final modelling under the hypothesis that only $(1, -1)$, $(2, -1)$ and $(2, +2)$ modes were observed in the CoRoT photometry of HD 43317 is summarized in Fig. 7.7. The location of the 20 best fitted MESA models did not change by including the five additional $(2, -1)$ mode frequencies. The three estimated physical parameters, as well as some other output variables, are listed in Table 7.2 and the χ^2 distributions for these parameters are shown in Fig. 7.8. Table 7.3 compares the observed frequencies with those predicted by GYRE based on the MESA model with the lowest χ^2. This model has parameters $M_\star$=5.8 $M_\odot$, X_c=0.54, and $f_{\rm ov}$=0.004.

7.4 Discussion

7.4.1 Seismic estimation of the stellar parameters

Instead of using the discrete step size of the grid as the confidence intervals for $M_\star$, X_c, and $f_{\rm ov}$ as deduced from the forward modelling, we used the properties of the χ^2 statistics. We computed the upper limit on the χ^2 value for a 2σ confidence interval (i.e., 95.4 % confidence interval) using Eq. (7.2). We included 16 frequencies in our final fitting process, resulting in 12 degrees of freedom, which led to $\chi^2_{2\sigma}$=12.85. This corresponds to the χ^2 value of the best 19 MESA models (s shown in Fig. 7.8), supporting the visual inspection of the best models during the procedure. The corresponding confidence intervals on the parameters were $M_\star$=$5.8^{+0.1}_{-0.2}$ $M_\odot$, X_c=$0.54^{+0.01}_{-0.02}$, and $f_{\rm ov}$=$0.004^{+0.014}_{-0.002}$. The skewed confidence intervals for $M_\star$ and $f_{\rm ov}$ resulted from a strong correlation between these parameters, as demonstrated in Fig. 7.9. We note that our grid of MESA models was limited from $f_{\rm ov}$=0.002 to 0.040, hence we could not exclude that $f_{\rm ov}$ had an even lower value than 0.002, in particular $f_{\rm ov} = 0.0$. The MESA models within this χ^2 valley had comparable values for the asymptotic period

Table 7.2: Parameters of the 20 best models based on the identification of 16 out of the 28 detected frequencies of HD 43317, ordered by the resulting χ^2 value. For each MESA model, the stellar mass, $M_\star$, central hydrogen mass fraction, X_c, convective core overshooting parameter, $f_{\rm ov}$, stellar radius, $R_\star$, asymptotic period spacing, $\Delta\Pi$, age, effective temperature, $T_{\rm eff}$, surface gravity, $\log g$, and fractional mass of the convective core, q_c, are given. Degeneracies among the stellar parameters occur when only considered the value for the asymptotic period spacing.

χ^2	$M_\star$ [$M_\odot$]	X_c	$f_{\rm ov}$	$R_\star$ [$R_\odot$]	$\Delta\Pi$ [s]	Age [Myr]	$T_{\rm eff}$ [K]	$\log g$ [dex]	q_c
7.23	5.8	0.54	0.004	3.39	12645	28.4	17822	4.14	0.229
7.76	5.8	0.53	0.004	3.43	12619	29.8	17782	4.13	0.226
8.46	5.7	0.54	0.010	3.39	12550	31.9	17652	4.13	0.231
8.82	5.8	0.54	0.006	3.41	12668	29.2	17826	4.14	0.230
8.89	5.7	0.53	0.010	3.43	12532	33.3	17617	4.12	0.229
9.31	5.8	0.53	0.002	3.42	12590	29.2	17772	4.13	0.225
9.40	5.8	0.54	0.002	3.39	12618	27.8	17812	4.14	0.227
9.44	5.8	0.53	0.006	3.44	12645	30.6	17788	4.13	0.227
10.00	5.7	0.53	0.008	3.42	12504	32.7	17605	4.13	0.227
10.15	5.7	0.54	0.008	3.38	12526	31.1	17646	4.14	0.230
10.21	5.7	0.54	0.012	3.40	12575	32.6	17663	4.13	0.232
10.87	5.8	0.55	0.004	3.36	12668	27.0	17859	4.15	0.231
11.58	5.6	0.54	0.016	3.38	12454	35.3	17489	4.13	0.233
11.61	5.7	0.53	0.012	3.44	12558	34.2	17624	4.12	0.230
11.72	5.7	0.55	0.010	3.35	12567	30.3	17690	4.14	0.234
12.05	5.8	0.55	0.006	3.37	12691	27.6	17868	4.15	0.233
12.11	5.8	0.52	0.004	3.47	12591	31.2	17742	4.12	0.223
12.37	5.7	0.55	0.012	3.36	12590	30.9	17701	4.14	0.235
12.41	5.6	0.53	0.016	3.43	12441	37.1	17449	4.12	0.231
13.00	5.6	0.53	0.014	3.42	12415	36.3	17440	4.12	0.230

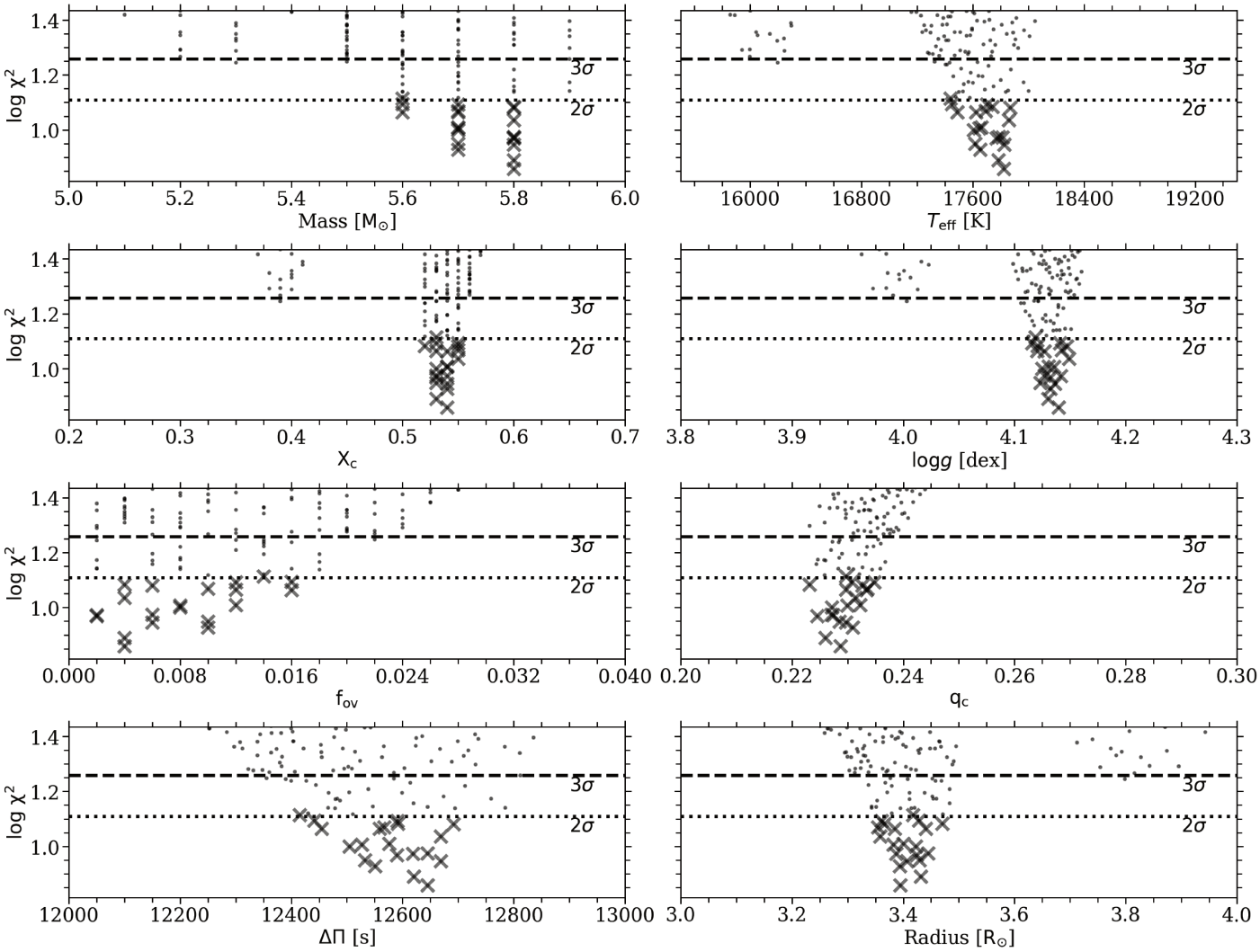

Figure 7.8: Distribution of the χ^2 values, computed during the forward seismic modelling of HD 43317 based on 16 of the 28 observed frequencies, using the refined grid of MESA models. The χ^2 values for the 2σ and 3σ confidence intervals are indicated by the dotted and dashed black line, respectively. The best 20 models are indicated by the black crosses. We refer to Table 7.2 for the description of the physical quantities.

Table 7.3: Comparison between the observed frequencies $f_{\rm obs}$, and the GYRE frequencies of the MESA model resulting in the best description of the CoRoT data of HD 43317 $f_{n_g,l,m}$. We compare the frequency shift due to rotation according to the traditional approximation with the frequency shift due to an internal (purely) poloidal magnetic field. For each observed frequency we provide the best model frequency for the estimated mode geometry. We compare the corresponding zonal pulsation mode frequencies $f_{n_g,l,0}$ with and without the traditional approximation applied to compute the frequencies. The magnetic frequency shift was computed following the approach of Hasan et al. (2005), for the lower and upper limit of the internal magnetic field at the convective core boundary, by extrapolating the surface field inward. We also included the magnetic splitting coefficient S_c and the quantity $\mathcal{I}$.

	$f_{\rm obs}$	n_g	ℓ	m	$f_{n_g,l,m}$	$f_{n_g,l,0}$	$f_{n_g,l,0}$	$f_{\rm shift}$	$f_{\rm shift}$	$f_{\rm shift}$	S_c	$\mathcal{I}$
					model	rot.	no rot.	rot.	26.1 kG	82.4 kG		
	[d^{-1}]				[d^{-1}]	[d^{-1}]	[d^{-1}]	[d^{-1}]	[d^{-1}]	[d^{-1}]	[G^{-2}]	
f_4	0.6916	-11	1	-1	0.6867	1.1927	0.8187	0.3740	0.0210	0.2092	$3.7661 \cdot 10^{-11}$	$1.5487 \cdot 10^{7}$
f_5	0.7529	-10	1	-1	0.7573	1.2595	0.8979	0.3617	0.0159	0.1592	$2.6131 \cdot 10^{-11}$	$1.2925 \cdot 10^{7}$
f_6	0.8278	-9	1	-1	0.8381	1.3388	0.9923	0.3465	0.0125	0.1250	$1.8565 \cdot 10^{-11}$	$1.1215 \cdot 10^{7}$
f_7	0.8752	-15	2	-1	0.8720	1.6623	1.0462	0.6161	0.0110	0.1101	$1.5515 \cdot 10^{-11}$	$4.3758 \cdot 10^{7}$
f_8	0.9279	-8	1	-1	0.9222	1.4236	1.0933	0.3303	0.0104	0.1041	$1.4035 \cdot 10^{-11}$	$1.0293 \cdot 10^{7}$
f_9	0.9954	-7	1	-1	1.0037	1.5086	1.1943	0.3143	0.0097	0.0972	$1.1994 \cdot 10^{-11}$	$1.0496 \cdot 10^{7}$
f_{11}	1.1004	-11	2	-1	1.1268	1.9545	1.4108	0.5438	0.0029	0.0288	$3.0120 \cdot 10^{-12}$	$1.5448 \cdot 10^{7}$
f_{13}	1.1754	-6	1	-1	1.1483	1.6594	1.3708	0.2887	0.0086	0.0861	$9.2633 \cdot 10^{-12}$	$1.0679 \cdot 10^{7}$
f_{14}	1.2280	-10	2	-1	1.2198	2.0621	1.5454	0.5167	0.0022	0.0220	$2.0968 \cdot 10^{-12}$	$1.2904 \cdot 10^{7}$
f_{15}	1.3424	-9	2	-1	1.3337	2.1920	1.7058	0.4861	0.0017	0.0173	$1.4932 \cdot 10^{-12}$	$1.1195 \cdot 10^{7}$
f_{16}	1.3529	-5	1	-1	1.3775	1.8992	1.6455	0.2537	0.0063	0.0626	$5.6119 \cdot 10^{-12}$	$9.3225 \cdot 10^{6}$
f_{20}	1.7045	-4	1	-1	1.7358	2.2719	2.0601	0.2118	0.0045	0.0451	$3.2246 \cdot 10^{-12}$	$8.3961 \cdot 10^{6}$

Continued on next page

Table 7.3 – continued from previous page

f_{21}	1.8156	-6	2	-1	1.8191	2.7238	2.3408	0.3829	0.0012	0.0121	$7.5960 \cdot 10^{-13}$	$1.0725 \cdot 10^{7}$
f_{29}	3.4958	-2	1	-1	3.4811	4.1058	3.9638	0.1420	0.0022	0.0221	$8.2084 \cdot 10^{-13}$	$7.9125 \cdot 10^{6}$
f_{31}	4.3311	-6	2	2	4.3408	2.7238	2.3408	0.3829	0.0048	0.0483	$3.0384 \cdot 10^{-12}$	$1.0725 \cdot 10^{7}$
f_{32}	5.0047	-1	1	-1	4.9948	6.1855	6.1084	0.0771	0.0015	0.0150	$3.6143 \cdot 10^{-13}$	$8.2739 \cdot 10^{6}$

spacing pattern (see Table 7.2) defined as:

$$\Delta\Pi = \frac{\pi}{\int \frac{N}{r} \mathrm{d}r} \,, \tag{7.3}$$

where N is the Brunt-Väisälä frequency, the integral is over the g-mode cavity, and $\Delta\Pi$ is given in seconds (omitting the factor 2π in the definition). Comparable $\Delta\Pi = 12650^{+50}_{-250}$ s values were caused by a similar value for the integral, following from the relation between the overall stellar mass and the mass inside the core and convective core overshooting region. We were unable to lift the degeneracy caused by this correlation without many more observed and well defined pulsation modes that had a different probing power in the near-core region. Additional observed trapped modes would be particularly helpful to achieve this, as they are most sensitive to the near-core layers. Such modes manifest themselves in the regions of the local minima in the period spacing patterns as observed with the *Kepler* satellite for numerous g-mode pulsators, but *Kepler* data have a ten times better frequency resolution than our CoRoT data.

Pápics et al. (2012) used the few dominant modes to estimate $\Delta\Pi$, without modelling the individual frequencies and while ignoring the rotation of the star. It turned out that we obtained a value about twice as high, pointing out the difficulty of deducing an appropriate $\Delta\Pi$ value without good knowledge of the rotation frequency of the star. We emphasize that the high-precision f_{rot} value of HD 43317 determined from the magnetic modelling of Chapter 6 was an essential ingredient for the successful seismic modelling of the star as presented here.

To investigate the pairwise correlation between the parameters of the grid of MESA models, we employed the marginalization technique to reduce the dimensionality of the χ^2 landscape. This technique took the minimum χ^2 value of the fit along the third axis of the grid, providing easily interpretable correlation maps (given in Fig. 7.9). These correlation maps indicated that the central hydrogen fraction, X_c, was well constrained, but these maps also illustrated the tight correlation between $M_\star$ and f_{ov}. These correlation maps also illustrated the existence of the (non-significant) secondary solution of MESA models, which was already apparent from the χ^2 landscape in the Kiel diagram (see Fig. 7.7) and from the χ^2 distribution of several parameters in Fig. 7.8. The bottom left panel of Fig. 7.8 demonstrated that these models had a comparable value for $\Delta\Pi$ to the global solution, thus explaining the reason why this secondary solution was (partly) retrieved.

The correlation between f_{ov} and $M_\star$ and the limited frequency resolution of the CoRoT data led to a relatively large confidence interval on the derived f_{ov} for

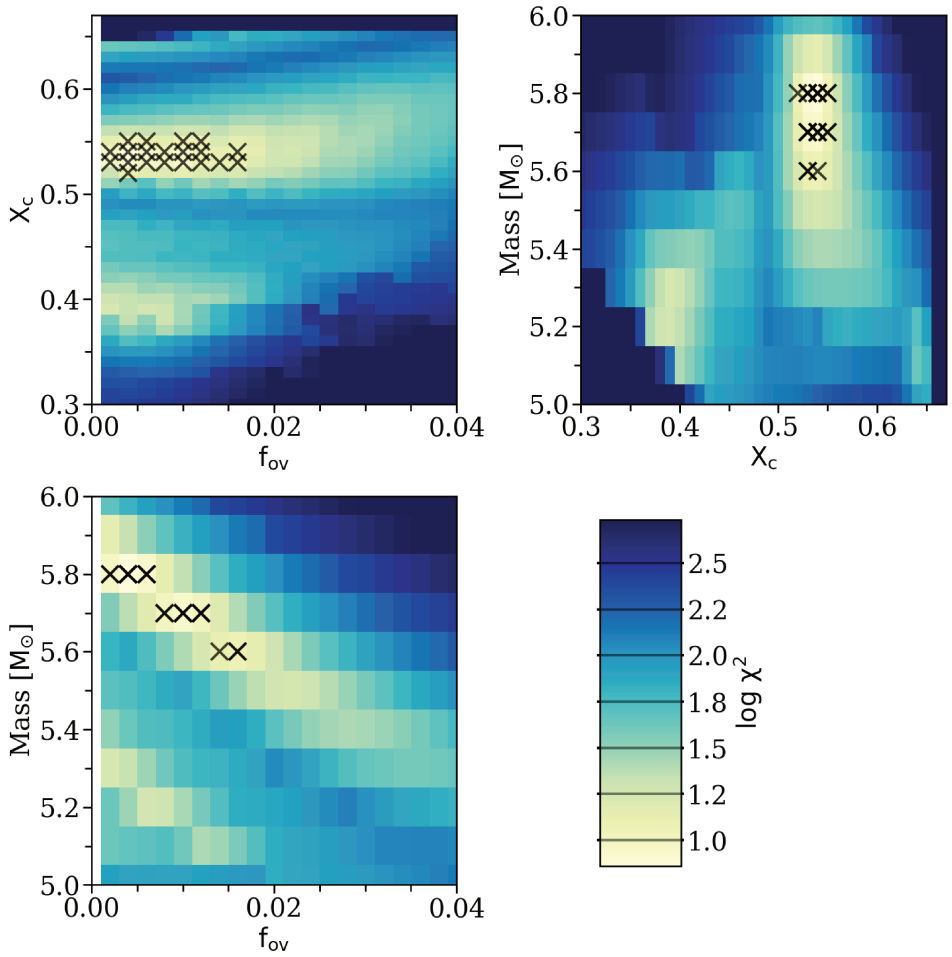

Figure 7.9: Colour maps indicating the pairwise (marginalized) correlation between the parameters in the (fine) grid of MESA models. *Top left*: correlation between X_c and $f_{\rm ov}$ after marginalizing over $M_\star$. *Top right*: correlation between $M_\star$ and X_c after marginalizing over $f_{\rm ov}$. *Bottom left*: correlation between $M_\star$ and $f_{\rm ov}$ after marginalizing over X_c, indicating the strong correlation caused by models with the same $\Delta\Pi$ value. The same colour scale was used for all panels. The 20 best MESA models are indicated by the black crosses.

HD 43317. The low value of the best model agreed well with the predictions from theory and simulations for hot stars hosting a detectable large-scale magnetic field and with the only other observational result (i.e., V2052 Oph, Briquet et al. 2012). The 2σ confidence interval on $f_{\rm ov}$ was also compatible with the seismic estimate of this parameter for the non-magnetic B-type star KIC 10526294 (Moravveji et al. 2015, see their Fig. B.1). However, KIC 10526294 is a slow rotator with a rotation period of about 190 d, while HD 43317 is a rapid rotator. The result for $f_{\rm ov}$ from the seismic modelling of the B-type star KIC 7760680 (Moravveji et al. 2016, their Fig. 6) with $P_{\rm rot} = 2.08 \pm 0.04$ d differs more than 2σ from the $f_{\rm ov}$-value for HD 43317. Thus, the forward seismic modelling of HD 43317 is compatible with the suppression of near-core mixing due to a large-scale magnetic field, but we could not exclude that other physical processes are involved in the limited overshooting, such as the near-core rotation.

By construction of the best models, the seismic estimates for $T_{\rm eff}$ and $\log g$ agreed well with the spectroscopic values by Pápics et al. (2012). The age estimate for the best model (28.4 Myr, see Table 7.2) is compatible with a literature value obtained from isochrone fitting to the spectroscopic parameters (i.e., 26 ± 6 Myr; Tetzlaff et al. 2011). Both results rely on stellar models that were computed with independent codes.

As a consistency check, we compared the Brunt-Väisälä frequency profiles and the mixing profiles in the near-core region of the 20 best fitted MESA models in Fig. 7.10. The lack of stringent constraints, due to the limited frequency resolution of the CoRoT data, for the extent of the convective-core overshooting layer was clearly visible, as not all these internal profiles overlapped. This was already expected from the χ^2 distribution in Fig. 7.8. Instead, these mixing profiles indicated the confidence interval on the extent of the overshooting layer. The mixing profiles of the 20 best models agreed well, however, inside the convective core and in the radiative layer, the latter being set by the value of $D_{\rm ext}$. Differences between the Brunt-Väisälä frequency profiles became negligible outside the g-mode cavity.

Further, we redetermined the inclination angle i using the radius of the best fitted MESA model (i.e., $R = 3.39\,{\rm R}_\odot$), the value for $v \sin i = 115 \pm 9\,{\rm km\,s^{-1}}$ (Pápics et al. 2012) and the rotation period $P_{\rm rot} = 0.897673(4)$ d (see Sect. 6.3.2). This resulted in an inclination angle $i = 37 \pm 3\,^\circ$, where the largest uncertainty came from the estimate of $v \sin i$. This a posteriori refinement of the inclination angle is compatible with the mode visibility of the dipole and quadrupole mode interpretation. With this inclination angle, we derived an updated value for the obliquity angle $\beta = 81 \pm 6\,^\circ$, employing the measurements for the longitudinal magnetic field of Sect. 6.4.2 for the LSD profiles with the complete line mask. Using these angles, the longitudinal magnetic field measurements of Sect. 6.4.2, the equation for the dipolar magnetic field strength of Schwarzschild (1950) and

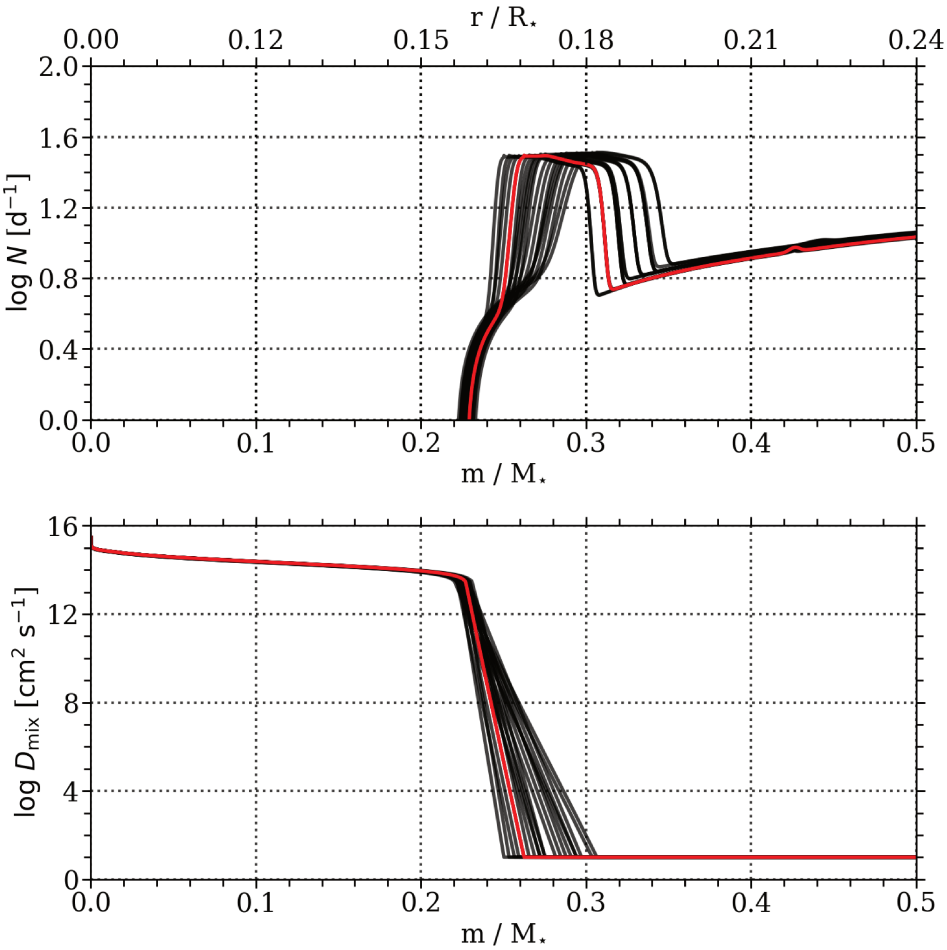

Figure 7.10: Brunt-Väisälä frequency (*top*) and internal mixing profiles (*bottom*) as a function of fractional mass coordinate of the best model. Solid black lines correspond to the best 20 models, while the best model is indicated by the red solid line. Conversion from fractional mass to fractional radius (also for the best model) is given on the upper coordinate axis of the top panel.

a linear limb-darking coefficient of $u = 0.3$ (appropriate for a B3.5V star, see e.g., Claret 2000), we deduced that the dipolar magnetic field of HD 43317 had a strength $B_{\rm dip} = 1312 \pm 332$ G. These values were all consistent with the ranges obtained in Chapter 6, which were based on the range of acceptable inclination angles from Pápics et al. (2012).

7.4.2 Dependences on the mode identification assumptions

During the forward seismic modelling, we were explicit on the assumptions about the mode geometry, and at which stage a given observed frequency entered the modelling scheme. Several of these frequencies did not have a unique mode identification (even for the best fitted MESA model). As an example, we discuss f_{15}, which we assumed to be a (ℓ, m)=$(2, -1)$ mode. However, the zonal mode frequency $f_{n_g,\ell,0}$ of f_6 also matched closely with f_{15}. Such a degeneracy occurred for several cases, but never in a systematic way. Moreover, these degeneracies did not significantly alter the confidence intervals of the parameters based on the selected MESA models as their corresponding GYRE frequencies had a good match with the observations. We considered it more sensible to use interrupted series of $(1, -1)$ and $(2, -1)$ modes (together with one $(2, +2)$ mode confirmed by spectroscopy) during the forward seismic modelling of HD 43317 than injecting zonal modes that did not belong to any series in radial order or rotationally split multiplets. Finally, we emphasize that the assumption of the initial four $(1, -1)$ modes with the spectroscopic identification of f_{31} and the enforced 2σ spectroscopic box sufficiently constrained the possible MESA models for HD 43317, while still complying with forward modelling results of *Kepler* B-type g-mode pulsators.

7.4.3 Assessment of the theoretical pulsation mode frequencies

In our computations of the mode frequencies, we made two important assumptions. The first one was uniform rotation, as the GYRE computations used the traditional approximation under this assumption. Following the results in Aerts et al. (2017b) and in Van Reeth et al. (submitted) for tens of g-mode pulsators, this was a valid assumption. Furthermore, uniform rotation in the radiative layer was theoretically predicted for stars with a stable large-scale magnetic field (e.g., Ferraro 1937; Moss 1992; Spruit 1999; Mathis & Zahn 2005; Zahn 2011).

The second assumption was that we ignored the effect of the magnetic field on the g-mode frequencies because we did not have observational information on

the interior properties of the large-scale magnetic field. Below we attempted to assess the consequences of these assumptions after we obtained a good model representing the stellar structure of the pulsating magnetic star HD 43317.

Frequency shifts of zonal modes due to the Coriolis force

For HD 43317, the independent measurement of the rotation frequency (at the stellar surface) was a necessary pre-requisite to be able to perform seismic modelling. Indeed, the well-known estimation procedure for $f_{\rm rot}$ from the period spacing patterns of g modes applied to *Kepler* data as in Moravveji et al. (2016), Van Reeth et al. (2016) or Ouazzani et al. (2017) was not possible for our CoRoT target. Prior knowledge of the rotation frequency allowed us to apply the traditional approximation for rotation, which ignores the latiduinal component of the rotation vector. This approximation is appropriate for g modes in B- and F-type stars thanks to their large horizontal displacements, as long as they do not rotate too close to their critical rotation velocity (Ouazzani et al. 2017). However, forward modelling of such pulsators was so far also still done without taking into account the Coriolis force for slow rotators (cf., Moravveji et al. 2015; Schmid & Aerts 2016).

Here, we wish to compare the effects of ignoring the Coriolis and Lorentz forces for the resulting theoretical predictions of the g-mode frequencies, taking the case of HD 43317 as the only concrete example of a magnetic g-mode pulsator so far. Such comparison is most easily done for zonal modes of stellar models, as these are not subject to transformation effects between the co-rotating and inertial reference frames.

Unlike a first-order perturbative approach for the effects of the Coriolis force (e.g., Ledoux 1951), the traditional approximation results in frequency shifts for zonal pulsation modes. We computed the frequency differences for the zonal mode frequencies $f_{n_g,\ell,0}$ of the identified modes in the best MESA model with $M_\star$=5.8 $\mathrm{M}_\odot$, X_c=0.54, and $f_{\rm ov}$=0.004, when ignoring and while taking into account the Coriolis force. The results are listed in Table 7.3. As expected, the frequency shift due to the Coriolis force is large for the rotation rate of HD 43317. It increases with increasing radial order n_g and with mode degree ℓ. For the pulsation modes with the highest n_g values, the frequency-shifted value easily exceeded 25 % of the non-rotating value $f_{n_g,\ell,0}$, clearly illustrating the need to account for the stellar rotation during the forward seismic modelling.

Frequency shifts due to the Lorentz force

To compute the shift in the pulsation mode frequency caused by an internal magnetic field, we followed the perturbative approach of Hasan et al. (2005), since it was one of the few available formalisms applicable to g modes. It assumes that the internal magnetic field corresponds to a poloidal axisymmetric field. While this is a limitation, there is currently no better prescription to apply.

Theoretical studies and numerical simulations showed that any extension of a large-scale magnetic field measured at the stellar surface towards the stellar interior needs to have both a toroidal and poloidal component of about equal strength to be stable over long time scales (e.g., Tayler 1980; Braithwaite & Nordlund 2006; Duez & Mathis 2010; Duez et al. 2010). However, Hasan et al. (2005) argued that the toroidal component of the internal magnetic field would lead to a lower frequency shift for high-radial order g modes than the poloidal component. Hence, we adopted their formulation here. The resulting frequency shift can be expressed as

$$\frac{\delta\omega}{\omega} = \left(\frac{\omega_{\rm A}}{\omega}\right)^2 \; C_{l,m}\; \mathcal{I} = S_{\rm c}\; B_0^2\,, \tag{7.4}$$

where

$$\omega_{\rm A} = \frac{B_0}{\sqrt{4\pi\rho_c}}\frac{1}{R_\star} \tag{7.5}$$

is the Alfvén frequency for an internal magnetic field with strength B_0. This expression led to the magnetic splitting coefficient $S_{\rm c}$ given as

$$S_{\rm c} = \frac{C_{\ell,m}\mathcal{I}}{8\pi\omega^2\rho_{\rm c}R_\star^2}\,, \tag{7.6}$$

where $\rho_{\rm c}$ is the central mass density, $R_\star$ is the stellar radius, ω is the cyclic frequency (in $\mathrm{rad\,s^{-1}}$) corresponding to the angular pulsation mode frequency $f_{n_g,\ell,m}$ and the Ledoux coefficients $C_{\ell,m}$ have been introduced (see Ledoux & Simon 1957 and Eq. (8) and (9) of Hasan et al. 2005). They describe the horizontal overlap between the g-mode displacement, assumed to be predominantly horizontal, with the dipolar magnetic field. Finally, $\mathcal{I}$ is defined as

$$\mathcal{I} = \frac{\int \left|\frac{2}{x}\frac{\mathrm{d}}{\mathrm{d}x}\left(b(x)\,\xi_{\rm h}(x)\right)\right|^2 x^2\,\mathrm{d}x}{\int \left|\xi_{\rm h}(x)\right|^2 \frac{\rho(x)}{\rho_{\rm c}} x^2\,\mathrm{d}x}\,, \tag{7.7}$$

with $x = r/R_\star$ the radial coordinate, $\xi_{\rm h}(x)$ the horizontal displacement for the pulsation mode with frequency $f_{n_g,\ell,m}$, $\rho(x)$ the internal density profile, and $b(x)$ the profile of the magnetic field as a function of the radial coordinate. We

followed the definition of Hasan et al. (2005) and assumed $b(x) = (x/x_c)^{-3}$, with x_c the radial coordinate of the outer edge of the convective core. For our best model of HD 43317 ($M_\star$=5.8 $M_\odot$, X_c=0.54, and f_{ov}=0.004), the MESA model delivered $x_c = 0.168$.

We estimated the strength of the frozen-in large-scale magnetic field of HD 43317 at x_c following the results provided by the simulations of Braithwaite (2008, we refer the reader to his Fig. 8). Depending on the age of the star, the internal magnetic field was 26.6 to 50.1 times as strong as at the stellar surface. Using our new estimate of the strength of the dipolar magnetic field at the surface of HD 43317, $B_{dip} = 1312 \pm 332$ G, we got a near-core magnetic field strength in the range B_0=26.1 − 82.4 kG. We computed the frequency shift using Eq. 7.4 for these two limiting values of B_0, the model frequencies $f_{n_g,\ell,0}$ of the non-rotating case (see Table 7.3) and the difference in Ledoux constants $\Delta C_{\ell,m}$ values to account for the mode geometry (similarly to Hasan et al. 2005). The values for the obtained frequency shifts due to the Lorentz force are given in Table 7.3 and are compared with the differences between the observed and the 20 best sets of model frequencies in Fig. 7.11.

As expected from Eq. (7.4), we found that the frequency shifts depended on the strength of B_0. Moreover, they increased with increasing radial order, since ω decreased and $\mathcal{I}$ increased. We found that the frequency shift was largest for the observed $(1, -1)$ modes, since the difference in the Ledoux constants $\Delta C_{\ell,m}$ were largest for such modes. All these results were compatible with those of Hasan et al. (2005).

The upper limit on the frequency shift due to the Lorentz force was almost always an order of magnitude smaller than that caused by the Coriolis force. Hence, correctly accounting for the (uniform) rotation rate remained not only necessary, but was also more important during the forward modelling than accounting for a possible internal magnetic field that resulted from extrapolation of the surface field strength when dealing with field amplitudes as the one measured for HD 43317. This can also be further understood when revisiting Eq. (7.4). First, the ratio of the Alfvén frequency and the pulsation mode frequencies was always very small (typically of the order of 10^{-9}) permitting us to adopt a perturbative treatment of the effect of the Lorentz force on the pulsation modes. Most of the observed modes during the modelling were sub-inertial gravito-inertial modes (i.e. $f < 2f_{rot}$). Therefore, they would be confined to an equatorial belt and thus propagate above a critical colatitude $\theta_c = \arccos(f/(2f_{rot}))$ (see e.g., Townsend 2003). In the formalism by Hasan et al. (2005), the non-rotating approximation was assumed and modes were thus expanded as spherical harmonics corresponding to modes propagating in the whole sphere. In this framework, the coefficient $C_{l,m}$ evaluated the horizontal overlap of the oscillation mode with the magnetic field with positive

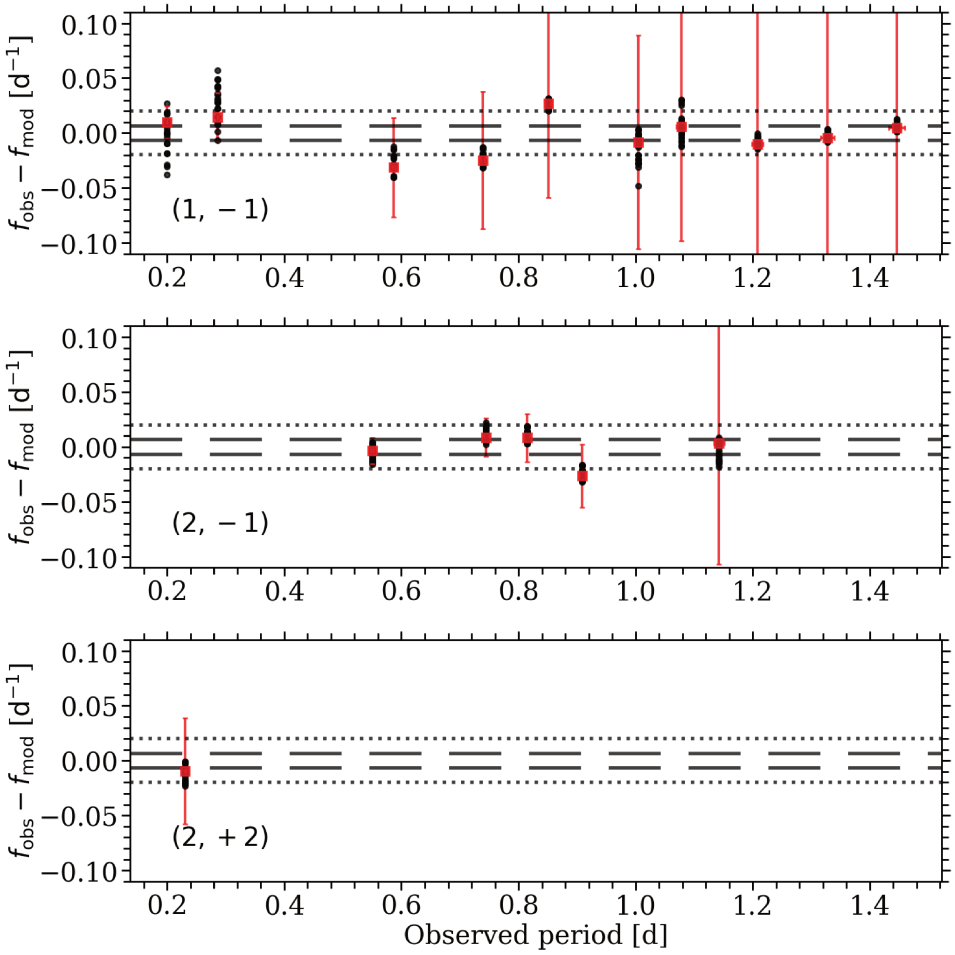

Figure 7.11: Difference in frequency between the observed pulsation mode frequencies and the GYRE frequencies of the 20 best MESA models, ordered according to the mode geometry. The red squares indicate the difference between the observations and the best model description. The red vertical errorbars indicate the frequency shift caused by an internal poloidal magnetic field of 82.4 kG and the red horizontal error bars represent the Rayleigh frequency resolution of the CoRoT light curve. Both were often similar to the symbol size, while the magnetic frequency shift for the highest period dipole modes was larger than the indicated panel (see also Table 7.3). The black dashed and dotted lines show the Rayleigh frequency resolution and $3\delta f_{\rm ray}$, respectively.

integrals (we refer the reader to Eq. (7) in Hasan et al. 2005). As such, the determined frequency shifts due to the magnetic field should be larger in the case of the non-rotating approximation compared to equatorially trapped sub-inertial gravito-inertial modes. The modification of the radial term from the non-rotating case to the case of a sub-inertial case is more difficult to infer. However, if $\omega_{\rm A} \ll 2\Omega$, it would not change the fact that the perturbative approach for the Lorentz force can be used.

In the case of super-inertial gravito-inertial modes (i.e., $f > 2f_{\rm rot}$), the situation would be much simpler since waves propagate in the whole sphere as in the non-rotating case and the eigenmodes would be less modified by the Coriolis acceleration (e.g., Lee & Saio 1997). Therefore, the evaluation of the frequency shift provided by Hasan et al. (2005) using the non-rotating assumption could be considered as a first reasonable step to evaluate the frequency shift induced by the Lorentz force. The next step would be to generalise their work using the traditional approximation to take into account the effect of the Coriolis acceleration on the oscillation modes, in particular in the sub-inertial regime. This would require a dedicated theoretical study and was far beyond the scope of the current paper.

We concluded, as an a posteriori check, that the working principle of our seismic modelling was acceptable for this star. Only for the higher-order dipole modes did the upper limit of the magnetic frequency shift become comparable with the frequency shift caused by the Coriolis force. Yet, only a few such pulsation mode frequencies were identified for HD 43317. In this case a non-perturbative approach, as the one derived in Mathis & de Brye (2011), should be adopted.

Comparing the magnetic frequency shift with the differences between the observed and model frequencies (see Fig. 7.11) led to the conclusion that the current description of the frequency shifts due to the Lorentz force failed to improve the differences. This was not surprising, given the simplification of the perturbative approach by Hasan et al. (2005), its assumptions on the geometry of the large-scale magnetic field, and because it neglects the Coriolis acceleration. Future inclusion of the frequency shifts due to a magnetic field under the traditional approximation would be valuable for proper seismic modelling of magnetic g-mode pulsators and to estimate the upper limit of the interior magnetic field strength for stars without measurable surface field.

7.5 Summary and conclusions

We performed forward seismic modelling of the only known magnetic B-type star exhibiting independent g-mode pulsation frequencies. The modelling was

based on a grid of non-rotating, non-magnetic 1D stellar evolution models (computed with MESA) coupled to the adiabatic module of the pulsation code GYRE, while accounting for the uniform rotation and using the traditional approximation. This procedure allowed us to explain 16 of the 28 independent frequencies determined from the ∼150 d CoRoT light curve. We identified these 16 pulsation mode frequencies as ten $(1, -1)$ modes, one $(2, 2)$ mode, and five $(2, -1)$ modes. With this, the star revealed two overlapping period spacing series. Other than f_{31}, zonal and prograde pulsation modes had to be excluded during the forward modelling, because the frequency resolution of the CoRoT light curve did not permit us to identify the theoretical counterparts of detected pulsation mode frequencies.

Some degeneracy on the mode geometry remained for a few of the used frequencies but this did not affect the three estimated stellar parameters, given their confidence intervals deduced from the best models. Most of the high frequencies in the CoRoT data were explained as rotationally shifted g modes. Hence, the interpretation by Pápics et al. (2012) of having detected isolated p modes in this star, in addition to g modes, turned out to be invalid. The seismic modelling indicated stellar models with $M_\star$=$5.8^{+0.1}_{-0.2}\,\mathrm{M}_\odot$, X_c=$0.54^{+0.01}_{-0.02}$, and $f_{\rm ov}$=$0.004^{+0.014}_{-0.002}$ to provide the best description of the observations. This makes HD 43317 the most massive g-mode pulsator with successful seismic modelling to date.

Using the model frequencies of the best fitted MESA model, we compared the shift of zonal pulsation mode frequencies by the Coriolis force, using the traditional approximation and adopting the measured rotation period at the surface, with those due to Lorentz force, following the perturbative approach of Hasan et al. (2005), the simulations of Braithwaite (2008), and our new estimate of the surface field value of $B_{\rm dip} = 1312 \pm 332\,\mathrm{G}$. The maximal magnetic frequency shift was almost always an order of magnitude smaller than the shift caused by the Coriolis force due to a uniform rotation with a period of 0.897673 d. Hence, under the adopted approximations, magnetism was a secondary effect compared to rotation when computing pulsation mode frequencies of HD 43317. This a posteriori check re-inforced the validity of our modelling approach.

New formalisms for the perturbation of gravito-inertial waves computed with the traditional approximation by a magnetic field or for the simultaneous non-perturbative treatment of the Coriolis acceleration and of the Lorentz force (e.g., Mathis & de Brye 2011) would be of great value for future seismic modelling of rapidly rotating magnetic massive stars. HD 43317 can serve as an important benchmark for such future improvement of stellar evolution and pulsation codes, as it is currently the only known magnetic hot star with a relatively rich g-mode frequency spectrum. Future year-long data sets to be assembled by the NASA

TESS mission in its Continuous Viewing zone (Ricker et al. 2016) and by the ESA PLATO mission (Rauer et al. 2014) will certainly bring more magnetic hot pulsators suitable for asteroseismology.

Part IV

Conclusions and Future Prospects

Ground-based high-resolution and high signal-to-noise optical spectropolarimetry has only been available for about two decades. It has proven to be a paramount observational technique to study the large-scale magnetic fields detected at the surface of OBA stars. These observations, combined with line averaging techniques (such as LSD), permit high-precision measurements of longitudinal magnetic fields of the order of just a few Gauss. This has led to many new discoveries of magnetic OBA stars and enabled detailed follow-up observations to obtain a meaningful characterization of the geometry and strength of the large-scale magnetic fields. Moreover, asteroseismology has stepped out of its infancy thanks to modern-era photometric space missions. These delivered high-precision observations with a high duty cycle over significant time bases that have sparked a greater understanding of the stellar structure properties. This is especially true for low- and intermediate-mass stars. Space-based photometric observations of hot massive stars were scarce at the beginning, since such stars were intrinsically too bright for these missions, and were avoided due to them disturbing the exoplanet hunting. New and detailed space missions have been steadily filling this void, although the number of OB-type stars observed comes nowhere near the level of low- and intermediate-mass stars. Most importantly for our PhD research, many OBA stars were for the first time accessible with both ground-based high-resolution spectropolarimetry and high-precision space-based photometry.

It is at this junction of techniques that the deep interior of magnetic OBA stars has become observable through asteroseismology with high-precision data, complemented by additional constraints from the magnetometric analysis at the stellar surface. We refer to this combined technique as magneto-asteroseismology. As a result, one can investigate the impact of a large-scale magnetic field on the stellar structure, in particular on the internal rotation rates, to observationally evaluate theoretical and numerical predictions. A magneto-asteroseismic study has been done only once before our PhD research started. The magnetic pulsating B2IV/V star V2052 Oph was the target of that study (Neiner et al. 2012a; Handler et al. 2012; Briquet et al. 2012), which combined multi-site ground-based photometry and spectroscopy with ground-based high-resolution spectropolarimetry. Matching the observations of a few pressure modes to state-of-the-art stellar structure models demonstrated that the star has a smaller convective core overshooting layer, compared to a very similar non-magnetic pulsator with the same identified pressure modes. However, three differences between these two stars occur, namely their rotation rates, their binarity, and their large-scale magnetic field. Further work is needed to ascertain which of these three effects is dominant for the difference in the determined value of convective core overshooting.

We started this work by investigating the collected high-precision space-based

photometry of magnetic hot stars and candidate magnetic hot stars identified by their peculiar photospheric abundance distributions. We searched for coherent periodic signal that could be interpreted as stellar pulsations. While most of these stars are in theoretical instability regions in the Hertzprung-Russell diagram where stellar pulsations are expected to occur, we only obtained clear detections for a handful of stars. In case stellar pulsations were detected, the few observed pulsation mode frequencies were insufficient for a detailed inference of the star's internal properties through a comparison with stellar structure models. The accompanying ground-based high-resolution optical spectropolarimetry confirmed the presence of a strong large-scale magnetic field for most of the stars in the sample, and for all that did pulsate. The apparent low number of pulsating magnetic hot stars with a rich frequency spectrum compared to their non-magnetic counterparts suggested that the large-scale magnetic field may inhibit the stellar pulsations. The damping of internal gravity waves by a magnetic field has recently been proposed from numerical simulations for red giants (Lecoanet et al. 2017), but it will require a study of a homogeneous sample of magnetic hot stars to test whether these results are also valid for such different type of stars.

The second part of this work focussed on the in-depth analysis of the magnetic and pulsating B3.5V star HD 43317. At first, we continued the characterization of the geometry and strength of the large-scale magnetic field with archival and new high-resolution spectropolarimetric data. This lead to a revised rotation period $P_{\rm rot} = 0.897673(4)\,{\rm d}$, a dipole field strength $B_{\rm p} = 1.0 - 1.5\,{\rm kG}$, and reasonable constraints on the inclination angle and obliquity angle. We analysed the available CoRoT photometry, deriving 30 independent frequencies that were unrelated to rotational signal and were likely pulsating mode frequencies. These anticipated pulsation mode frequencies fell in the frequency domain of gravity modes that are dominantly sensitive to the near-core domain. We fitted the observed modes to gravito-inertial modes computed in the adiabatic approximation with the pulsation code GYRE coupled to a grid of non-rotating non-magnetic 1D MESA stellar structure models. The best models were able to explain at least 16 of the observed 28 candidate pulsation mode frequencies as either $(\ell, m) = (1, -1)$ modes, $(2, -1)$ modes, and $(2, 2)$ modes. The resulting parameters of the MESA models ($M_\star = 5.8^{+0.1}_{-0.3}\,{\rm M}_\odot$, $X_c = 0.54^{+0.01}_{-0.02}\,{\rm dex}$, and $f_{\rm ov} = 0.004^{+0.018}_{-0.002}$) did not allow to evaluate the theoretical and numerical predictions of a smaller convective core overshooting layer compared to non-magnetic stars, because of a degeneracy between models with similar values for the asymptotic period spacing. These degeneracies can only be lifted from higher-precision pulsation mode frequencies based on at least ten times longer time-series. Including more observed stellar pulsations during the forward seismic modelling might lift part of the degeneracy caused by the asymptotic period spacing. However, that would require a less conservative frequency

extraction of the available CoRoT data, which is not in line with the most recent analyses of gravito-inertial modes deduced from the ten times longer *Kepler* light curves of similar stars.

Magnetism has so far been ignored during our GYRE computations. Furthermore, magnetism as well as rotation were avoided during the MESA calculations because their inclusions needs a myriad of free parameters to describe their instabilities (e.g., Heger et al. 2000). Moreover, the inclusion of such instabilities accounting to their description in the literature (as it has been done in MESA) led to numerical misbehaviour in the Brunt-Väisälä frequency and, hence, untrustworthy mode predictions. We demonstrated that the internal part of the large-scale magnetic field had a secondary effect on the pulsation mode frequencies compared to the effects of the Coriolis force for HD 43317. These results were obtained with a perturbative approach and assuming a purely poloidal magnetic field. A more general description for the magnetic frequency shift caused by a field with general properties such as configuration and strength is currently lacking. Once such a description becomes available in pulsation codes, forward seismic modelling of magnetic stars will further improve. Moreover, it may enable the first indirect measurements of the internal magnetic field that can then be compared to detailed MHD simulations.

Even after our dedicated observational campaigns, the known magnetic hot stars with sufficient gravity mode pulsations for forward seismic modelling remains limited to HD 43317. About a dozen other magnetic pulsating hot stars are known. Yet, these have a limited number of detected pulsation mode frequencies, which are often pressure modes that are less sensitive to the near-core region, or these stars are part of a binary system causing problems with the allocation of the pulsation mode frequencies to the magnetic component of the binary system. Continued observational efforts are needed to evaluate the effect of magnetism on stellar interiors. Future space-based photometric missions, such as the Transiting Exoplanet Survey Satellite (TESS, Ricker et al. 2015) to be launched in 2018 and the PLAnetary Transits of Oscillations of Stars (PLATO, Rauer et al. 2014) in 2026, can test further whether strong large-scale magnetic fields influence the stellar pulsations by observing a statistically significant sample.

Suitable magnetic hot stars for seismic modelling will likely be detected following indirect evidence of a large-scale magnetic field at the surface of pulsating hot stars, such as peculiar photospheric abundance distributions or rotational modulation related to surface abundance inhomogeneities or magnetospheres. These candidate magnetic stars will likely be selected from the systematic survey of TESS, in particular stars in the continuous viewing zones that will have light curves with a substantial time base of 351 days. However, high-resolution spectroscopy is still required for the indirect

diagnostics, as well as subsequent dedicated high-resolution and high-signal-to-noise spectropolarimetric campaigns to confirm the presence of the large-scale magnetic field for the most interesting targets and to perform a detailed magnetometric analysis.

At present, no new ground-based optical spectropolarimetric instruments have been announced for 8-m class telescopes. Such useful instruments, however, will be needed to detect magnetic fields for fainter stars to increase the synergy with the photometric space missions for successful magneto-asteroseismology. It is expected that the community pressure will decrease on the current 8-m class telescopes when the European Extremely Large Telescope, the Giant Magellan Telescope, and the Thirty Meter Telescope become operational in the early to mid 2020s. This could then permit the installation of new generation of optical spectropolarimeters at the 8-m class telescopes. The advancements in IR spectropolarimetry will likely be of limited use for the pulsating magnetic hot stars, except for the study of their magnetospheres (Eikenberry et al. 2014; Oksala et al. 2015a). Spectropolarimetry in the UV, however, would be an ideal tool to study hot stars and their magnetosphere. Such space mission projects are currently under study (e.g., POLLUX on-board NASA's LUVOIR).

A future route on the computational and theoretical side is to assess the frequency shifts due to an internal magnetic field and to investigate whether it could explain the frequency differences between observed *Kepler* pulsation mode frequencies and predictions from pulsation codes. This first requires detailed forward seismic modeling of a large sample of (magnetic) gravito-inertial pulsators.

Appendix A

Additional matter to Chapter 4

Table A.1: Observing log of the spectropolarimetric sequences of *o* Lup. The first letter of the ID indicates whether the spectropolarimetric sequence was taken with HARPS (H) or ESPaDOnS (E). For each sequence, the mid-exposure HJD, the exposure time, and the rotation phase $\phi_{\rm rot}$, are indicated. The latter was determined with $P_{\rm rot} = 2.95333$ d and $T_0 = 2455702.5$ d. The provided S/N is that of the LSD Stokes I profile calculated with various line masks. In addition, the magnetic detection status is provided (DD = Definite Detection, MD = Marginal Detection, and ND = Non Detection) in case not all observations resulted in a DD for the given LSD line mask. **Remarks**: *a* This observation was discarded because the last two sub-exposures in the sequence did not contain any signal due to bad weather.

ID	HJD [d] -2450000	$t_{\rm exp}$ [s]	$\phi_{\rm rot}$	complete S/N	He excluded S/N	He I S/N	He I Detect.	Fe II S/N	Si II S/N	Balmer S/N	Balmer Detect.
H01	5704.72965	4×100	0.754961	5186	4154	567	DD	2879	920	137	DD
H02	5708.75948	4×300	0.119465	4868	3959	595	ND	2768	933	143	DD
H03	5709.73559	4×750	0.449976	4875	3984	562	DD	2809	914	138	DD
H04	5709.77216	4×750	0.462360	4798	3816	547	ND	2752	897	143	DD
H05	6123.56357	4×300	0.572476	5101	3794	548	DD	2664	826	154	DD
H06	6124.70439	4×300	0.958758	5094	3862	627	DD	2767	916	134	DD
H07	6125.45930	4×300	0.214371	5300	4055	626	ND	3067	1012	140	ND
H08	6125.57061	4×300	0.252060	5289	4059	562	ND	3173	1038	128	ND
H09	6126.56054	4×300	0.587252	5130	3798	617	DD	2753	858	128	DD
H10	6127.46812	4×300	0.894560	5350	4064	534	ND	2943	955	147	DD
H11	6129.59043	4×600	0.613176	5010	3809	609	DD	2682	837	157	DD
H12	6130.51806	4×600	0.927273	5350	3997	581	DD	2861	933	152	DD
E01	6758.06034	4×85	0.413611	3214	2736	408	DD	2234	714	60	DD
E02	6819.85180	4×85	0.336251	3335	2664	611	ND	2383	676	60	DD
H13	7481.61063	4×207	0.408343	5134	4163	584	DD	3100	965	141	DD
H14	7481.62175	4×207	0.412107	5092	4041	582	DD	3006	958	138	DD
H15	7481.63287	4×207	0.415871	5251	4079	582	DD	2988	961	139	DD

Continued on next page

Table A.1 – continued from previous page

H16	7481.64398	4×207	0.419634	5212	4119	579	DD	3039	960	158	DD
H17	7481.65509	4×207	0.423396	5133	4050	576	DD	2989	940	156	DD
H18	7481.66620	4×207	0.427159	5150	4035	576	DD	2974	943	151	DD
H19	7481.67731	4×207	0.430921	5099	4010	574	DD	2908	929	150	DD
H20	7481.68842	4×207	0.434684	4914	3884	537	DD	2857	922	154	DD
H21	7481.82751	4×207	0.481777	4513	3573	508	ND	2488	804	156	DD
H22	7481.83862	4×207	0.485539	3772	3138	589	ND	2170	740	143	ND
H23	7482.65216	4×207	0.761005	4810	3734	577	DD	2666	897	139	DD
H24	7482.66327	4×207	0.764767	4603	3639	561	ND	2585	883	159	MD
H25[a]	7482.67438	4×207	0.768530	–	–	–	–	–	–	–	–
H26	7484.69562	4×207	0.452922	4728	3707	570	DD	2737	886	155	DD
H27	7484.70673	4×207	0.456684	4738	3748	564	ND	2772	890	160	DD
H28	7484.79338	4×207	0.486023	4727	3710	563	DD	2693	866	153	DD
H29	7484.80449	4×207	0.489786	4749	3726	546	DD	2677	867	137	DD
H30	7484.88788	4×207	0.518020	4720	3682	545	DD	2621	812	146	DD
H31	7484.89899	4×207	0.521782	4759	3704	604	DD	2627	808	156	DD
H32	7485.73598	4×207	0.805188	5107	4035	604	DD	2908	951	153	DD
H33	7485.74709	4×207	0.808952	5073	3971	601	DD	2912	957	159	DD
H34	7485.83035	4×207	0.837143	5101	3939	600	DD	2828	895	157	DD
H35	7485.84146	4×207	0.840905	5072	3939	367	DD	2830	909	161	DD

Table A.2: Overview of the measured longitudinal magnetic field values for o Lup. For each observation, the HJD at mid-exposure, the corresponding rotation phase, $\phi_{\rm rot}$, calculated using $P_{\rm rot} = 2.95333\,{\rm d}$ and $T_0 = 2455702.5\,{\rm d}$, and the measured longitudinal magnetic field B_l for various LSD line masks are indicated.

HJD [d] -2450000	$\phi_{\rm rot}$	B_l [G] complete	B_l [G] He excluded	B_l [G] Balmer	B_l [G] Fe II	B_l [G] Si II	B_l [G] He I
5704.72965	0.754961	400 ± 26	976 ± 41	618 ± 142	2038 ± 111	752 ± 79	66 ± 42
5708.75948	0.119465	-199 ± 26	-478 ± 43	-262 ± 138	-1179 ± 128	-140 ± 102	-47 ± 41
5709.73559	0.449976	940 ± 27	2243 ± 45	1239 ± 143	4770 ± 133	1904 ± 83	132 ± 43
5709.77216	0.462360	908 ± 32	2213 ± 51	1177 ± 165	4607 ± 147	1707 ± 97	66 ± 53
6123.56357	0.572476	840 ± 22	1976 ± 35	1446 ± 127	4285 ± 106	1617 ± 65	103 ± 39
6124.70439	0.958758	-133 ± 26	-270 ± 43	-408 ± 138	-674 ± 129	-167 ± 103	-53 ± 42
6125.45930	0.214371	99 ± 29	204 ± 50	513 ± 155	56 ± 158	385 ± 105	-13 ± 44
6125.57061	0.252060	206 ± 32	524 ± 56	570 ± 170	1167 ± 173	592 ± 115	1 ± 48
6126.56054	0.587252	837 ± 22	1967 ± 36	1327 ± 125	4260 ± 108	1649 ± 68	118 ± 37
6127.46812	0.894560	20 ± 23	93 ± 38	-201 ± 123	268 ± 113	-74 ± 81	-29 ± 37
6129.59043	0.613176	810 ± 31	1896 ± 47	1227 ± 171	3881 ± 133	1567 ± 86	92 ± 53
6130.51806	0.927273	-34 ± 22	-91 ± 34	-329 ± 114	-206 ± 100	-104 ± 76	3 ± 36
6758.06034	0.413611	844 ± 31	1986 ± 51	1165 ± 137	4354 ± 156	1571 ± 85	106 ± 50
6819.85180	0.336251	559 ± 23	1443 ± 40	967 ± 98	3230 ± 130	1158 ± 67	-2 ± 36
7481.61063	0.408343	834 ± 26	1948 ± 42	1275 ± 139	4148 ± 125	1642 ± 80	101 ± 43
7481.62175	0.412107	820 ± 25	1981 ± 41	1343 ± 136	4242 ± 122	1658 ± 77	53 ± 42
7481.63287	0.415871	835 ± 25	2018 ± 42	1327 ± 137	4391 ± 124	1609 ± 78	59 ± 42
7481.64398	0.419634	845 ± 25	2011 ± 41	1249 ± 133	4234 ± 119	1621 ± 76	65 ± 42
7481.65509	0.423396	876 ± 26	2043 ± 43	1399 ± 141	4228 ± 123	1684 ± 81	132 ± 44
7481.66620	0.427159	878 ± 27	2102 ± 43	1252 ± 145	4276 ± 124	1733 ± 81	78 ± 45
7481.67731	0.430921	860 ± 28	2109 ± 46	1225 ± 154	4440 ± 134	1716 ± 86	62 ± 47

Continued on next page

Table A.2 – continued from previous page

7481.68842	0.434684	856 ± 34	2037 ± 54	1393 ± 183	4330 ± 157	1604 ± 101	112 ± 56
7481.82751	0.481777	952 ± 47	2201 ± 71	1238 ± 262	4835 ± 200	1805 ± 136	112 ± 82
7481.83862	0.485539	861 ± 72	2088 ± 109	1526 ± 396	5059 ± 335	1639 ± 209	24 ± 127
7482.65216	0.761005	434 ± 39	910 ± 62	611 ± 219	1989 ± 172	758 ± 124	96 ± 66
7482.66327	0.764767	401 ± 46	862 ± 73	758 ± 253	1932 ± 206	777 ± 146	91 ± 77
7484.69562	0.452922	842 ± 37	2083 ± 61	1535 ± 207	4765 ± 177	1747 ± 121	63 ± 62
7484.70673	0.456684	815 ± 35	2039 ± 58	1257 ± 201	4444 ± 167	1652 ± 115	76 ± 58
7484.79338	0.486023	884 ± 28	2145 ± 46	1267 ± 146	4486 ± 130	1893 ± 91	67 ± 47
7484.80449	0.489786	884 ± 29	2147 ± 47	1309 ± 159	4576 ± 133	1842 ± 93	97 ± 48
7484.88788	0.518020	956 ± 27	2179 ± 44	1392 ± 156	4677 ± 125	1876 ± 86	165 ± 47
7484.89899	0.521782	935 ± 27	2204 ± 43	1481 ± 157	4676 ± 123	1830 ± 84	62 ± 47
7485.73598	0.805188	264 ± 20	649 ± 34	164 ± 107	1174 ± 92	382 ± 72	30 ± 32
7485.74709	0.808952	254 ± 20	610 ± 33	212 ± 107	1128 ± 91	371 ± 71	25 ± 33
7485.83035	0.837143	175 ± 22	431 ± 35	222 ± 113	744 ± 93	194 ± 78	18 ± 36
7485.84146	0.840905	201 ± 23	472 ± 37	126 ± 120	875 ± 98	339 ± 83	14 ± 38

Appendix B

Additional matter to Chapter 5

B.1 Data reduction of BRITE-photometry

Since the data reduction and preparation of BRITE photometry is not trivial, we provide some additional information on its processing. The points raised here mainly originate from the treatment of ζ Ori in Chapter 5, but can be generalized for most targets observed by the BRITE-Constellation. We decided to make the dedicated *Python* routines publicly available to the community so they could be used and improved upon to serve for all different data releases. These routines are available for download on Github[1], and adopt our previous experience with space photometry and the BRITE Cookbook by A. Pigulski[2] (see also Pigulski et al. 2016; Pigulski 2018). Several issues are treated by the developed routines. First, a timing issue occurs, most pronounced for certain observing modes during some of the earlier observing campaigns. Next, we expand upon the different types of data outliers encountered and how they are treated. Third, we discuss the various instrumental correlations we observed. Here, we put an additional focus on the temperature dependent point spread function (PSF) shape changes, causing a time dependent instrumental correlation between the observed signal and the CCD centroid positions. Finally, we give a few comments on the merging of different BRITE datasets.

[1] `http://github.com/bbuysschaert/BRITE_decor`
[2] `http://brite.craq-astro.ca/doku.php?id=cookbook`

B.1.1 Mid-exposure times

During some of the earlier observing campaigns by the BRITE-Constellation (including parts of the Orion II campaign), experiments were conducted on the feasibility and usefulness of on-board stacked data. As such, several exposures were merged on board, and once downlinked, they were considered as an individual datapoint. The released data, however, only provide the time at the beginning of the exposure, making it difficult to merge various datasets with distinct exposure times and a various amount of stacked images, i.e., with different durations. To this end, we determined the mid-exposure time for all observations, permitting an easier combination of datasets. These mid-exposure times were deduced for the on-board reference frame of the nano-satellite before applying the heliocentric correction.

In addition to the exposure time, the different time intervals between consecutive stacked images were accounted for. Combining this information leads to

$$\mathrm{JD_{mid}} = \mathrm{JD_{start}} + \frac{\mathrm{t_{exp}} \cdot N + \mathrm{t_{stack}} \cdot (N-1)}{2} \ , \tag{B.1}$$

where $\mathrm{JD_{mid}}$ and $\mathrm{JD_{start}}$ are the mid-exposure and start of the exposure Julian Date, respectively. The exposure time is given by $\mathrm{t_{exp}}$, the time difference between consecutive stacked images by $\mathrm{t_{stack}}$, and N is the number of stacked images corresponding to the observation. Typically, $\mathrm{t_{exp}}$ is 1 s. Different settings were accepted for the on-board stacking, but were kept constant for the duration of a given setup. Typically, the adopted $\mathrm{t_{stack}}$ varies between 13 s and 21 s while N ranges from 1 to 5. Therefore, the applied correction can add up to 30 s. Although the correction on the timing is minimal for non-stacked data, we consider it good practice to calculate and apply it nonetheless. We determined and applied this correction for all BRITE photometry, as a first step in the preparation process.

B.1.2 Outlier removal

Here, we provide an overview on the different types on spurious datapoints we encountered during our analysis of the measurements of ζ Ori. In addition, several remarks are made for some of the outliers, and suggestions given for an effective treatment. This process was performed on the full datafile corresponding to one observational setup of a given BRITE nano-satellite. In the case of strongly gapped measurements, different parts can be treated separately.

The first type of spurious signal is caused by an incomplete rendering of the aperture on the saved CCD raster. Because of the movement of the target over

the CCD raster, some of the signal was lost. These observational points were marked during the extraction since data release 2; therefore, we remove these flagged datapoints for the remainder of the analysis.

Next, we studied the behaviour of the CCD centroid position with respect to time. Not only does the centroid position have a clear relation with respect to time, but there are also outliers with respect to this trend. In the majority of cases, these outliers show anomalous behaviour along both CCD dimensions and in flux, indicating that their removal is necessary. We accounted for the relation between the centroid position and time by means of a local linear regression fit. The outliers themselves were identified by studying the distribution of the residual centroid positions. We applied the rejection scheme for both CCD dimensions simultaneously, because often measurements were found to be an outlier along both dimensions (and in flux). Additionally, this also ensured a homogeneous treatment of both CCD dimensions. Finally, we note that a rejection slightly stronger than that suggested by a visual inspection is favored. Typically, we aimed to reject up to the outer 5 % of the residual positions. This permitted an easier and clearer correction for any instrumental effects during subsequent steps, in particular for the PSF fluctuations. An example of the outlier rejection process on the CCD centroid positions is shown in Fig. B.1 for the setup 6 file of ζ Ori of BLb during the Orion II campaign.

The subsequent type of spurious signal we removed is due to a differently behaving CCD temperature, T_{CCD}, with respect to time. In addition, the temperature for satellite orbits just after significant time gaps is slightly different from the long-term relation of temperature with time. We show an example of this behaviour in Fig. B.2. There are several satellite orbits with a lower temperature than expected (even when accounting for variations with a period of 1 d). We aimed to be as conservative as possible, yet we removed these measurements to aid the subsequent instrumental correction process. Hence, we marked such datapoints for exclusions with a Graphical User Interface.

Finally, we flagged any remaining spurious flux measurements as outliers. The exact reason for such anomalous behaviour can range from mild charge transfer inefficiency (CTI) to actual stellar signal (Pablo et al. 2016). Since a basic or rough model is needed to represent the stellar signal (e.g., for pulsators or eclipsing binaries) before such outliers become apparent, this is an iterative process, that is heavily tweaked for the star under examination.

With all outliers removed, we performed one final test before applying instrumental corrections. Here, we investigated the number of observations per satellite orbit, and forced the threshold to correspond to a pre-set minimum. This permitted us to treat all satellite orbits in a coherent manner, and avoid influence from small number statistics. Typically, we aimed to have at least ten

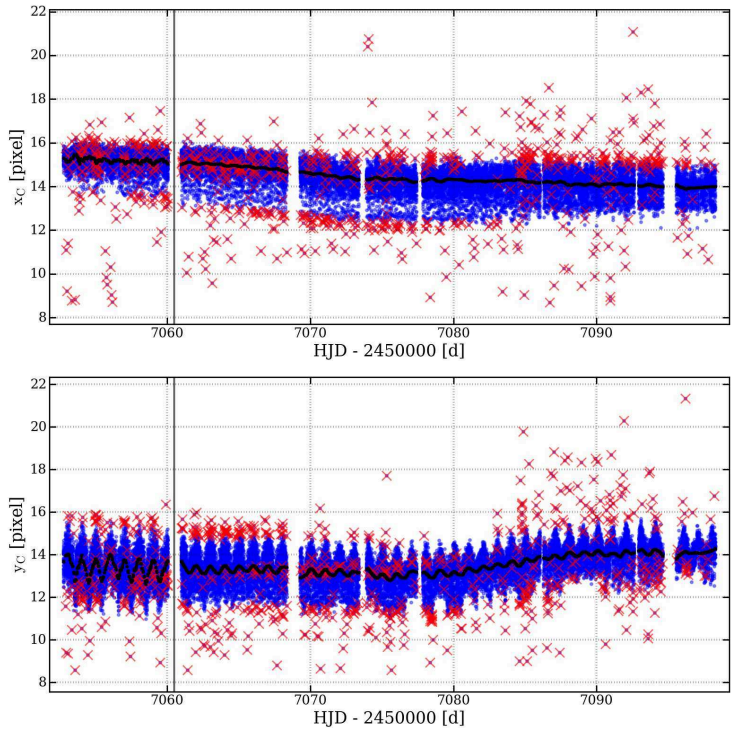

Figure B.1: Behaviour of the CCD centroid positions with respect to time for the setup 6 file of ζ Ori of BLb during the Orion II campaign at blue wavelengths. The model for the behaviour is marked in black, while the merged outliers from both centroid positions are marked by the red crosses. These outliers occur in the outer 0.8% of the model corrected centroid positions. This data file was corrected with different models for each one of the two distinct regions, indicated by the vertical line at HJD=2457060.5d.

photometric measurements per orbit passage, while accounting for on-board stackings of consecutive images.

B.1.3 Temperature-dependent PSF fluctuations

We started from the outlier-rejected photometry to correct for any possible instrumental trends or correlations. During our study of the BRITE photometry of ζ Ori, we noted one particular correlation that was much stricter than all the others and present in almost all datasets. It is now understood that this instrumental effect was caused by minor distortions in the lenses of the optical design, due to the fluctuating on-board temperature distorting the shape of the PSF. This PSF has a shape which heavily depends on the orientation with the optical axis, and strongly differs from an airy disk for targets that fall close

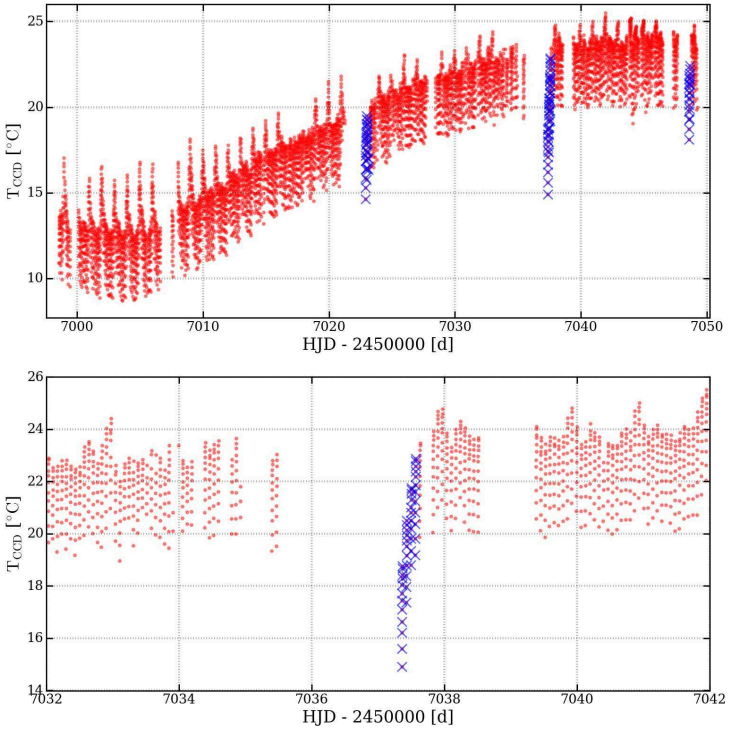

Figure B.2: *Top*: Varying on-board temperature, measured at the CCD, is indicated in red for the setup 5 file of ζ Ori of BHr during the Orion II campaign. The orbits having a different long-term behaviour are rejected and indicated by blue crosses, which mostly happens after a significant data gap. *Bottom*: Zoom of the top panel around the second gap region at HJD=2457037.

to the edge of the CCD (see Fig. 6 of Pablo et al. 2016, for the effect on the PSF with the orientation with respect to the optical axis). Therefore, the time dependent temperature variations produce a time dependent PSF shape, causing a correlation between flux and the CCD centroid position of the PSF (which was the provided metadata diagnostic). This is most likely further enhanced by intra-pixel variations. In Fig. B.3, we indicate two different CCD images for ζ Ori for the BHr setup 7 data, with different on-board temperatures (measured at the CCD). Since the centroid position is the average position of this shape on the CCD, one indeed expects the observed correlation between position and CCD temperature (and eventually flux). In the following, we discuss our correction procedure for this instrumental trend.

As the temperature on board the BRITE nano-satellites is highly variable with time, the correlation between flux and centroid position is smeared out when the full data of a given observational setup are investigated. Therefore, it is best to discretize the dataset, so that the trend becomes more apparent within each individual subset. We constructed these subsets, or time windows, by

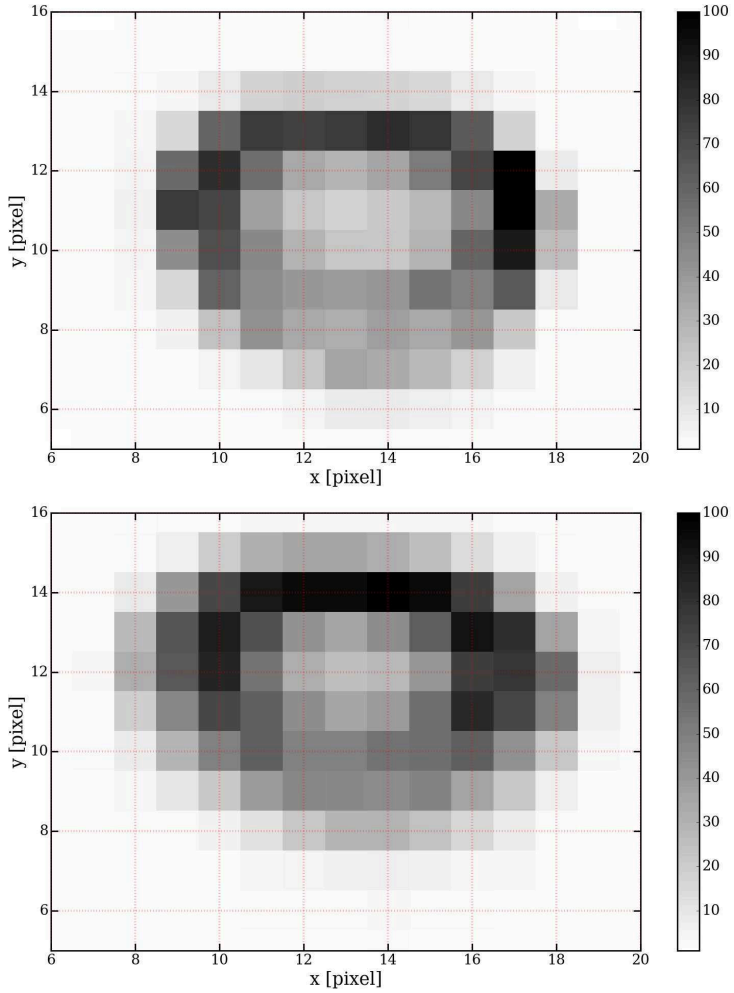

Figure B.3: Two different observations of ζ Ori during the setup 7 Orion II campaign for BHr. The top image was taken with an on-board temperature of 21.49 °C, while the bottom image has a T_{CCD} of 17.57 °C. The normalized counts per pixel is represented by the grayscale. Differences are seen in the width, the sharpness, and the location of the maximum of the non-Gaussian PSF.

studying the long-term temperature behaviour with respect to time, indicated in Fig. B.4 for BLb data of ζ Ori. This long-term behaviour was approximated by a local linear regression of the actual CCD temperature. From this trend, we defined a time window when the temperature difference was either larger than the set threshold, typically 1 ° C to 2 ° C, or when the size of a data gap was too large. These limits were then slightly refined in a consecutive step in order not to treat the same satellite orbit passage differently. We include the limits of these windows in Fig. B.4.

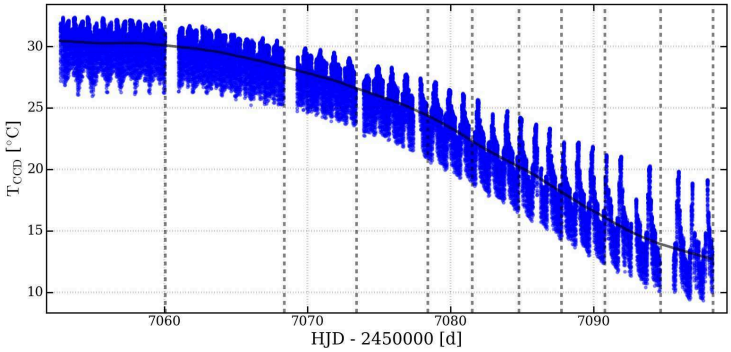

Figure B.4: Changing on-board CCD temperature with respect to time for the setup 6 data of ζ Ori of the Orion II campaign of BLb. The long-term behaviour is approximated by a local linear regression filter, which constructs a total of ten different time windows using both a temperature threshold of 2 °C and a data gap criterion of 0.5 d. The correlation for the first window is shown in Fig. B.5.

Within each time window, we intended to determine a description for the instrumental flux. Since the centroid positions are the only two parameters provided to study the PSF (for most data releases; the more recent releases have two additional parameters, see also Pigulski et al. 2016), we use these as fitting variables. This leads to the approximation

$$\begin{aligned} F(t) &= F_{\rm inst}(t) + F_{\rm star}(t) \\ &\approx F_{\rm inst}(\mathrm{PSF}(T_{\rm CCD}(t))) + F_{\rm star}(t) \\ &\approx F_{\rm inst}(x_{\rm c}(t),\, y_{\rm c}(t)) + F_{\rm star}(t)\ , \end{aligned} \tag{B.2}$$

where $F(t)$ is the total flux, containing the instrumental flux, $F_{\rm inst}(t)$, and the stellar signal, $F_{\rm star}(t)$. We assume that we can approximate $F_{\rm inst}(x_{\rm c}(t),\, y_{\rm c}(t))$ as $F_{\rm inst}(x_{\rm c}(t)) + F_{\rm inst}(y_{\rm c}(t))$, which is only fully valid if both terms are uncorrelated. This simple approximation permits the usage of one-dimensional B-splines to recover $F_{\rm inst}(x_{\rm c}(t))$ and $F_{\rm inst}(y_{\rm c}(t))$ individually. The constant length of the fitting regions along the centroid position and the order of the spline are also considered as free parameters during the fitting process. We use both the Aikaike Information Criterion (AIC) and Bayesian Information Criterion (BIC)[3], given as

$$\mathrm{AIC}(\Theta) = 2k - 2\mathcal{L}(\Theta)\ , \tag{B.3}$$

$$\mathrm{BIC}(\Theta) = -2\mathcal{L}(\Theta) + k\ln(N)\ , \tag{B.4}$$

[3]Because of the different nature of the two criteria, they might favor a slightly different solution. When this happened, we used the best $\mathcal{L}(\Theta)$ value to guide us between the proposed solutions.

to determine the optimal fit and the dominance of the respective CCD axes. Here, N is the total number of datapoints within the given time window, k is the number of estimated fitting parameters, given as

$$k = (n+1) \cdot (o+1) \ , \tag{B.5}$$

where $n+1$ is the total number of defined fitting regions, and o the order of the B-spline, respectively. We define the log-likelihood, $\mathcal{L}(\Theta)$, as

$$\mathcal{L}(\Theta) = \sum_i \left\{ \ln\left(|\mathcal{M}(\Theta; i)|\right) + \frac{|\mathcal{D}(i)|}{|\mathcal{M}(\Theta; i)|} \right\} \tag{B.6}$$

for a parameter set $\Theta = (\Theta_1, \Theta_2, \ldots, \Theta_k)$, dataset $\mathcal{D}$, and model $\mathcal{M}(\Theta)$ (see e.g., Duvall & Harvey 1986; Anderson et al. 1990). In our case, $\mathcal{D}$ contains the flux measurements as a function of a centroid position, and $\mathcal{M}(\Theta)$ its B-spline representation, within a given time window.

Typically, we found the B-spline to be of order 3, and the constant knotpoint spacing between 0.1 and 0.5 pixel. An example for such a spline representation and its effect on the BRITE-photometry is given in Fig. B.5 for the first time window of the BLb data of ζ Ori for setup file 6 shown in Fig. B.4. Again, we recommend subtracting an approximative model for the stellar flux, $F_{\rm star}(t)$, while performing the decorrelation process in an iterative manner.

Figure B.5 indicates that the main effect of this correction is a significant reduction of the instrumental noise. This noise reduction ranges from roughly a factor of 1.2 in the case of on-board stacked photometry and up to a factor of 2.5 for the non-stacked data. Thus, we encourage the application of this correction before remedying other instrumental effects.

B.1.4 Instrumental signal decorrelation

The final step in the preparation of the BRITE observations accounted for any remaining instrumental effects. Here, we consider four different possible observables that can correlate with the measured signal: i) the on-board temperature, $T_{\rm CCD}$, measured at the CCD; ii) the x-dimension and iii) the y-dimension of the CCD centroid position; and iv) the satellite orbital phase, ϕ_s. The most recent data releases of BRITE photometry provide two additional observables, indicating the sharpness of the PSF and the variations of the background of the CCD (Popowicz et al. 2017). These can also be used for this decorrelation process. Currently, the full data per observational setting of a given satellite is decorrelated as a whole, but, except for $T_{\rm CCD}$, the decorrelation process can be performed on smaller subsets of the data. An example of this

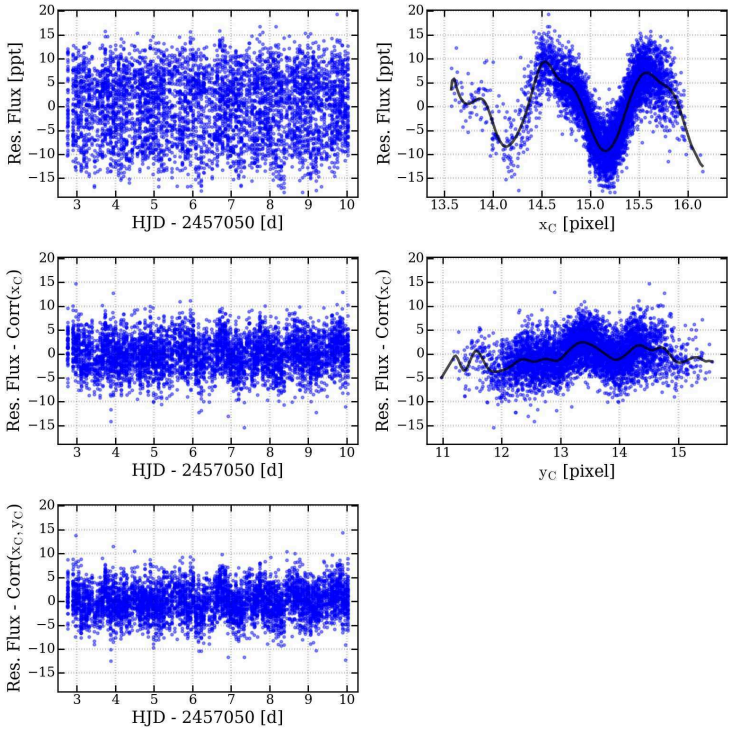

Figure B.5: *Top left*: BLb residual flux of ζ Ori given in blue, from the first correction window of Fig. B.4, which was subtracted by a local linear regression of the flux acting as a model for the stellar signal, $F_{\rm star}(t)$, and for the long-term instrumental signal. *Top right*: Same residual flux as a function of the CCD centroid position x_c indicating the correlation, which is approximated by the B-spline given in black. The correlation between flux and x_c is more dominant than with y_c, hence it is decorrelated first, as indicated by the AIC and BIC. *Middle left*: Same BLb flux residuals, now corrected for the correlation with x_c. *Middle right*: Correlation between the corrected flux residuals and y_c, together with the B-spline representation in black. *Bottom left*: Final flux residuals, corrected for the correlation with both CCD centroid positions, ready to correct for remaining instrumental effects. The periodic variations in this final product is caused by the periodic $T_{\rm CCD}$ fluctuations (see Fig. B.4).

was discussed in the previous section. In addition, working on data subsets can also aid the decorrelation with ϕ_s in certain special cases. However, we advise against doing so for $T_{\rm CCD}$, since it complicates the correction for the long-term temperature trend with respect to time.

To determine the most suitable correcting sequence, we use the normalized correlation matrix for $[{\rm F}, T_{\rm CCD}, x_c, y_c, \phi_s]$. We correct for the dominant correlation between flux and a diagnostic parameter first, but only when it is greater than 10% in absolute value. If the correlation does not pass the set

threshold, the process ends. Otherwise, we use a similar B-spline fitting scheme as in Sect. B.1.3 to represent and correct for the correlations. Once corrected, we recalculate the correlation matrix, and search for the next most significant correlation to repeat the procedure.

For the decorrelation process, we mention several caveats. First, we permit each diagnostic parameter to be used only once, if at all. Repetitive fitting with and correction for the same parameter leads to overfitting. Second, if the CCD temperature was not used for the correction, we enforced this for the case of ζ Ori since we were mainly interested in the very low-frequency regime ($< 0.5\,$). Hence, any possible effect of the long-term temperature behaviour should be accounted for. Next, because the adopted information criteria penalize representations with too many free parameters, we tried to avoid over-describing the data. Nevertheless, sensible limits should be provided to the B-spline fitting algorithm. Finally, the correlation matrix is only sensitive to linear correlations between the different parameters. Therefore, we suggest a final, visual check to ensure no remaining correlation is present in the final data product.

For our processing of ζ Ori, we only needed to correct for the on-board temperature, or we needed to enforce it. Only on a few occasions did we deduce a significant correlation with the satellite orbital phase. Thanks to the decorrelation process for the varying PSF shape, no significant correlation remained between the observed flux and the centroid positions.

Finally, after completion of the correction process, we performed a final outlier rejection for the corrected flux. As such, possible significantly altered flux is dealt with in a coherent manner. These flux outliers were flagged with a sigma filter.

B.1.5 Merging different datasets

Merging of different BRITE datasets, either from different nano-satellites or from the same one, is most often straightforward when the same exposure time and number of on-board stacking, N, were used. In the case of differences between the on-board stacking, the data should be treated with care, and detailed techniques or weighting are advised. A common method is to merge each satellite passage to one individual datapoint (e.g., Baade et al. 2016). This is only advisable, however, when one is not interested in the high-frequency region (i.e., above $f_{\rm sat}/2$), the low-frequency regime (i.e., below $\sim 0.5\,$) or when only considering model fitting. Otherwise, proper weighting is mandatory, accounting for differences in N and preferably differences in data quality (e.g., Handler 2003). There is no unique method for combining these techniques, hence the weighting method will most likely be decided on a star-by-star basis.

Table B.1: Amplitudes of the extracted frequencies for the Orion I BRITE photometry of ζ Ori. First column of each dataset presents the amplitude of the extracted frequencies for the full dataset and the second column is for the non-periodic-event excluded photometry. All amplitudes are given in ppt.

	Combined	Orion I			
Frequency		Blue		Red	
δA	± 0.14	± 0.06	± 0.07	± 0.05	± 0.06
$f_{\rm rot}$	2.14	1.92			
$2f_{\rm rot}$	3.07	4.26	3.82	4.50	4.63
$3f_{\rm rot}$					
$4f_{\rm rot}$		2.53		1.86	
$f_{\rm env}$	3.22	4.68	4.24	4.17	4.07
$2f_{\rm env}$					2.46
$4f_{\rm env}$				1.96	
$f_{\rm x}$	2.26	3.34		3.30	
$f_{\rm rot} + f_{\rm env}$	2.03	1.94			
$3f_{\rm rot} + f_{\rm env}$					
$4f_{\rm rot} + f_{\rm env}$					
$f_{\rm env} + f_{\rm x}$	2.35	4.29	2.94	5.17	
$f_{\rm env} + f_{\rm x}$	3.24				
$f_{\rm env} + f_{\rm x}$	2.65				
$f_{\rm env} - f_{\rm x}$	2.35				
$f_{\rm rot} - f_{\rm x}$	1.84				
$2f_{\rm rot} + f_{\rm x}$	1.88	1.84		3.08	
$2f_{\rm rot} - f_{\rm x}$	1.82				

B.2 Tables

Here, we provide some more information related to the extracted frequencies, presented in Table 5.3. Table B.1 and B.2 overview the amplitudes of the individual extracted frequencies. The confidence interval on the determined amplitudes is calculated using

$$\delta A = \sqrt{\frac{2}{N}} \delta N \ , \tag{B.7}$$

for which N is the number of measurements, and δN is the standard deviation on the final flux residuals (Montgomery & O'Donoghue 1999). The considerable number of corrections applied to the BRITE photometry also has an impact on the noise characteristics of the data, causing this formalism to be a strong

Table B.2: Same as Table B.1, but for the Orion II campaign BRITE photometry.

	Combined	Orion IIa				Orion IIb			
Frequency		Blue		Red		Blue		Red	
δA	± 0.14	± 0.10	± 0.13	± 0.10	± 0.11	± 0.05	± 0.07	± 0.06	± 0.07
$f_{\rm rot}$	2.14		2.81			3.13	2.66	4.13	
$2f_{\rm rot}$	3.07	2.13		2.97	3.77	2.05		5.19	3.22
$3f_{\rm rot}$				2.61	3.02	2.44		3.04	
$4f_{\rm rot}$		2.85	3.48	3.12	3.35		2.08		
$f_{\rm env}$	3.22	4.83		5.05				5.89	
$2f_{\rm env}$		4.32		4.95		2.46	2.29		
$4f_{\rm env}$		2.02	3.40			2.56			
$f_{\rm x}$	2.26		2.68	4.19	2.19			4.49	
$f_{\rm rot} + f_{\rm env}$	2.03	3.82	2.36	4.35					
$3f_{\rm rot} + f_{\rm env}$		2.53	2.10	2.80		2.48			
$4f_{\rm rot} + f_{\rm env}$					2.45			2.67	2.71
$f_{\rm env} + f_{\rm x}$	2.35	2.15							
$f_{\rm env} + f_{\rm x}$	3.24								
$f_{\rm env} + f_{\rm x}$	2.65								
$f_{\rm env} - f_{\rm x}$	2.35			2.99	4.41	4.53	3.55	3.47	4.40
$f_{\rm rot} - f_{\rm x}$	1.84								
$2f_{\rm rot} + f_{\rm x}$	1.88								
$2f_{\rm rot} - f_{\rm x}$	1.82			2.34	2.67	2.20		5.05	

underestimation of the real uncertainty. The S/N of the individual frequencies are shown in Table B.3.

Information about the different CHIRON observations is given in Table B.4.

Table B.3: S/N of the extracted frequencies for the BRITE photometry of ζ Ori.

	Combined	Orion I				Orion IIa				Orion IIb			
Frequency		Blue		Red		Blue		Red		Blue		Red	
$f_{\rm rot}$	4.6	4.7					4.4			6.0	5.2	5.1	
$2f_{\rm rot}$	5.8	7.3	5.9	7.1	7.0	4.8		5.4	4.8	4.6		5.2	4.3
$3f_{\rm rot}$								5.8	5.4	4.7		4.5	
$4f_{\rm rot}$		4.3		4.5		5.8	4.8	5.4	5.0		4.1		
$f_{\rm env}$	6.0	7.6	7.3	6.9	6.7	8.6		6.4				6.4	
$2f_{\rm env}$					4.7	6.7		6.6		4.9	4.2		
$4f_{\rm env}$				4.3		4.5	4.7			4.8			
$f_{\rm x}$	5.4	5.3		6.3			4.4	5.5	4.4			4.8	
$f_{\rm rot} + f_{\rm env}$	4.8	4.3				5.3	4.5	6.7					
$3f_{\rm rot} + f_{\rm env}$						5.6	4.3	5.8		4.4			
$4f_{\rm rot} + f_{\rm env}$									4.4			4.1	4.2
$f_{\rm env} + f_{\rm x}$	5.3	4.1	5.2	7.2		4.1							
$f_{\rm env} + f_{\rm x}$	6.2												
$f_{\rm env} + f_{\rm x}$	4.6												
$f_{\rm env} - f_{\rm x}$	5.2							5.7	6.3	7.5	6.4	4.3	4.6
$f_{\rm rot} - f_{\rm x}$	4.4												
$2f_{\rm rot} + f_{\rm x}$	4.6	4.2		5.6									
$2f_{\rm rot} - f_{\rm x}$	4.3							4.2	4.3	5.1		5.3	

Table B.4: Journal of the CTIO 1.5 m/CHIRON observations of ζ Ori A. Each spectrum consists of two co-added 8 s observations. The indicated S/N is measured at the continuum around the Hα line.

Nr.	Date	UT	Mid-HJD -2450000	Seeing [arcsec]	S/N
1	2015-02-07	01:15:18	7060.555345	0.56	81
2	2015-02-07	03:25:05	7060.645468	0.86	94
3	2015-02-08	00:39:35	7061.530469	0.68	93
4	2015-02-08	03:17:17	7061.639974	0.90	98
5	2015-02-09	01:14:17	7062.554493	0.63	95
6	2015-02-09	03:17:46	7062.640235	0.54	100
7	2015-02-11	01:55:07	7064.582692	0.88	88
8	2015-02-11	04:24:01	7064.686092	0.60	73
9	2015-02-12	01:51:37	7065.580189	0.62	87
10	2015-02-12	04:10:03	7065.676312	0.93	78
11	2015-02-13	02:00:05	7066.585985	0.97	82
12	2015-02-13	02:52:05	7066.622102	0.94	86
13	2015-02-14	02:40:06	7067.613698	1.08	89
14	2015-02-14	03:27:30	7067.646611	0.94	73
15	2015-02-15	01:50:24	7068.579105	0.83	83
16	2015-02-15	03:29:21	7068.647824	0.55	86
17	2015-02-17	01:02:54	7070.545964	0.97	79
18	2015-02-17	01:52:09	7070.580162	0.61	90
19	2015-02-18	01:01:54	7071.545180	0.87	87
20	2015-02-18	01:24:50	7071.561120	0.75	96
21	2015-02-19	02:06:47	7072.590148	0.57	90
22	2015-02-19	03:13:17	7072.636337	0.59	83
23	2015-02-20	00:48:56	7073.536020	0.94	89
24	2015-02-21	01:21:11	7074.558330	1.06	83
25	2015-02-22	01:12:48	7075.552431	1.37	93
26	2015-02-22	03:31:39	7075.648848	1.41	78
27	2015-02-23	01:29:23	7076.563859	0.92	90
28	2015-02-23	03:16:12	7076.638031	0.83	88
29	2015-02-24	00:53:07	7077.538599	0.79	88
30	2015-02-24	03:05:38	7077.630605	0.84	81
31	2015-02-25	01:51:19	7078.578924	0.92	88
32	2015-02-25	02:53:19	7078.621971	0.92	94
33	2015-02-26	02:05:12	7079.588471	0.92	99
34	2015-02-26	02:34:35	7079.608877	0.92	95
35	2015-02-27	01:56:58	7080.582671	1.11	94

Continued on next page

Table B.4 – continued from previous page

36	2015-02-27	02:50:33	7080.619881	1.05	86
37	2015-03-04	00:29:06	7085.521220	0.90	96
38	2015-03-05	01:43:53	7086.573066	0.55	86
39	2015-03-05	02:26:10	7086.602417	0.47	82
40	2015-03-06	01:19:35	7087.556104	0.69	89
41	2015-03-06	02:55:20	7087.622590	0.55	82
42	2015-03-07	01:16:27	7088.553834	0.53	78
43	2015-03-07	02:28:51	7088.604116	0.63	77
44	2015-03-08	00:52:48	7089.537330	0.66	95
45	2015-03-08	02:11:50	7089.592212	0.66	85
46	2015-03-09	01:15:40	7090.553118	0.66	88
47	2015-03-09	02:29:04	7090.604082	0.66	81
48	2015-03-10	01:54:35	7091.580048	0.59	89
49	2015-03-10	02:29:23	7091.604207	0.85	80
50	2015-03-11	01:22:10	7092.557446	0.82	86
51	2015-03-11	02:38:55	7092.610737	1.29	93
52	2015-03-12	00:48:08	7093.533717	0.79	90
53	2015-03-12	02:07:38	7093.588928	0.57	80
54	2015-03-13	00:51:32	7094.535998	0.71	83
55	2015-03-13	02:31:15	7094.605229	0.77	88
56	2015-03-14	00:46:33	7095.532448	0.99	91
57	2015-03-15	00:45:08	7096.531369	0.93	87
58	2015-03-15	02:00:03	7096.583391	0.70	91
59	2015-03-16	00:51:42	7097.535847	0.41	95
60	2015-03-16	01:44:33	7097.572541	0.41	77

List of Figures

List of Tables

Bibliography

Aerts, C. 1992, in Lecture Notes in Physics, Berlin Springer Verlag, Vol. 401, The Atmospheres of Early-Type Stars, ed. U. Heber & C. S. Jeffery, 163

Aerts, C. 1996, A&A, 314, 115

Aerts, C. 2015, in IAU Symposium, Vol. 307, IAU Symposium, 154

Aerts, C., Bowman, D. M., Símon-Díaz, S., et al. 2018, MNRAS, 476, 1234

Aerts, C., Christensen-Dalsgaard, J., & Kurtz, D. W. 2010, Asteroseismology (Springer, Heidelberg)

Aerts, C. & De Cat, P. 2003, SSRv, 105, 453

Aerts, C. & Rogers, T. M. 2015, ApJl, 806, L33

Aerts, C., Símon-Díaz, S., Bloemen, S., et al. 2017a, A&A, 602, A32

Aerts, C., Simón-Díaz, S., Groot, P. J., & Degroote, P. 2014, A&A, 569, A118

Aerts, C., Van Reeth, T., & Tkachenko, A. 2017b, ApJl, 847, L7

Aigrain, S., Hodgkin, S. T., Irwin, M. J., Lewis, J. R., & Roberts, S. J. 2015, MNRAS, 447, 2880

Aigrain, S., Parviainen, H., & Pope, B. J. S. 2016, MNRAS, 459, 2408

Aigrain, S., Parviainen, H., Roberts, S., Reece, S., & Evans, T. 2017, MNRAS, 471, 759

Alecian, E., Catala, C., Wade, G. A., et al. 2008, MNRAS, 385, 391

Alecian, E., Kochukhov, O., Neiner, C., et al. 2011, A&A, 536, L6

Alecian, E., Neiner, C., Wade, G. A., et al. 2015, in IAU Symposium, Vol. 307, IAU Symposium, 330

Alecian, G. 2015, MNRAS, 454, 3143

Alecian, G. & Stift, M. J. 2017, MNRAS, 468, 1023

Alecian, G. & Vauclair, S. 1981, A&A, 101, 16

Alentiev, D., Kochukhov, O., Ryabchikova, T., et al. 2012, MNRAS, 421, L82

Anderson, E. R., Duvall, Jr., T. L., & Jefferies, S. M. 1990, ApJ, 364, 699

Asplund, M., Grevesse, N., Sauval, A. J., & Scott, P. 2009, ARA&A, 47, 481

Augustson, K. C., Brun, A. S., & Toomre, J. 2016, ApJ, 829, 92

Aurière, M. 2003, in EAS Publications Series, Vol. 9, EAS Publications Series, ed. J. Arnaud & N. Meunier, 105

Auvergne, M., Bodin, P., Boisnard, L., et al. 2009, A&A, 506, 411

Baade, D., Rivinius, T., Pigulski, A., et al. 2016, A&A, 588, A56

Babcock, H. W. 1949, The Observatory, 69, 191

Babcock, H. W. & Burd, S. 1952, ApJ, 116, 8

Badnell, N. R., Bautista, M. A., Butler, K., et al. 2005, MNRAS, 360, 458

Baglin, A., Auvergne, M., Boisnard, L., et al. 2006, in COSPAR Meeting, Vol. 36, 36th COSPAR Scientific Assembly

Bagnulo, S., Landstreet, J. D., Mason, E., et al. 2006, A&A, 450, 777

Beck, P. G., Hambleton, K., Vos, J., et al. 2014, A&A, 564, A36

Berghoefer, T. W., Schmitt, J. H. M. M., & Cassinelli, J. P. 1996, A&As, 118, 481

Berghofer, T. W. & Schmitt, J. H. M. M. 1994, Science, 265, 1689

Bernhard, K., Hümmerich, S., Otero, S., & Paunzen, E. 2015, A&A, 581, A138

Bigot, L., Provost, J., Berthomieu, G., Dziembowski, W. A., & Goode, P. R. 2000, A&A, 356, 218

Bironi, D., Goossens, M., Cousens, A., & Mestel, L. 1982, MNRAS, 201, 619

Blaauw, A. 1964, ARA&A, 2, 213

Blazère, A., Neiner, C., Tkachenko, A., Bouret, J.-C., & Rivinius, T. 2015, A&A, 582, A110

Blomme, R., Mahy, L., Catala, C., et al. 2011, A&A, 533, A4

Bohlender, D. A. & Monin, D. 2011, AJ, 141, 169

Bohlin, R. C., Mészáros, S., Fleming, S. W., et al. 2017, AJ, 153, 234

Böhm-Vitense, E. 1958, Zeitschrift für Astrophysik, 46, 108

Bonnell, I. A. & Bate, M. R. 2002, MNRAS, 336, 659

Bonnell, I. A., Bate, M. R., & Zinnecker, H. 1998, MNRAS, 298, 93

Borra, E. F. & Landstreet, J. D. 1979, ApJ, 228, 809

Borucki, W. J., Koch, D., Basri, G., et al. 2010, Science, 327, 977

Bouret, J.-C., Donati, J.-F., Martins, F., et al. 2008, MNRAS, 389, 75

Bowman, D. M. 2017, Amplitude Modulation of Pulsation Modes in Delta Scuti Stars

Bowman, D. M., Buysschaert, B., Neiner, C., et al. 2018, A&A, Submitted

Braithwaite, J. 2007, A&A, 469, 275

Braithwaite, J. 2008, MNRAS, 386, 1947

Braithwaite, J. & Nordlund, Å. 2006, A&A, 450, 1077

Braithwaite, J. & Spruit, H. C. 2004, Nature, 431, 819

Breger, M. 2000, in Astronomical Society of the Pacific Conference Series, Vol. 210, Delta Scuti and Related Stars, ed. M. Breger & M. Montgomery, 3

Breger, M., Stich, J., Garrido, R., et al. 1993, A&A, 271, 482

Briquet, M. & Aerts, C. 2003, A&A, 398, 687

Briquet, M., Aerts, C., Baglin, A., et al. 2011, A&A, 527, A112

Briquet, M., Neiner, C., Aerts, C., et al. 2012, MNRAS, 427, 483

Briquet, M., Neiner, C., Leroy, B., Pápics, P. I., & MiMeS Collaboration. 2013, A&A, 557, L16

Bron, E., Daudon, C., Pety, J., et al. 2018, A&A, 610, A12

Browning, M. K., Brun, A. S., & Toomre, J. 2004, ApJ, 601, 512

Brun, A. S., Browning, M. K., & Toomre, J. 2005, ApJ, 629, 461

Buysschaert, B., Neiner, C., Briquet, M., & Aerts, C. 2017, A&A, 605, A104

Cantiello, M. & Braithwaite, J. 2011, A&A, 534, A140

Carrier, F., North, P., Udry, S., & Babel, J. 2002, A&A, 394, 151

Carroll, T. A., Strassmeier, K. G., Rice, J. B., & Künstler, A. 2012, A&A, 548, A95

Castor, J. I. 1986, PASP, 98, 52

Castor, J. I., Abbott, D. C., & Klein, R. I. 1975, ApJ, 195, 157

Chandrasekhar, S. 1961, Hydrodynamic and hydromagnetic stability

Chaplin, W. J. & Miglio, A. 2013, ARA&A, 51, 353

Charbonneau, P. & MacGregor, K. B. 2001, ApJ, 559, 1094

Charbonnel, C. & Talon, S. 2005, Science, 309, 2189

Choi, J., Dotter, A., Conroy, C., et al. 2016, ApJ, 823, 102

Christensen-Dalsgaard, J. 2002, Reviews of Modern Physics, 74, 1073

Christensen-Dalsgaard, J., Dappen, W., Ajukov, S. V., et al. 1996, Science, 272, 1286

Claret, A. 2000, A&A, 363, 1081

Cohen, D. H., Li, Z., Gayley, K. G., et al. 2014, MNRAS, 444, 3729

Correia, A. C. M., Boué, G., & Laskar, J. 2012, ApJl, 744, L23

Cowley, C. R., Hubrig, S., Ryabchikova, T. A., et al. 2001, A&A, 367, 939

Cox, J. P. & Giuli, R. T. 1968, Principles of stellar structure (Gordon and Breach, New York)

Cramer, N. & Maeder, A. 1979, A&A, 78, 305

Cramer, N. & Maeder, A. 1980a, A&As, 41, 111

Cramer, N. & Maeder, A. 1980b, A&A, 88, 135

Cranmer, S. R. & Owocki, S. P. 1996, ApJ, 462, 469

Cunha, M. S. 2002, MNRAS, 333, 47

Cunha, M. S., Alentiev, D., Brandão, I. M., & Perraut, K. 2013, MNRAS, 436, 1639

Cuypers, J., Aerts, C., De Cat, P., et al. 2009, A&A, 499, 967

David-Uraz, A., Wade, G. A., Petit, V., et al. 2014, MNRAS, 444, 429

De Cat, P. & Aerts, C. 2002, A&A, 393, 965

De Cat, P., Briquet, M., Aerts, C., et al. 2007, A&A, 463, 243

Degroote, P., Aerts, C., Baglin, A., et al. 2010a, Nature, 464, 259

Degroote, P., Aerts, C., Michel, E., et al. 2012, A&A, 542, A88

Degroote, P., Aerts, C., Ollivier, M., et al. 2009a, A&A, 506, 471

Degroote, P., Briquet, M., Auvergne, M., et al. 2010b, A&A, 519, A38

Degroote, P., Briquet, M., Catala, C., et al. 2009b, A&A, 506, 111

Dimitrijevic, M. S. & Sahal-Brechot, S. 1984, A&A, 136, 289

Donati, J.-F., Catala, C., Landstreet, J. D., & Petit, P. 2006, in Astronomical Society of the Pacific Conference Series, Vol. 358, Astronomical Society of the Pacific Conference Series, ed. R. Casini & B. W. Lites, 362

Donati, J.-F., Semel, M., Carter, B. D., Rees, D. E., & Collier Cameron, A. 1997, MNRAS, 291, 658

Donati, J.-F., Semel, M., & Rees, D. E. 1992, A&A, 265, 669

Duez, V., Braithwaite, J., & Mathis, S. 2010, ApJl, 724, L34

Duez, V. & Mathis, S. 2010, A&A, 517, A58

Dupret, M.-A., Grigahcène, A., Garrido, R., Gabriel, M., & Scuflaire, R. 2005, A&A, 435, 927

Duvall, Jr., T. L. & Harvey, J. W. 1986, in NATO ASIC Proc. 169: Seismology of the Sun and the Distant Stars, ed. D. O. Gough, 105–116

Dziembowski, W. & Goode, P. R. 1985, ApJL, 296, L27

Dziembowski, W. A. & Goode, P. R. 1992, ApJ, 394, 670

Dziembowski, W. A. & Goode, P. R. 1996, ApJ, 458, 338

Dziembowski, W. A., Moskalik, P., & Pamyatnykh, A. A. 1993, MNRAS, 265, 588

Dziembowski, W. A. & Pamiatnykh, A. A. 1993, MNRAS, 262, 204

Eckart, C. 1960, Hydrodynamics of Oceans and Atmospheres (Pergamon Press, Oxford)

Eikenberry, S. S., Chojnowski, S. D., Wisniewski, J., et al. 2014, ApJL, 784, L30

El'kin, V. G. 1998, Contributions of the Astronomical Observatory Skalnate Pleso, 27, 452

ESA, ed. 1997, ESA Special Publication, Vol. 1200, The HIPPARCOS and TYCHO catalogues. Astrometric and photometric star catalogues derived from the ESA HIPPARCOS Space Astrometry Mission

Featherstone, N. A., Browning, M. K., Brun, A. S., & Toomre, J. 2009, ApJ, 705, 1000

Ferrario, L., Pringle, J. E., Tout, C. A., & Wickramasinghe, D. T. 2009, MNRAS, 400, L71

Ferraro, V. C. A. 1937, MNRAS, 97, 458

Finsen, W. S. 1951, Circular of the Union Observatory Johannesburg, 112, 94

Foreman-Mackey, D., Hogg, D. W., Lang, D., & Goodman, J. 2013, PASP, 125, 306

Fossati, L., Schneider, F. R. N., Castro, N., et al. 2016, A&A, 592, A84

Freytag, B., Ludwig, H.-G., & Steffen, M. 1996, A&A, 313, 497

Fullerton, A. W., Gies, D. R., & Bolton, C. T. 1996, ApJS, 103, 475

Gautschy, A. 2009, A&A, 498, 273

Gautschy, A. & Saio, H. 1993, MNRAS, 262, 213

Gies, D. R. & Kullavanijaya, A. 1988, ApJ, 326, 813

Gilliland, R. L., Chaplin, W. J., Dunham, E. W., et al. 2011, ApJS, 197, 6

Glatzel, W. 2009, Communications in Asteroseismology, 158, 252

Głębocki, R. & Gnaciński, P. 2005, in ESA Special Publication, Vol. 560, 13th Cambridge Workshop on Cool Stars, Stellar Systems and the Sun, ed. F. Favata, G. A. J. Hussain, & B. Battrick, 571

Godart, M., Dupret, M.-A., Noels, A., et al. 2011, in IAU Symposium, Vol. 272, Active OB Stars: Structure, Evolution, Mass Loss, and Critical Limits, ed. C. Neiner, G. Wade, G. Meynet, & G. Peters, 503–504

Godart, M., Noels, A., Dupret, M.-A., & Lebreton, Y. 2009, MNRAS, 396, 1833

Goldreich, P. & Kumar, P. 1990, ApJ, 363, 694

Goode, P. R. & Thompson, M. J. 1992, ApJ, 395, 307

Gough, D. O. & Taylor, P. P. 1984, MmSAI, 55, 215

Gough, D. O. & Thompson, M. J. 1990, MNRAS, 242, 25

Gray, D. F. 2005, The Observation and Analysis of Stellar Photospheres (Cambridge University Press)

Grunhut, J. H., Wade, G. A., Leutenegger, M., et al. 2013, MNRAS, 428, 1686

Grunhut, J. H., Wade, G. A., Neiner, C., et al. 2017, MNRAS, 465, 2432

Handler, G. 2003, Baltic Astronomy, 12, 253

Handler, G., Jerzykiewicz, M., Rodríguez, E., et al. 2006, MNRAS, 365, 327

Handler, G., Matthews, J. M., Eaton, J. A., et al. 2009, ApJL, 698, L56

Handler, G., Rybicka, M., Popowicz, A., et al. 2017, MNRAS, 464, 2249

Handler, G., Shobbrook, R. R., Jerzykiewicz, M., et al. 2004, MNRAS, 347, 454

Handler, G., Shobbrook, R. R., Uytterhoeven, K., et al. 2012, MNRAS, 424, 2380

Hasan, S. S., Zahn, J.-P., & Christensen-Dalsgaard, J. 2005, A&A, 444, L29

Heger, A., Langer, N., & Woosley, S. E. 2000, ApJ, 528, 368

Heintz, W. D. 1982, A&As, 47

Hekker, S. & Christensen-Dalsgaard, J. 2017, A&ARv, 25, 1

Henrichs, H. F., Kaper, L., & Nichols, J. S. 1994, in IAU Symposium, Vol. 162, Pulsation; Rotation; and Mass Loss in Early-Type Stars, ed. L. A. Balona, H. F. Henrichs, & J. M. Le Contel, 517

Henyey, L., Vardya, M. S., & Bodenheimer, P. 1965, ApJ, 142, 841

Henyey, L. G., Wilets, L., Böhm, K. H., Lelevier, R., & Levee, R. D. 1959, ApJ, 129, 628

Herwig, F. 2000, A&A, 360, 952

Holdsworth, D. L., Kurtz, D. W., Smalley, B., et al. 2016, MNRAS, 462, 876

Holdsworth, D. L., Smalley, B., Kurtz, D. W., et al. 2014, MNRAS, 443, 2049

Howarth, I. D., Goss, K. J. F., Stevens, I. R., Chaplin, W. J., & Elsworth, Y. 2014, MNRAS, 440, 1674

Howarth, I. D. & Prinja, R. K. 1989, ApJs, 69, 527

Howarth, I. D. & Stevens, I. R. 2014, MNRAS, 445, 2878

Howell, S. B., Sobeck, C., Haas, M., et al. 2014, PASP, 126, 398

Huat, A.-L., Hubert, A.-M., Baudin, F., et al. 2009, A&A, 506, 95

Hubeny, I. & Lanz, T. 2011, Synspec: General Spectrum Synthesis Program, Astrophysics Source Code Library

Hubrig, S., Schöller, M., & Kholtygin, A. F. 2014, MNRAS, 440, 1779

Hummel, C. A., Rivinius, T., Nieva, M.-F., et al. 2013, A&A, 554, A52

Hummel, C. A., White, N. M., Elias, II, N. M., Hajian, A. R., & Nordgren, T. E. 2000, ApJl, 540, L91

Hümmerich, S., Paunzen, E., & Bernhard, K. 2016, AJ, 152, 104

Iglesias, C. A. & Rogers, F. J. 1993, ApJ, 412, 752

Iglesias, C. A. & Rogers, F. J. 1996, ApJ, 464, 943

Jackson, B. V., Buffington, A., Hick, P. P., et al. 2004, SoPh, 225, 177

Jaschek, M. & Jaschek, C. 1974, Vistas in Astronomy, 16, 131

Jeffery, C. S. & Saio, H. 2016, MNRAS, 458, 1352

Johnston, C., Buysschaert, B., Tkachenko, A., Aerts, C., & Neiner, C. 2017, MNRAS, 469, L118

Kallinger, T., Weiss, W. W., Beck, P. G., et al. 2017, A&A, 603, A13

Kaper, L., Henrichs, H. F., Nichols, J. S., et al. 1996, A&As, 116, 257

Kaper, L., Henrichs, H. F., Nichols, J. S., & Telting, J. H. 1999, A&A, 344, 231

Kholtygin, A. F., Hubrig, S., Dushin, V. V., et al. 2017, ArXiv e-prints, 1701.00733

Kippenhahn, R., Weigert, A., & Weiss, A. 2012, Stellar Structure and Evolution (Springer-Verlag, Berlin Heidelberg)

Koch, D. G., Borucki, W. J., Basri, G., et al. 2010, ApJL, 713, L79

Kochukhov, O., Bagnulo, S., & Barklem, P. S. 2002, ApJL, 578, L75

Kochukhov, O., Lüftinger, T., Neiner, C., Alecian, E., & MiMeS Collaboration. 2014, A&A, 565, A83

Kochukhov, O., Makaganiuk, V., & Piskunov, N. 2010, A&A, 524, A5

Kochukhov, O., Rusomarov, N., Valenti, J. A., et al. 2015, A&A, 574, A79

Kochukhov, O. & Ryabchikova, T. A. 2018, MNRAS, 474, 2787

Kochukhov, O., Silvester, J., Bailey, J. D., Landstreet, J. D., & Wade, G. A. 2017, A&A, 605, A13

Kochukhov, O. & Wade, G. A. 2016, A&A, 586, A30

Kubiak, K., Alves, J., Bouy, H., et al. 2017, A&A, 598, A124

Kudritzki, R.-P. & Puls, J. 2000, ARA&A, 38, 613

Kumar, P. & Quataert, E. J. 1997, ApJL, 475, L143

Kurtz, D. W. 1982, MNRAS, 200, 807

Kurtz, D. W. 1990, ARA&A, 28, 607

Kurtz, D. W., Cameron, C., Cunha, M. S., et al. 2005, MNRAS, 358, 651

Kurtz, D. W. & Martinez, P. 2000, Baltic Astronomy, 9, 253

Kurtz, D. W., Shibahashi, H., Murphy, S. J., Bedding, T. R., & Bowman, D. M. 2015, MNRAS, 450, 3015

Kurucz, R. 1993, Opacities for Stellar Atmospheres: [+0.0],[+0.5],[+1.0]. Kurucz CD-ROM No. 2. Smithsonian Astrophysical Observatory, Cambridge, MA

Kurucz, R. L. 1979, ApJs, 40, 1

Lamers, H. J. G. L. M. & Cassinelli, J. P. 1999, Introduction to Stellar Winds (Cambridge University Press), 452

Landstreet, J. D., Bagnulo, S., Andretta, V., et al. 2007, A&A, 470, 685

Landstreet, J. D., Bagnulo, S., Valyavin, G. G., et al. 2015, A&A, 580, A120

Landstreet, J. D., Borra, E. F., Angel, J. R. P., & Illing, R. M. E. 1975, ApJ, 201, 624

Landstreet, J. D., Borra, E. F., & Fontaine, G. 1979, MNRAS, 188, 609

Landstreet, J. D., Silaj, J., Andretta, V., et al. 2008, A&A, 481, 465

Lanz, T. & Hubeny, I. 2003, ApJS, 146, 417

Lanz, T. & Hubeny, I. 2007, ApJs, 169, 83

Lecoanet, D. & Quataert, E. 2013, MNRAS, 430, 2363

Lecoanet, D., Vasil, G. M., Fuller, J., Cantiello, M., & Burns, K. J. 2017, MNRAS, 466, 2181

Ledoux, P. 1951, ApJ, 114, 373

Ledoux, P. & Simon, R. 1957, Annales d'Astrophysique, 20, 185

Lee, U. & Saio, H. 1997, ApJ, 491, 839

Lefever, K., Puls, J., & Aerts, C. 2007, A&A, 463, 1093

Lehmann, H., Tkachenko, A., Semaan, T., et al. 2011, A&A, 526, A124

Leitzinger, M., Odert, P., Zaqarashvili, T. V., et al. 2016, MNRAS, 463, 965

Levato, H., Malaroda, S., Morrell, N., & Solivella, G. 1987, ApJs, 64, 487

Linder, N., Rauw, G., Martins, F., et al. 2008, A&A, 489, 713

Lomb, N. R. 1976, AP&SS, 39, 447

Loumos, G. L. & Deeming, T. J. 1978, Ap&SS, 56, 285

MacGregor, K. B. & Cassinelli, J. P. 2003, ApJ, 586, 480

Maeder, A. 2009, Physics, Formation and Evolution of Rotating Stars (Springer, Heidelberg)

Mahy, L., Gosset, E., Baudin, F., et al. 2011, A&A, 525, A101

Makaganiuk, V., Kochukhov, O., Piskunov, N., et al. 2011, A&A, 525, A97

Mantegazza, L. 2000, in Astronomical Society of the Pacific Conference Series, Vol. 210, Delta Scuti and Related Stars, ed. M. Breger & M. Montgomery, 138

Markey, P. & Tayler, R. J. 1973, MNRAS, 163, 77

Martin, A. J., Stift, M. J., Fossati, L., et al. 2017, MNRAS, 466, 613

Martins, F., Marcolino, W., Hillier, D. J., Donati, J.-F., & Bouret, J.-C. 2015, A&A, 574, A142

Mason, B. D., Wycoff, G. L., Hartkopf, W. I., Douglass, G. G., & Worley, C. E. 2001, AJ, 122, 3466

Mathis, S. & de Brye, N. 2011, A&A, 526, A65

Mathis, S., Neiner, C., & Tran Minh, N. 2014, A&A, 565, A47

Mathis, S., Palacios, A., & Zahn, J.-P. 2004, A&A, 425, 243

Mathis, S. & Zahn, J.-P. 2005, A&A, 440, 653

Mathys, G. 1991, A&AS, 89, 121

Mathys, G. 2017, A&A, 601, A14

Mathys, G., Hubrig, S., Landstreet, J. D., Lanz, T., & Manfroid, J. 1997, A&As, 123, 353

Mayor, M., Pepe, F., Queloz, D., et al. 2003, The Messenger, 114, 20

Mestel, L. 1999, Stellar magnetism (Oxford)

Michaud, G. 1970, ApJ, 160, 641

Montalbán, J. & Schatzman, E. 2000, A&A, 354, 943

Montgomery, M. H. & O'Donoghue, D. 1999, Delta Scuti Star Newsletter, 13, 28

Moravveji, E. 2016, MNRAS, 455, L67

Moravveji, E., Aerts, C., Pápics, P. I., Triana, S. A., & Vandoren, B. 2015, A&A, 580, A27

Moravveji, E., Moya, A., & Guinan, E. F. 2012, ApJ, 749, 74

Moravveji, E., Townsend, R. H. D., Aerts, C., & Mathis, S. 2016, ApJ, 823, 130

Morel, T., Castro, N., Fossati, L., et al. 2015, in IAU Symposium, Vol. 307, New Windows on Massive Stars, ed. G. Meynet, C. Georgy, J. Groh, & P. Stee, 342–347

Morel, T., Marchenko, S. V., Pati, A. K., et al. 2004, MNRAS, 351, 552

Moss, D. 1989, MNRAS, 236, 629

Moss, D. 1992, MNRAS, 257, 593

Mullan, D. J. 1984, ApJ, 283, 303

Mullan, D. J. 1986, A&A, 165, 157

Nazé, Y., Petit, V., Rinbrand, M., et al. 2014, ApJs, 215, 10

Neiner, C., Alecian, E., Briquet, M., et al. 2012a, A&A, 537, A148

Neiner, C., Briquet, M., Mathis, S., & Degroote, P. 2015, in IAU Symposium, Vol. 307, IAU Symposium, 443

Neiner, C., Floquet, M., Samadi, R., et al. 2012b, A&A, 546, A47

Neiner, C., Mathis, S., Saio, H., & Lee, U. 2013, in Astronomical Society of the Pacific Conference Series, Vol. 479, Progress in Physics of the Sun and Stars: A New Era in Helio- and Asteroseismology, ed. H. Shibahashi & A. E. Lynas-Gray, 319

Neiner, C., Mathis, S., Saio, H., et al. 2012c, A&A, 539, A90

Neiner, C., Monin, D., Leroy, B., Mathis, S., & Bohlender, D. 2014, A&A, 562, A59

Neiner, C., Wade, G., Marsden, S., & Blazère, A. 2016, ArXiv e-prints, 1611.03285

Niemczura, E., Murphy, S. J., Smalley, B., et al. 2015, MNRAS, 450, 2764

Norris, J. 1971, ApJs, 23, 213

North, P. & Cramer, N. 1984, A&As, 58, 387

Oksala, M. E., Grunhut, J. H., Kraus, M., et al. 2015a, A&A, 578, A112

Oksala, M. E., Kochukhov, O., Krtička, J., et al. 2015b, MNRAS, 451, 2015

Oksala, M. E., Silvester, J., Kochukhov, O., et al. 2018, MNRAS, 473, 3367

Oskinova, L. M., Todt, H., Ignace, R., et al. 2011, MNRAS, 416, 1456

Ouazzani, R.-M., Salmon, S. J. A. J., Antoci, V., et al. 2017, MNRAS, 465, 2294

Pablo, H., Richardson, N. D., Fuller, J., et al. 2017, MNRAS, 467, 2494

Pablo, H., Richardson, N. D., Moffat, A. F. J., et al. 2015, ApJ, 809, 134

Pablo, H., Whittaker, G. N., Popowicz, A., et al. 2016, PASP, 128, 125001

Pantillon, F. P., Talon, S., & Charbonnel, C. 2007, A&A, 474, 155

Pápics, P. I., Briquet, M., Baglin, A., et al. 2012, A&A, 542, A55

Pápics, P. I., Moravveji, E., Aerts, C., et al. 2014, A&A, 570, A8

Pápics, P. I., Tkachenko, A., Aerts, C., et al. 2013, A&A, 553, A127

Pápics, P. I., Tkachenko, A., Aerts, C., et al. 2015, ApJl, 803, L25

Pápics, P. I., Tkachenko, A., Van Reeth, T., et al. 2017, A&A, 598, A74

Paxton, B., Bildsten, L., Dotter, A., et al. 2011, ApJs, 192, 3

Paxton, B., Cantiello, M., Arras, P., et al. 2013, ApJs, 208, 4

Paxton, B., Marchant, P., Schwab, J., et al. 2015, ApJs, 220, 15

Pedersen, M. G., Aerts, C., Pápics, P. I., & Rogers, T. M. 2018, A&A, accepted [[arXiv]1802.02051]

Perryman, M. A. C., de Boer, K. S., Gilmore, G., et al. 2001, A&A, 369, 339

Petit, V., Owocki, S. P., Wade, G. A., et al. 2013, MNRAS, 429, 398

Pigulski, A. 2018, ArXiv e-prints, 1801.08496

Pigulski, A., Cugier, H., Popowicz, A., et al. 2016, A&A, 588, A55

Piskunov, N., Snik, F., Dolgopolov, A., et al. 2011, The Messenger, 143, 7

Piskunov, N. E. & Valenti, J. A. 2002, A&A, 385, 1095

Popowicz, A., Pigulski, A., Bernacki, K., et al. 2017, A&A, 605, A26

Press, W. H. 1981, ApJ, 245, 286

Preston, G. W. 1967, ApJ, 150, 547

Prinja, R. K., Massa, D., & Fullerton, A. W. 2002, A&A, 388, 587

Rainer, M., Poretti, E., Mistò, A., et al. 2016, AJ, 152, 207

Ramiaramanantsoa, T., Moffat, A. F. J., Chené, A.-N., et al. 2014, MNRAS, 441, 910

Ramiaramanantsoa, T., Moffat, A. F. J., Harmon, R., et al. 2018, MRNAS, 473, 5532

Raskin, G., van Winckel, H., Hensberge, H., et al. 2011, A&A, 526, A69

Rauer, H., Catala, C., Aerts, C., et al. 2014, Experimental Astronomy, 38, 249

Rauw, G., De Becker, M., van Winckel, H., et al. 2008, A&A, 487, 659

Rees, D. E. & Semel, M. D. 1979, A&A, 74, 1

Renson, P. & Manfroid, J. 2009, A&A, 498, 961

Ricker, G. R., Vanderspek, R., Winn, J., et al. 2016, in SPIE, Vol. 9904, Space Telescopes and Instrumentation 2016: Optical, Infrared, and Millimeter Wave, 99042B

Ricker, G. R., Winn, J. N., Vanderspek, R., et al. 2015, Journal of Astronomical Telescopes, Instruments, and Systems, 1, 014003

Rivinius, T., Baade, D., Stefl, S., & et al. 1998, in Cyclical Variability in Stellar Winds, ed. L. Kaper & A. W. Fullerton, 207

Rivinius, T., Baade, D., & Štefl, S. 2003, A&A, 411, 229

Rizzuto, A. C., Ireland, M. J., & Robertson, J. G. 2011, MNRAS, 416, 3108

Rizzuto, A. C., Ireland, M. J., Robertson, J. G., et al. 2013, MNRAS, 436, 1694

Roberts, D. H., Lehar, J., & Dreher, J. W. 1987, AJ, 93, 968

Rogers, F. J. & Iglesias, C. A. 1992, ApJs, 79, 507

Rogers, T. M. 2015, ApJL, 815, L30

Rogers, T. M. & Glatzmaier, G. A. 2005, MNRAS, 364, 1135

Rogers, T. M., Lin, D. N. C., McElwaine, J. N., & Lau, H. H. B. 2013, ApJ, 772, 21

Rogers, T. M. & MacGregor, K. B. 2010, MNRAS, 401, 191

Rogers, T. M. & MacGregor, K. B. 2011, MNRAS, 410, 946

Rogers, T. M. & McElwaine, J. N. 2017, ApJl, 848, L1

Romanyuk, I. I. & Kudryavtsev, D. O. 2008, Astrophysical Bulletin, 63, 139

Romanyuk, I. I., Semenko, E. A., & Kudryavtsev, D. O. 2014, Astrophysical Bulletin, 69, 427

Romanyuk, I. I., Semenko, E. A., & Kudryavtsev, D. O. 2015, Astrophysical Bulletin, 70, 444

Ryabchikova, T., Piskunov, N., Kurucz, R. L., et al. 2015, PhyS, 90, 054005

Saesen, S., Briquet, M., & Aerts, C. 2006, Communications in Asteroseismology, 147, 109

Saesen, S., Briquet, M., Aerts, C., Miglio, A., & Carrier, F. 2013, AJ, 146, 102

Saio, H. 2009, Communications in Asteroseismology, 158, 245

Saio, H. 2011, MNRAS, 412, 1814

Saio, H., Baker, N. H., & Gautschy, A. 1998, MNRAS, 294, 622

Saio, H., Ekström, S., Mowlavi, N., et al. 2017, MNRAS, 467, 3864

Saio, H., Kuschnig, R., Gautschy, A., et al. 2006, ApJ, 650, 1111

Samadi, R., Belkacem, K., Goupil, M. J., et al. 2010, AP&SS, 328, 253

Sana, H., de Mink, S. E., de Koter, A., et al. 2012, Science, 337, 444

Sargent, W. L. W. 1964, ARA&A, 2, 297

Savonije, G. J. 2013, A&A, 559, A25

Scargle, J. D. 1982, ApJ, 263, 835

Schatzman, E. 1962, Annales d'Astrophysique, 25, 18

Schmid, V. S. & Aerts, C. 2016, A&A, 592, A116

Schneider, F. R. N., Podsiadlowski, P., Langer, N., Castro, N., & Fossati, L. 2016, MNRAS, 457, 2355

Schwarzenberg-Czerny, A. 2003, in Astronomical Society of the Pacific Conference Series, Vol. 292, Interplay of Periodic, Cyclic and Stochastic Variability in Selected Areas of the H-R Diagram, ed. C. Sterken, 383

Schwarzschild, M. 1950, ApJ, 112, 222

Scuflaire, R., Théado, S., Montalbán, J., et al. 2008, AP&SS, 316, 83

Shibahashi, H. & Osaki, Y. 1981, PASJ, 33, 427

Shibahashi, H. & Takata, M. 1993, PASJ, 45, 617

Shiode, J. H., Quataert, E., Cantiello, M., & Bildsten, L. 2013, MNRAS, 430, 1736

Shore, S. N. 1987, AJ, 94, 731

Shore, S. N. & Brown, D. N. 1990, ApJ, 365, 665

Shultz, M., Rivinius, T., Folsom, C. P., et al. 2015a, MNRAS, 449, 3945

Shultz, M., Wade, G. A., Alecian, E., & BinaMIcS Collaboration. 2015b, MNRAS, 454, L1

Shulyak, D., Tsymbal, V., Ryabchikova, T., Stütz, C., & Weiss, W. W. 2004, A&A, 428, 993

Simón-Díaz, S., Aerts, C., Urbaneja, M. A., et al. 2017, A&A, accepted, 1711.08994

Simón-Díaz, S. & Herrero, A. 2014, A&A, 562, A135

Smalley, B., Niemczura, E., Murphy, S. J., et al. 2015, MNRAS, 452, 3334

Sota, A., Maíz Apellániz, J., Morrell, N. I., et al. 2014, ApJs, 211, 10

Soufi, F., Goupil, M. J., & Dziembowski, W. A. 1998, A&A, 334, 911

Spruit, H. C. 1999, A&A, 349, 189

Spruit, H. C. 2002, A&A, 381, 923

Stankov, A. & Handler, G. 2005, ApJS, 158, 193

Stibbs, D. W. N. 1950, MNRAS, 110, 395

Takata, M. & Shibahashi, H. 1995, PASJ, 47, 219

Talon, S. & Charbonnel, C. 2003, A&A, 405, 1025

Talon, S. & Charbonnel, C. 2004, A&A, 418, 1051

Talon, S. & Charbonnel, C. 2005, A&A, 440, 981

Talon, S. & Charbonnel, C. 2008, A&A, 482, 597

Tassoul, M. 1980, ApJS, 43, 469

Tayler, R. J. 1980, MNRAS, 191, 151

Telting, J. H. & Schrijvers, C. 1997, A&A, 317, 723

Tetzlaff, N., Neuhäuser, R., & Hohle, M. M. 2011, MNRAS, 410, 190

Tkachenko, A. 2015, A&A, 581, A129

Tkachenko, A., Aerts, C., Pavlovski, K., et al. 2014, MNRAS, 442, 616

Tkachenko, A., Aerts, C., Yakushechkin, A., et al. 2013, A&A, 556, A52

Tkachenko, A., Lehmann, H., Smalley, B., Debosscher, J., & Aerts, C. 2012, MNRAS, 422, 2960

Tokovinin, A., Fischer, D. A., Bonati, M., et al. 2013, PASP, 125, 1336

Townsend, R. H. D. 2003, MNRAS, 343, 125

Townsend, R. H. D. 2005, MNRAS, 364, 573

Townsend, R. H. D. 2008, MNRAS, 389, 559

Townsend, R. H. D., Goldstein, J., & Zweibel, E. G. 2018, MNRAS, 475, 879

Townsend, R. H. D. & Owocki, S. P. 2005, MNRAS, 357, 251

Townsend, R. H. D. & Teitler, S. A. 2013, MNRAS, 435, 3406

Tsymbal, V. 1996, in Astronomical Society of the Pacific Conference Series, Vol. 108, M.A.S.S., Model Atmospheres and Spectrum Synthesis, ed. S. J. Adelman, F. Kupka, & W. W. Weiss, 198

Turner, N. H., ten Brummelaar, T. A., Roberts, L. C., et al. 2008, AJ, 136, 554

ud-Doula, A. & Owocki, S. P. 2002, ApJ, 576, 413

Unno, W., Osaki, Y., Ando, H., Saio, H., & Shibahashi, H. 1989, Nonradial oscillations of stars (University of Tokyo Press)

Van Reeth, T., Tkachenko, A., & Aerts, C. 2016, A&A, 593, A120

Van Reeth, T., Tkachenko, A., Aerts, C., et al. 2015, A&A, 574, A17

van Winckel, H., Lloyd Evans, T., Briquet, M., et al. 2009, A&A, 505, 1221

Vanderburg, A. 2014, ArXiv e-prints

Vanderburg, A. & Johnson, J. A. 2014, PASP, 126, 948

Vauclair, S., Hardorp, J., & Peterson, D. M. 1979, ApJ, 227, 526

Villebrun, F., Alecian, E., Bouvier, J., Hussain, G., & Folsom, C. P. 2016, in SF2A-2016: Proceedings of the Annual meeting of the French Society of Astronomy and Astrophysics, ed. C. Reylé, J. Richard, L. Cambrésy, M. Deleuil, E. Pécontal, L. Tresse, & I. Vauglin, 199–202

Vink, J. S., de Koter, A., & Lamers, H. J. G. L. M. 2001, A&A, 369, 574

Wade, G. A., Folsom, C. P., Petit, P., et al. 2014, MNRAS, 444, 1993

Wade, G. A., Neiner, C., Alecian, E., et al. 2016, MNRAS, 456, 2

Waelkens, C. 1991, A&A, 246, 453

Waldron, W. L. & Cassinelli, J. P. 2001, ApJl, 548, L45

Walker, G., Matthews, J., Kuschnig, R., et al. 2003, PASP, 115, 1023

Watson, C. L., Henden, A. A., & Price, A. 2006, Society for Astronomical Sciences Annual Symposium, 25, 47

Weiss, W. W., Rucinski, S. M., Moffat, A. F. J., et al. 2014, PASP, 126, 573

Willson, L. A. 1986, PASP, 98, 37

Wraight, K. T., Fossati, L., Netopil, M., et al. 2012, MNRAS, 420, 757

Yakunin, I., Wade, G., Bohlender, D., et al. 2015, MNRAS, 447, 1418

Zahn, J.-P. 2011, in IAU Symposium, Vol. 272, IAU Symposium, ed. C. Neiner, G. Wade, G. Meynet, & G. Peters, 14

Zahn, J.-P., Brun, A. S., & Mathis, S. 2007, A&A, 474, 145

Zima, W. 2006, A&A, 455, 227

Zima, W. 2008, Communications in Asteroseismology, 155, 17

List of Publications

Publications in refereed journals

1. C. Aerts, G. Molenberghs, M. Michielsen, M. G. Pedersen, R. Björklund, C. C. Johnston, J. S. G. Mombarg, D. M Bowman, **B. Buysschaert**, P. I. Pápics, S. Sekaran, J. O. Sundqvist, A. Tkachenko, T. Van. Reeth, and E. Vermeyen: "Foward asteroseismic modeling of stars with a convective core from gravity-mode oscillations: parameter prediction and stellar model selection", The Astrophysical Journal Supplement Series, 2018, under peer-reviewed revision

2. T. Van Reeth, J. S. G. Mombarg, S. Mathis, A. Tkachenko, J. Fuller, D. M. Bowman, **B. Buysschaert**, C. Johnston, A. García Hernández, J. Goldstein, R. H. D. Townsend, and C. Aerts: "Sounding differential rotation in intermediate-mass main-sequence stars using gravito-inertial modes: new observational constraints and theoretical seismic diagnosis", Astronomy & Astrophysics, 2018, under peer-reviewed revision

3. **B. Buysschaert**, C. Aerts, D. M. Bowman, C. Johnston, T. Van Reeth, M. G. Pedersen, and C. Neiner: "Forward seismic modelling of the pulsating magnetic B-type star HD 43317", Astronomy & Astrophysics, 2018, under peer-reviewed revision

4. **B. Buysschaert**, C. Neiner, A. J. Martin, C. Aerts, M. E. Oksala, D. M. Bowman, and T. Van Reeth: "Detection of magnetic fields in chemically peculiar stars observed with the K2 space mission", Monthly Notices of the Royal Astronomical Society, 2018, under peer-reviewed revision

5. **B. Buysschaert**, C. Neiner, A. J. Martin, M. E. Oksala, C. Aerts, A. Tkachenko, E. Alecian, and the MiMeS Collaboration: "Magnetic characterization and variability study of the magnetic SPB star *o* Lup", Astronomy & Astrophysics, 2018, 476, 1234

6. C. Aerts, D. M. Bowman, S. Símon-Díaz, **B. Buysschaert**, C. Johnston, E. Moravveji, P. G. Beck, P. De Cat, S. Triana, S. Aigrain, N. Castro, D. Huber, and T. White: "K2 photometry and Hermes spectroscopy of the blue supergiant ρ Leo: rotational wind modulation and low-frequency waves", Monthly Notices of the Royal Astronomical Society, 2018, accepted for publication

7. T. Ramiaramanantsoa, A. F. J. Moffat, R. Harmon, R. Ignace, N. St-Louis, D. Vanbeveren, T. Shenar, H. Pablo, N. D. Richardson, I. D. Howarth, I. R. Stevens, C. Piaulet, L. St-Jean, T. Eversberg, A. Pigulski, A. Popowicz, R. Kuschnig, E. Zocĺońska, **B. Buysschaert**, G. Handler, W. W. Weiss, S. M. Rucinski, K. Zwintz, P. Luckas, B. Heathcote, P. Cacella, J. Powles, M. Locke, T. Bohlsen, A.-N. Chené, B. Miszalski, W. L. Waldron, M. M. Kotze, E. J. Kotze, and T. Böhm: "BRITE-Constellation high-precision time-dependent photometry of the early O-type supergiant ζ Puppis unveils the photospheric drivers of its small- and large-scale wind stuctures", Monthly Notices of the Royal Astronomical Society, 2018, 473, 5532

8. C. Neiner, M. E. Oksala, C. Georgy, N. Przybilla, S. Mathis, G. A. Wade, M. Kondrak, L. Fossati, A. Blazère, **B. Buysschaert**, and J. Grunhut: "Discovery of magnetic A supergiants: the descendants of magnetic main-sequence B stars", Monthly Notices of the Royal Astronomical Society, 2017, 471, 1926

9. **B. Buysschaert**, C. Neiner, M. Briquet, and C. Aerts: "Magnetic characterization of the SPB/β Cep hybrid pulsator HD 43317", Astronomy & Astrophysics, 2017, 605, A104

10. C. Johnston, **B. Buysschaert**, A. Tkachenko C. Aerts, and C. Neiner: "Detection of intrinsic variability in the eclipsing massive main-sequence O+B binary HD 165246", Monthly Notices of the Royal Astronomical Society, 2017, 469, L118

11. **B. Buysschaert**, C. Neiner, N. D. Richardson, T. Ramiaramanantsoa, A. David-Uraz, H. Pablo, M. E. Oksala, A. F. J. Moffat, R. E. Mennickent, S. Legeza, C. Aerts, R. Kuschnig, G. N. Whittaker, A. Popowicz, G. Handler, G. A. Wade, and W. W. Weiss: "Studying the photometric and spectroscopic variability of the magnetic hot supergiant ζ Orionis Aa, Astronomy & Astrophysics, 2017, 602, A91

12. H. Pablo, N. D. Richardson, J. Fuller, J. Rowe, A. F. J. Moffat, R. Kuschnig, A. Popowicz, G. Handler, C. Neiner, A. Pigulski, G. A. Wade, W. W. Weiss, **B. Buysschaert**, T. Ramiaramanantsoa, A. D. Bratcher, C. J. Gerhartz, J. J. Greco, K. Hardegree-Ullman, L. Lembryk, and W. L. Oswald: "The

most massive heartbeat: an in-depth analysis of ι Orionis", Monthly Notices of the Royal Astronomical Society, 2017, 467, 2494

13. **B. Buysschaert**, P. G. Beck, E. Corsaro. J. Christensen-Dalsgaard, C. Aerts, T. Arentoft, H. Kjeldsen, R. A. García, V. Silva Aguirre, and P. Degroote: "Testing the asymptotic relation for period spacings from mixed modes of red giants observed with the *Kepler* mission", Astronomy & Astrophysics, 2016, 588, A82

14. C. Neiner, **B. Buysschaert**, M. E. Oksala, and A. Blazère: "Discovery of two new magnetic bright magnetic B stars: i Car and Atlas", Monthly Notices of the Royal Astronomical Society, 2015, 454, L56

15. **B. Buysschaert**, C. Aerts, S. Bloemen, J. Debosscher, C. Neiner, M. Briquet, J. Vos, R. Manick, V. S. Schmid, H. Van Winckel, and A. Tkachenko: "*Kepler*'s first view of O-star variability: the K2 data of five O stars in Campaign 0 as a proof of concept for O-star asteroseismology", Monthly Notices of the Royal Astronomical Society, 2015, 453, 89

Publications in conference proceedings

1. **B. Buysschaert**, C. Neiner, A. J. Martin, M. E. Oksala, and C. Aerts: "Detecting magnetic fields in Ap/Bp stars observed with the K2 space mission", Contributions of the Astronomical Observatory Skalnaté Pleso, 2018, submitted, "*Stars with a stable magnetic field: from pre-main sequence to compact remnants*", August 28 – September 01, 2017, Brno (Czech Republic), Editors: M. Netopil, E. Paunzen, and V. Petit

2. **B. Buysschaert**, C. Neiner, and C. Aerts: "Magneto-asteroseismology of massive magnetic pulsators", IAU Symposium, 2017, 329, 146, "*The lives and death-throes of massive stars*", November 28 – December 02, 2016, Auckland (New Zealand), Editors: J. J. Eldridge, J. C. Bray, L. A. S. McClelland, and L. Xiao

3. M. E. Oksala, C. Neiner, C. Georgy, N. Przybilla, Z. Kesthelyi, G. A. Wade, S. Mathis, A. Blazère, and **B. Buysschaert**: "The evolution of magnetic fields in hot stars", IAU Symposium, 2017, 329, 141, "*The lives and death-throes of massive stars*", November 28 – December 02, 2016, Auckland (New Zealand), Editors: J. J. Eldridge, J. C. Bray, L. A. S. McClelland, and L. Xiao

4. **B. Buysschaert**, C. Neiner, T. Ramiaramanantsoa, N. D. Richardson, A. David-Uraz, A. F. J. Moffat, and the BRITE team: "Understanding the photometric variability of ζ Ori Aa", Proceedings of the Polish Astronomical Society, 2017, Volume 5, 101, "*Second BRITE-Constellation Science conference: Small sattelites – big science*", August 22 – 26, 2016, Innsbruck (Austria), Editors: K. Zwintz, and E. Poretti

5. **B. Buysschaert**, H. Pablo, and C. Neiner: "Preparing and correcting extracted BRITE observations", Proceedings of the Polish Astronomical Society, 2017, Volume 5, 32, "*Second BRITE-Constellation Science conference: Small sattelites – big science*", August 22 – 26, 2016, Innsbruck (Austria), Editors: K. Zwintz, and E. Poretti

6. **B. Buysschaert**, and C. Neiner: "The photometric variability of ζ Orionis Aa observed by BRITE", Proceedings of the Annual meeting of the French Society of Astronomy and Astrophysics, 2016, 229, "*SF2A-2016*", June 14 – 17, 2016, Lyon (France), Editors: C. Reylé, L. Cambrésy, M. Deleuil, E. Pécontal, L. Tresse, and I. Vauglin

Résumé

Des champs magnétiques stables et à grand échelle sont détectés à la surface de ~10% des étoiles chaudes. La théorie et les simulations numériques montrent que ces champs sont forts dans ces étoiles et modifient leur intérieur. Cette thèse étudie l'importance de ces changements de structure dus au champ magnétique. L'astérosismologie permet de sonder l'intérieur de l'étoile tandis que la magnétométrie sert à caractériser les champs magnétiques à la surface. J'ai accumulé de la photométrie spatiale de haute qualité et de la spectropolarimétrie à haute résolution pour des étoiles magnétiques connues ou candidates. Avec la photométrie, j'ai pu détecter des pulsations dans plusieurs étoiles. J'ai confirmé la présence d'un champ magnétique avec la spectropolarimétrie et obtenus les caractéristiques des champs. Ensuite, j'ai comparé les modes de pulsations observés de l'étoile magnétique HD43317 avec les fréquences théoriques issues de modèles de structure stellaire. J'ai contraint la géométrie des modes et la physique de l'intérieur stellaire. Les résultats suggèrent que l'intérieur est modifié, mais ne sont pas catégoriques. Les efforts futurs devront inclure la rotation, le magnétisme et le transport de moment angulaire dans les modèles afin d'examiner si les signatures magnétiques sont présentes dans les nombreux pulsateurs découverts par les missions astérosismiques.

Mots Clés

Étoiles chaudes, étoiles pulsantes, étoiles magnetiques, astérosismologie, magnétisme stellaire

Abstract

Stable large-scale magnetic fields are detected at the surface for ~10% of the early-type stars. Theoretical work and numerical simulations show that these fields are present and strong throughout the star, altering the deep interior. Here, we observationally investigate how signficiant these stellar structure changes caused by the magnetic field are. We use asteroseismology to probe the interior and combine it with magnetometry to characterize the large-scale magnetic field at the surface. I gather high-quality space photometry and high-resolution spectropolarimetry for known magnetic stars and candidates. With the photometry, I detect stellar pulsations for several stars. The presence of a magnetic field is confirmed with spectropolarimetry and the characteristics of the field studied. Next, I compare the observed pulsation modes of the magnetic star HD43317 with theoretical frequencies from stellar structure models. I constrain the mode geometry and the physics in the deep interior. While the results are suggestive for an altered interior, they do also agree with those for some non-magnetic stars. Further efforts to include rotation, magnetism and angular momentum transport at various levels of the employed models are worthwhile to examine whether magnetic signatures are present in the numerous pulsators found by major asteroseismic missions.

Keywords

Hot stars, pulsating stars, magnetic stars, asteroseismology, magnetic fields